UNIVERSITY OF SOUTHAMPTON

A Lagrangian Study of the Diurnal Heating of the Upper Ocean

by

Karen J. H. Thomas

Submitted in fulfillment of the requirements for the degree of

Doctor of Philosophy

December 1986

Acknowledgements

I would like to acknowledge the support of the Natural Environment Research Council who awarded me a CASE postgraduate research studentship at the University of Southampton in collaboration with the Institute of Oceanographic Sciences, Wormley. I have greatly appreciated the facilities and expertise made available to me at IOS. I thank my supervisors, Dr. Neil Wells and Dr. Raymond Pollard, for their advice and guidance. Thanks are also due to Dr. Kelvin Richards for taking over the reading of the draft thesis after Neil's car accident, particularly for his comments on the two- dimensional model and chapter 8.

I am especially grateful to Dr. Steven Alderson for his help in developing the two- dimensional model; for his patient explanations of the mysteries of mixed layer models; and for his encouragement and good humour at all times.

Without the hard work and enthusiasm of Dr. Peter K. Taylor in calibrating the meteorological instruments and advising on the calculation of the heat fluxes, this thesis would not have been possible. I would like to thank Professor S.A. Thorpe for his interest in my work, for valuable discussions of Langmuir circulations and for his comments on a draft version of chapter 6. Thanks are also due to Dr. Peter Killworth for his freely- given advice and help with mixed layer models.

I would like to thank Dr. Brian King and Dr. Meric Srokosz for the time they gave so generously to read draft versions of various chapters, and for their helpful comments and suggestions. I am also grateful to all those involved with Cruise 145 of RRS Discovery, who enabled a high quality data set to be obtained.

There are many others to whom I feel indebted; thank you to all those, particularly at IOS Wormley, who through their enthusiasm and interest in this research have given me the encouragement to persevere at times when I might have given up.

Finally, special thanks to my husband Jeremy, for his invaluable help in proof- reading and printing, for his moral support and patience, and for sharing with me both the tribulations and the successes of the past three years.

Contents

UNIVERSITY OF SOUTHAMPTON

ABSTRACT

FACULTY OF SCIENCE

OCEANOGRAPHY

Doctor of Philosophy

A LAGRANGIAN STUDY OF THE DIURNAL HEATING OF THE UPPER OCEAN

by Karen Joy Heywood Thomas

The diurnal heat budget of the upper ocean boundary layer is described for a six- day case study conducted at 46°N, 14°W during March 1984. Temperature time series were obtained at various depths between 15m and 145m below a freely- drifting spar buoy. Diurnal temperature variations of between 10mK and 30mK were observed in a mixed layer of depth 250m. Contributions to the heat budget from surface meteorological forcing and horizontal advection are calculated, but are unable to account for the large daily heating and cooling. It is suggested that the spar buoy drifted into a convergence zone, where, during the day, warm water is drawn in at the surface and carried downwards, enhancing the observed heating signal.

Possible mechanisms for such downwelling are reviewed; frontal activity is found to be of too large a scale and to produce downwelling velocities that are too small. The convergence zone may have been associated with Langmuir circulations (Langmuir, 1938). Observations of such longitudinal rolls are discussed, and the theories of their generation are described. The horizontal variability of the upper ocean is examined in closer detail for each occasion when the ship passed the spar buoy, using data from a SeaSoar survey. Variations on a scale of a few hundred metres are revealed, suggesting that the Langmuir circulations have a cell width of between 50m and 200m.

An upper ocean model is developed, comprising a row of one-dimensional models. These span the Langmuir circulation in the x-z plane and the ocean is assumed uniform along the roll. Heat is transported horizontally and vertically at each time step, by means of an imposed, non- divergent, circulating velocity field. Surface heat and momentum fluxes calculated from the meteorological measurements are applied. The spar buoy is assumed to lie in the downwelling region. The simulation of the observed heating signal in the mixed layer is greatly improved by the imposed circulation. The observed phase and amplitude are achieved by an imposed circulation giving a mean vertical velocity in the downwelling zone of about 1cm/s.

Langmuir circulations are likely to influence upper ocean experiments involving drifting buoys or floats. It should therefore be determined whether such circulations are present during the investigation, by sprinkling surface drifters onto the water and observing whether or not they converge into regular rows. Temperatures recorded by instruments drifting into downwelling zones will be anomalously warm during the heating period and anomalously cool at night.

List of figures

List of Symbols

Roman letters

a	albedo of sea surface (%)
A	cloud- dependent parameter in the solar radiation model of Smith and Dobson (1984)
B	cloud- dependent parameter in the solar radiation model of Smith and Dobson (1984)
B0	turbulent kinetic energy produced by buoyancy forcing (J)
BAROM	barometric air pressure (mb)
BFLUX	buoyancy flux (W/kg)
c	velocity of internal waves on the thermocline (m/s)
C	fractional cloud cover (eighths)
Cd	drag coefficient over sea surface
Cl	latent heat transfer coefficient
Cp	specific heat capacity of sea water (here taken as 3.99^{3}x 10 J/kg/K)
Cpair	specific heat capacity of air at constant pressure (1004J/kg/K)
Ct	sensible heat transfer coefficient
d	declination of the sun
D	cloud- dependent parameter in the solar radiation model of Smith and Dobson (1984)
dP	energy required to entrain the next level down into the mixed layer
dt	time interval or time step (seconds)
dz	vertical increment or grid spacing (m)
E	cloud- dependent parameter in the solar radiation model of Smith and Dobson (1984)
EA	surface water vapour pressure (mb)

ETA rate of evaporation from the sea surface ($kg/m^2/s$)

Ewind work done by wind stress on sea surface, $\rho 0\ (U^*)^3$

f Coriolis parameter, $2\Omega \sin\phi$

F(C) correction to longwave radiation calculation due to cloud cover

g acceleration due to gravity, $9.81 m/s^2$

GYRO ship's compass bearing

h mixed layer depth (m)

H total heat loss from the sea surface (W/m^2)

HULLTEMP temperature (°C) measured at the hull temperature sensor, 2.5m below sea surface

i level number in model

I available solar irradiance (W/m^2)

j attenuation coefficient in the parameterisation of the exponential decay of solar irradiance with depth

k attenuation coefficient in the parameterisation of the exponential decay of solar irradiance with depth

$\underline{k}$ unit vector in the vertically downwards direction

LFLUX latent heat flux (W/m^2)

LH latent heat of evaporation of water (J/kg)

LW longwave flux at the ocean surface (W/m^2)

m proportionality constant in mixed layer model

M Monin- Obukhov length (m)

n level number in model

N number of oktas of cloud cover

p pressure

P energy available for entrainment (J)

PDRY port dry bulb temperature (°C)

PDRY-WET port dry bulb minus wet bulb depression (°C)

q	mixing ratio of air
Q	total heat flux entering the ocean (W/m^2)
Q0	radiative solar flux at the top of the atmosphere, $1380 W/m^2$
QA	specific humidity of air
QS	specific humidity of air at sea surface temperature
r	fraction of a vertical grid box that is in mixed layer
Rb	bulk Richardson number
Rc	critical Reynolds number
Re	Reynolds number
Rg	gradient Richardson number
RHO	density of air (kg/m^3)
RW	relative humidity of air
RWDIR	wind direction relative to the ship
RWSPD	wind speed relative to the ship (m/s)
s	mixed layer model parameter
S	salinity (parts per thousand, ppt)
SDRY	starboard dry bulb temperature (°C)
SDRY-WET	starboard dry bulb minus wet bulb depression (°C)
SE	sine of the solar elevation
SFLUX	sensible heat flux (W/m^2)
SOLAR	incident solar radiation at the sea surface (W/m^2)
SST	sea surface temperature (°C)
SVP	saturated vapour pressure (mb)
t	time (seconds)
T	temperature (°C)
T0	typical sea temperature, defined here as 11.97°C
Ta	dry air temperature (K) = Td + 273.15
Td	dry air temperature (°C)
TVIRT	virtual temperature of air (°C)

Tw	wet bulb air temperature (°C)
u,U	horizontal velocity, x direction (m/s)
U*	oceanic friction velocity (m/s)
$\underline{v}$	horizontal velocity vector (u,v)
v,V	horizontal velocity, y direction (m/s)
Vk	Von Karman's constant, 0.42
w	vertical velocity (m/s)
W	wind energy available for mixing (J)
we	entrainment velocity (m/s)
WDIR	wind direction
WSPD	wind speed (m/s)
x,y	cross- roll and along- roll directions (m)
z	depth in ocean, positive downwards (m)
Z0	parameter in the exponential decay of turbulent energy with depth (m)

Greek letters

α	thermal expansion coefficient of sea water ($^{\circ}C^{-1}$)
β	Ekman depth (m)
γ	dissipation
Γ	stratification (°C/m)
δ	fraction of penetrative convection
ΔT	temperature difference between two vertically dispaced locations
ϵ	emissivity of the ocean surface
ζ	eddy diffusion coefficient of momentum
η	eddy diffusion coefficient of heat
θ	hour angle of the sun
κ	kinetic energy
λ	angle of Ekman roll instability

μ generalised drag coefficient

ν viscosity

ξ parameter determining shape of Stommel solution for a wind-driven gyre

ρ density of sea water (kg/m^3)

$\rho 0$ a constant density, taken as $1027.1 kg/m^3$

σ Stefan- Boltzmann constant, 5.67×10^8 $W/m^2/K$

$\tau(\tau x, \tau y)$ wind stress (x and y components, N/m^2)

Υ vertical shear (s^{-1})

ϕ latitude

χ coefficient in two- exponential decay of solar radiation in the ocean

Ψ stream function

ω parameter determining shape of Stommel solution for a wind-driven gyre

Ω angular speed of rotation of the earth about its axis

Acronyms

CL	Craik- Leibovich (theories)
CTD	Conductivity, Temperature and Depth measuring instrument
EM	ElectroMagnetic
IOS	Institute of Oceanographic Sciences, Wormley, U.K.
JASIN	Joint Air- Sea Interaction (experiment)
KT	Kraus- Turner (model)
MILE	MIxed Layer Experiment
NATO	North Atlantic Treaty Organisation
NERC	Natural Environment Research Council
PRT	Pollard- Rhines- Thompson (model)
PWP	Price- Weller- Pinkel (model)
RRS	Royal Research Ship
VACM	Vector Averaging Current Meter
VAECM	Vector Averaging Electromagnetic Current Meter

Chapter 1

Introduction

This thesis describes an experimental study of the diurnal heat budget of the upper ocean. The data suggest methods of modelling numerically the penetration of the daily solar heating effect. Many different physical processes will be shown to be at work in the upper ocean. Before summarising the aims and achievements of the work, these processes will be discussed, together with the importance of further understanding of upper ocean thermodynamics.

During the last decade, there have been several large international experiments dedicated to measurement of mixed layer evolution, including the Joint Air- Sea Interaction Project (JASIN, Pollard et al., 1983a) and the Mixed Layer Experiment (MILE, Davis et al., 1981). Effort has been directed towards the development of upper ocean models, and therefore to parameterising the physical effects observed in situ and in laboratory experiments. The advent of remote sensing as a valuable tool in understanding the oceans has prompted questions about small scale processes occurring at the ocean surface, so that the interaction between microwave radar and the ocean surface roughness may be understood.

The oceanic surface boundary layer is important for several reasons. Firstly, it is in this zone that the ocean and atmosphere interact. The current trend in climate simulation is towards coupled ocean- atmosphere models. These may be used, for example, to estimate the long- term atmospheric temperature increase due to carbon dioxide emissions, or for the prediction of large- scale changes in ocean currents, such as El Nino events. The physics must be understood whereby heat and momentum enter, and are stored by, the ocean. In the field of ocean acoustics, interest has arisen in predicting the temperature or density profile of the upper ocean, so that the speed of

sound is known. One should not forget also the influence that the mixed layer temperature and depth exert on biological activity in the upper ocean; studies of the plankton require a knowledge of mixing and turbulent heat transport. There is a need to model the physical processes on a diurnal time scale, so that one may model the chemical and biological processes which usually occur on time scales of less than a day.

Oceanic turbulence is discussed by Phillips (1977). A 'turbulent flow' is defined by Chambers Dictionary of Science and Technology as 'fluid flow in which the particle motion at any point varies rapidly in magnitude and direction'. This definition is not satisfactory since it would include a random wave field; turbulence implies some degree of mixing which a random wave field does not possess. A more useful definition in this context is given by Scorer (1978): 'turbulence is a complex motion which causes diffusion'. Thus heat and momentum are stirred into the ocean surface layers, in an irreversible process which involves a cascade of energy from large to small scales. Scorer's more precise definition is 'chaotic vorticity' which summarises well the concept of eddies causing diffusion. Turbulence is the means by which a mixed layer is formed and sustained, but its action is not fully understood. Thorpe (1985) reviews current thinking on small scale processes in the upper ocean and comments that the fundamental question still to be answered is 'What is the nature of turbulence below the sea surface?'

Shay and Gregg (1984) have presented the first direct measurements of oceanic turbulence due to surface cooling. They find that turbulent dissipation rates in the ocean vary with the buoyancy flux in a similar way to those in the atmosphere. In that part of the mixed layer where the turbulent energy balance is maintained predominantly by the surface buoyancy flux rather than wind stress (i.e. at depths greater than the

Monin- Obukhov length), turbulent dissipation is uniform and proportional to the surface buoyancy flux. In their more recent paper (Shay and Gregg, 1987), they point out that the mixed layer depth may only be found by studying the microstructure. Unless a profiling instrument can detect a temperature change of 5-20mK, the mixed layer depth may be overestimated by a factor of two.

When the wind blows across the sea surface, momentum is imparted to the ocean. This is driven partly directly by the interfacial stress, and also indirectly by the surface waves losing momentum to the mean flow by processes such as wave breaking. Much attention has been devoted to parameterising these effects. In other words, given a certain wind speed, the amount of turbulent energy transferred to the upper ocean is required. (e.g. Kato and Phillips, 1969; Denman and Miyake, 1973; Kantha et al., 1977). These results will be discussed further in chapter 5. Here it should be noted only that some fraction of the wind's energy provides turbulence to break down stratification in the water and produce a mixed layer. The phrase 'mixed layer' is increasingly being replaced in the literature by 'mixing layer', since the assumption of an instantaneously well- mixed layer may not be valid during, for example, daytime stratification. However, in common with most of the current literature, the former phrase shall be used throughout this thesis. Density gradients in the mixed layer are always much less than in the thermocline.

Warmer water is lighter than cooler water at the same salinity. Therefore heating of the ocean surface layers by the sun provides stable stratification against which the wind must work in order to mix the water. Conversely, cooling at the sea surface creates cool, dense water which will initiate overturning and mixing in the upper layers by convection.

These three processes (wind mixing, stratification and convection) are further complicated by horizontal advection of water. If a mixed layer data set is to be used to test models, the heat budget for the location must balance. Measurements of mixed layer depth and temperature are compared with measured surface heat fluxes. Rarely does the heat budget balance; the difference is usually attributed to the (unmeasured) horizontal advection (e.g. Price et al., 1986). Bowers et al. (1986) use the heat budget to identify those occasions on which horizontal advection dominates, and eliminate these from their data record. The resulting data set is then compared with models. This somewhat dubious process means that one may not identify advective effects when they happen to be equal and opposite to that of some other event. Denman and Miyake (1973) conclude from the data of Tabata (1965) that at Ocean Station Papa (50°N, 140°W) advection is not important on time scales of less than a month. This fact has since been exploited to test upper ocean models at Ocean Station Papa (see chapter 5). Garwood (1979) points out that Ocean Station Papa provides the longest uninterrupted series of synoptic meteorological and oceanographic observations.

The Mixed Layer Experiment (MILE) (Davis et al., 1981) examined the upper ocean near Ocean Station Papa during a 20- day period in autumn 1977. Temperature and horizontal velocity measurements were obtained at various depths both in and below the mixed layer, at two fixed surface moorings. The heat and momentum budgets are discussed by Davis et al. and both are found to balance satisfactorily. The horizontal advection of heat is neglected since, although a time series of horizontal velocities is available, the horizontal temperature gradient is not known. However, using towed thermistor chain observations in the same area to estimate the temperature gradient, Davis et al. claim that the heat flux due to horizontal advection is

only 20% of the 20- day average surface heat flux. The assumption that this is negligible may be permissible if one is only interested in the closure of the 20- day heat budget. However, if the diurnal heating of the mixed layer is of interest, this approach may not be valid, since it is not known whether the effect of advection is constant in time. It is more likely that both velocities and temperature gradients vary with time. Davis et al. comment that for short periods of time the observed currents were very much larger than usual, and here advection would be expected to be important.

Davis et al. estimate vertical advection by observing the rise or fall of isotherms beneath the mixed layer. Above this, the vertical velocity is assumed to decrease linearly to be zero at the surface. Measurements in the thermocline show that the thermocline moves vertically as a whole, mainly in response to storms. This is probably the result of Ekman pumping, caused by wind stress curl producing surface convergence. It should be noted that measuring the vertical motion of isotherms below the mixed layer will not reveal any vertical motion that occurs only in the mixed layer.

The heat budget is calculated using 12.5 hour averages so the diurnal signal is largely filtered out. When the effect of vertical advection is included, Davis et al. find that the heat budget will balance to about 20% accuracy or $20 W/m^2$. They comment that such success depends on a sound knowledge of the vertical advection as well as the surface heating, that horizontal advection must be small, and that the time series must be sampled frequently in order to identify noise such as internal waves.

During the JASIN experiment (Pollard et al., 1983a) an intensive survey of the upper ocean in an area of deep water around 59°N, 12°30'W was undertaken using 14 ships and three aircraft. Data were collected between July and September 1978; for much of this period there were

light winds and high pressure. Spatial coverage of the area revealed that eddies and frontal structures were important. A Lagrangian experiment was performed over several days (Pollard, 1983) using a freely drifting, upper ocean spar buoy. Instruments hanging beneath the buoy measured temperature and horizontal current velocities. Pollard discusses the wind- driven momentum budget using the velocity measurements at the current meters. He finds that the vertical velocity structure in the mixed layer cannot be accounted for by wind stress and Coriolis force alone. He concludes that horizontal density gradients are required to balance the momentum budget, due primarily to the slope of the mixed layer base. The heat budget was not examined.

It is important, then, to know the horizontal advection at upper ocean instruments, if a heat budget is to be calculated. Measurements of temperature and velocity are required throughout the mixed layer, and also well into the thermocline if the effects of Ekman pumping are to be estimated. This thesis is concerned with a six- day temperature and velocity data set obtained at current meters in the upper half of a deep (O(200)m) mixed layer. The aim was to use upper ocean temperature data to test and develop one- dimensional mixed layer models on a diurnal time scale. By a combination of ship surveys and freely drifting instrumentation, the influence of advection could be quantified; at the spar buoy such effects should be small since a Lagrangian reference frame drifting with the instrumentation is used. The data set and experimental details are described in chapter 2. A time series of temperature at various depths in the mixed layer beneath the drifting spar buoy over a period of six days is presented.

In order to model air- sea interaction, it is necessary to have a good knowledge of the meteorological surface fluxes such as wind stress, sensible and latent heat fluxes, precipitation and solar heating. Chapter 3 discusses the meteorological observations made, and

the derivation and magnitudes of the fluxes. During the six- day deployment, the winds were strong (greater than 10m/s) but there were several days of substantial solar radiation (more than 500W/m^2). This therefore provides an ideal case study to investigate the diurnal heating of the upper ocean. One wishes to know how quickly and how deeply the heating signal penetrates into the ocean, to what extent wind mixing is inhibited by density stratification, and whether a one-dimensional model is applicable.

The surface heat flux data are used in chapter 4 together with temperature and velocity data from the drifting spar instrumentation to study the heat budget of the mixed layer. It is shown that the heat budget does not balance. A number of possible reasons for this are debated. The usual explanation of horizontal advection is ruled out since it proves to be too small an effect and is in anti- phase with the observed signal. It is suggested that the spar buoy may tend to drift preferentially into a surface convergence zone, where downwelling helps to convey heat downwards.

Chapter 5 describes the development of the various types of upper ocean model. Mixed layer models are introduced together with the underlying equations. Two main types of mixed layer model are discussed: the Kraus- Turner type model, which uses an energy budget to predict entrainment, and the Pollard- Rhines- Thompson type model, which uses a stability criterion on the shear at the base of the mixed layer. Various modifications to the models suggested in the literature are studied. Results of a set of tests are presented, in which a sinusoidal surface heating is applied. Uncertainties in the model parameterisations are reviewed. Finally each model is run using the meteorological forcing calculated in chapter 3, to compare the prediction of each model with the real data. These runs are not expected to simulate the real data exactly, since the heat budget was

shown in chapter 4 not to balance. However they provide a useful standard against which to judge the more complex models developed in chapter 8.

In chapter 6 is presented a literature review of two- dimensional oceanic features that might cause the surface convergence proposed in chapter 4. The most likely causes are either Langmuir circulations or frontal activity and these are discussed at length. Langmuir circulations may be caused either by wave- current interaction or by Ekman instability of the mixed layer. Likely scales of these phenomena are debated, and fronts are shown to be of too large a scale to cause the small- scale, narrow downwelling region required. The chapter includes a discussion of various experiments in which anomalously large downwind currents have been experienced by near- surface drifters or drogues; these may be influenced by Langmuir circulations.

In chapter 7 evidence for or against fronts and Langmuir circulations is sought and discussed. It is argued that a front would be unable to supply sufficient downwelling to resolve the heat budget described in chapter 4. The SeaSoar data are examined to reveal the horizontal scale of variations in temperature. The data support the existence of Langmuir circulations having a cell width of about 100-300m. This is in accord with the observations and numerical model predictions that cell width is usually of the same order as the mixed layer depth.

A quasi- two- dimensional model is developed in chapter 8, consisting of a row of one- dimensional Kraus- Turner models. Advection in both vertical and horizontal directions is achieved by means of an imposed non- divergent velocity field. Temperatures in the convergence and downwelling zone are compared with those predicted by the one- dimensional Kraus- Turner model of chapter 5. The effect of the circulation on the mixed layer structure is described. It is found

that the simulation of the diurnal heating signal is improved by the imposed circulation. Suggestions are made for future work to model the interaction between mixed layer dynamics and thermodynamics, and the Langmuir circulations.

The final chapter draws together the conclusions of the project and discusses the implications of the findings for air- sea interaction. Further experimental studies of the upper ocean are required to determine the dominant processes by which the diurnal heating signal reaches the upper few hundred metres of the ocean. If drifting floats or buoys are deployed, it is important to remember that they will exhibit a tendency to drift into convergence zones, and that they may therefore experience more downwelling than the upper ocean as a whole. Instrumentation such as that attached to the spar buoy (chapter 2) should include meters measuring vertical current as well as horizontal current. Surface drifters (such as computer cards) should be sprinkled routinely on the ocean surface during mixed layer experiments, so that Langmuir circulations are identified and their effect on upper ocean structure may be taken into account.

Chapter 2

Description of the Experiment

2.1 Introduction

The data to be discussed were collected on Cruise 145 of the NERC research vessel RRS Discovery (Pollard et al., 1984). The aim of the cruise was to observe the structure of the upper ocean at the end of winter. In particular, it was hoped to examine the efficiency and relative strengths of convection and wind mixing in conveying the diurnal signal of solar heating downwards into the ocean. If the heat budget balanced, it would be deduced that the assumption of a horizontally homogeneous ocean was valid. In this way, the eddy coefficient for diffusion of heat might be estimated. The intention was to obtain an accurately- calibrated, comprehensive data set, with good coverage of the mixed layer and thermocline, and a horizontal extent of a few tens of kilometres. Combining this with a high quality meteorological data set from the same area would enable the testing and calibration of upper ocean, one- dimensional mixed layer models. The cruise was undertaken at the end of winter since at this time the mixed layer is deep, so the diurnal heating effect is more obvious than in a shallow mixed layer depth where the diurnal input may be complicated by the remnants of the previous day's structure (Stommel et al., 1969). Also strong winds (more than 10m/s) might be expected. Two sites were chosen, at which different mixed layer depths were expected: around 40°15'N 15°0'W and 45°45'N 13°40'W. Previous cruises in this area (e.g. Discovery Cruise 132, Pollard et al., 1983a) had suggested that the southern site would give a mixed layer depth of the order of 100m while the northern site would have a mixed layer depth of about 300m, approaching the limit of the profiling depth of the instrumentation used.

The cruise took place during February and March 1984. A track plot is given in figure 2.1 and is annotated with day of year, and time. The ship left Gibraltar on 25th February (day 56) and laid a mooring at the southern site (40°15'N, 15°0'W) on day 60. The northern site (45°45'N, 13°40'W) was surveyed between days 62 and 73, after which the ship steamed back south to study the southern site. A similar six- day survey preceded the final leg into port at Oporto. The main instrumentation comprised a drifting spar buoy and a SeaSoar. The spar buoy drifts freely with the current in the upper ten metres. Beneath it are suspended current meters measuring temperature and horizontal current velocity. The SeaSoar is a profiling CTD fish producing detailed measurement of the upper ocean temperature and salinity. It is towed behind the ship during a survey. The instrumentation will be discussed further in section 2.2.

At the southern site, the mixed layer was shown to be 150-200m deep. The SeaSoar survey showed that the water there was frontal, since horizontal gradients of temperature were particularly large. The spar was caught up into what may have been a frontal jet. It moved northwards at an average speed of more than 14cm/s. This unfortunately means that the southern area site is not suitable using the present instrumentation for a study of the mixed layer physical processes, since these would be dominated by horizontal advection of structure in the water due to the front. The study of mixed layer processes in the region of a front will require a concerted oceanographic effort beyond the resources of this experiment; at present even the mixing and stratification in non- frontal regions require more understanding.

After leaving the southern site, RRS Discovery steamed northwards towing the SeaSoar to obtain a vertical section of the upper 400m temperature and salinity structure. Figure 2.2 (Pollard, personal communication) shows the density structure found. ~~Isobars~~ Isopycnals are of

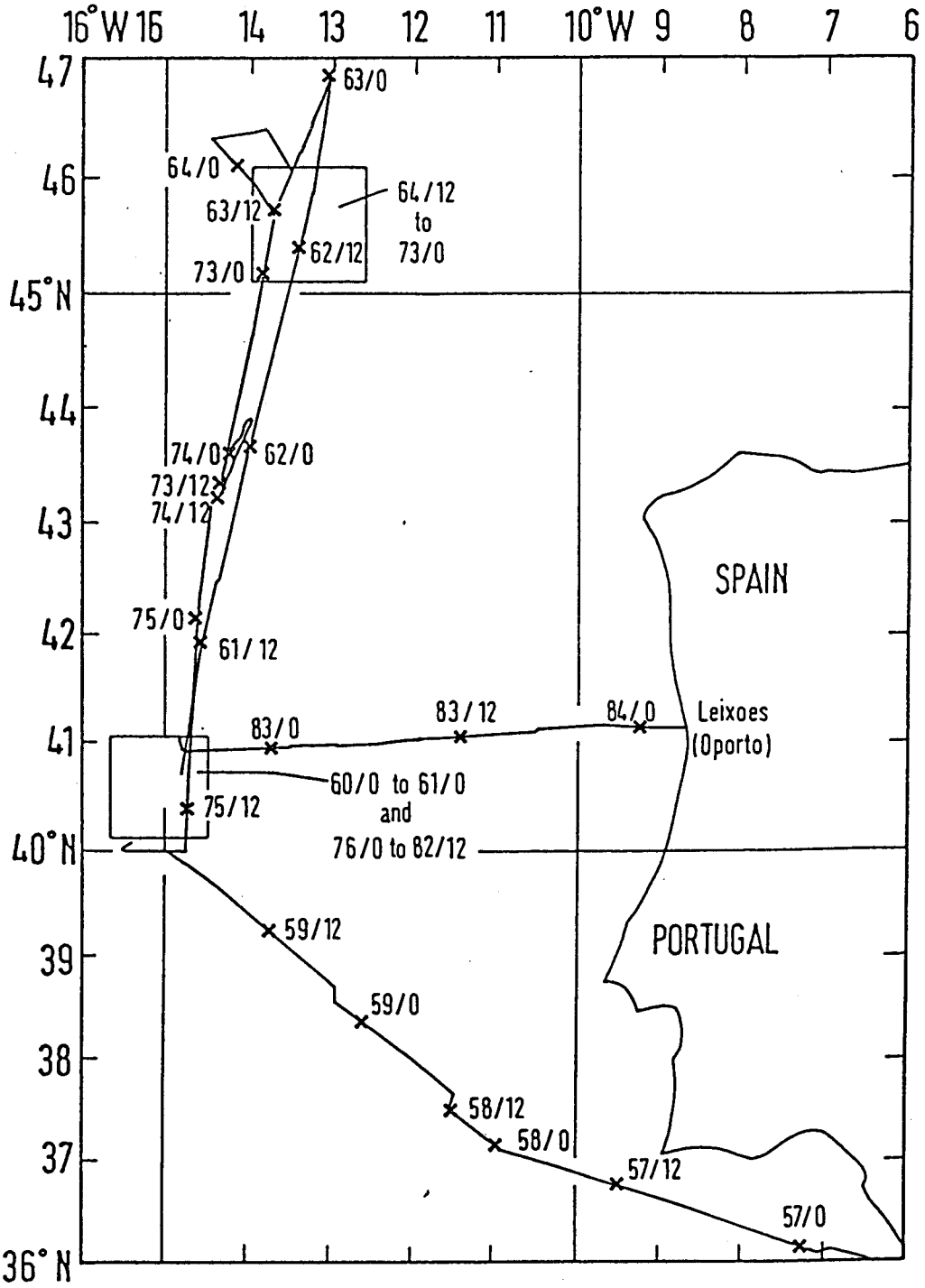

Figure 2.1 : Ship track plot, RRS Discovery Cruise 145. Day number and time are annotated along the track (from Pollard et al., 1984)

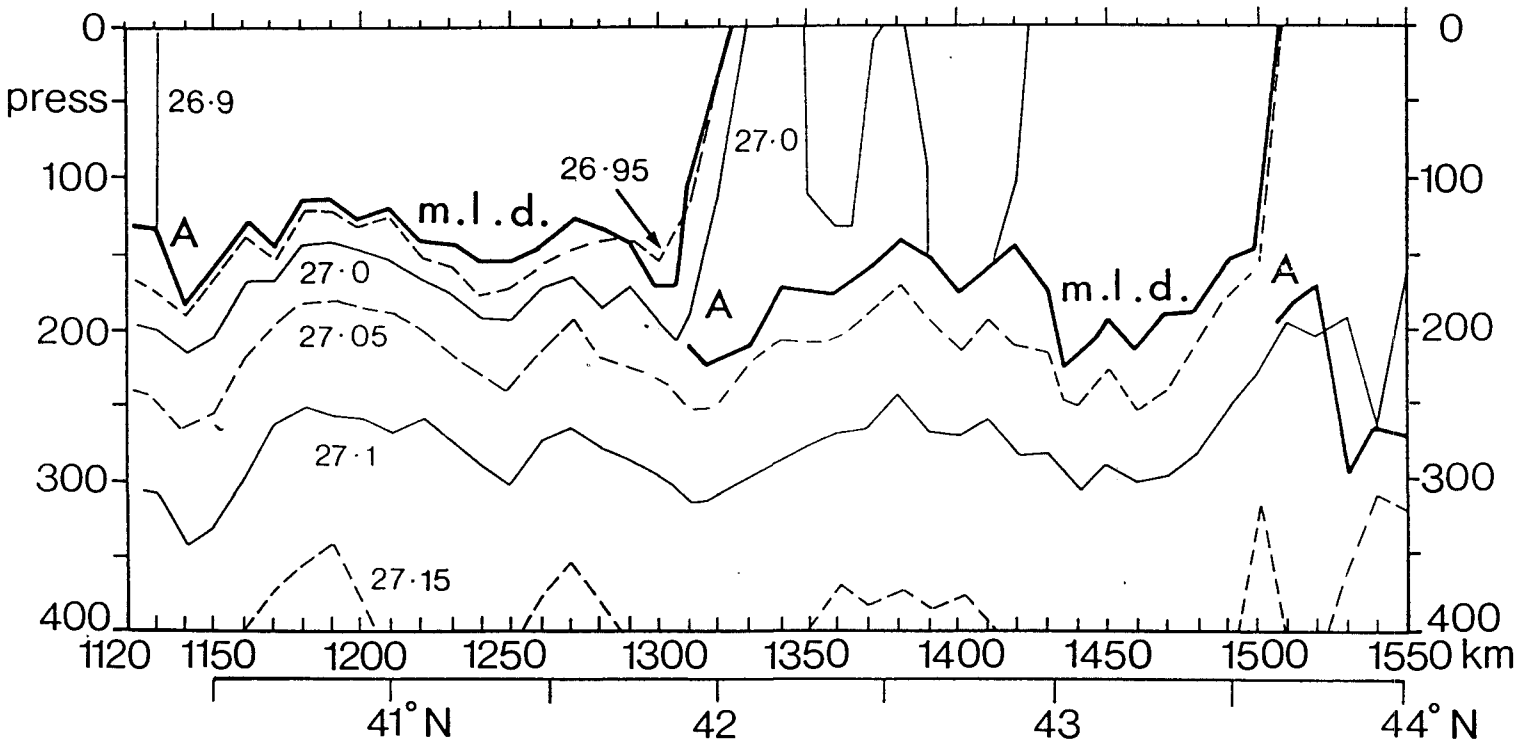

Figure 2.2 : A long meridional density section at 14°W shows the mixed layer depth controlled primarily by fronts (marked A) and mesoscale features in the thermocline. The SeaSoar section was sampled between 29th February and 1st March 1984. The solid line depicts the mixed layer depth while contours of potential density are drawn every 0.05kg/m^3.

potential density minus 1000kg/m^3. The mixed layer depth is shown as a heavy line. It is found that the mixed layer depth is controlled mainly by fronts (marked A) and mesoscale features in the pycnocline, suggesting that, on some scales, air- sea interaction is not the major influence on mixed layer depth.

Figure 2.3 gives a more detailed meridional section of the temperature structure at the northern site. Notice the pronounced front at about 1780km, the water to the right (north) being stratified almost to the surface. After encountering this water, the ship turned back south to deploy the spar away from the influence of the front. The SeaSoar survey revealed warmer water (12°C at about 100m) on the northern side of the spar, and cooler water (11.95°C at about 100m) on the southern side. It was therefore deduced that the spar must have been deployed somewhere in the region marked on figure 2.3. Vertical temperature gradients in the upper 200m are about 0.1°C per 100m, as opposed to at least 0.3°C per 100m in the frontal region. Horizontal temperature gradients near the spar are of the order of 0.01°C per kilometre (see chapter 4 for discussion of the spatial temperature structure). Further details concerning the northern area spar deployment will be given in section 2.3.

2.2 Instrumentation

2.2.1 Spar buoy

The drifting spar buoy (Pollard et al., 1987) is the same as was used during JASIN (Pollard, 1983). A diagram of the spar and current meter rig is shown in figure 2.4, together with a schematic picture of the surface rig. The spar buoy consists of an aluminium cylinder, 8.9m long and 0.25m in diameter, which floats vertically just below the sea surface. More inertia, to increase the natural period of oscillation of the spar, is provided by a canvas sleeve of 0.5m diameter, covering the bottom 3.0m. A smaller section of the spar, diameter 0.11m,

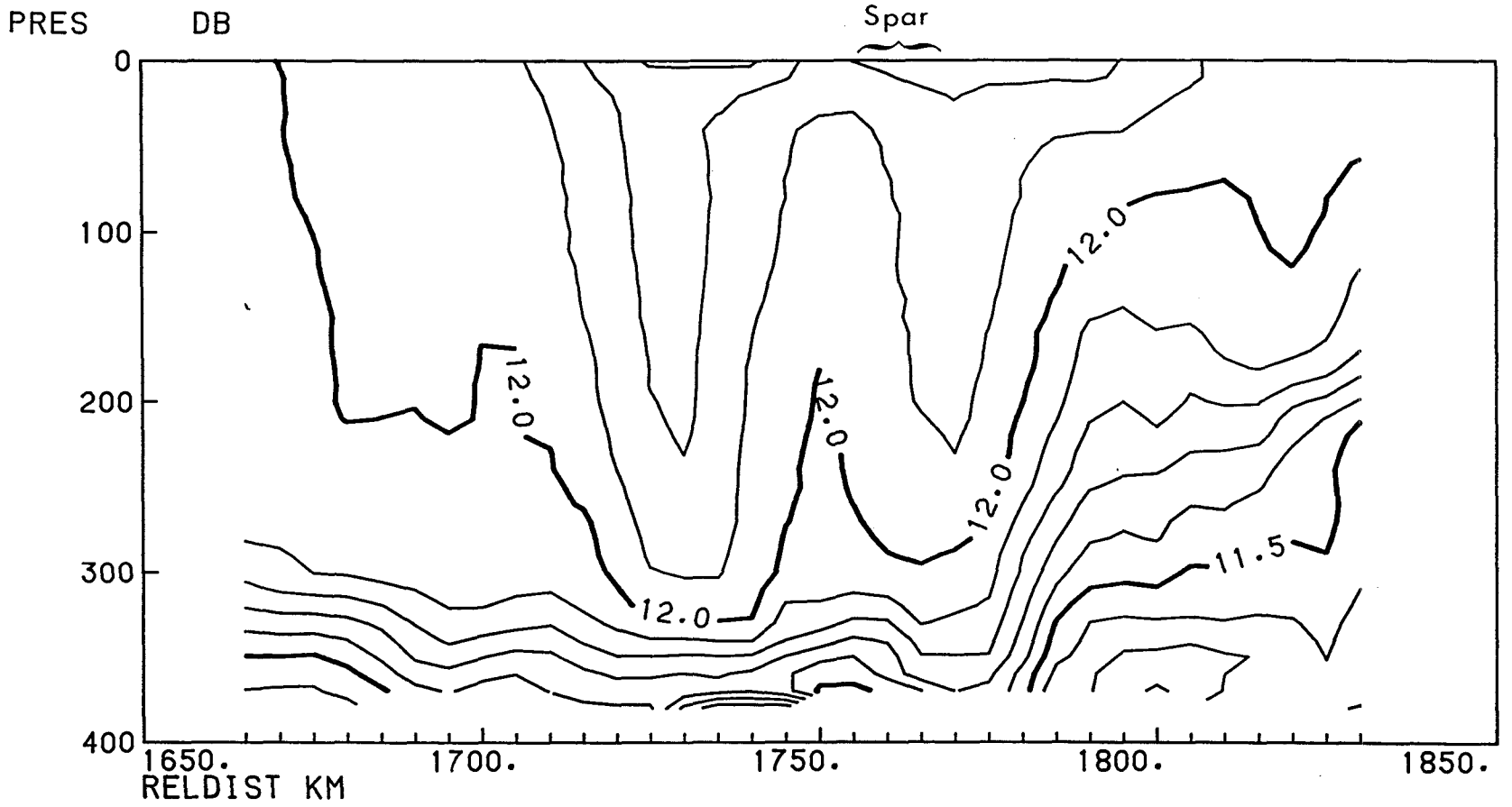

Figure 2.3 : Detailed temperature structure of the region in which the spar buoy was deployed. Notice the frontal structure to the right (north). The estimated position of the spar deployment is marked.

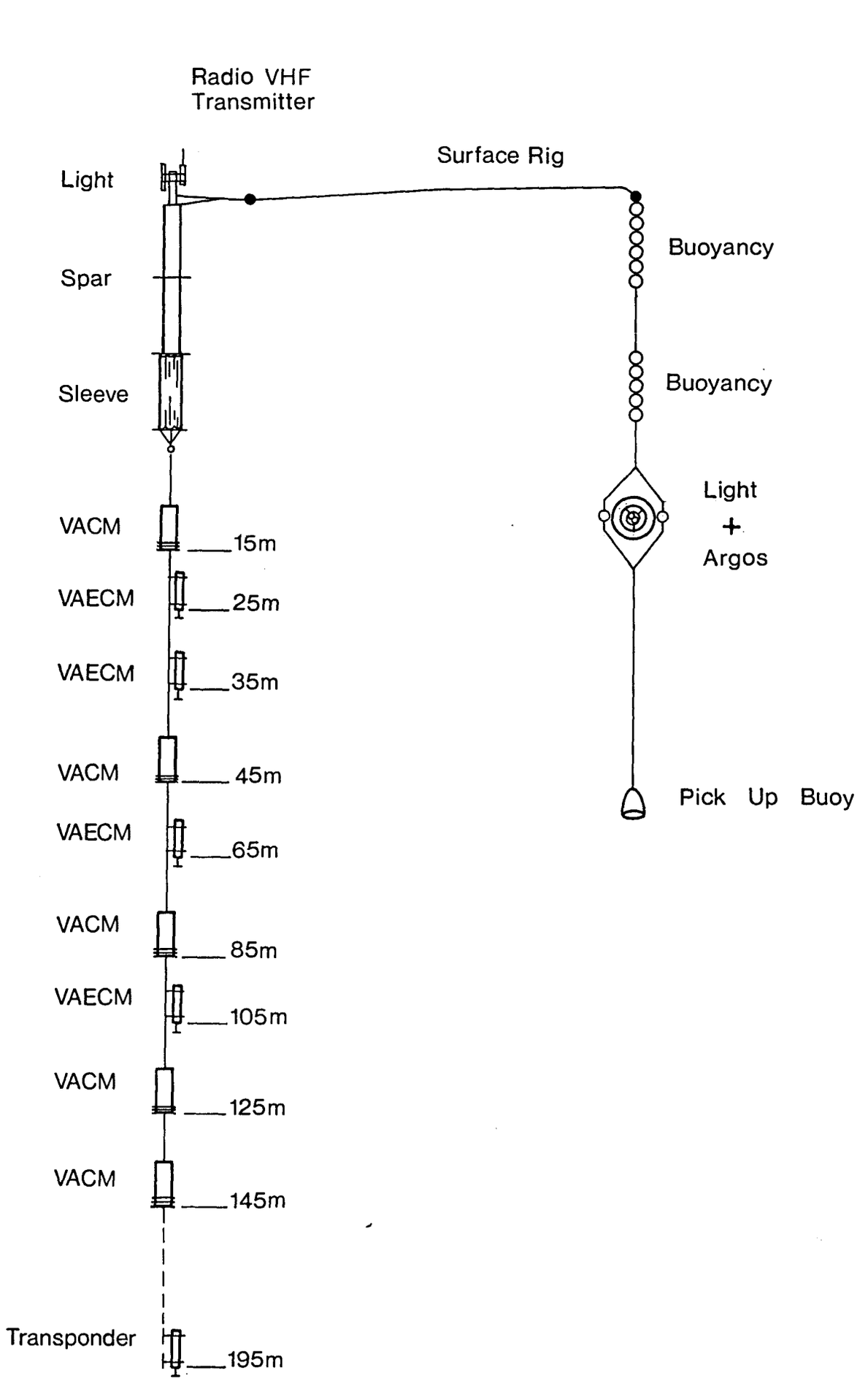

Figure 2.4 : Drifting spar rig as used during the northern area spar deployment.

pierces the sea surface and extends 1.0m into the air. Since it presents a cross- section of only 0.22m^2 to the wind, windage on the spar itself is minimised.

The spar should then drift with the current in the upper one to ten metres. However some windage is inevitable, since it is necessary to tether the spar to an uninstrumented pitch-roll buoy to provide backup buoyancy, and to a marker buoy. Pollard (1983) found during JASIN in 1978 that the windage on this configuration was about 0.1m/s for a 15m/s wind. It will be seen later (chapter 4) that advection of water past the spar is negligibly small. The marker buoy carries a radar reflector for navigation and location. During spar deployments, Discovery navigated relative to the spar, using four possible means of locating it: VHF transmitter from the ship, flashing light on the spar, acoustic methods using a standard 10Hz transponder and Argos fixes. These are discussed in more detail in the cruise report (Pollard et al., 1984).

Beneath the spar buoy were suspended nine current meters, at depths between 15m and 145m (see figure 2.4), each measuring the horizontal current and temperature. Five were standard vector-averaging currents meters (VACMs) at depths of 15, 45, 85, 125 and 145m. The remaining four were VAECMs, electromagnetic vector-averaging current meters, designed and built at the Institute of Oceanographic Sciences (IOS), at depths of 25, 35, 65 and 105m. The averaging period was 112.5s. The total cross- section presented to the horizontal current was 2.84m^2 for all nine instruments, and 3.14m^2 for the spar and sleeve.

The temperature sensors of the current meters were calibrated before the experiment to an absolute accuracy of about 10mK. During the deployment, data were recorded automatically onto magnetic tape which was collected when the spar was recovered.

2.2.2 SeaSoar

After deploying the instrumented spar buoy, RRS Discovery surveyed the surrounding water, repeatedly sampling the upper 400m using a Neil Brown Instrument Systems CTD mounted in an IOS SeaSoar. The CTD measures Conductivity, Temperature and Depth, from which salinity and density may be calculated. The SeaSoar unit was developed by IOS from the Hermes Batfish (Dessureault, 1976). It is a highly manoeuvrable instrument, towed behind the ship, undulating in the vertical to sample the upper ocean water. The turning points and ascending and descending speeds may be determined from the ship via a computer. In this data set, the upper 400m was sampled, so that the whole of the mixed layer plus some thermocline could be studied. During very stormy conditions however, the ship was unable to travel fast enough (at least four knots is required) for the SeaSoar to undulate controllably, and it was necessary to tow the instrument at a constant depth. Even this was difficult to attain.

Data from the SeaSoar were logged continuously during tows, using the ship- borne computer system (PDP11/34). Various minor problems with the SeaSoar instrumentation are described in the cruise report (Pollard et al., 1984). Calibration was carried out prior to the cruise, and the SeaSoar CTD was in fact our most accurate instrument. Temperatures are accurate to within 1mK. The thermistors for the drifting spar rig were calibrated against the SeaSoar CTD. However, the conductivity cell of the CTD tended to become fouled. To keep a check on this, and general performance of the instrument, temperature-salinity curves and profiles of temperature, salinity and density were plotted every two hours. If the cell had fouled, it was momentarily surfaced to clear it. In this way the data were checked as they were stored.

2.2.3 Navigation instrumentation

The data from the two- component electromagnetic (EM) ship's log were integrated to find the distance travelled relative to the water, RELDIST. The ship's speed and gyro heading were initially recorded, but these were later corrected using the current velocity, deduced from satellite fixes of the ship's position. Navigation data were used in the calculation of the surface fluxes from the meteorological observations (see chapter 3).

2.3 Data collected during the northern area spar deployment

The spar buoy was deployed during day 66, and drifted freely until recovery on day 72. Figure 2.5 shows a progressive vector diagram of the observed surface wind, commencing at the beginning of day 67 (see chapter 3 for further discussion of the surface wind observations). The wind blows initially from the east and finally from the north. The spar buoy's motion is shown in figure 2.6; this gives absolute positions relative to 45°30'N, 13°0'W, as determined from satellite fixes. The spar buoy travels for three days almost directly into wind, although during days 68 and 69 it comes almost to a standstill. It begins to drift southwards during day 70 (although the wind does not shift to blow southwards until day 71). During the last two days of deployment, the spar buoy moves southwards, with the wind. Since the spar buoy initially moved into wind, it is likely that the large- scale motion of these near- surface waters is not wind- driven, but forced mainly by eddies, fronts or geostrophic flow.

Figure 2.7 illustrates the temperature time series from the VACMs during the northern deployment. A thorough post- cruise intercalibration has been carried out (Pollard et al., 1987), so that the relative accuracy in differences between current meter temperatures is increased to $\pm$ 2mK. These data will be used to study the heat budget of the upper 150m (chapter 4). There are two main features

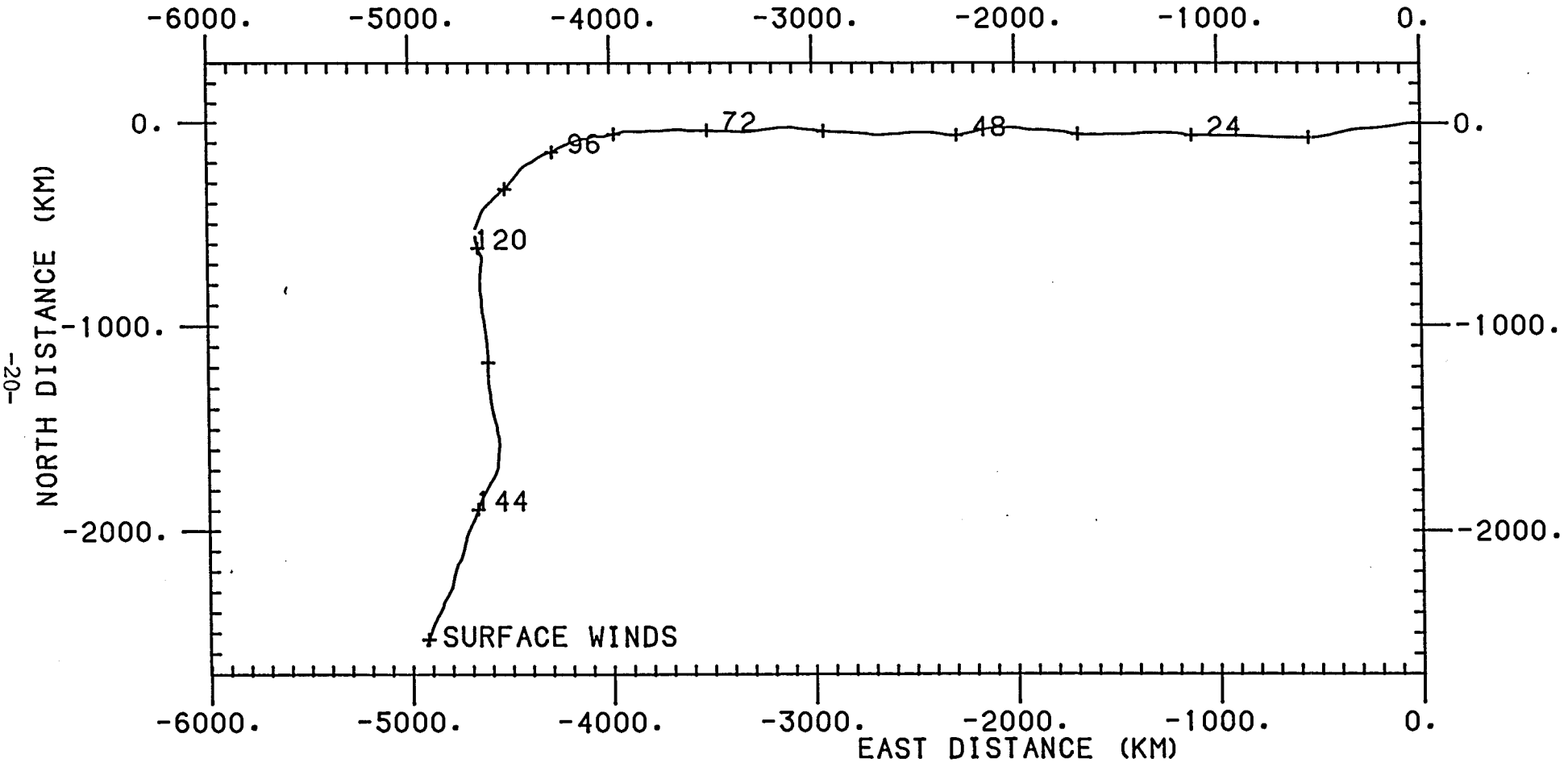

Figure 2.5 : Progressive vector diagram of observed surface wind. The origin is at the beginning of day 67; annotation is every 24 hours.

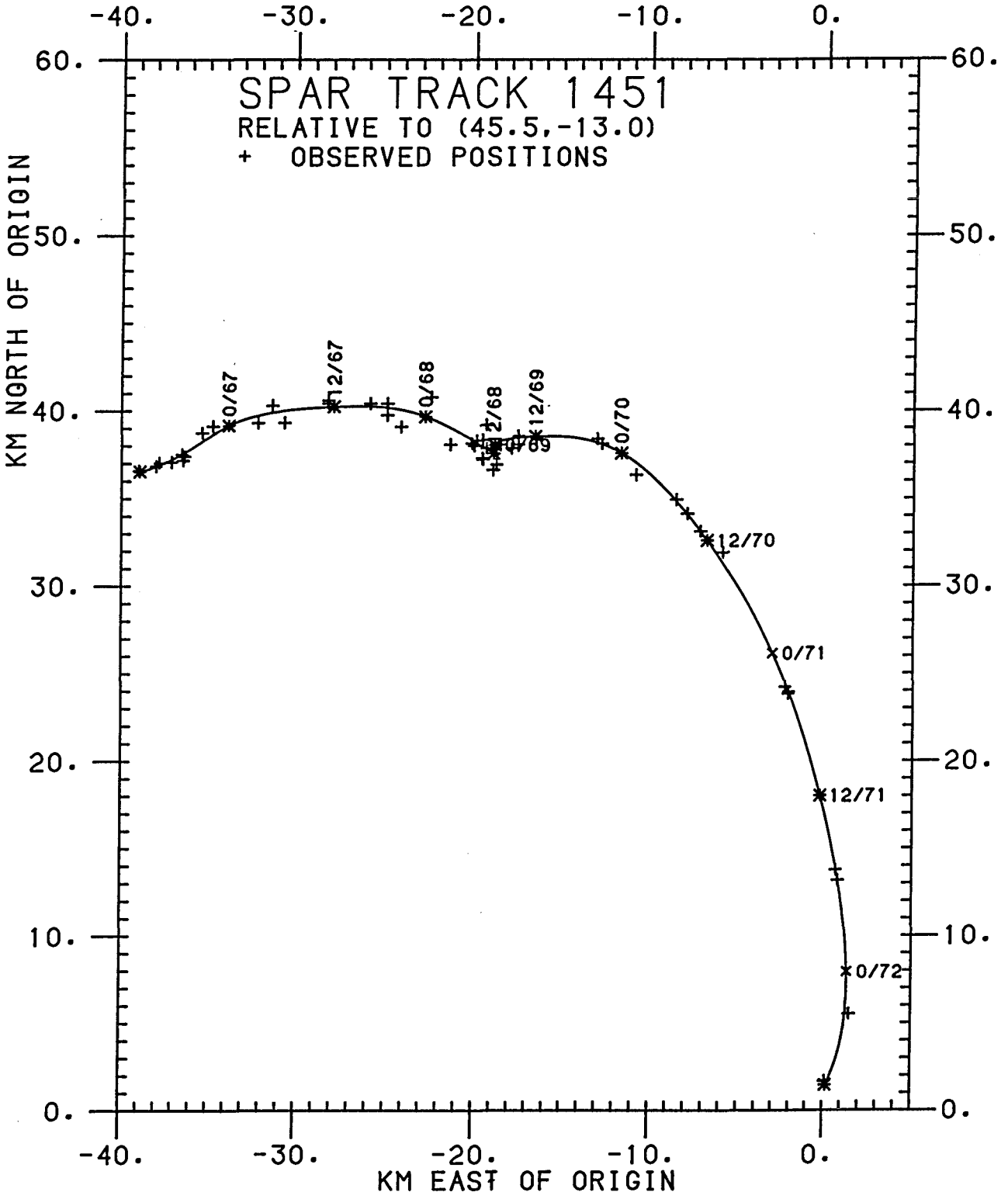

Figure 2.6 : Track of the spar in an Eulerian reference frame (i.e. relative to the earth) from satellite fixes. The track is annotated every 12 hours, and is plotted relative to 45°30'N, 13°0'W.

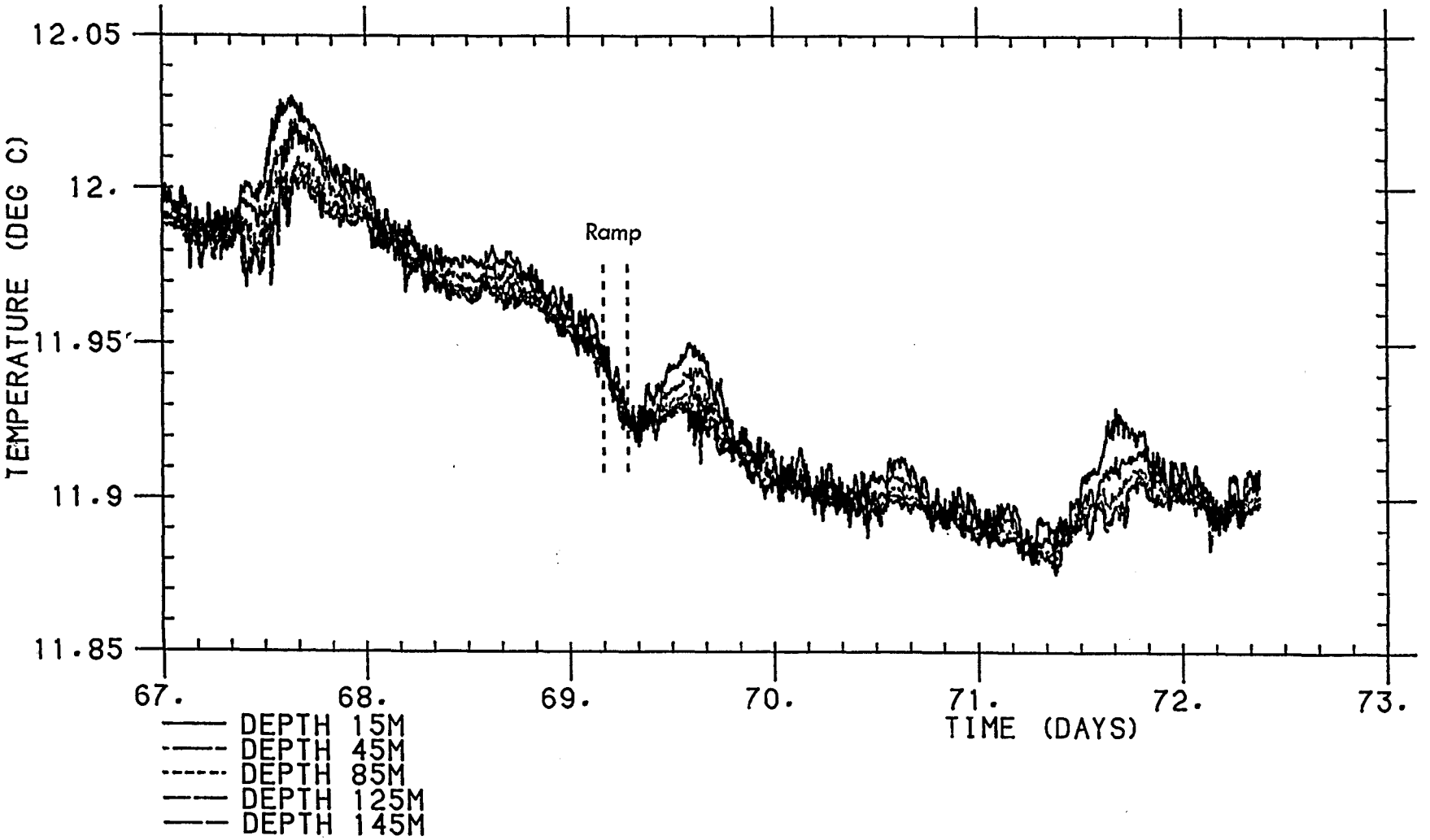

Figure 2.7 : Spar buoy temperature data from the VACMs at the depths stated, intercalibrated so that temperature differences are known to within 2mK. Notice the ramp marked early on day 69, when all the thermistors cooled together (see chapter 4).

apparent in the data; a general cooling of the water during the five days, and a diurnal signal of heating and cooling.

Figure 2.7 evidently includes some high frequency noise, probably caused by internal waves. In order to study the diurnal heating signal, the data have been subjected to a low- pass filter (figure 2.8). The filter used here was the IOS standard programme, PHILOW (Cartwright, personal communication), which passes signals of period greater than 12.5 hours, and suppresses those of period less than 5 hours, with a linear ramp in between. Now the diurnal signal of heating and cooling at all depths is more easily seen. At night the upper 150m becomes nearly homogeneous, while during the day it stratifies. This is discussed in detail in chapter 4.

The temperature sensors on the VAECMs exhibit a similar diurnal signal (figure 2.9) when intercalibrated. As figure 2.9 shows, the signal is somewhat quantised and does not vary as smoothly as in figure 2.7. In discussion of the temperatures at the spar buoy in future chapters, the VACMs will be used since they are the more reliable instruments.

In addition to temperature data, measurements of the horizontal current velocity are available from the VACMs and VAECMs. Figures 2.10 and 2.11 show eastwards and northwards current velocities measured by the VACMs. The data are one- hourly averages. Figure 2.10 shows that during days 67 to 69 the dominant current shear is approximately $10^{-3}\ s^{-1}$ downwind. There is no sign of an inertial oscillation which would have a period of 17 hours. There does however appear to be some small diurnal variation in the crosswind shear during the first three days (figure 2.11). The magnitude of this variation does not seem to change in the same way as the diurnal signal in temperature i.e. it is not noticeably smaller or larger on sunnier days. The crosswind shear is greatest during the afternoon and evening, and small during the

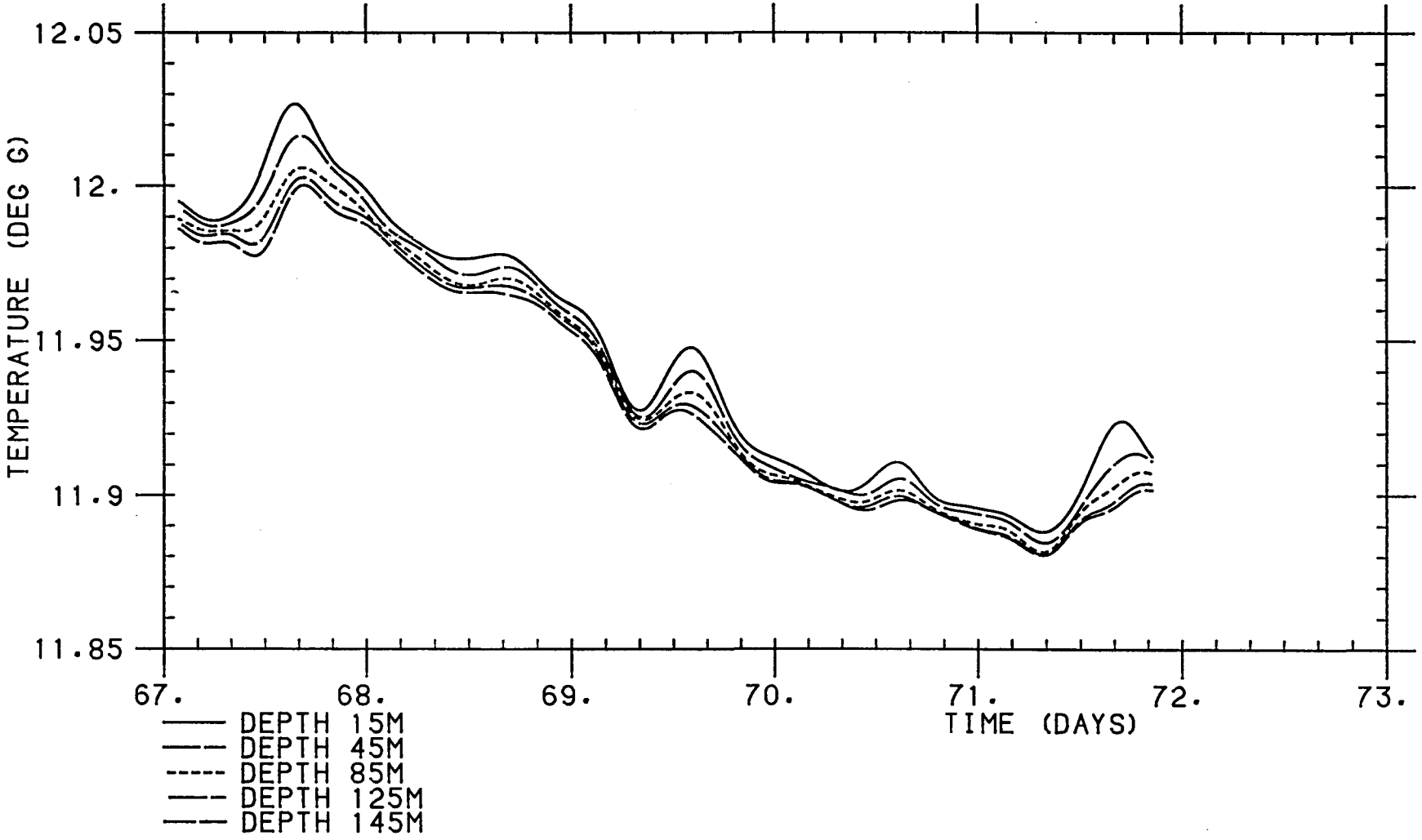

Figure 2.8 : Filtered temperature time series from the VACMs. Signals of less than 12 hours have been removed (see text).

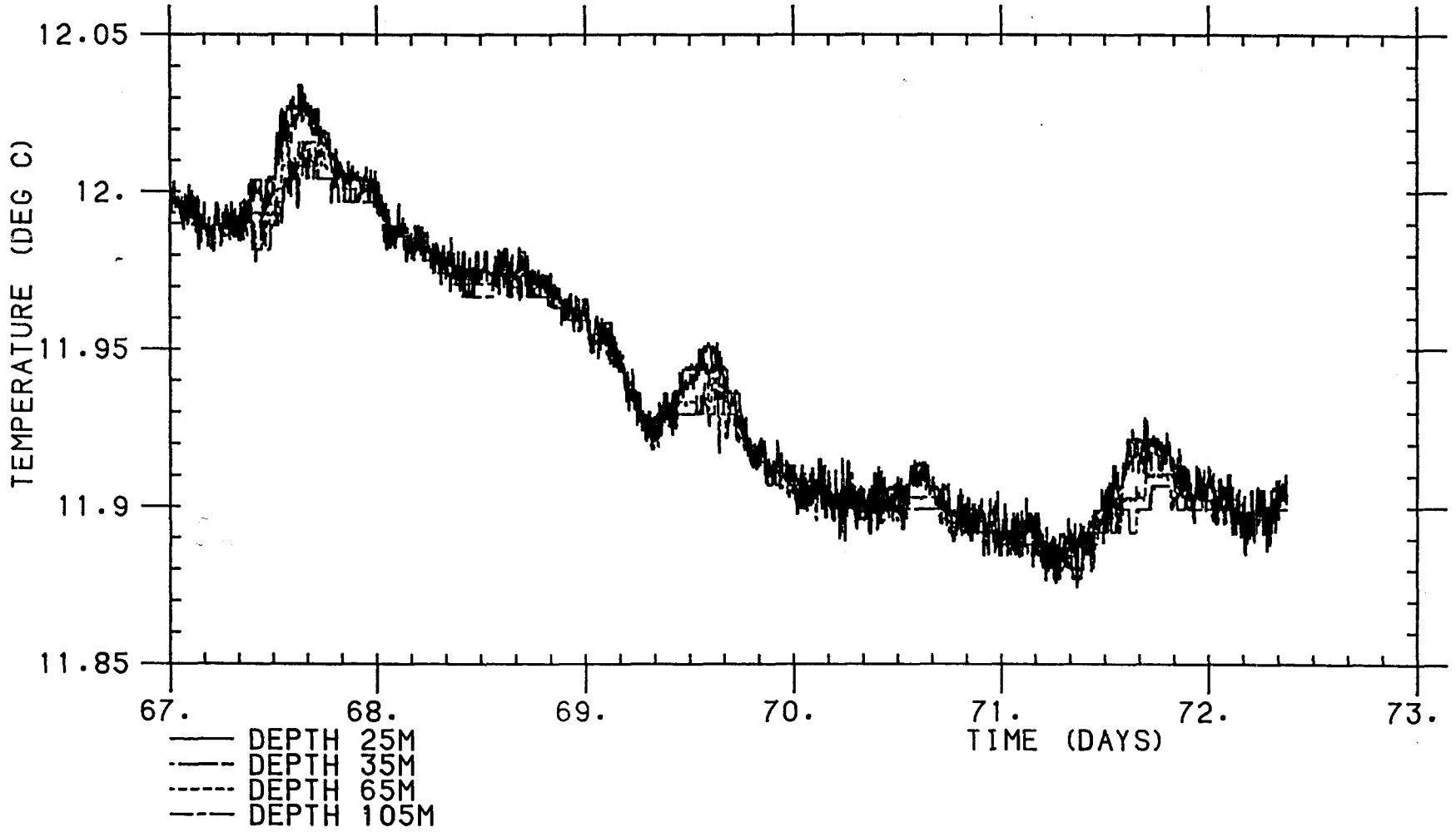

Figure 2.9 : Spar buoy temperature data from the VAECMs at the depths stated, intercalibrated so that temperature differences are known to within 2mK.

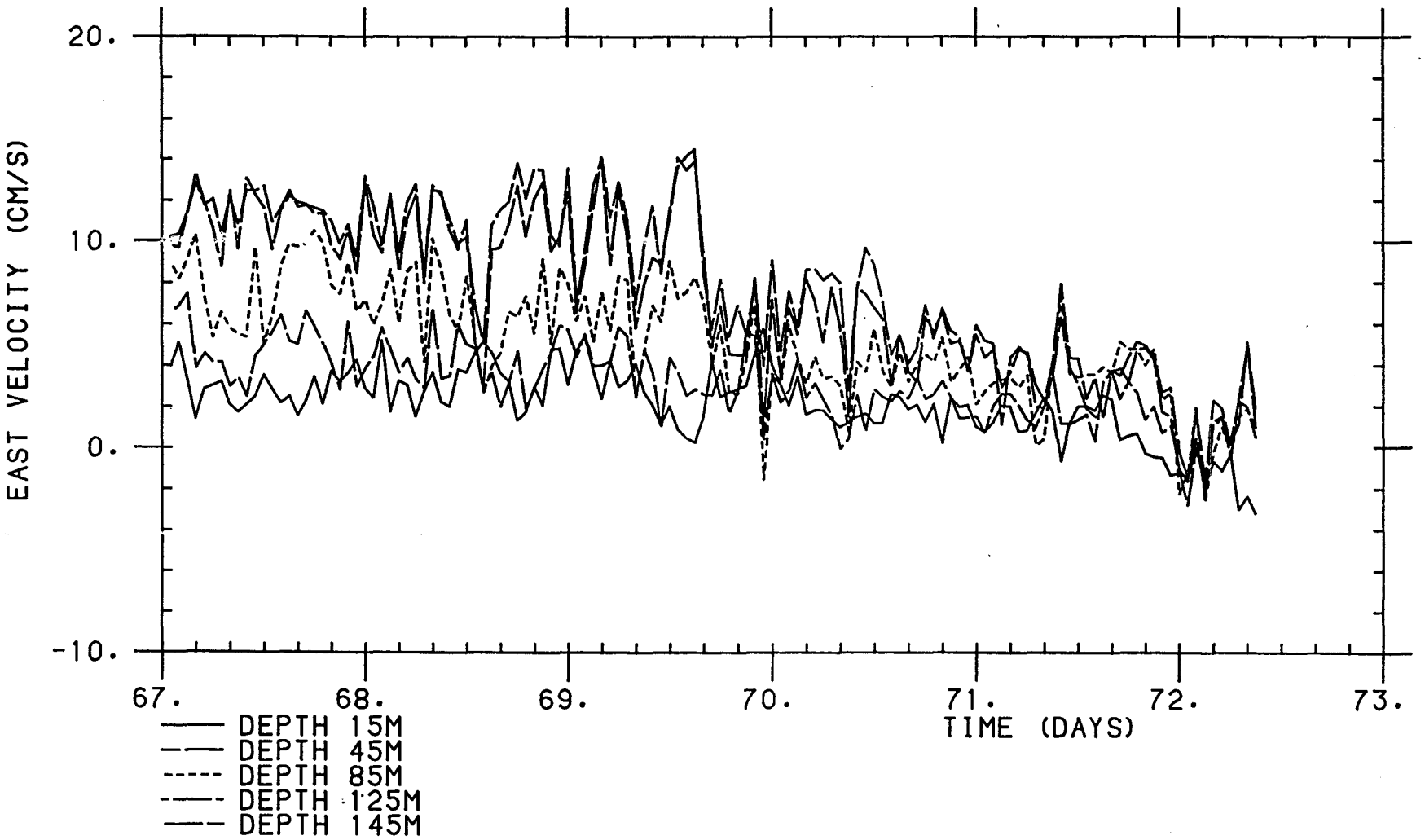

Figure 2.10 : One- hourly averaged data of eastward velocity measured by the VACMs during the northern area spar deployment.

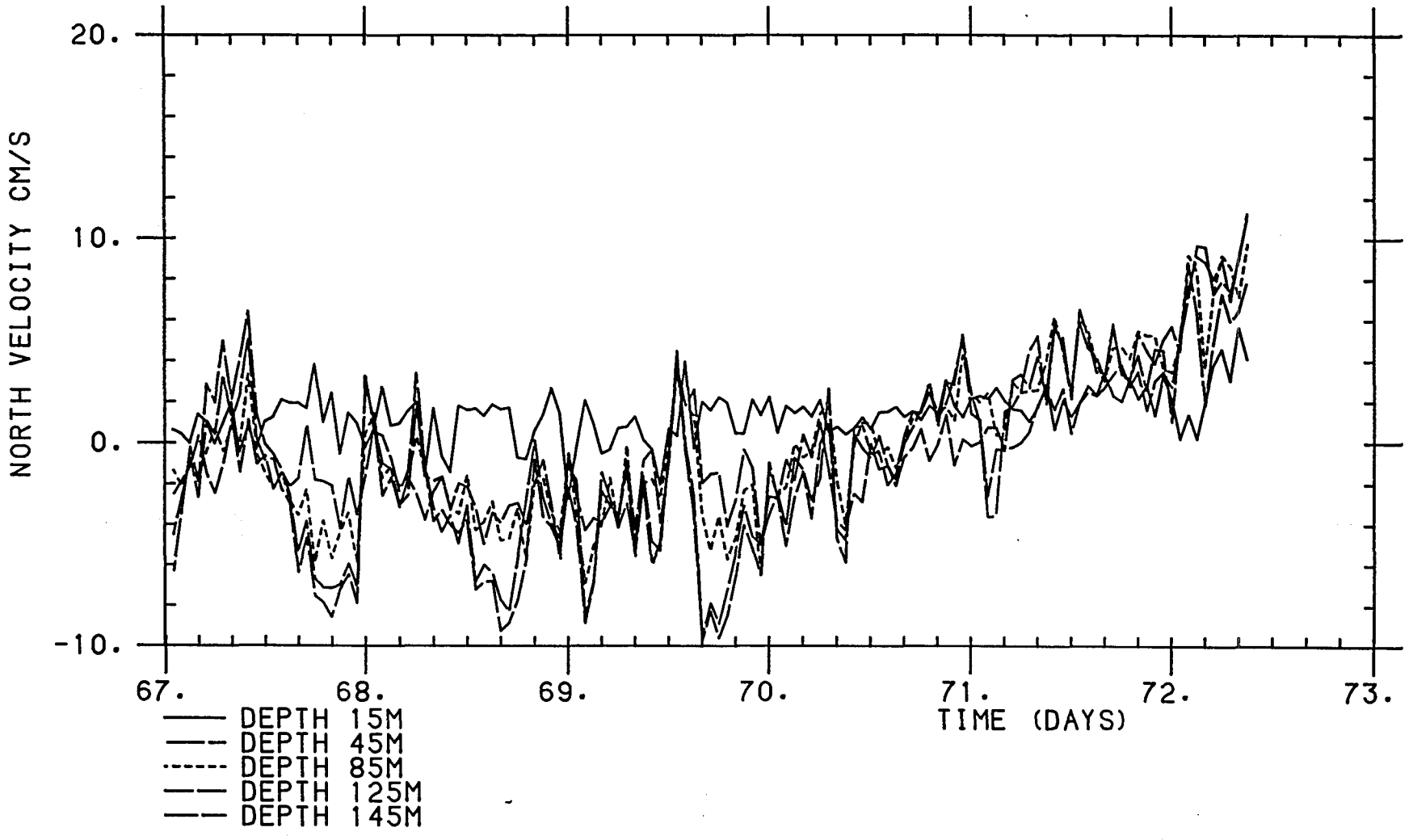

Figure 2.11 : One- hourly averaged data of northward velocity measured by the VACMs during the northern area spar deployment.

first half of the day.

During the spar deployment in the northern area RRS Discovery navigated relative to the drifting spar in a triangular pattern (figure 2.12), whilst towing the SeaSoar. The pattern was designed to give information about the horizontal structure in the upper ocean near the spar in three directions. The inner triangle was repeated about three times a day to try to resolve diurnal changes, while the outer triangle was surveyed once a day to give us a broader spatial coverage. The triangle was orientated so that one inner leg (C) was downwind. The pattern was surveyed in the order ABCDE- BCAFG- CABHJ. Given a ship speed of eight knots, twelve nautical mile or 22km sides were chosen so that a complete survey took about a day. It was not possible to allow the spar to be at the centre of the inner triangle because of limited acoustic ranges for navigation relative to the spar. It was positioned 1.5 nautical miles from the ship at beam- on positions, as marked in figure 2.12. Further details are given by Pollard et al. (1984).

The Seasoar produces alternate up- and down- casts as the ship proceeds. It takes approximately five minutes for the SeaSoar to travel between the sea surface and 400m. During this time, the ship will have travelled typically between one and two kilometres. It is important to remember that a profile may therefore span a horizontal distance of between three and five times its depth. Some examples of profiles are discussed in chapters 4 and 7. The SeaSoar data are subsequently gridded into rectangles of depth and horizontal along-track distance and can then be contoured to show the isotherm variation as the area is surveyed. Figures 2.2 and 2.3 were obtained by contouring potential density and temperature respectively. Some examples of the spatial horizontal temperature structure obtained from the SeaSoar survey are discussed in chapter 4.

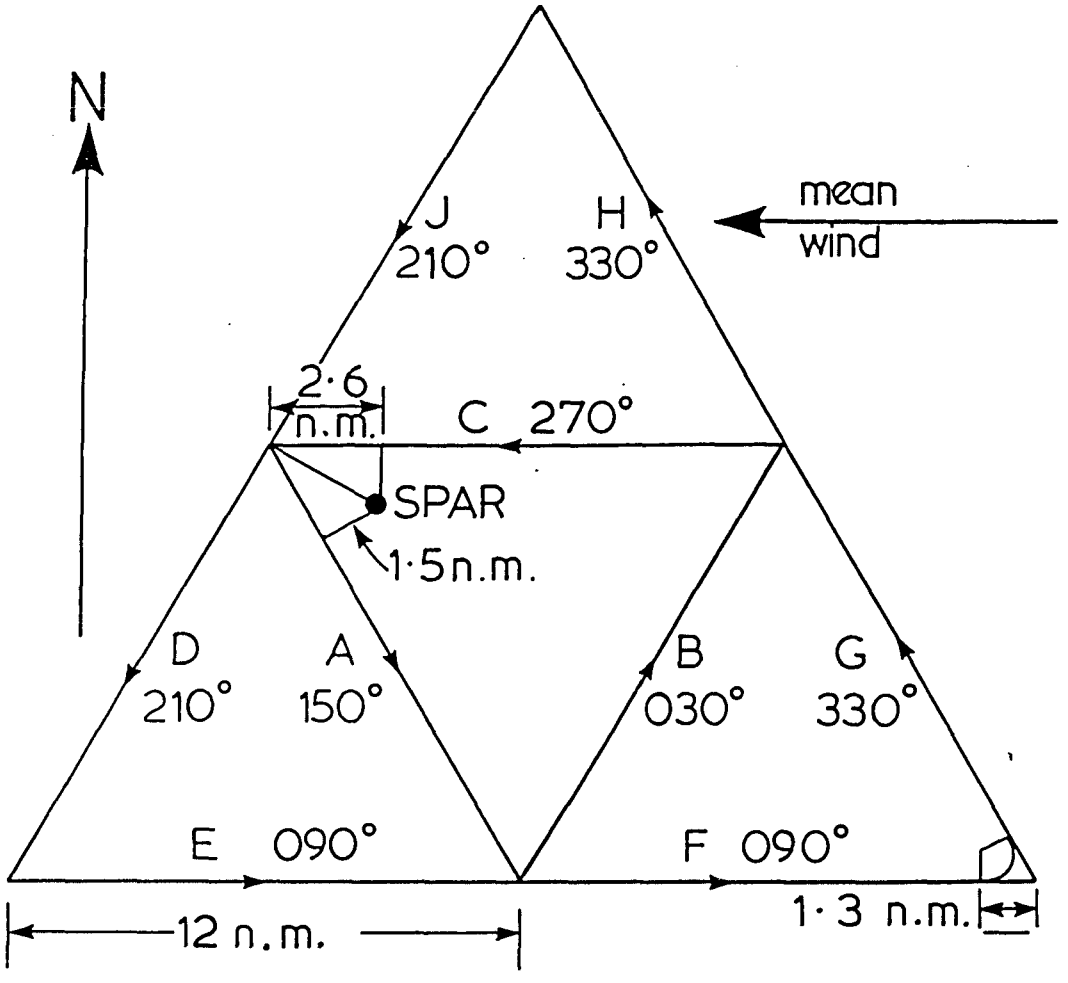

Figure 2.12 : Plan of northern site SeaSoar survey. The pattern followed was ABCDE- BCAFG- CABHJ, which was completed in approximately one day. Navigation was relative to the spar buoy, which was kept in the northwest corner of the inner triangle. The abbreviation n.m. refers to nautical miles.

Chapter 3

Surface Meteorological Forcing of the Upper Ocean

3.1 Introduction

In order to study the heat budget of the upper ocean, or to model deepening or stratification, it is necessary to have a good knowledge of the surface heat fluxes and wind forcing. The accuracy of these quantities will depend upon the accuracy of the initial meteorological observations. This chapter will present and assess the meteorological observations, and discuss their calibration and correction (section 3.2). In section 3.3 the various air- sea heat fluxes are defined and calculated. The total heat flux is deduced. Finally, the absorption of this heat flux into the ocean surface layers is discussed (section 3.4).

Meteorological observations were logged automatically throughout Cruise 145 at one- minute intervals by the ship- borne computer system. These consisted of:-

a) dry and wet bulb platinum resistance thermometer readings situated in Stevenson Screens on Monkey Island (above the bridge) on both port and starboard sides of the ship (PDRY, PDRY-WET, SDRY, SDRY-WET, °C)

b) sea surface temperature, measured using the hull temperature sensor at a depth of 2.5m below sea level (HULLTEMP, °C)

c) barometric air pressure (BAROM, mb)

d) wind speed and direction relative to the ship (RWSPD, m/s, and RWDIR, degrees), and hence true wind speed and direction (WSPD and WDIR) when the ship's velocity is taken into account

e) ship's velocity (m/s), from the two- component electromagnetic (EM) ship's log, measuring the speed of the water parallel to and perpendicular to the ship's axis, and a gyro- compass giving ship's heading (degrees)

f) downward shortwave solar radiation, measured by a Kipp and Zonen solarimeter on Monkey Island (SOLAR, W/m^2)

g) cloud observations in oktas (N), made every three hours by a scientist on watch and also by an officer on the bridge every six hours

h) a visual estimate of wave height and direction at regular intervals

i) qualitative description of precipitation; this was negligible during the northern area spar deployment and will not be mentioned further.

3.2 Calibrations and corrections

3.2.1 Radio interference

Use of the HF radio on board the ship was found to produce erroneous data on the computer logging system. The most significant of these spikes were identified by studying the hull temperature and the barometric pressure, since these normally varied gradually and smoothly. The effects of radio interference were removed from the dry and wet bulb temperatures, the solarimeter readings, barometric pressure and hull temperature. They were not removed from the winds because it was not obvious that the winds were affected, due to the natural spikiness of the signal.

3.2.2 Spikes

Spikes may be caused by other instrumental malfunctions as well as by radio interference. The obvious spikes were removed by applying the following thresholds for spike magnitude:-

temperatures	0.5°C
BAROM	0.2mb
HULLTEMP	0.5°C

3.2.3 Winds

The wind vane on the computer- logged, ship's anemometer was found to be wrongly set despite an intensive effort a year previously (Discovery Cruise 132) to obtain accurate winds. It was assumed that the vane had been altered during refit. By comparing the logged wind directions with those obtained by a newly- calibrated anemometer mounted on the foremast, an offset of 20° was deduced and the measured wind

direction adjusted accordingly. The ship's anemometer was found to give a significantly lower wind speed than the new one gave, probably because the ship's anemometer had become dirty and encrusted with salt. The correction necessary was found to vary with wind speed (in m/s) as follows:

Correct RWSPD = RWSPD + 0.37 + 0.073 RWSPD (3.1)

The true winds (i.e. relative to the earth, rather than relative to the ship) were then recalculated. Unfortunately the ship's heading (GYRO) had not been archived after being used to calculate the corrected wind and ship's course. Therefore the corrected winds calculated on board were used to work back to ship's heading. Other input quantities were:-

RWSPD	original value
RWDIR	original value
Ship's velocity	after correction by satellite fixes
Current velocity	from satellite fixes

Original values of the ship's velocity from the EM log prior to correction by satellite fixes were not available, hence it was necessary to use the current velocity to deduce the value taken for the ship's velocity when the corrected wind velocity was originally calculated.

Having found GYRO, the true winds (magnitude WSPD, m/s) were recalculated, using the calibrated values of RWSPD and RWDIR and the ship's velocity after correction by satellite fixes. These corrected values of wind speed and direction were used to produce the progressive vector diagram of one- hourly surface winds (figure 2.5) discussed in chapter 2. Figure 3.1 shows the corrected wind speed components every minute. A strong (15m/s) steady wind blew from the east during much of the period, but towards the end the wind abated (to about 8m/s) and backed, eventually blowing from the north (at about 20m/s).

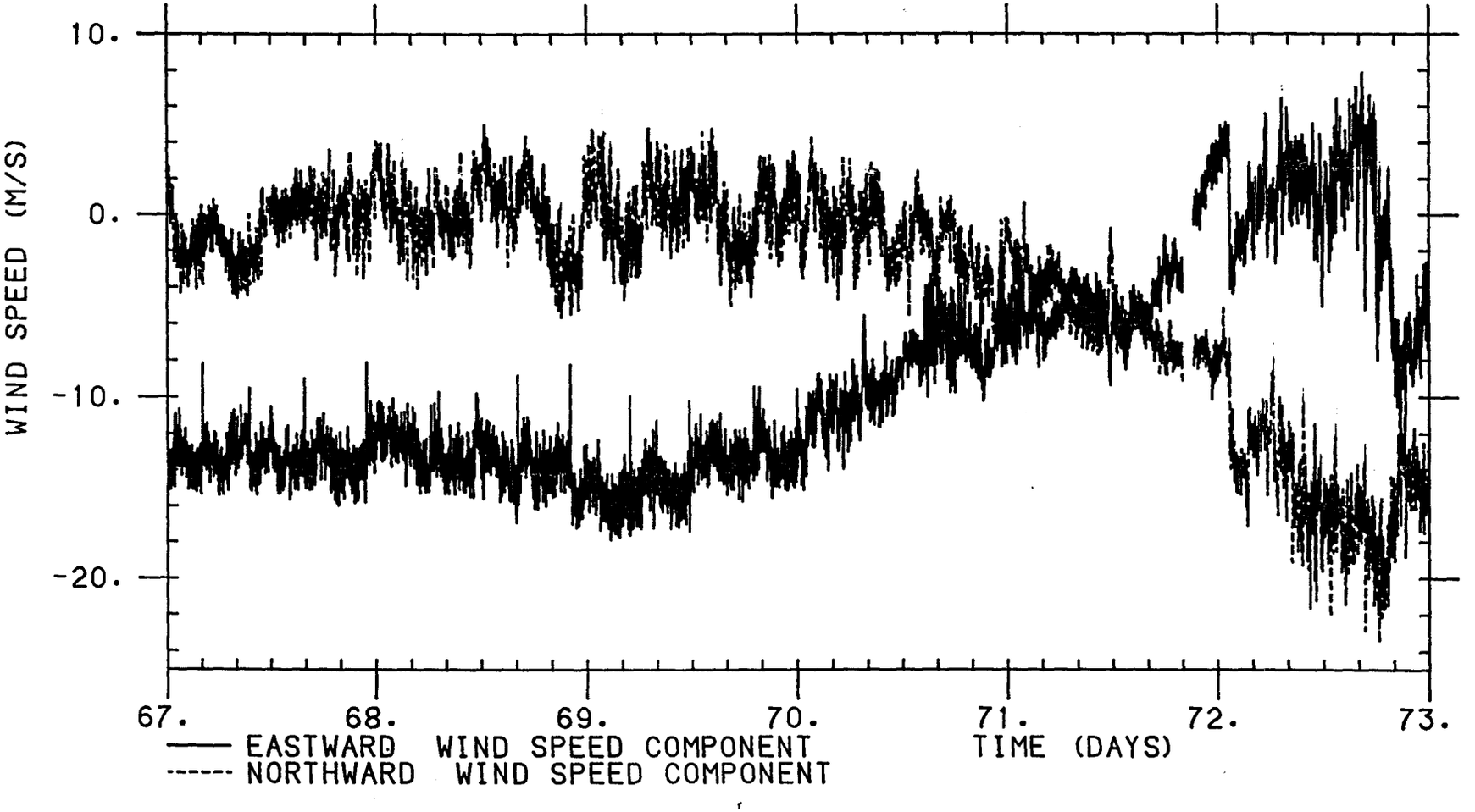

Figure 3.1 : Corrected wind speed components in eastward and northward directions. Values are at a one- minute sampling interval.

3.2.4 Wet bulb temperatures

At various times during the cruise, the wet bulb thermometers were found to have dried out. At these times, the measured dry minus wet bulb depression should have been identically zero, within experimental error. Means of port and starboard dry minus wet values (PDRY-WET and SDRY-WET) were calculated for all the dried out periods throughout the cruise; the results were as follows:-

Port dry-wet	+0.030 $\pm$0.005	°C
Starboard dry-wet	-0.250 $\pm$0.005	°C

The uncertainty (0.005°C) is the standard error of the mean and gives a measure of confidence in the mean value. Thus 0.03°C was subtracted from port dry-wet temperatures, and 0.25°C added to starboard dry-wet temperatures. These values were supported by mean values of the temperatures during the whole cruise, as shown:-

Port dry	11.16 $\pm$0.01	°C
Starboard dry	11.18 $\pm$0.01	°C
Port dry-wet	2.52 $\pm$0.01	°C
Starboard dry-wet	2.53 $\pm$0.01	°C

Obviously, this intercomparison only determines the accuracy of the temperature differences between dry and wet bulbs, and not the absolute accuracy of any of the readings. Figure 3.2 shows port and starboard dry bulb temperatures after correction. Notice the large spikes which occur at regular intervals. This happens when warm, dry air from the funnel blows over the Stevenson Screens. Figure 3.3 gives port and starboard values of dry bulb temperature minus wet bulb temperature. Again the spikes are obvious.

3.2.5 Sea surface temperature

The sea surface temperature from the hull temperature sensor at a depth of 2.5m (HULLTEMP) was compared with

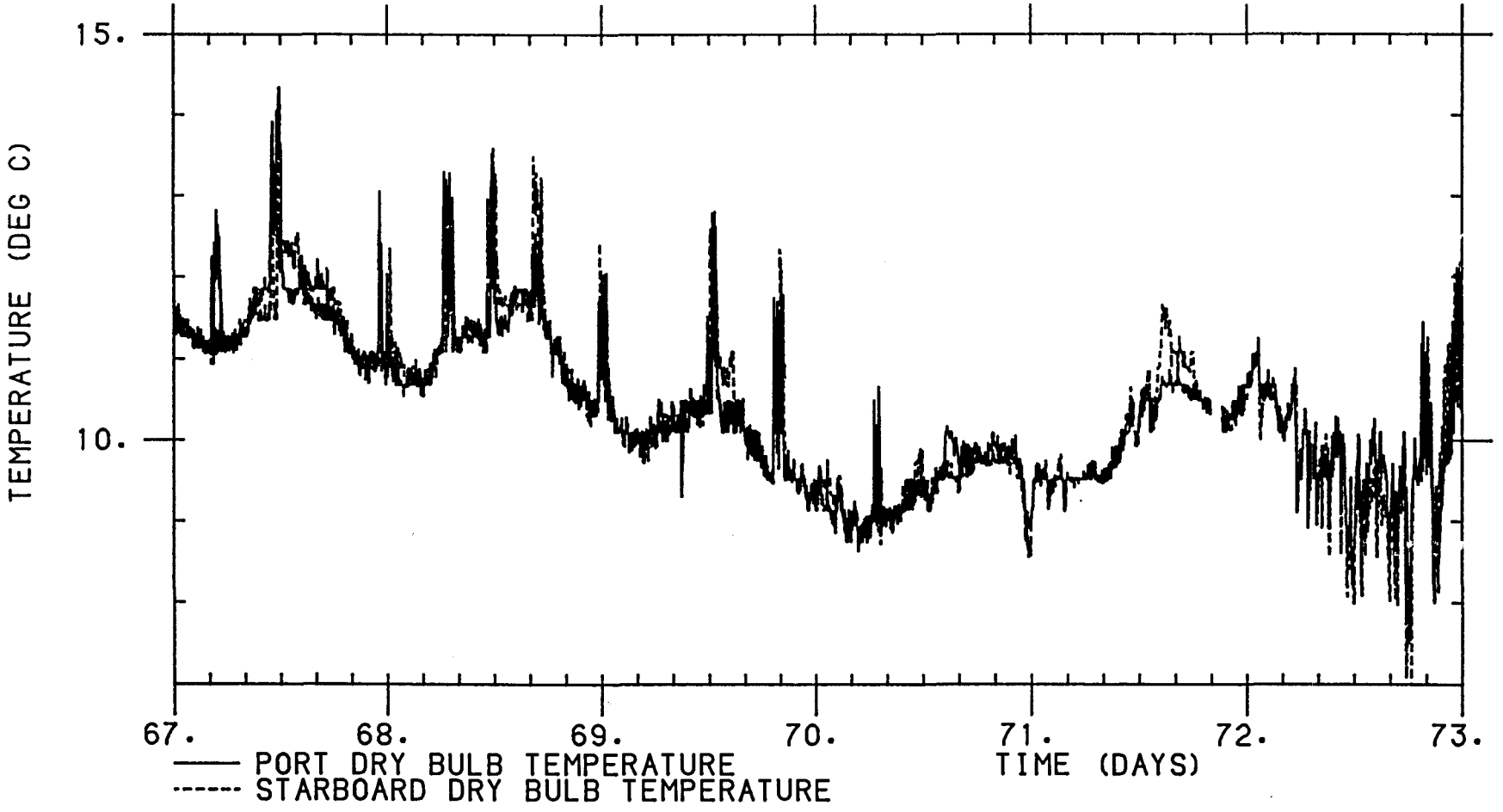

Figure 3.2 : Port and starboard dry bulb temperatures. Values are at a one- minute sampling interval. Notice the regular spikes which occur when warm air from the funnel blows over the thermometers.

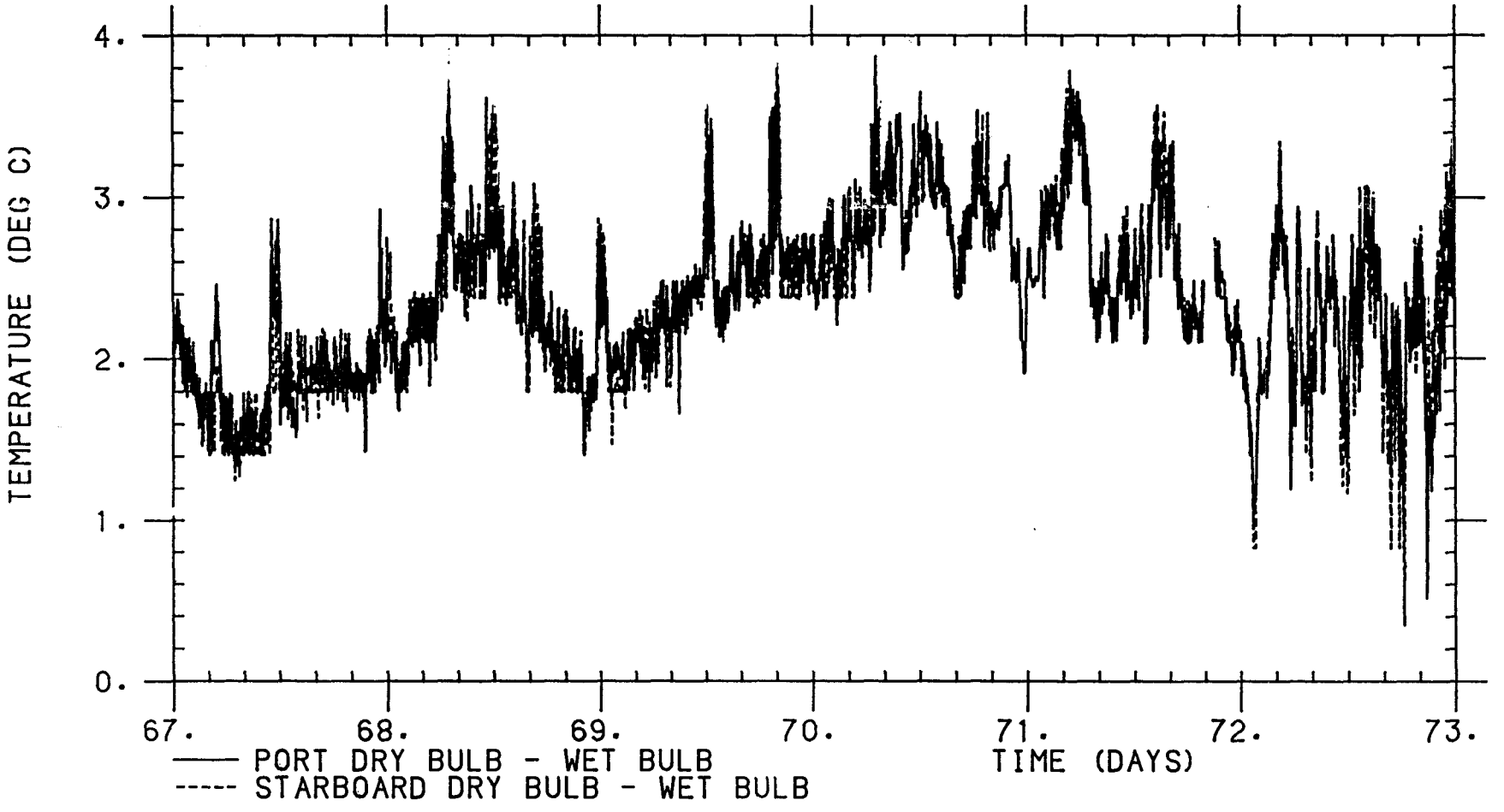

Figure 3.3 : Port and starboard dry bulb minus wet bulb depression. Values are at a one-minute sampling interval. Notice the regular spikes which occur when warm air from the funnel blows over the thermometers.

i) values of SST from CTD casts during the northern area spar deployment. Readings as near to the surface as possible were taken, at least within the top three metres.

ii) values of SST each time the SeaSoar neared the surface during the northern area spar deployment. A mean was taken of all the readings recorded when the SeaSoar was in the top three metres.

iii) temperatures from the thermosalinograph.

The hull temperature sensor was found to be reading 0.10°C too high during the northern area triangles relative to the SeaSoar and CTD (which are accurately calibrated to within 10mK, see chapter 2). The thermosalinograph and hull temperature sensor agreed during the northern area spar deployment, but during other periods of the cruise there was a significant difference, which did not appear to vary simply with time or temperature. The correction of 0.1°C was applied to the whole HULLTEMP data set. Figure 3.4 illustrates the sea surface temperature during this period.

3.2.6 Cloud observations

The downward shortwave solar radiation (SOLAR), measured directly on the ship's solarimeter, was compared with the model of Smith and Dobson (1984) to check the three- hourly cloud observations. The model uses the following equations for shortwave radiation:-

$$SOLAR = Q0\ SE\ (A + B\ SE) \qquad \text{for } i=6,7,8 \text{ oktas} \qquad (3.2)$$

$$SOLAR = Q0\ [E + SE \exp(-D0/SE)\ [C \exp(-D/SE) + 1 - C]\} \qquad \text{for } i=0,1,\ldots,5 \text{ oktas} \qquad (3.3)$$

SOLAR is the downward solar radiation received (W/m^2)

Q0 is the radiative flux at the top of the atmosphere, 1380 W/m^2

SE is the sine of the solar elevation. For this study, when the mean solar radiation for a short period was taken, a representative SE for the period was calculated.

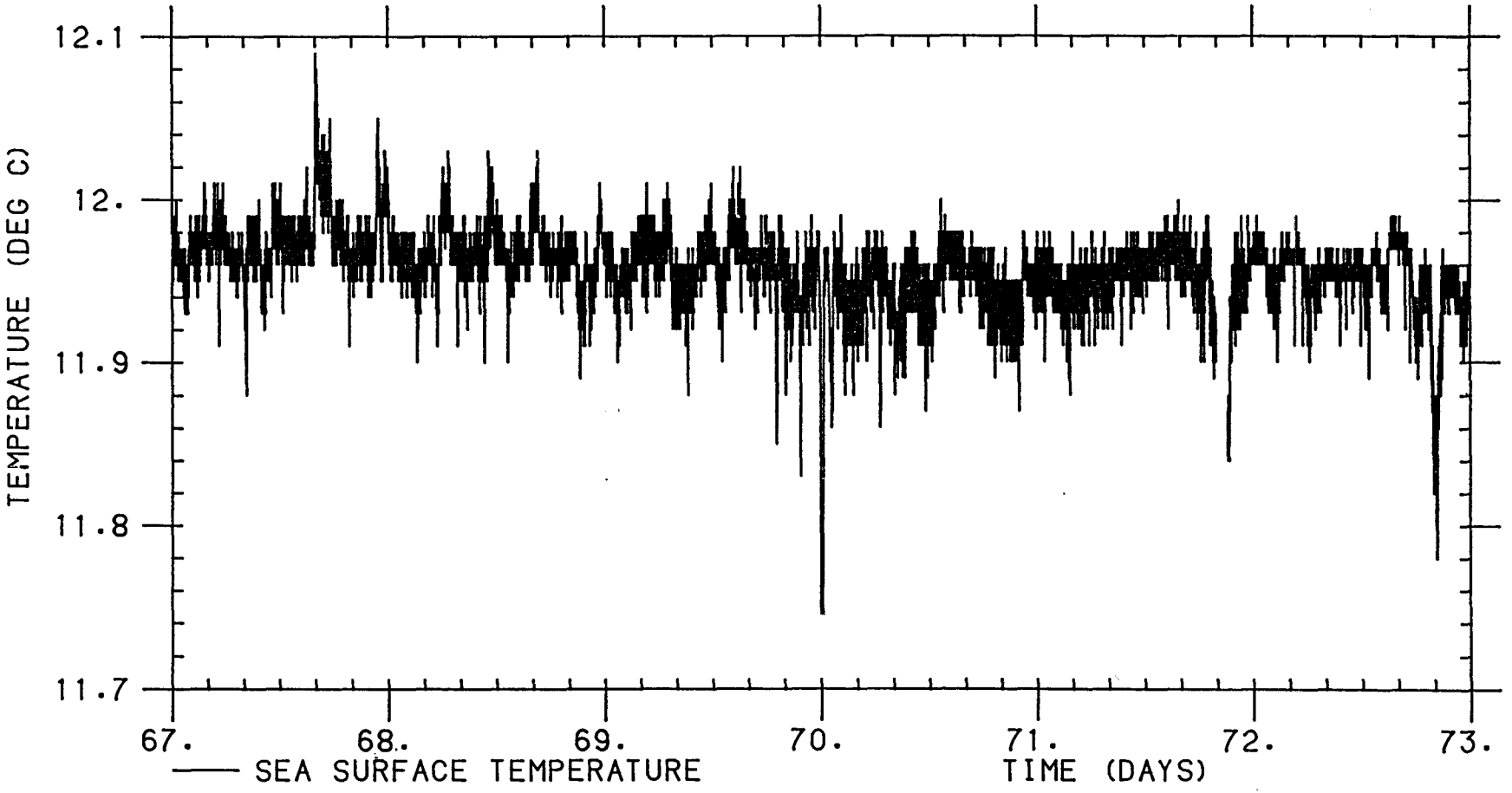

Figure 3.4 : Sea surface temperature measurements from the hull temperature sensor. Values are at a one- minute sampling interval.

$$SE = \sin\phi \sin d + \cos\phi \cos d \cos\theta \qquad (3.4)$$

ϕ = latitude of observer (45°N)

d = declination of the sun. For early March, this is -5 degrees (Smithsonian Meteorological Tables)

θ = hour angle of the sun, given by:

$$\theta = \frac{180}{12} \left| \text{solar time (hours)} - 12 \right|$$

Here solar time is obtained from GMT as follows. First, 4 minutes are added for each degree of longitude the observer is east of Greenwich. The northern area triangles were 14° west of Greenwich, thus one hour is subtracted. Then a small correction is required to convert local solar time to true solar time (Smithsonian Meteorological Tables). Using the value for early March, 10 minutes was subtracted, to give true solar time.

C is the cloud fraction (eighths) (N = 8C)

D0 is the constant D given below for no cloud cover

A, B, D, E are empirical constants for a given number, N, of oktas of cloud, given by Smith and Dobson (1984):

Cloud cover, N	A	B	D	E
0			0.240	0.0520
1			0.070	0.0525
2			-0.010	0.0430
3			0.055	0.0395
4			0.070	0.0375
5			0.090	0.0345
6	0.310	0.439		
7	0.235	0.388		
8	0.103	0.296		

From equations 3.2 and 3.3, the expected solar radiation was calculated for each value of N (number of oktas, 8C) for the three times during the day at which cloud observations were taken (0900, 1200, 1500 GMT). Obviously the model cannot be applied at night. Half hour and three hour averages of the solarimeter readings centred around these times were calculated and thus N predicted. Table 3.1 gives the

Day	Mean solar flux 1/2 hrs (W/m^2)	Mean solar flux 3 hrs (W/m^2)	Observed N (bridge)	Half-hour N from model	3-hour N from model	N taken
67.375	196	153	2	2.5	5.5	2
67.5	638	497	- (3)	2	5.5	3
67.625	331	352	6	7.2	7	6
68.375	79	82	6	7.8	7.5	7
68.5	123	166	7 (8)	>8	>8	8
68.625	165	163	7	>8	>8	8
69.375	146	135	5	6.4	6.5	5
68.5	500	371	7	6	7	7
68.625	165	163	7	>8	>8	8
69.375	146	135	5	6.4	6.5	5
69.5	500	371	7	6	7	7
69.625	302	292	7	7.5	7.5	7
70.375	71	80	7	8	7.5	7
70.5	202	167	7	>8	>8	7
70.625	145	118	-	>8	>8	8
71.375	51	51	8	>8	>8	8
71.5	107	165	8	>8	>8	8
71.625	473	345	6	6	7	6
72.375	151	184	6	6	3	6
72.5	449	433	7	6.5	6.5	7
72.625	612	496	3	0	4	3

Table 3.1. Observed and calculated values of the number of oktas of cloud cover, N, at 6- hourly intervals. Columns 2 and 3 give the mean solar irradiance from the solarimeter over a period of 0.5 and 3.0 hours respectively. From these, the cloud cover is predicted (columns 5 and 6). Column 4 gives the observed cloud cover and also three observations of cloud cover made by the officers on the bridge. The last column gives the value of N that was taken to calculate the net longwave radiation.

predicted and observed values of N.

Bearing in mind that the observed cloud coverage is an 'instantaneous' reading, one would not expect a half- hour or three-hour prediction to be the same as that observed. There are many assumptions made in the model which may not be valid; it is felt that it over- predicted the cloud cover, since on several occasions the radiation was too low to be accounted for even by a cloud cover of eight oktas. However this does give us an idea of the uncertainty in the cloud observations - say one or two oktas. It was found that an error of one okta would produce an error of approximately $10W/m^2$ in the final longwave heat flux. Since it is unlikely that cloud cover was consistently under- or over- estimated (observations were made by several observers), it is probable that for an average of several days the error in the longwave flux will be reduced.

3.3 Calculation of air- sea heat and momentum fluxes

3.3.1 Definitions of variables

The following quantities are defined:-

1/ Saturated vapour pressure (mb) as a function of temperature T in °C (Henderson-Sellers, 1984)

$$SVP(T) = 2.1718 \times 10^8 \exp(-4157 / (T + 239.25)) \quad (3.5)$$

2/ Surface water vapour pressure (mb)

$$EA = SVP(Tw) - \left[6.6 \times 10^{-4} \ (1+0.00115Tw) \ BAROM \ (Td-Tw) \ \frac{7.99}{6.666}\right] \quad (3.6)$$

Here Tw and Td are relevant wet and dry bulb temperatures (°C). The factor of (7.99/6.666) is necessary because the equation applies to thermometer readings from an aspirated psychrometer whereas our thermometers were in Stevenson Screens (Smithsonian Meteorological Tables, Meteorological Office Tables).

3/ Specific humidity of air (%)

$$QA = \frac{0.622 \quad EA}{(BAROM - 0.378\ EA)} \tag{3.7}$$

4/ Specific humidity of air at sea surface temperature (%)

$$QS = \frac{0.610 \quad SVP(HULLTEMP)}{(BAROM - 0.37\ SVP(HULLTEMP))} \tag{3.8}$$

5/ Latent heat of evaporation of water (J/kg) as a function of the sea surface temperature (Henderson-Sellers, 1984)

$$LH = 1.918 \times 10^6 \quad \frac{SST}{(SST - 33.91)} \tag{3.9}$$

6/ Relative humidity of air (%)

$$RW = \frac{0.624 \quad SVP(Td)}{(BAROM - 1.004\ SVP(Td))} \tag{3.10}$$

7/ Virtual temperature (K) of air

$$TVIRT = \left[\frac{0.608\ (Td + 273.15)\ EA\ RW}{(1 + RW)\ SVP(Td)}\right] + Td \tag{3.11}$$

8/ Virtual density of air (kg/m^3)

$$RHO = \frac{0.34838 \quad BAROM}{(TVIRT + 273.15)} \tag{3.12}$$

9/ Sea surface temperature (K)

$$SST = HULLTEMP + 273.15 \tag{3.13}$$

10/ Equation of state for sea water

For calculating surface fluxes, it is necessary to express the density of sea water, ρ (kg/m^3), in the following approximate form:-

$$\rho = \rho 0\ (1 - \alpha(T - T0)) \tag{3.14}$$

$\rho 0$ is a typical density corresponding to temperature T0.

α is the volumetric thermal coefficient of expansion.

Strictly, the density is a complicated function of both temperature T and salinity S. The IOS standard algorithm EOS83 was used to plot density against T at a suitable fixed value of S (35.65ppt), as shown in figure 3.5. It was found that for the relevant range of T (11.85

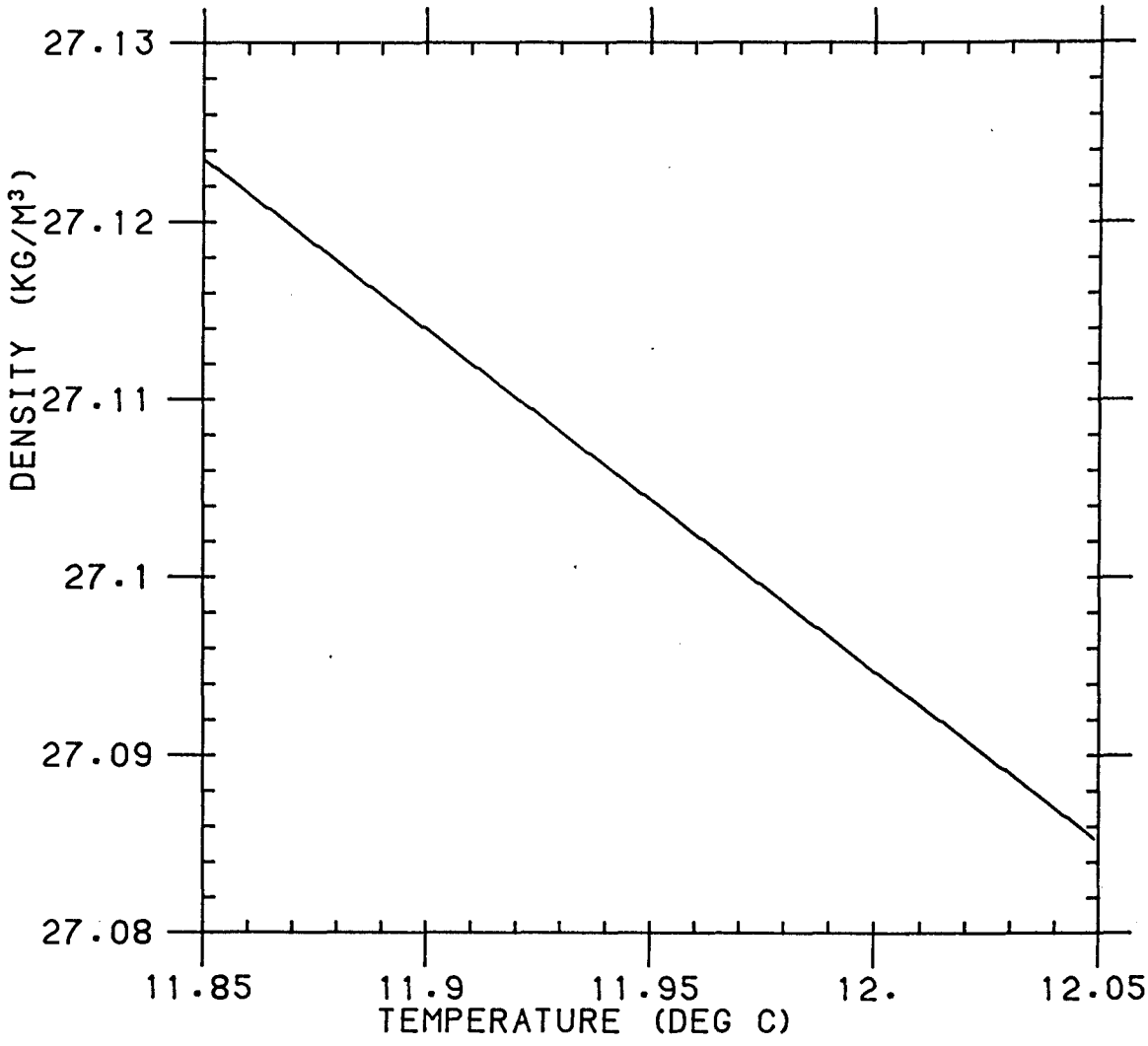

Figure 3.5 : Potential density minus 1000kg/m^3 as a function of temperature, calculated using the IOS package EOS83. Salinity was taken as 35.65 ppt. For this range of temperatures, the relationship may be described as a straight line (see text).

to 12.05°C) the density could well be described by the above equation with $\rho 0=1027.1 kg/m^3$, T0=11.97°C and $\alpha = 1.874 \times 10^{-4} °C^{-1}$.

3.3.2 Introductory remarks

The total heat flux between the ocean and the atmosphere is the sum of the latent heat flux, the sensible heat flux, the longwave radiative heat flux and the shortwave radiative heat flux. These quantities will now be calculated from the meteorological observations discussed earlier. The latent and sensible heat fluxes, and the wind stresses, were calculated using the standard bulk formulae (Smith and Dobson, 1984). The transfer coefficients (Cd, Cl and Ct) were calculated using the subroutines of Large (see Large and Pond, 1981 and 1982). These vary with the wind speed, the heights of the various instruments and the air- sea temperature difference. After analysis of the data by Dr. Peter K. Taylor, some precautions were found to be necessary:-

a) Windward temperatures (dry and wet bulb) were taken, unless these were absent, in which case the leeward ones were used. Hence Td is either PDRY or SDRY, depending upon the value of RWDIR.

b) Fluxes were not calculated for those data cycles where the direction of the wind relative to the ship (RWDIR) lay between 55° and 85°, or between 140° and 220°. Directions in the first range produce erroneous temperatures because the screens are shielded by the mast, while those in the second yield temperatures which are too high because the warm air from the funnel blows over the screens.

Note that all figures that show air- sea fluxes will give half- hourly averaged data. Missing values have been interpolated.

3.3.3 Latent heat flux

The latent heat flux, LFLUX (W/m^2), is defined as:-

$$LFLUX = RHO\ LH\ Cl\ WSPD\ (QS - QA) \qquad (3.15)$$

This represents the heat loss from the sea surface due to evaporation. Cl is the latent heat flux coefficient. Figure 3.6 (solid line) shows

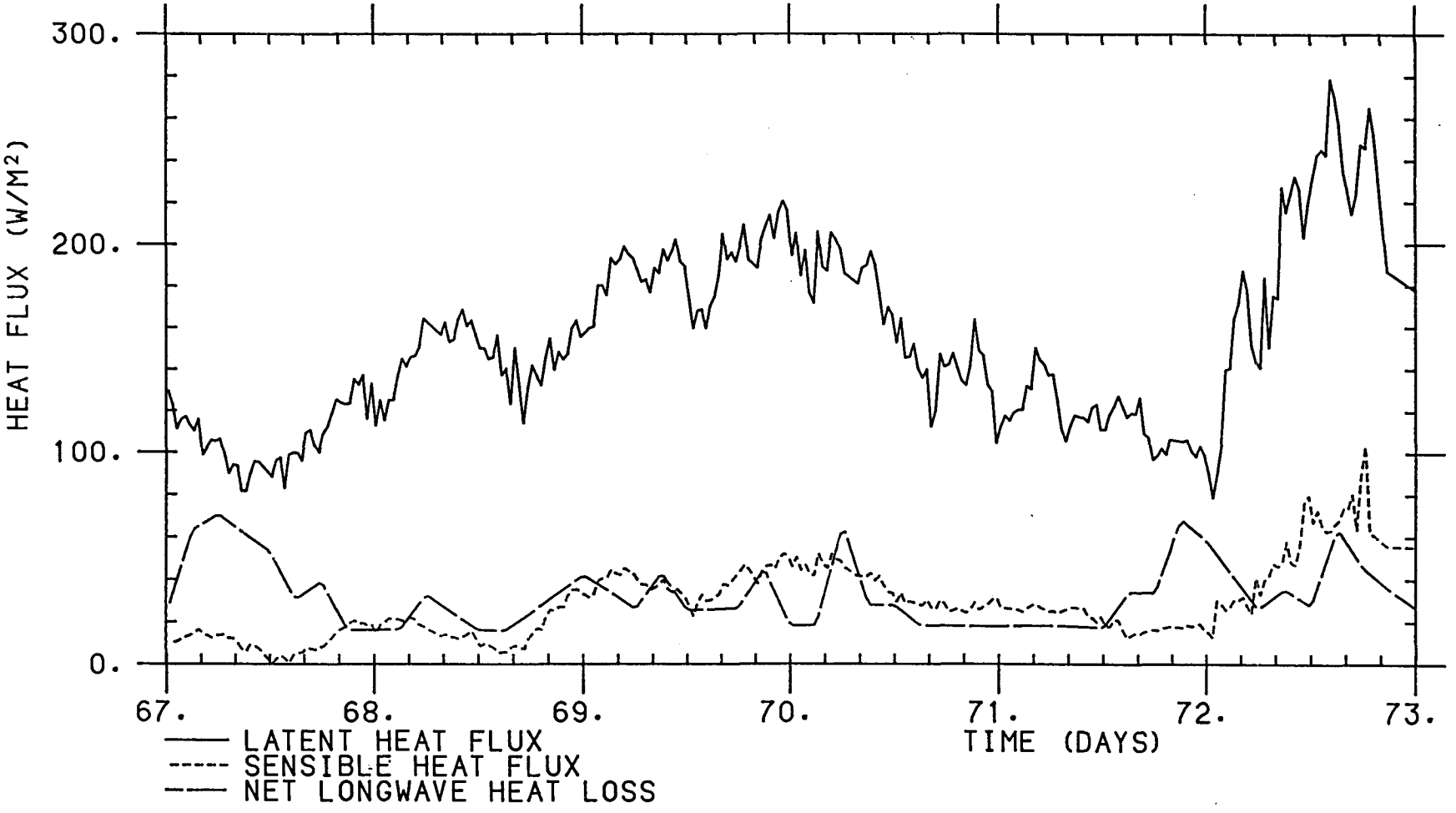

Figure 3.6 : Latent and sensible heat fluxes and net longwave radiation calculated using the observed meteorological quantities. Half- hourly averaged values.

the latent heat flux calculated using equation 3.15. It was estimated that the errors in wind speed, transfer coefficient and (QS-QA) were about 4%, 15-20% and 2% respectively. Thus there is an uncertainty of up to 21% in the latent heat flux.

3.3.4 Sensible heat flux

The sensible heat flux, SFLUX, is defined as:-

SFLUX = RHO Cpair Ct WSPD (HULLTEMP - Td) (3.16)

Cpair is the specific heat capacity of air at constant pressure (1004J/kg/K). Ct is the sensible heat flux coefficient, and RHO is the density of air, as defined earlier. Figure 3.6 (dotted line) shows the sensible heat flux calculated from equation 3.16. The error in the transfer coefficient, Ct, was estimated to be 10%, and about 40% in the difference (HULLTEMP-Td). Together with the 4% in the wind speed, this gives a total uncertainty of about 41%.

3.3.5 Wind stress

The wind stress τ in the eastward and northward directions (τx, τy) (N/m^2) was calculated from the wind velocity components in these directions, as follows:-

$$\tau = RHO\ Cd\ (WSPD)^2 \qquad (3.17)$$

Cd is the drag coefficient. East and north components of the wind stress are given in figure 3.7. The uncertainty in the drag coefficient Cd is estimated to be 10%, which together with the 4% error in the wind speed gives an error estimate in wind stress of 20%. The oceanic friction velocity U^* is then defined by:

$$U^* = \sqrt{\frac{\tau}{\rho 0}} \qquad (3.18)$$

and the rate of work of the wind stress, Ewind (W/m^2) by:

$$Ewind = \rho 0\ (U^*)^3 \qquad (3.19)$$

This is shown in figure 3.8. Uncertainty is estimated at 30%.

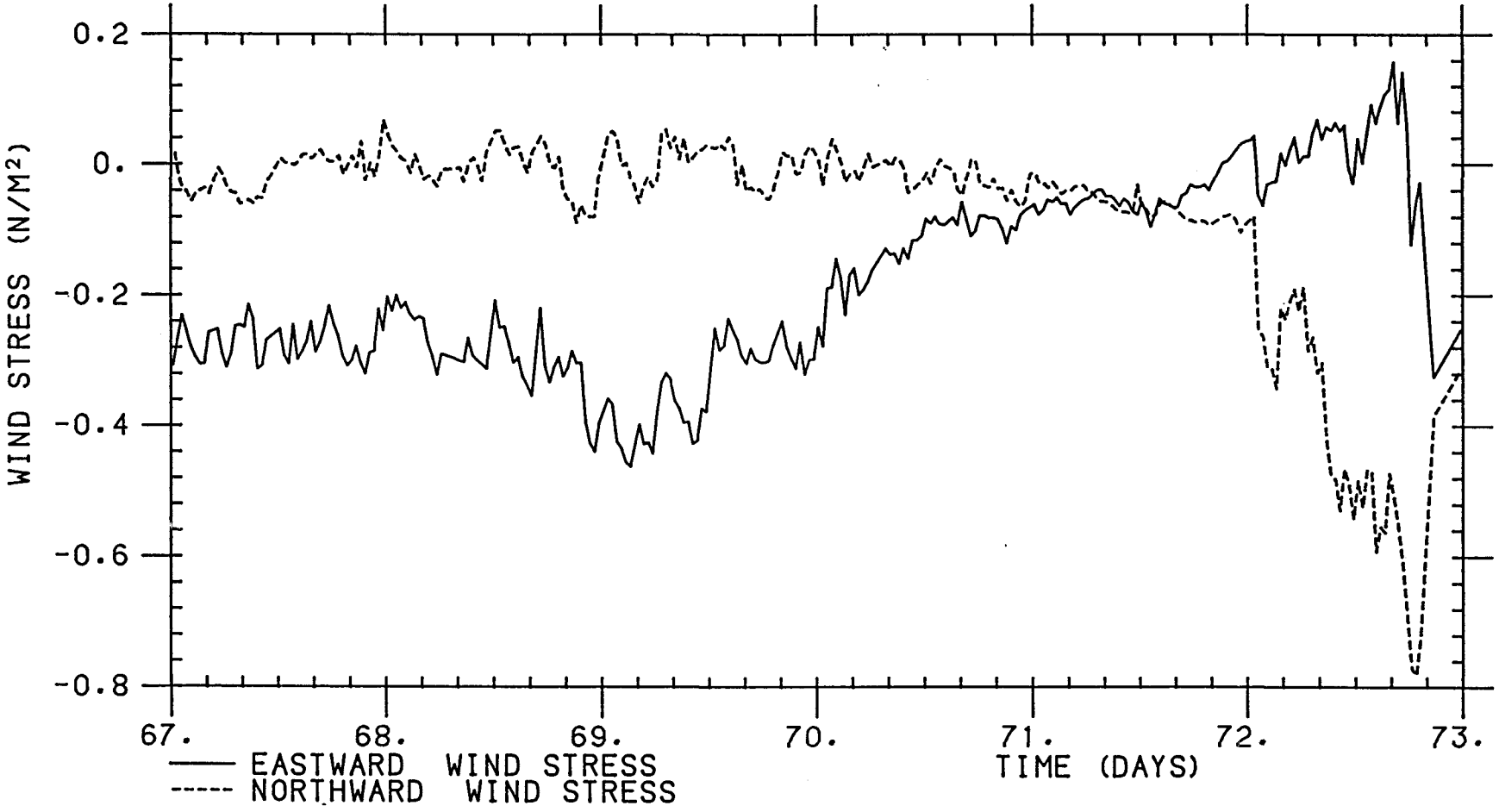

Figure 3.7 : Calculated wind stress components at the sea surface. Half- hourly averaged values.

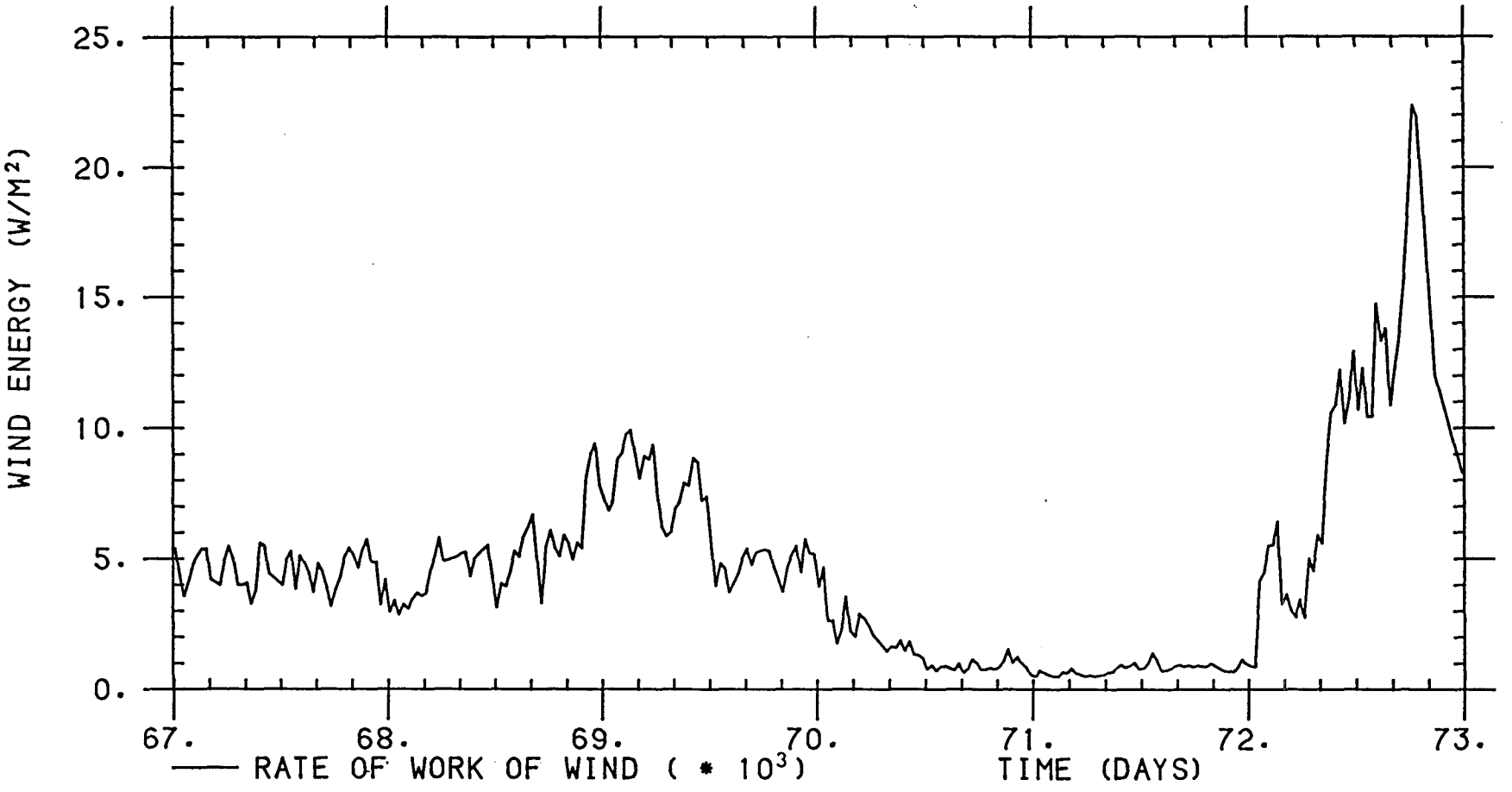

Figure 3.8 : Energy given to the ocean per second by the surface wind stress. Values have been multiplied by 1000 for clarity. Half- hourly averaged values.

3.3.6 Upward and downward shortwave radiation

Radiation absorbed and emitted by the sea surface can be divided into shortwave and longwave. Shortwave radiation is emitted by the sun, and may subsequently be scattered by clouds and the atmosphere. It includes wavelengths from 300nm to 3000nm, with maximum intensity at about 500nm. The downward shortwave radiation, SOLAR, was measured directly during the cruise using the solarimeter, which measures radiation in the wavelength range 305nm to 2800nm (50% transmission points). The upward shortwave radiation (representing that proportion of the downward which is reflected by the sea) is usually defined as a times SOLAR, where a is the albedo of the sea surface.

Payne (1972) measured the albedo for a variety of latitudes and solar elevations. For the Atlantic Ocean at about 45°N in March, he gives an albedo of 7-8%. Simpson and Paulson (1979) measured the albedo at 35°N and found it to be consistently lower than Payne's, although within experimental error. Lind et al. (1984) during the JASIN experiment at about 60°N found an average albedo of 6% whereas Payne predicts about 7%. They attribute this to the increased wind speeds averaging 7m/s compared to Payne's average of 3.7m/s. During the period of the northern area spar deployment, wind speeds were mostly greater than 10m/s, so it seems justifiable to take an albedo of 6%. The value of SOLAR was therefore reduced by 6% to allow for the proportion reflected. It should be noted that albedos are extremely difficult to measure accurately. However, in view of the much larger uncertainties in measurement, the precise value of the albedo has little importance here. Figure 3.9 shows the net shortwave radiation (solid line). It is estimated that the error in SOLAR is about 10%.

3.3.7 Longwave radiation

Longwave radiation, more correctly called terrestrial radiation, is emitted from the earth, ocean, atmosphere and clouds, approximately

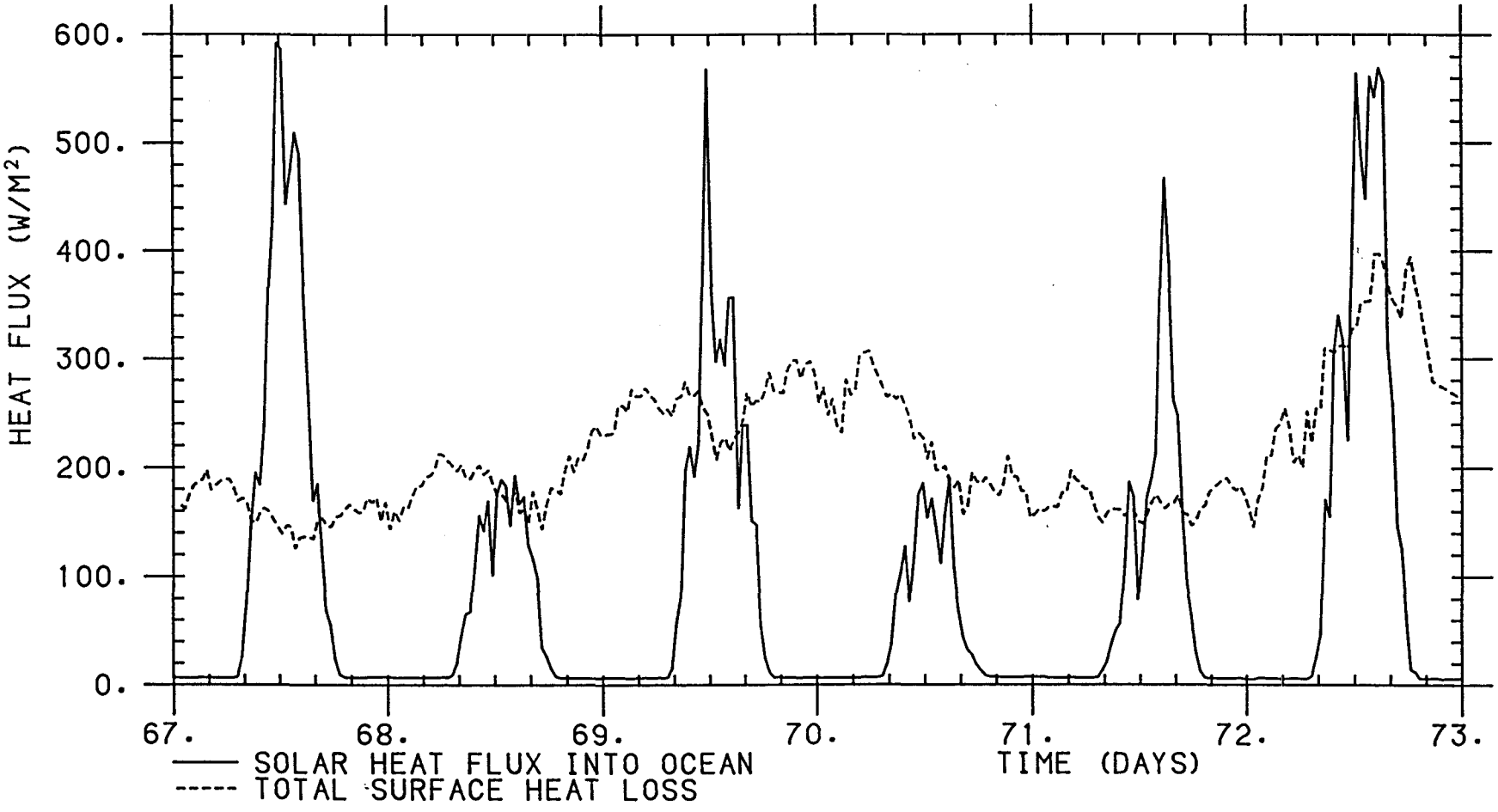

Figure 3.9 : Shortwave solar radiation into the ocean and total surface heat loss (sensible and latent heat fluxes plus net longwave radiation). Half- hourly averaged values.

according to the Stefan-Boltzmann law. It includes wavelengths from 3 to 100 microns (3000 to 100000nm) with a maximum intensity at about 10 microns. Several models (bulk formulae) commonly used to estimate the net longwave radiation LW (W/m^2) received at the ocean surface have been reviewed by Fung et al. (1984) and Simpson and Paulson (1979). The formulae provide the net longwave radiative heat flux out of the ocean, since they calculate the radiation emitted by the sea surface, minus the radiation received from the clouds and atmosphere. They include the models of Anderson (1952):

$$LW = \epsilon \sigma \{(SST)^4 - (Ta)^4 (0.74 + 0.0049 EA)\} F(C) \quad (3.20)$$

and of Bunker (1976):

$$LW = 0.022 \{\epsilon \sigma (Ta)^4 (11.7-0.23 EA) F(C)\} + 4\epsilon\sigma(Ta) (SST-Ta)) \quad (3.21)$$

Smith and Dobson (1984) use the formula of Budyko (1974) in their heat budget study:

$$LW = \epsilon \sigma (Ta)^3 [Ta \{0.254 - 0.0066 EA\} F(C) + 4\{Ta - SST\}] \quad (3.22)$$

Here $\epsilon = 0.97$ is the emissivity of the ocean surface (Anderson (1952))

σ is the Stefan-Boltzmann constant ($5.67 \times 10^{-8} W/m^2/K^4$)

Ta is the near surface air temperature (K) = Td + 273.15

F(C) is a correction depending on the fractional cloud cover, C (N = 8C)

Various estimates of F(C) have been made:

F(C) =	1 - 0.8C	at 35°N (Simpson and Paulson,1979)
=	1 - 0.7C	at 45°N (Bunker,1976)
=	1 - 0.9C	for stratocumulus (Laevastu,1967)
=	1 - 0.9C	for low stratus and stratocumulus clouds typical of middle and high latitudes (Reed,1976)

A cloud factor of F(C) = 1 - 0.8C was decided upon.

A more detailed model has been developed by Lind and Katsaros (1982) which takes into account the cloud type and height (see also Lind

et al., 1984). It will not be described in detail here.

These four models were compared using data from radiosondes launched during the period of interest. Since during the northern area spar deployment the cloud was nearly always low, Lind and Katsaros' model was simplified for ease of computation to include only the low-level clouds. Cloud heights and temperature, sky temperature (taken as the temperature at 500mb), the mixing ratio (q) of the water vapour layer at the ocean surface, and the mean temperature of the water vapour layer were all taken from the radiosonde data. The vapour pressure EA was found from q by

$$EA = \frac{q \times \text{pressure}}{0.622} \qquad (3.23)$$

Results were as follows, where LW is positive upwards, i.e. a cooling:-

Cloud Cover C	Net Longwave Radiation LW (W/m^2)					
	Anderson	Bunker	Budyko	Lind and Katsaros		
				Stratocumulus C15	Cumulus C11	Cumulonimbus C13
2/8	68	69	64	70	62	48
4/8	51	54	50	63	46	37
6/8	34	40	37	38	25	25
8/8	17	25	23	14	14	14

The numerical values used for this comparison were:-

SST = 285K; Ta = 283K; sky temperature = 253K.

q = 6/1000g/g; EA = 9.65mb and pressure = 1000mb.

Since Lind and Katsaros' model takes into account the cloud type and air column characteristics, it is likely to be the most accurate. However, given the inaccuracy of our cloud observations ($\pm$ one or two oktas at least), and the infrequency of radiosonde ascents (less than one per day during the northern area spar deployment), it was felt that the large computational effort involved in applying it was not justified. During the northern area spar deployment, the cloud was nearly always stratocumulus (except for two three- hour periods during the six days), and so Anderson's models was considered to be most

appropriate. Simpson and Paulson (1979) recommend the use of Anderson's formula with a cloud factor of 1 - 0.8C ,and estimate that this can give fluxes within $\pm 20 W/m^2$. Of course, they may have had more frequent and accurate cloud observations than were available to us. Reed (1976) and Fung et al. (1984) both consider Anderson's model to be as good as any simple parameterisation.

Anderson's model was therefore used to calculate the net longwave flux. The near surface water vapour pressure EA was calculated as a function of temperature as defined earlier. Three- hourly means of the temperatures and EA were calculated, centered around the times of cloud observations. The resulting three- hourly longwave fluxes were then linearly interpolated to give fluxes at the same sampling time as the other variables. Figure 3.6 (dashed line) illustrates the net longwave radiation calculated. It is estimated that the error in these values may be up to $20 W/m^2$.

3.3.8 Total surface heat flux

The total heat flux Q entering the ocean is:

$$Q = SOLAR - SFLUX - LFLUX - LW \qquad (3.24)$$

Except for the solar radiation (shortwave), these fluxes may be considered to be surface effects, occurring in at most the top few millimetres of the mixed layer. Longwave radiation does not significantly penetrate the sea water, whereas shortwave radiation may penetrate tens of metres. We therefore define a net surface heat loss H (W/m^2):-

$$H = SFLUX + LFLUX + LW \qquad (3.25)$$

H is given in figure 3.9 (dotted line) together with the solar heat gain; it can be seen from this figure when the ocean is gaining or losing heat to the atmosphere. Obviously there is a net heat loss to the atmosphere if the six day period is taken as a whole. However, on days 67, 69, 71 and 72, there are periods during which there is a net

heating of the ocean.

Remember that the uncertainty in the shortwave radiation is about 10% (section 3.3.6). Figure 3.6 shows that the largest contribution to H comes from the latent heat flux, LFLUX. Although the error of 40% in the sensible heat flux appears large, SFLUX is only a tenth as large as LFLUX. The uncertainty in the total surface heat loss of figure 3.9 is therefore approximately 20-25%. In chapter 4, the error in the net heat flux is required for several periods of a few hours during the experiment. This is calculated using the sum of absolute errors (in W/m^2) in each component of the heat flux during that period.

3.3.9 Monin- Obukhov length

The buoyancy flux, BFLUX (W/kg), is defined as:-

$$BFLUX = \frac{g}{\rho 0}\left(\frac{Q\,\alpha}{Cp} - ETA\ S\right) \qquad (3.26)$$

ETA is the mass of water evaporating from the surface per square metre per second, i.e. LFLUX/LH. S is a typical salinity, taken as 35.65ppt. The freshwater flux due to precipitation is ignored. α and $\rho 0$ are as defined earlier. Cp is the specific heat capacity of sea water, taken as 3.99×10^3 J/kg/K (a suitable value for sea water at about 12°C and 35ppt, taken from Millero et al., 1973). g is the acceleration due to gravity, $9.81 m/s^2$.

The Monin- Obukhov length M gives the relative strengths of the wind mixing and the convection. |M| is the depth at which these two types of forcing are equally effective in producing turbulence in the mixed layer. It is defined by:-

$$M = \frac{(U^*)^3}{Vk\ BFLUX} \qquad (3.27)$$

Vk is Von Karman's constant, 0.42. Since BFLUX is proportional to Q, it will be positive during the day and negative at night. This means that |M| will tend to infinity as BFLUX passes through zero. The Monin-

Obukhov length is only meaningful during a convective regime, and hence I have calculated M using H (the total heat loss) instead of Q in equation 3.26. Figure 3.10 shows the Monin- Obukhov length calculated in this way. The uncertainty is estimated as 30%. Remember that it is only valid during the night. During days 67 to 69, the Monin- Obukhov length is of the same order as the mixed layer depth. Turbulence at this time is controlled by both convection and wind forcing. For days 70 to 72, however, the Monin- Obukhov length is only a few tens of metres, and therefore convection is the major turbulent mechanism.

3.4 Absorption of solar radiation

The different wavelengths of shortwave radiation are absorbed at different rates in the upper ocean, as described by Ivanoff (1977). Infra- red light is absorbed most quickly, and does not penetrate much beyond 1m. Green or blue light, of wavelengths 350-700nm, may penetrate to much greater depths, depending upon the turbidity of the water. At 100m there might be 1% of the incident solar radiation remaining in very clear water.

The decrease of available light may be described approximately as an exponential decay. Kraus (1972) proposed a double exponential form:

$$\frac{I(z)}{SOLAR} = \chi \exp(-jz) + (1-\chi) \exp(-kz) \qquad (3.28)$$

j and k are attenuation coefficients, and χ is a constant for a particular water mass. Paulson and Simpson (1977) measured irradiance in various Jerlov water types and fitted the absorption to an equation of this form. Horch et al.(1983) suggest that one extra exponential term is necessary to model the rapid absorption of the infra- red. They give the relevant attenuation coefficients and constants (χ, $1-\chi$, etc.) for several different types of water, classified according to Jerlov (1968).

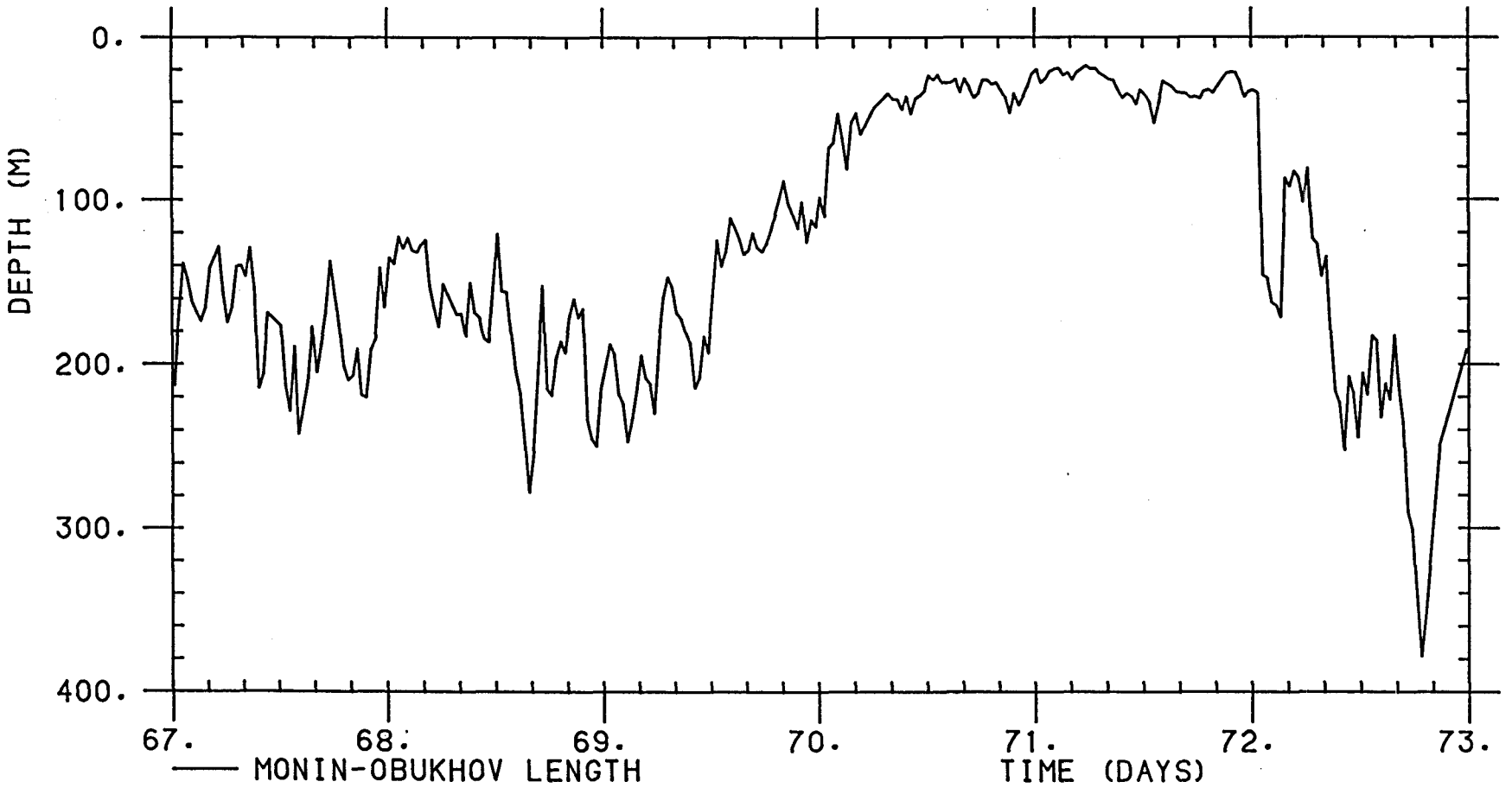

Figure 3.10 : Monin- Obukhov length calculated using the total surface heat loss and the wind stress forcing. It is only meaningful during the night since the solar flux has been neglected.

No measurements of solar irradiance in the ocean were made during Cruise 145. During Cruise 146 however, which surveyed the same area in the following month, many of the shallow CTD casts included an irradiance meter (Angel et al., 1984). In the northern area a CTD yo-yo was undertaken with the irradiance meter (Discovery station number 11054), producing more than 24 hours of continuous dips in the upper 300m. The dates of this CTD cast were 8th - 9th April, and the Spring phytoplankton bloom had not yet occurred. It is therefore assumed that the water characteristics will be the same as those of the water in the same area a month earlier.

The irradiance meter records the light available for photosynthesis, i.e. that in the wavelength band 350-750nm (blue-green). The solarimeter, however, measures the incident solar radiation from 305nm to 2800nm. It is necessary therefore to use a model to describe the absorption of the red end of the spectrum. However, below 1m, where little red light penetrates, the data could be used to find the attenuation coefficients and hence to classify the water type.

The quantity recorded was log (base 10) of the available irradiance I. If log I is plotted against depth, the gradient is the attenuation coefficient divided by log e (e=2.718). Figure 3.11 shows some of the raw data obtained. It is apparent that there is a change in gradient at a depth of about 100m. Below this, the attenuation coefficient is fairly uniform at about 0.035/m. Above 100m depth, the coefficient appears to vary slightly according to the time of day, ranging from 0.060/m at about ten o'clock, through 0.075/m in late morning to 0.080/m when the sun is near its highest point (approximately 1300 GMT, see equation 3.4). During the afternoon, it decreases again, being about 0.07/m in mid-afternoon. It was decided that a value of 0.075/m was a representative value, bearing in mind that the attenuation coefficient should be weighted towards the midday values, when the incident solar

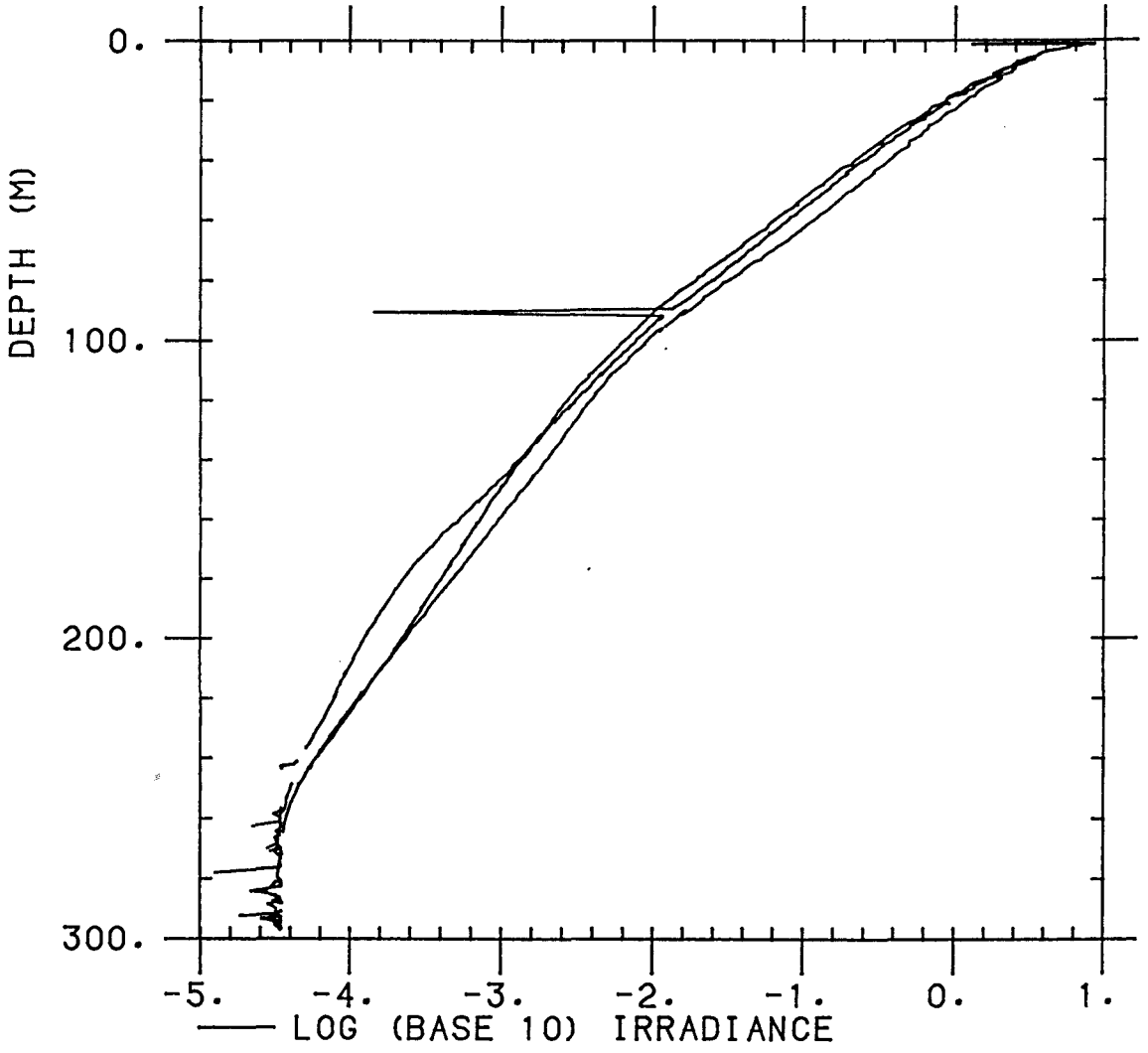

Figure 3.11 : Raw data from CTD station 11054 on Cruise 146. Log (base 10) of irradiance in the wavelength band 350-750nm is shown as a function of depth.

radiation is highest.

Some attempts to model the attenuation using a two- exponential decay were not satisfactory, and it was found to be better to use two single exponential equations, one for each region. The attenuation coefficients were calculated from graphs of the data. In the top few metres, however, a single exponential was found to be unsuitable, even for blue- green light. Hence for the absorption in the top 5m, Horch et al.'s (1983) parameterisation for Class II water was used. This equation seemed to fit the data in the 1 - 100m depth range better than their parameterisations for other water types. The equation applies to all shortwave wavelengths, and thus will account for the red end of the spectrum, which we did not measure.

In conclusion, the equations used for the available irradiance I (W/m^2) as a function of depth z were:-

For z < 5m: (equation 3.29) (Horch et al., 1983)

$$\frac{I}{SOLAR} = 0.219 \exp(-0.0684z) + 0.2452 \exp(-0.2098z) + 0.533 \exp(-7.19z)$$

For 5m < z < 100m:

$$\frac{I}{SOLAR} = c1 \exp(-0.075 z) \qquad (3.30)$$

For z > 100m:

$$\frac{I}{SOLAR} = c2 \exp(-0.035 z) \qquad (3.31)$$

By specifying continuity at z=5m and z=100m, the constants c1 and c2 were found to be 0.3514 and 0.0064 respectively. The resulting modelled irradiance profile is shown in figure 3.12. Also shown is the modelled irradiance predicted using the Horch et al. (1983) parameterisation throughout the profile, not just the upper 5m. If a surface flux of $500W/m^2$ is incident, then using equations 3.29 to 3.31, the solar flux below 100m is negligible (figure 3.13).

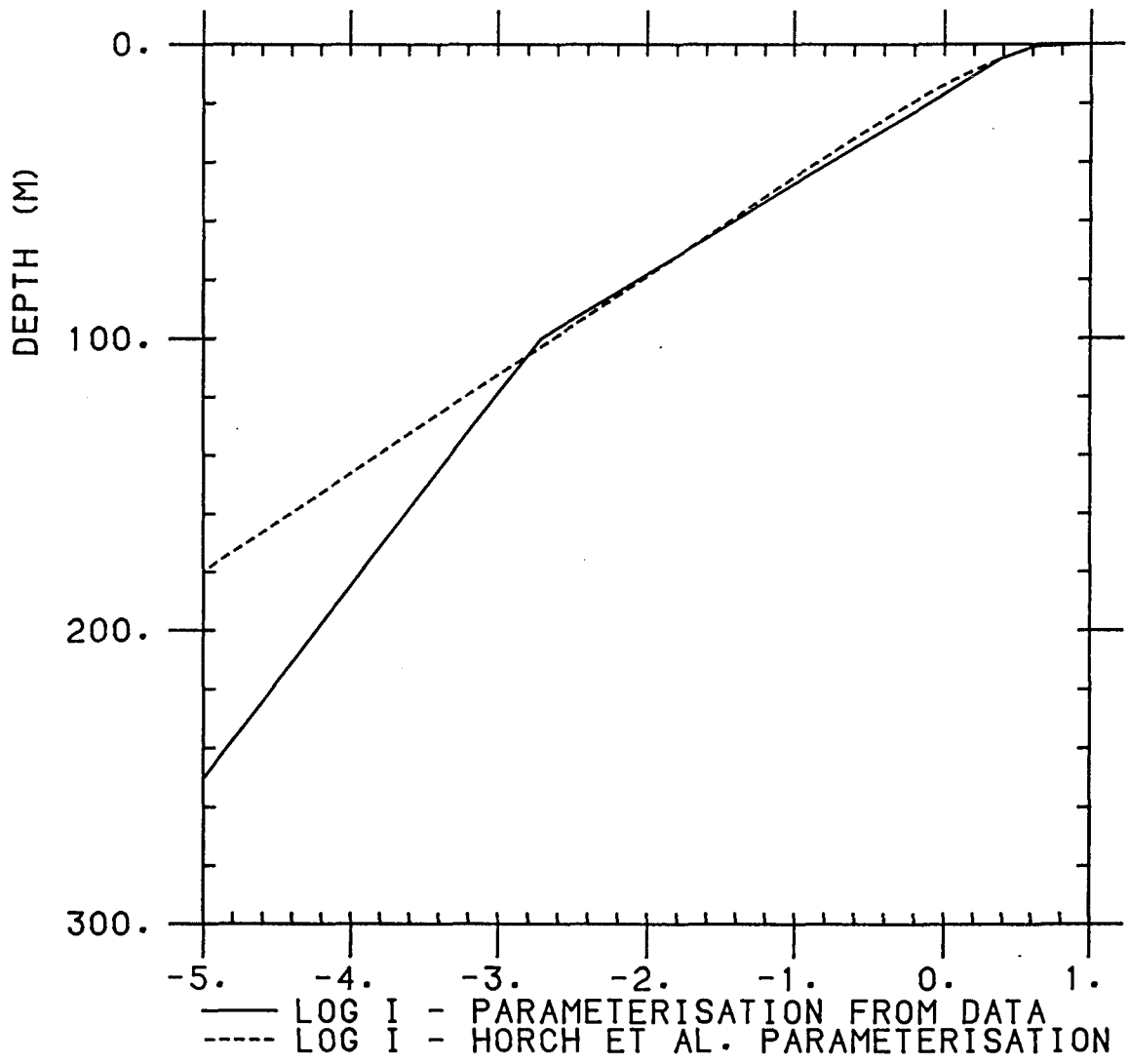

Figure 3.12 : Modelled absorption of solar radiation with depth. The graph shows log (base 10) of the irradiance I (W/m^2) as a function of depth. The solid line denotes the parameterisation from figure 3.11 discussed in the text, while the dotted line shows the parameterisation of Horch et al. (1983) for class II water.

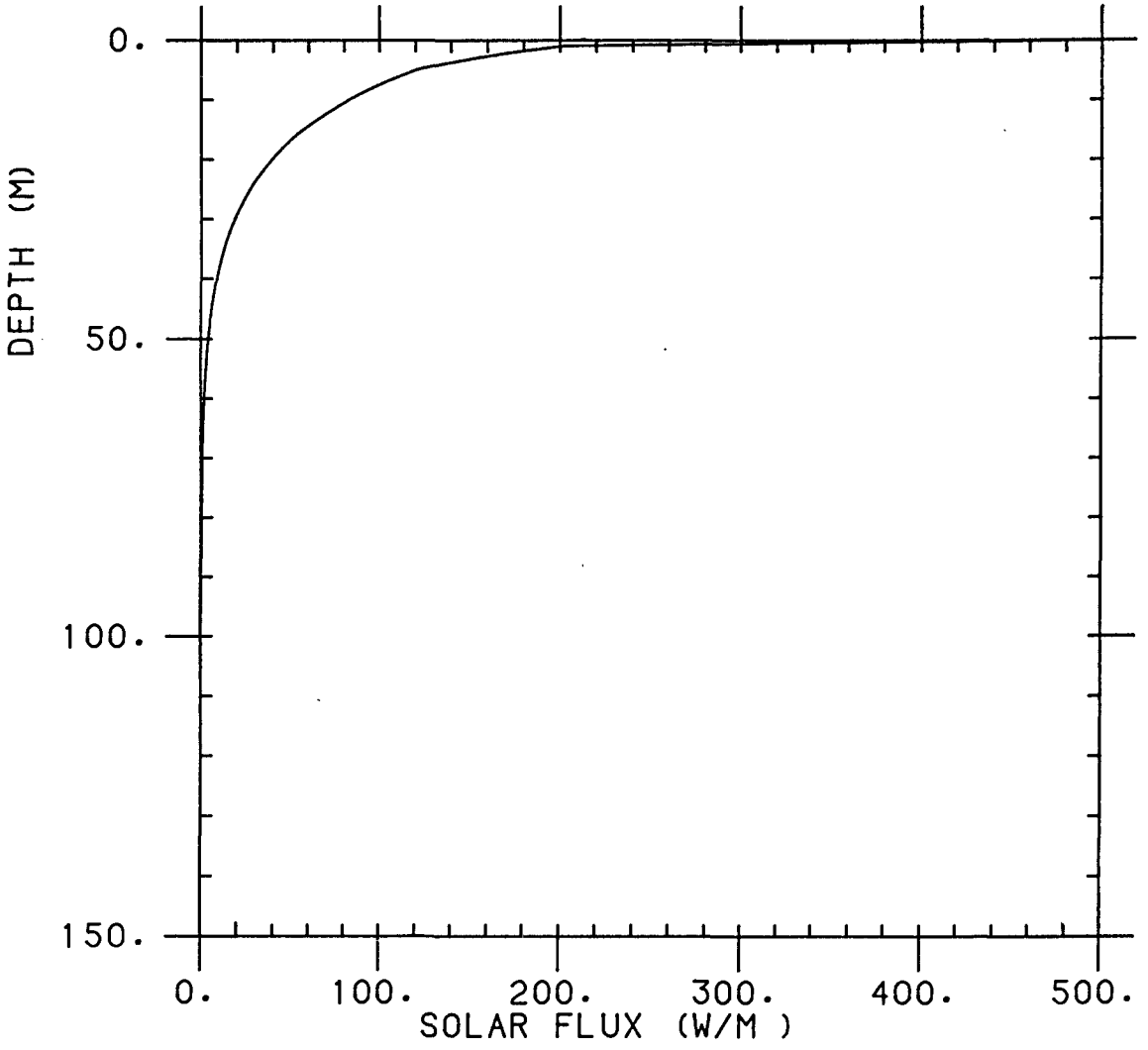

Figure 3.13 : Solar flux penetration in the upper 150m, assuming a surface flux of 500W/m^2.

Chapter 4

Heat Budget of the Upper Ocean

4.1 Introduction

Using the surface heat fluxes described in chapter 3, a heat budget for the upper 145m was evaluated for the northern area spar deployment. The bulk formulae provide the total surface heat loss due to sensible and latent heat fluxes, plus the longwave radiation, while solar radiation was measured using the solarimeter (figure 3.9). The net heat loss or gain by the ocean may be compared with the heating signal observed at the current meters (VACMs) (figure 2.7) at depths between 15m and 145m, as described in chapter 2.

If figures 3.9 and 2.7 are compared, it will be noticed that the days on which the heating signal in the ocean is greatest are the sunniest days, as one would expect. Thus the signal is likely to be caused by solar heating. This would suggest that, for the water with which the spar buoy is drifting, air- sea interaction is the dominant process controlling the mixed layer structure, rather than frontal or eddy dynamics. The heat budget will now be examined in closer detail.

Consider the column of water in which the spar buoy and its instrumentation are situated. Let the horizontal cross- section of the box be $1m^2$, and the box extend downwards from the surface to a depth ΔZ. Let the change of temperature in a time dt at a depth z be dT(z). Then the change in heat content of the box is simply the sum of the heat fluxes through the top, bottom and sides. This may be written as:

$$\int_0^{\Delta} dT(z)\, dz = \frac{Q\, dt}{\rho 0\, Cp} + dt \int_0^{\Delta} \underline{v}(z).\underline{\nabla}T(z)\, dz + dt\, w(\Delta Z)\, \Delta T \qquad (4.1)$$

A B C D

Term A is the total change in heat content of the column between the surface and depth ΔZ. Term B is the net heat loss or gain between the ocean and the atmosphere. Q is the heat flux through the surface, as

defined in chapter 3. Term C represents the transport of heat through the sides of the box due to horizontal advection. Term D is the change in heat content due to the vertical transport (velocity w) of warm or cold water (temperature difference ΔT) through the bottom of the box.

4.2 Fluxes through the bottom of the box

The heat flux through the bottom of the box might be caused by a large scale vertical velocity induced by Ekman pumping, producing a rise or fall of the isotherms. The magnitude of the Ekman pumping may be calculated using the values of the wind stress at the corner points of the triangular survey performed by the ship (figure 2.12). Taking three consecutive points, the curl of the wind stress may be calculated. The upwelling velocity, w, at the mixed layer base is then given by:

$$w = \frac{1}{f\,\rho 0}\left(\frac{\partial \tau y}{\partial x} - \frac{\partial \tau x}{\partial y}\right) \qquad (4.2)$$

Using this equation, eleven estimates of upwelling or downwelling were obtained at regular intervals during the northern area spar deployment. The mean velocity calculated was a downwelling of 7×10^{-6} m/s with a standard deviation of 4×10^{-6} m/s (the large standard deviation is due to day to day variability). This is equivalent to about 0.6m/day, and is extremely small compared to other sources of heating or cooling at the spar.

Larger vertical velocities through the base of the box will be caused by turbulent mixing taking warmer water out of the box and replacing it with cooler water entrained from a deeper level. To estimate this, one requires not only the rate of deepening of the mixed layer (w), but also an estimate of the temperature of the water being entrained from below (temperature difference ΔT).

Figures 4.1, 4.2 and 4.3 show three examples of profiles from the SeaSoar data. They have been chosen as periods during which the ship

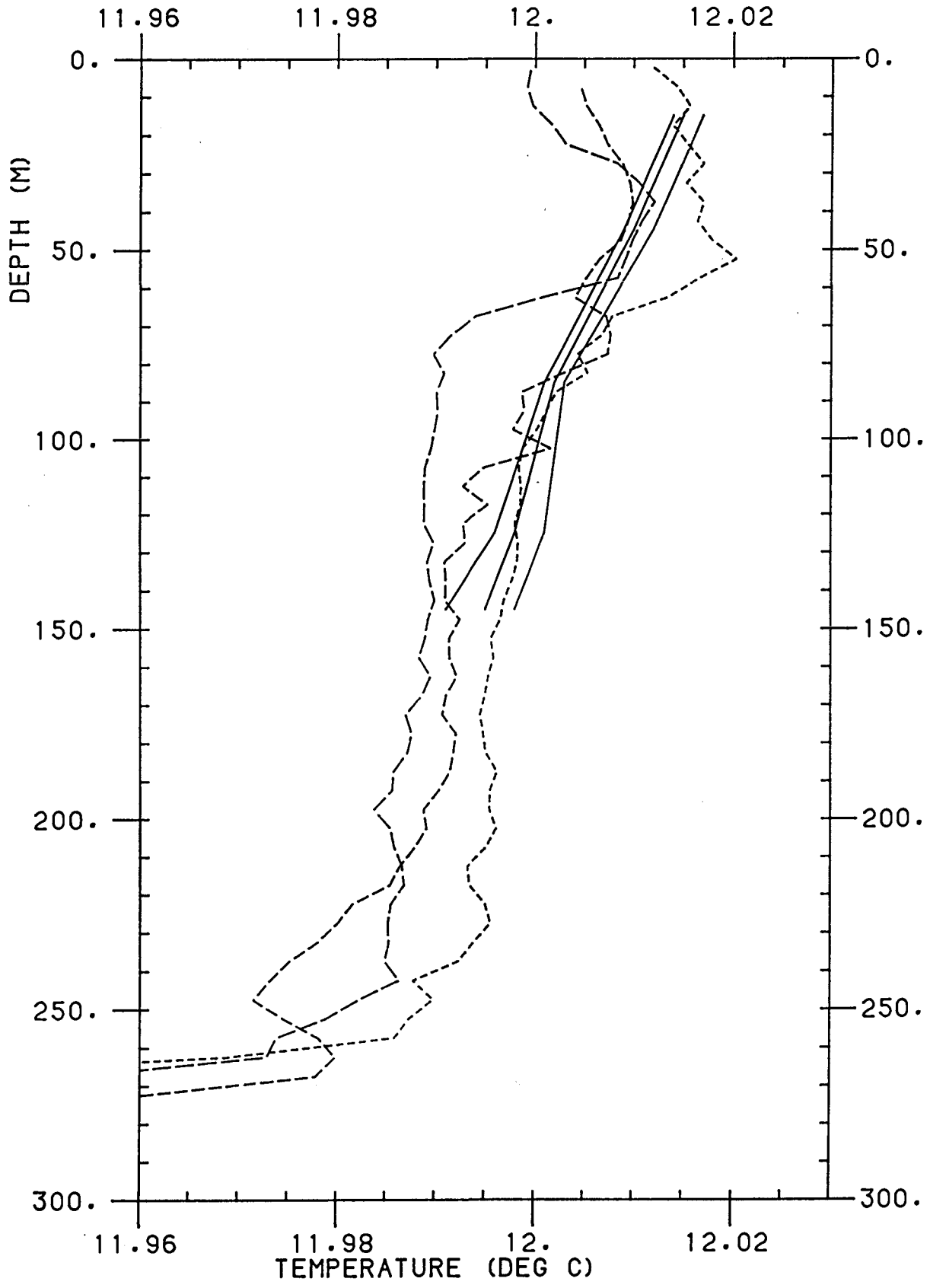

Figure 4.1 : Consecutive SeaSoar profiles between 67/1830 and 67/1845. The first profile is dotted; subsequent profiles have longer dashes. Several examples of profiles from the VACMs during the same period are shown as solid lines.

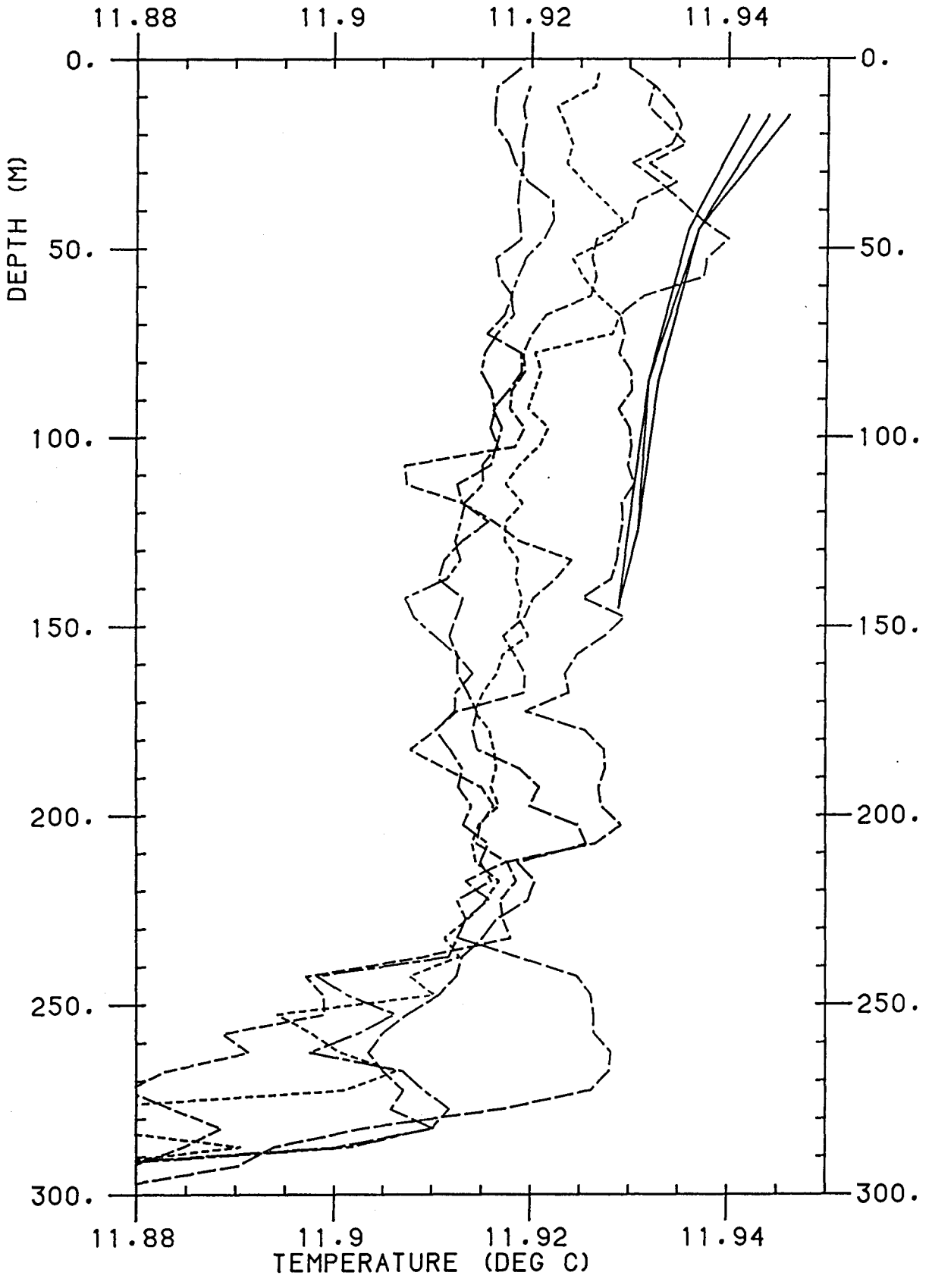

Figure 4.2 : Consecutive SeaSoar profiles between 69/1230 and 69/1300. The first profile is dotted; subsequent profiles have longer dashes; the final one is dash- dot. Several examples of profiles from the VACMs during the same period are shown as solid lines.

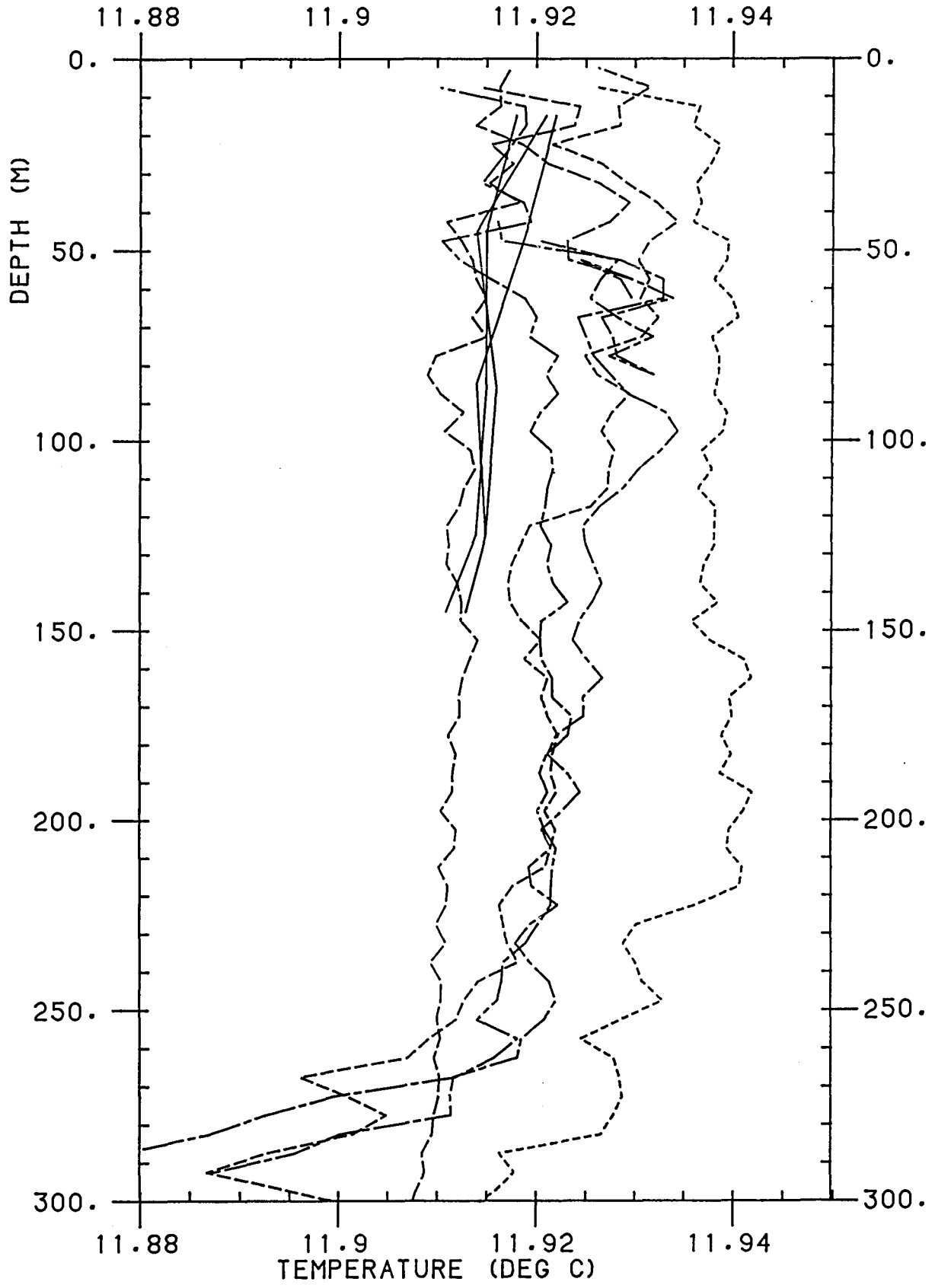

Figure 4.3 : Consecutive SeaSoar profiles between 69/1950 and 69/2020. The first profile is dotted; subsequent profiles have longer dashes; the final two are dash- dot. Several examples of profiles from the VACMs during the same period are shown as dotted lines.

passed close to the drifting spar buoy. The solid lines show some sample temperatures at the VACMs during the same period; it can be seen that the two instruments are in broad agreement (within 5mK). A check of the positions of the SeaSoar profiles which were in agreement with the VACMs showed that on each occasion the patch of water being sampled was upstream of the spar buoy and therefore in a feasible position (see further discussion in section 4.5). It might therefore be suggested that these profiles be used to estimate both the entrainment velocity and the temperature jump at the base of the mixed layer. I do not believe, however, that this can be done with any degree of certainty, for the following reasons:

1/ From figures 4.1 to 4.3, one may see that the difference in mixed layer depth between adjacent profiles may be as large as 50m. It would be impossible to guess which one to use for estimating the mixed layer depth.

2/ If an average of several profiles in the area were taken, ambiguities would be introduced by the arbitrary choosing of profiles to average. It will be seen in chapter 7 that horizontal temperature structure appears to be important; therefore a horizontal average of profiles will not produce a deepening rate applicable at the spar buoy.

3/ As is apparent in figures 4.1 to 4.3, there is no obvious value to take for the temperature jump across the mixed layer base. There is much variability between profiles. If the data below 300m are plotted, the profiles do not converge to a uniform temperature gradient, suggesting that horizontal variability dominates the temperature found at depths in the thermocline. The SeaSoar penetrated only 50-150m of the thermocline.

4/ The SeaSoar passed the drifting spar buoy only three times per day, on average. It would therefore be necessary to assume that entrainment was uniform during each period. It is likely that entrainment would be

considerably larger at night when both convective cooling and wind mixing are active in deepening the layer. Estimates of entrainment would therefore be invalid except as averages over several days.

During the heating period of each day, entrainment at the base of the mixed layer will be much reduced, since stratification inhibits wind mixing and convection. Heat budgets will therefore be calculated primarily for heating periods, since the entrainment is small. There will be some entrainment during the day due to Kelvin- Helmholtz instability and the breaking of internal waves. This will slightly cool the mixed layer; therefore the calculated heat required to raise the temperature of the water by the observed amount will be an underestimate.

At night, entrainment will be large and may be the main source of cooling of the layer. Since this cannot be quantified for the reasons stated above, the heat budget is not as meaningful as that for heating periods.

4.3 Horizontal Advection

Term C in equation 4.1 expressed the effect of advection of warm or cool water through the sides of the box. When heat budgets are performed for the atmosphere, it is usually found that horizontal advection plays an important role. If an oceanic heat budget does not balance, horizontal advection is frequently invoked to supply the deficit, but without justification of its effect. With this data set, however, horizontal structure information is available from the SeaSoar surveys and the magnitude of the advection can be calculated.

Figures 4.4 and 4.5 show the structure at days 67 and 69. Temperature data from the triangular SeaSoar survey have been gridded by depth; the figures show data at 75m. Contours have been drawn in where they seem reasonable. At the beginning of the survey, there is a significant 30mK ramp lying east-west, with warm water to the north and

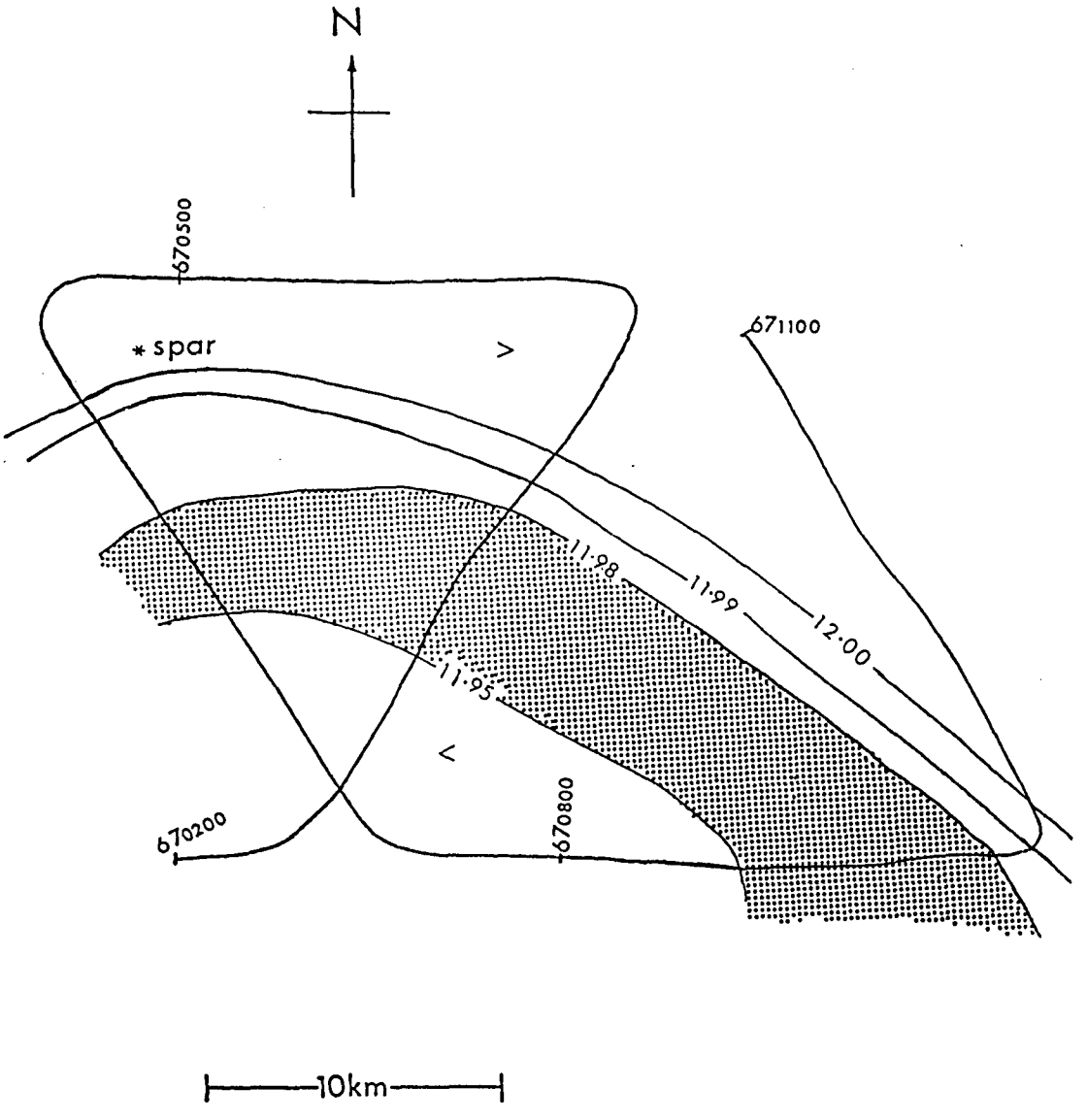

Figure 4.4 : Horizontal temperature structure at the beginning of the SeaSoar survey (day 67) at a depth of 75m. Day and time are annotated along the track. The 30mK ramp is shaded.

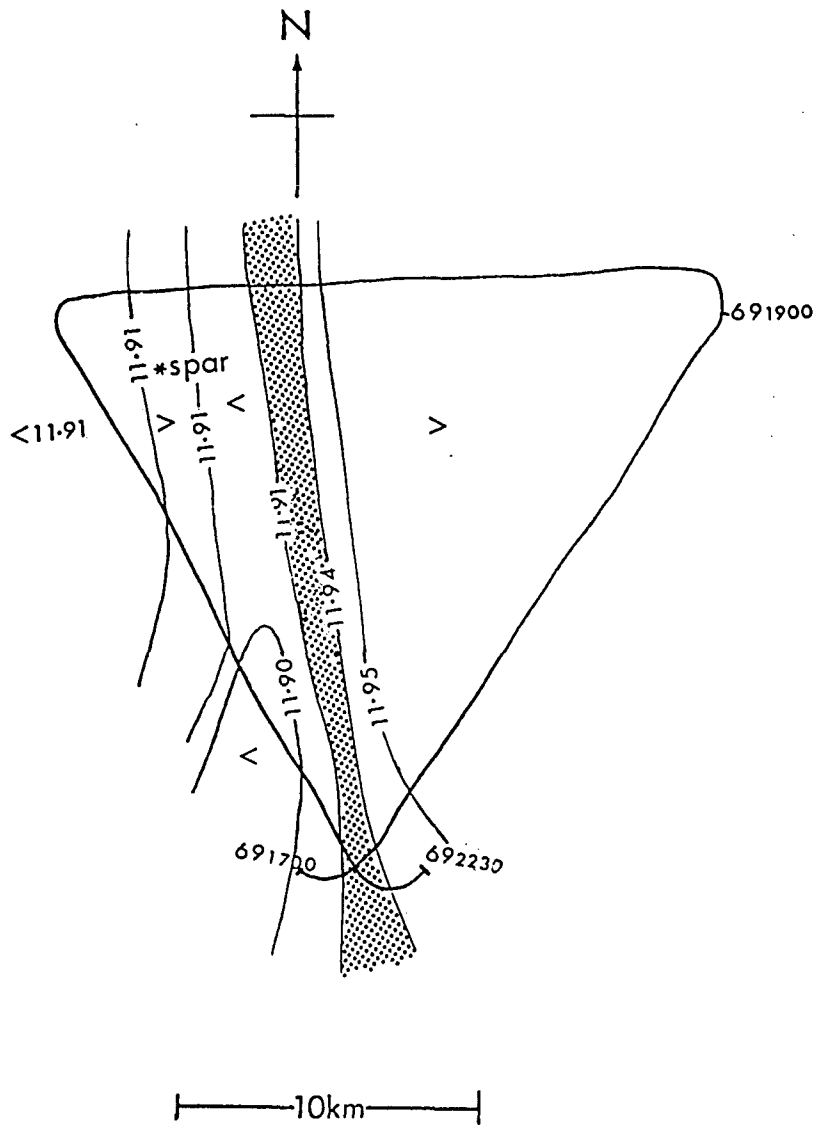

Figure 4.5 : Horizontal temperature structure at the end of the SeaSoar survey (day 69) at a depth of 75m. Day and time are annotated along the track. The 30mK ramp is shaded. Notice that it has cooled by about 40mK from day 67. It has also rotated clockwise by about 90°.

colder water to the south. The spar is initially on the warmer side. During the period of the survey, the ramp rotates relative to the spar and the water, until it lies nearly north-south, with the warmer water to the east. During the early morning of day 69, the spar rapidly crosses the ramp, and ends on the colder side. This can be seen in the temperature time series (figure 2.7) at this time, when there is an anomalously strong cooling of all layers simultaneously.

This rapid cooling is therefore predominantly an advective effect. Analysis of the SeaSoar data (Pollard, personal communication) provides numerical values for the cooling at the spar buoy due to its traverse of the ramp (2.0×10^{-7} °C/s between 67/2100 and 69/0300; 14.4×10^{-7} °C/s between 69/0300 and 69/0730). Consideration of the heat budget must therefore include the advection of cooler water during this period.

Obviously very little diurnal oscillation would be required in this region of strong horizontal gradients to produce a sizable diurnal heating signal. A number of points would seem to support this hypothesis:

a) It would explain the simultaneous heating of all the VACMs (figure 2.7): there does not seem to be more than a two hour time lag between the heating signal near the surface and that below 100m.

b) There does appear to be a small diurnal signal in the currents past the spar (figure 4.6), particularly those at 125m and 145m. This is probably owing to the slight diurnal variation observed in the wind velocity.

c) The ramp is about 30mK which is about the magnitude of the heating signal observed.

However, it shall be shown that diurnal advection does not dominate the diurnal heat budget, for the following reasons:

REF.

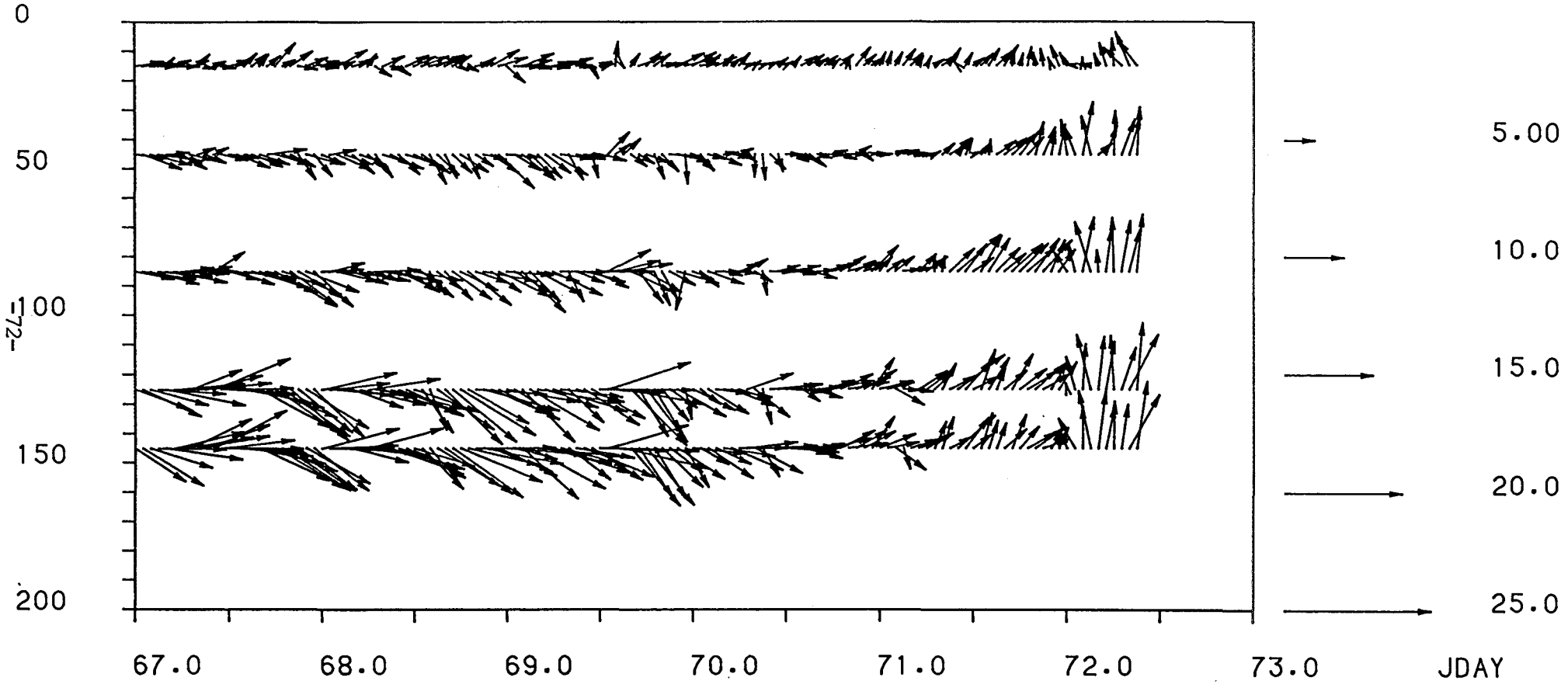

Figure 4.6 : Hourly averages of horizontal currents relative to the spar buoy at depths as marked on the vertical axis. Arrows in the y- direction imply currents moving northwards past the spar, the x- direction is eastward. The scale of arrow length is given on the right- hand-side; velocity units are cm/s.

a)The heating signal coincides with the sunniest days, being negligible on cloudy days. An advective effect would be likely to be independent of the surface fluxes. It seems implausible that an advective effect would occur at the same time each afternoon in phase with the solar heating.

b)An estimate of the advective effect shows that it is too small to account for the observed heating. The spar is moving with the water in the top 10-15m. As can be seen from figure 4.6, the currents past the spar are small (less than 4cm/s) at the upper VACMs and only significant at 125m and 145m (say 10-15cm/s). Figures 4.7 and 4.8 show progressive vector diagrams of the velocity of the water past the spar at 15m and 145m respectively. Taking day 67, when there is a large observed heating effect, it is seen that the water past the spar at 145m moves less than 2km in the north-south direction. Remember that the structure at this time lies in the east-west direction (figure 4.4), so the steep gradient of the ramp is north-south. From the SeaSoar surveys across the ramp, the horizontal temperature gradient is estimated to be approximately 0.1°C in 10km. So a heating signal of up to 20mK at 145m could be explained. This does indeed seem to be of the right magnitude. However, figure 4.7 shows that the diurnal motion of the water past the spar at 15m is at most 0.5km. Hence a heating signal of less than 5mK could be provided by horizontal advection at 15m, whereas we observe about 30-40mK.

c)A close look at the diurnal motion of the water past the spar in figure 4.8 reveals that at 145m, the spar is furthest towards the cold water during the day, and towards the warmer water at night. (Remember that the plot shows the water past the spar, so the spar motion relative to the water structure is the reverse.) Thus the horizontal advection effect is 180° out of phase with the observed heating. Horizontal advection therefore does not provide the observed diurnal

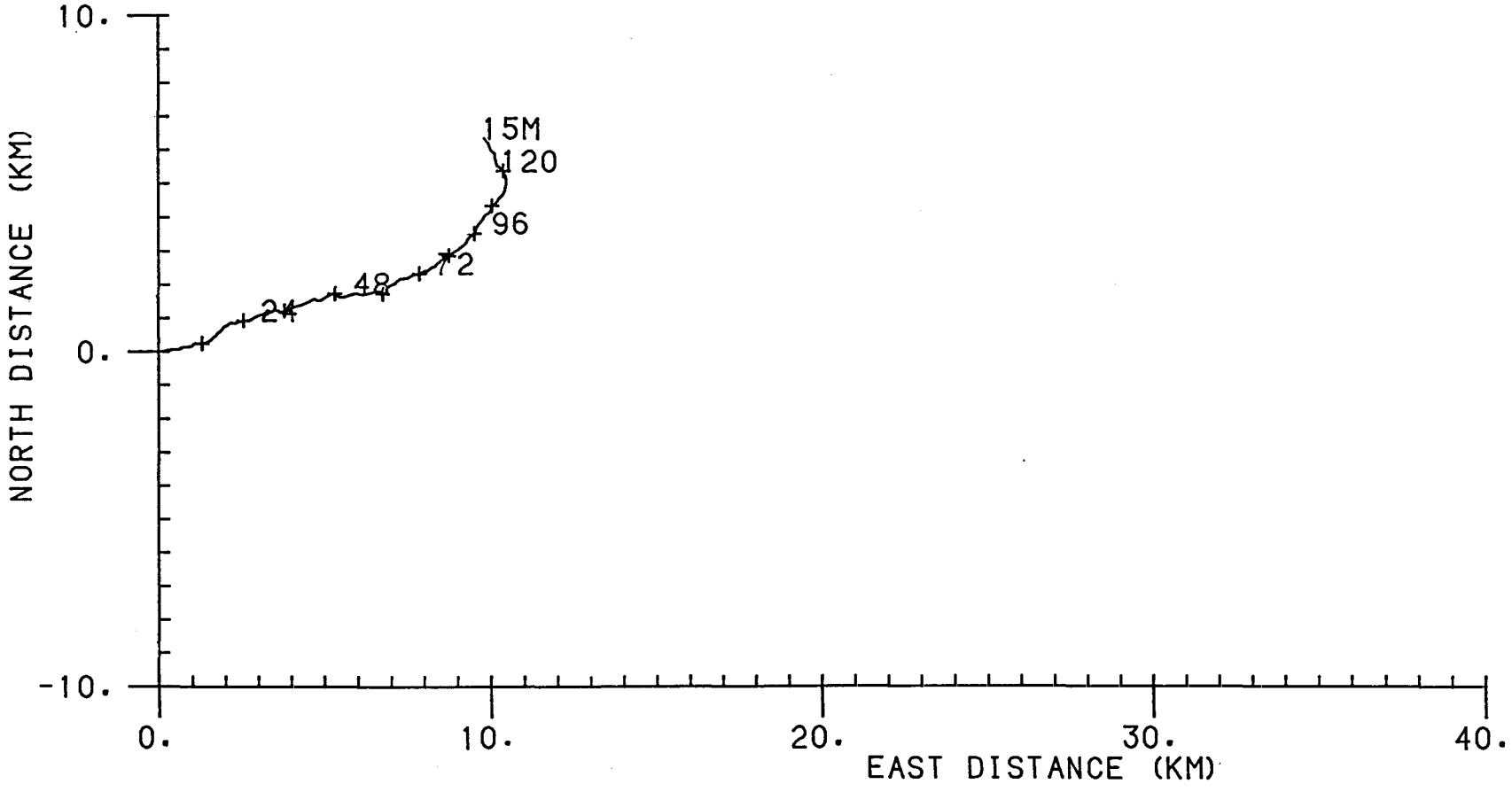

Figure 4.7 : Progressive vector diagram of the current past the drifting spar at 15m. The plot starts at day 67.0. 24- hourly positions are annotated.

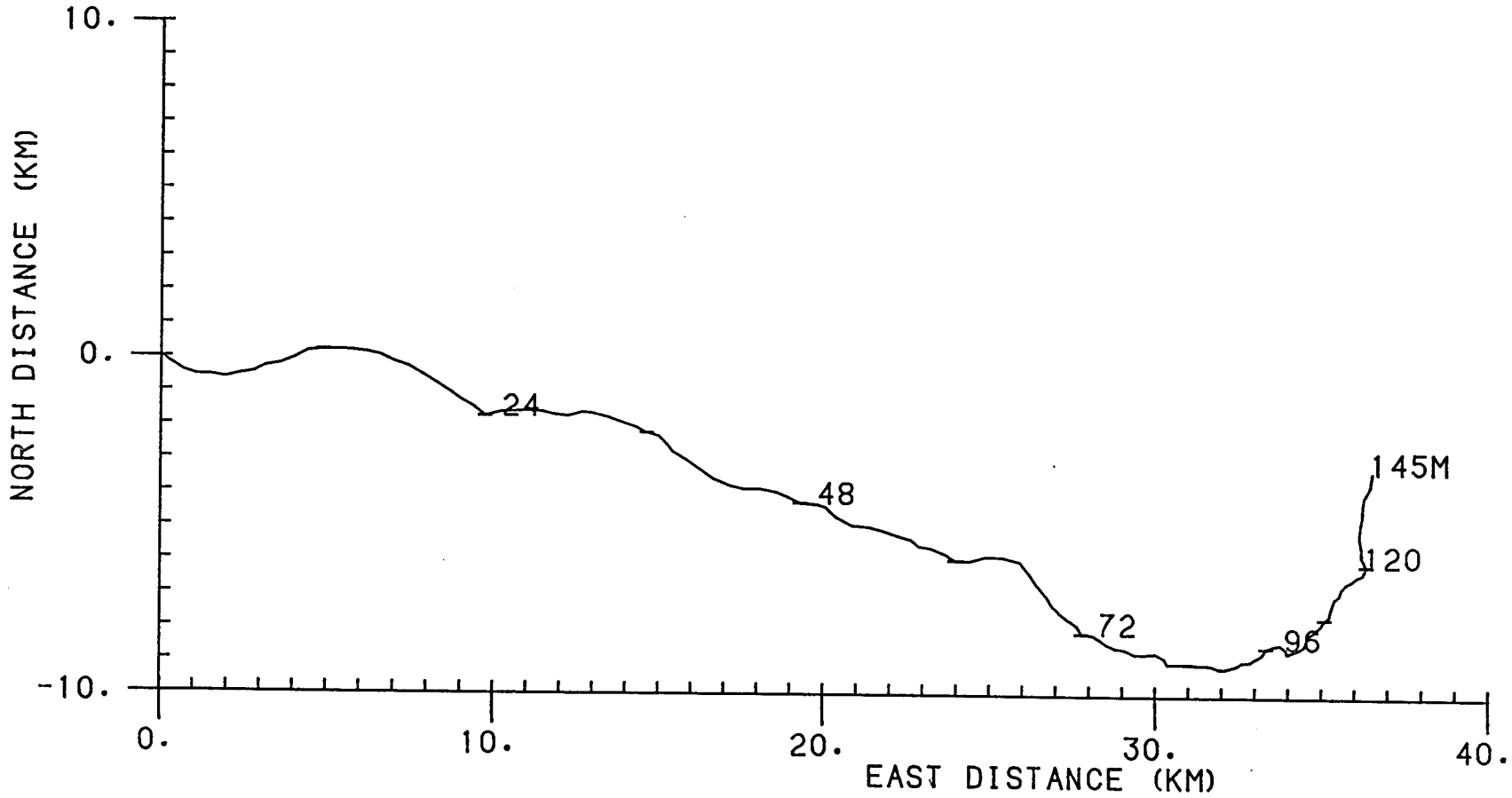

Figure 4.8 : Progressive vector diagram of the current past the drifting spar at 145m. The plot starts at day 67.0. 24- hourly positions are annotated.

signal of heating and cooling; in fact, it will reduce the amount of heating or cooling observed.

4.4 Calculation of the budget

For calculation of the heat budget, it will therefore be assumed that the dominant source of heating or cooling is the surface heat flux. Taking the temperature time series from the VACMs, (unfiltered data, figure 2.7), the quantity of heat required to warm the water column by the observed amount is calculated. It has been assumed that all the water between the surface and 15m is heated to the 15m temperature, while all the water at depths of 15-45m is heated to the 45m temperature, and so on. In reality, it is likely that during daytime stratification, the water above a particular current meter will be heated more than the water at the same level as the current meter. Moreover, there may be a significant diurnal heating signal below the lowest current meter, and this has been neglected. It was seen in section 4.3 that horizontal advection will also play a small part in reducing the observed diurnal signal. Thus the smallest possible amount of heat required to heat the water column has been calculated.

Figure 4.9 shows the heat provided by the meteorological forcing (dotted line) and the heat required to produce the observed VACM signal (solid line). The cooling observed as the spar buoy crossed the ramp (section 4.3) has been subtracted from the required cooling. Therefore the change in heat content of the water column should be caused by the surface forcing and by entrainment. However, figure 4.9 shows that the ocean cools less over the five day period than one would expect from the surface fluxes.

Taking the period from 67/0600 to 71/0600 a cooling of $34(\pm 5)MJ/m^2$ is required and a cooling of $42MJ/m^2$ is available. The uncertainty in the total heat flux over the period is probably about $20MJ/m^2$; this is difficult to estimate when periods of heating and cooling are

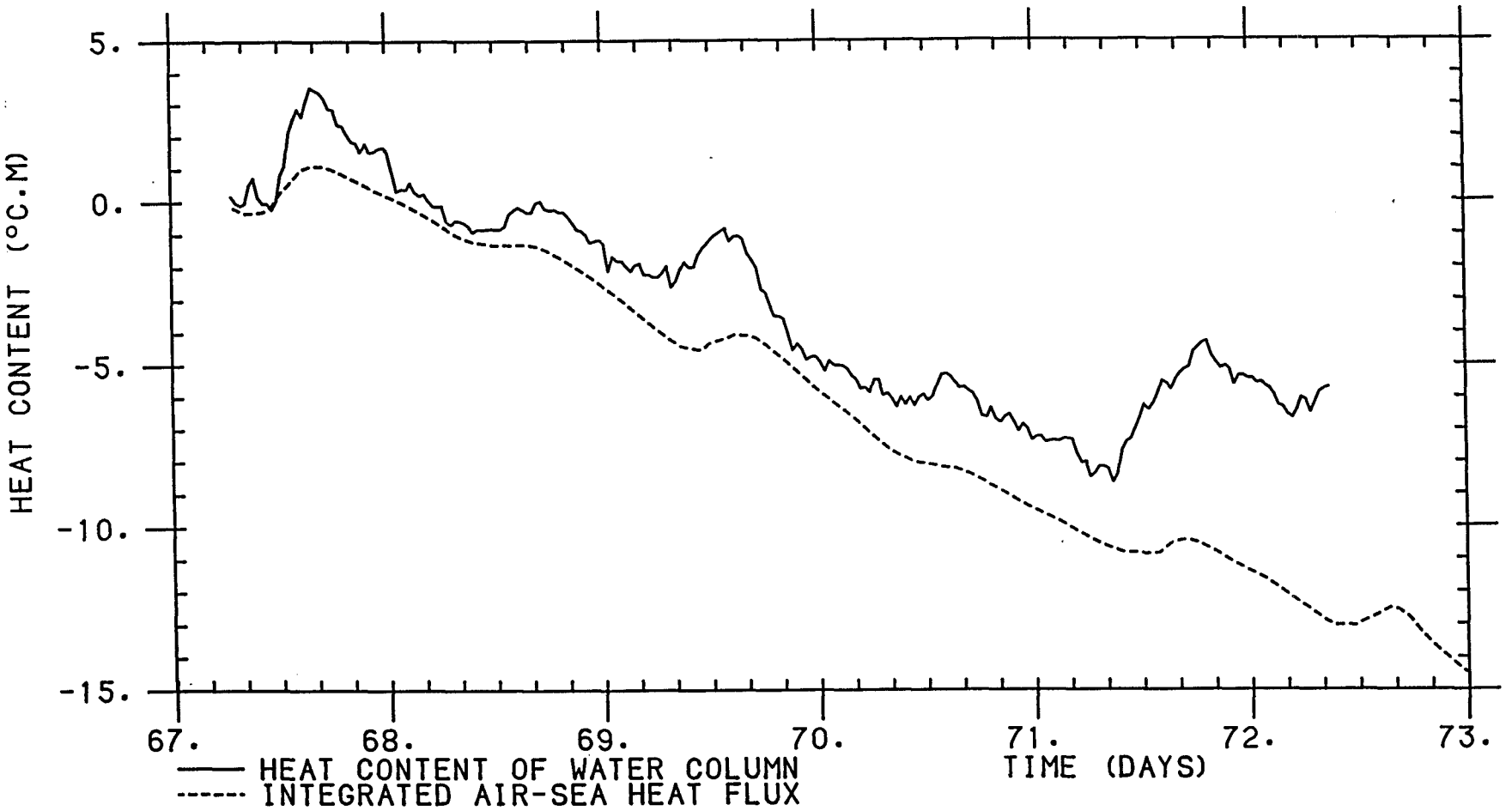

Figure 4.9 : Heat budget of the upper 145m during the northern area spar deployment. The solid line shows the change in heat content of the upper ocean from the VACM temperature signal. The dotted line gives the integrated air- sea heat flux. Both are designated zero at 67/0600 and use half- hourly averaged values.

considered together, since if solar heating and the latent heat flux are of similar magnitude, the net heat flux is small but the uncertainty is large. During the heating periods the heat required will be an underestimate due to stratification, while at night the upper ocean is more uniform due to mixing, or may even be statically unstable for a short time. Part of the observed cooling will be due to the entrainment of cooler water. Because of the large uncertainty in the surface heat flux over a several day period, it is more useful to consider heating and cooling regimes separately. Figure 4.9 suggests that, particularly on day 67, there is an anomalous source of warming during the heating period followed by an anomalous source of cooling at night. Therefore the heat budgets for distinct periods of heating or cooling will now be considered.

Table 4.1 gives the amount of heat required and available for heating during the three main heating periods. Units are MJ/m^2 i.e. $10^6 J/m^2$.

Table 4.1 - Heat Budget for Heating Periods

Time Interval (day/ hour)	Heat Available (MJ/m^2)	Heat Required (MJ/m^2)
67/0930 - 67/1600	5.8 ± 2.6	13.0 ± 1.5
69/1100 - 69/1500	2.0 ± 1.5	3.7 ± 1.5
71/1230 - 71/1700	1.7 ± 1.3	4.8 ± 1.5

The heat available is the net heat flux, i.e. the total of shortwave and longwave radiation, sensible and latent heat fluxes. The error denotes the maximum possible bounds, taking the largest possible uncertainties involved in the transfer coefficients, air and water temperatures, and wind speed. The next column shows the amount of heat required to raise the temperature of the water column by the observed amount in the same time interval.

Thus for day 69, the heating observed could just about be provided by the observed heat flux if all the assumptions made are true, and if all the uncertainties are taken to have their maximum values. This would seem unlikely. For days 67 and 71, the heat budget cannot balance even taking the largest uncertainties. In fact for day 67, a maximum of only 73% of the required heat can be provided by the surface fluxes.

The cooling periods are more difficult to analyse. The following table shows the available and required cooling.

Table 4.2 - Heat Budget for Cooling Periods

Time Interval (day/ hour)	Heat Available (MJ/m^2)	Heat Required (MJ/m^2)
67/1600 - 68/0600	-7.3 ± 1.4	-18.9 ± 1.5
69/1500 - 70/0100	-7.8 ± 1.5	-17.7 ± 1.5

Information is not available to say how much of the observed cooling is due to entrainment (caused both by convection and by wind mixing) as discussed in section 4.2. One can however make an order of magnitude estimate. SeaSoar profiles near the spar suggest a deepening of the thermocline of about 10m/day. The SeaSoar did not sample more than the upper 100m of the thermocline, but the temperature jump might be estimated as 0.5°C. Over the 14 hour cooling period mentioned above (67/1600 - 68/0600), these figures would imply an entrainment cooling of about $12MJ/m^2$. A deepening of 5m/day with a jump of 0.5°C would give a cooling of $6MJ/m^2$, while a deepening of 15m/day with a jump of 1°C would give a cooling of $36MJ/m^2$. It is impossible to say which of these is the most realistic. However it is feasible that there is an anomalous source of cooling during the night just as there is such an anomalous source of heating during the day.

No significant heating is observed on day 68, but day 70 is more interesting:

Table 4.3 - Heat Budget for Day 70

Time Interval (day/ hour)	Heat Available (MJ/m^2)	Heat Required (MJ/m^2)
70/1200 - 70/1400	-0.4 ± 0.6	3.1 ± 1.5

The thermistors measure a rise in temperature even though the net surface flux implies a cooling. However a heat budget over only two hours is unlikely to be significant since there is considerable noise in the signal (probably internal waves) over such a short time scale. The heating observed is in any case very small.

4.5 Discussion

It can be seen therefore that the heat budget does not balance. In particular, an explanation is required for the anomalously large heating signal observed at the spar during days 67, 69 and 71. There are various possible solutions to this problem:

1) Instrumental Errors

The VACM temperature sensors are intended to measure to within a few millidegrees. It was thought that they might be incorrectly calibrated or defective. However, using the SeaSoar data as discussed in section 4.2, it is possible to show that each time the drifting spar is passed, a patch of water can be found, in which the temperature gradients and absolute values agree with those at the VACMs. The patch that matches is always upstream of the spar; for example, when the temperature structure in the water is banded east- west (figure 4.4), the matching patch lies west of the spar buoy.

Figures 4.1, 4.2 and 4.3 gave examples of the matching between SeaSoar and VACM temperature profiles. Figure 4.1 refers to the early evening of day 67; there is significant stratification (of order 10mK in 100m). SeaSoar profiles are shown dashed; later profiles have longer dashes. The SeaSoar data have been averaged using a vertical bin of 5m. Some examples of temperatures from the VACMs during the

same period are drawn in solid lines. Similarly, figures 4.2 and 4.3 refer to midday and evening on day 69 respectively. On each occasion it is found that the VACM temperatures and gradients are reasonable, in that differences between the VACM temperatures and the matching SeaSoar profile are less than the differences between adjacent SeaSoar profiles. In figure 4.2 the VACM temperatures agree with only one of the SeaSoar profiles. It is important to note that although each SeaSoar profile is drawn separately, the instrument is really surveying up and down continuously as the ship steams. Therefore during one 400m profile, the ship may have travelled between 1km and 2km horizontally, the path of the SeaSoar through the water having a gradient of between 1 in 3 and 1 in 5. Hence it is not surprising that the VACM temperatures are not in exact agreement with the entire SeaSoar 'profile'. Further discussion of this may be found in chapter 7. Differences are however sufficiently small for instrumental errors to be neglected. It should also be noted that the VAECMs, which are a different type of instrument, measure a similar diurnal temperature signal (figure 2.7). Both types of instrument were independently calibrated prior to the cruise.

2)Direct Heating Effect

The current meters are large aluminium cylinders, and may absorb solar heating directly (analogous to the overheating of a mercury thermometer placed in the sun). However this effect is likely to be insignificant for several reasons. First, any heating effect from the sun will soon be lost to the surrounding water, since all the current meters are in the turbulent mixed layer. An order of magnitude estimate using the equations for a hot wire anemometer (Hinze, 1959) gave a temperature rise of less than 1mK at 15m. Secondly, solar radiation entering at the sea surface is soon absorbed, as was shown in chapter 3. At 15m the direct heating might be significant but the signal below 100m

cannot be accounted for in this way. Thirdly, it was shown that a patch of water may be found near the drifting spar buoy in which the temperature profiles from VACMs and the SeaSoar agree (figures 4.1 to 4.3). These arguments may also be used to show that the flow of heat down the wires between instruments is negligible.

3) Errors in surface fluxes

Generous estimates of the uncertainties in the calculations of the surface heat fluxes were made in chapter 3; these have been used in the heat budgets of tables 4.1 to 4.3. There remains, however, the possibility that one of the meteorological instruments was completely miscalibrated. In view of the detailed intercomparison between various instruments described in chapter 3, this cannot be the case for air temperatures, wind speed or direction. The heat budget might balance if the solar radiation were increased by some 25% to 50% at least. For example, for the heating period on day 67 (table 4.1) an extra $200W/m^2$ is required. Yet the theoretical maximum solar radiation at midday for this time of year is (using equations 3.3 and 3.4) only $850W/m^2$ for a clear sky. The maximum solar flux observed instantaneously by the solarimeter during this period is more than $700W/m^2$ on day 67. Since the sky was not clear (table 3.1) the solarimeter cannot be underestimating fluxes by the amount required, since the theoretical maximum would be exceeded. In any case, the cloud cover predicted using a solar radiation model and the observed solar flux (chapter 3) was in fair agreement with the observed cloud cover. It is believed that the 10% uncertainty in solar flux is a reasonable one; errors in meteorological forcing cannot balance the heat budget.

4) Convergence Zone

The only explanation that seems feasible is that the spar lies in a convergence zone. It is postulated that warmer water is drawn in horizontally at the surface, above the uppermost current meter at 15m,

and carried downwards by vertical advection. This would provide an extra heat source which would be in phase with the solar heating. It might also explain how the heating signal reaches the lower depths so quickly. It would seem plausible that the spar might preferentially drift into a convergence zone since it is freely moving with the currents in the upper 10m. Since the heat budgets on days 67, 69 and 71 all showed an anomalous source of heating, the spar buoy would need to be in a convergence zone for several days, unless it drifted from one to another.

No measurements were made of vertical velocity at the spar buoy and current meters. In order to obtain an order of magnitude estimate, it is assumed that the vertical velocity is constant between 15m and 145m. From the filtered temperature time series at the VACMs (figure 2.8) it is found that the time difference between the maximum of the diurnal heating signal reaching 15m and 145m varies between one and three hours. This therefore yields an estimate of mean vertical velocity of between 0.04m/s and 0.01m/s. Similarly one may compare the times at which the heating signal commences at the beginning of each day. The difference between 15m and 145m varies between one and five hours giving vertical velocity estimates of between 0.04m/s and 0.007m/s. It should be remembered that small advective effects may influence these estimates of times at which signals reach a certain depth. It must also be stressed that the vertical velocity in the mixed layer is unlikely to be uniform with depth, as has been assumed here.

An alternative estimate of vertical velocity, w, can be made by attempting to balance the heat budget. The term in the heat budget due to the vertical advection of heat in time dt is:

$$\rho 0 \; Cp \iint w \frac{\partial T}{\partial z} \, dt \, dz \qquad (J/m^2)$$

Integrating in the vertical between two current meters, one may obtain $\rho 0 \; Cp \; w \; \Delta T \; dt$. Here ΔT is the difference in temperature in between the two current meters, assumed to be constant during time interval dt. Vertical velocity w is also assumed constant between current meters and in time. For the three cases cited in table 4.1, the temperature differences, ΔT, between current meters at 15m and 145m were taken to be 30mK, 20mK and 20mK respectively. Assuming that the deficit in the heat budget is provided by the vertical advection term above, estimates of w may be obtained. The three heating periods (days 67,69 and 71) yield vertical velocity values of 0.003m/s, 0.001m/s and 0.002m/s respectively. Remember that the uncertainties in the heat budget deficit are large (table 4.1), and also that the temperature difference ΔT will not be constant in reality. In view of the approximations in the method, these are order of magnitude estimates only.

It will be noticed that these vertical velocities are an order of magnitude smaller than those evaluated from the time lag of the heating signal. It is expected that the estimates from the heat budget deficit will give a lower bound to the vertical velocities, because it was seen in section 4.4 that the heat budget deficit will be larger than stated, due to stratification and to neglect of the diurnal signal below 145m. Additional cooling due to the very small advective diurnal signal and to any entrainment of cooler water have also been neglected here. Taking the results of both methods together, a mean vertical velocity of the order of 1cm/s seems likely. In chapter 8, a model will be used to analyse both phase and amplitude of the diurnal signal as a function of vertical velocity; more precise estimates of the vertical velocity will be calculated there.

Before leaving this analysis of the heating signal, it is interesting to look at the cooling of the water column. Figure 2.7 shows that the cooling begins at the lowest current meter some hours after it commences at the meter nearest to the surface. However the water column has not yet mixed; there is still stratification in the upper 150m. It is usually expected that cooling of the upper ocean occurs only through convection or by wind mixing, both of which cause a uniform mixed layer. In a mixed layer model (such as those to be discussed in chapter 5) the only way cooling could occur at any current meter is if the mixing had created a uniform layer to that depth. Cooling throughout the mixing layer simultaneously, while maintaining stratification, is not possible in a mixed layer model. Of course, the stratification is very small (typically 30mK between 15m and 145m) compared to the gradient in the thermocline (typically 500mK in 100m). In chapter 2 it was seen that there is also some shear (of order $10^{-3}s^{-1}$) across the 'mixed layer'. The approximation of the mixed layer as a slab is therefore not strictly valid.

The following chapter reviews one- dimensional upper ocean models and tests two mixed layer models. In view of the problems revealed in this chapter, it is not to be expected that such models will be able to simulate well the time series of temperature observed at the VACMs. Chapter 6 returns to this issue with a review of the literature concerning convergence zones and downwelling in the ocean.

Chapter 5

One- dimensional Upper Ocean Models

5.1 Introduction

One- dimensional models of the upper ocean can be valuable because quantities such as temperature usually vary more in a hundred metres vertically than a thousand metres horizontally. Tabata (1965) showed that at Ocean Station Papa local air- sea interaction affects the heating of the upper ocean much more than horizontal advection of warmer or cooler water, and therefore mixed layer models are often tuned to fit the data available for the station. In this experiment, the instrumentation drifts freely with the near- surface current, so a Lagrangian reference frame is expected. Indeed, in chapter 4 it was found that horizontal advection at the VACMs was negligible, particularly at the instruments in the upper 100m. Under such circumstances, a one- dimensional model is usually applicable. In this chapter, these models are considered, and the characteristics of two mixed layer models are discussed. This provides the groundwork for chapter 8 in which a model including convergence and downwelling is introduced. First, the development of upper ocean models shall be reviewed.

The first upper ocean model was that of Munk and Anderson (1948). They assumed eddy diffusion coefficients of viscosity and conductivity which varied with depth according to the vertical temperature and velocity gradients. Steady state solutions for the depth and shape of the thermocline were obtained. The sharp temperature gradient at the base of the mixed layer was explained by letting the turbulent mixing depend on the Richardson number. They suggested that convective stirring could be as important as wind mixing. Their predicted layer depths were however less than half the observed depths.

Kraus and Turner (1967) (henceforth abbreviated KT) adopt a different approach. They assume that there exists a uniform mixed layer, thus eliminating the need for eddy diffusion coefficients. Heat entering at the surface or cooler water entrained at the base are mixed immediately throughout the layer. They propose that, in order to predict the rate of entrainment at the base of the mixed layer, the turbulent kinetic energy budget be considered. Thus the energy available to entrain deeper, cooler water into the mixed layer, P, is the sum of the turbulent kinetic energy input by the wind and waves, W, and the turbulent kinetic energy generated or dissipated by buoyancy forces, B0. The model assumes that W is proportional to the cube of the oceanic friction velocity, U^*, so the energy budget becomes:

$$P = \rho\, m\, (U^*)^3 + B0 \qquad (5.1)$$

where m is a constant.

The laboratory experiments of Kato and Phillips (1969) found the value of m to be 1.25, with an uncertainty of about 30% (Denman, 1973). They used an annular tank filled with stratified fluid initially at rest to model oceanic entrainment. A surface stress was applied, and the rate of entrainment was measured as the upper layer mixed and deepened. Kantha et al. (1977) performed the same experiment but with two homogeneous layers of different density. Entrainment rates were found to be 'approximately twice as large' as Kato and Philips'. They explained this as being due to internal waves in the stratified region below the mixed layer radiating energy away in Kato and Phillips' case. Thompson (1978) claims that both Kato and Phillips' and Kantha et al.'s results can be explained by including the effect of side- wall friction. Thompson uses a model which assumes a constant critical Froude number (reciprocal of bulk Richardson number, see equation 5.3) to predict when friction is dominant. In Kato and Phillips' experiment, as much as half of the applied stress is used to overcome

friction, therefore there is about half the entrainment of Kantha et al.'s experiment.

Denman and Miyake (1973) fit a model similar to the KT model (Denman, 1973) to upper ocean data at Ocean Station Papa. Although they define a slightly different proportionality constant, their value of m as defined by Kato and Phillips is 1.0. This is in fair agreement with Kato and Phillips' value of 1.25, considering the experimental and other model errors. Turner (1969) however finds that a value for m of about 8.0 is required to explain the rapid mixed layer deepening observed by Stommel et al. (1969). Pollard et al. (1973) maintain that the large deepening observed by Stommel et al. may well have been partially caused by surface cooling adding to the wind mixing effect. There is still no agreement on a suitable value of m for use in models, but Kantha (1977) suggests that further study of internal waves may help to explain the discrepancies.

Gill and Turner (1976) point out that the KT model overestimates the amount of mixing and entrainment since all of the potential energy released by convection following surface cooling is used for entrainment. Kraus and Turner thus have 100% penetrative convection, which they define as 'the overshooting of sinking water parcels below the compensation level'. The term simply refers to the amount of energy released by convection (hereafter referred to as convective energy) that is available for entrainment. Gill and Turner suggest that equation 5.1 should be replaced by:

$$P = \rho\, m\, (U^*)^3 + \delta\, B0 \qquad (5.2)$$

δ is an adjustable parameter representing the amount of penetrative convection. Gill and Turner test δ=0.0 and δ=0.15, and find that either is acceptable in a comparison with data. The value of 0.15 was suggested by the laboratory experiments of Deardorff et al. (1969, 1974). Farmer (1975) measured the deepening of the mixed layer under

ice, thus eliminating wind mixing effects. He found that the fraction of convective energy used for deepening was 36%, giving δ=0.36.

It is generally agreed that the turbulent kinetic energy in the model should decay downwards with depth. One of the suitable treatments of this dissipation is the exponential decay suggested by Elsberry et al. (1976). They propose that P, the available mixing energy, is multiplied by exp(-z/Z0), where Z0 is a constant scale depth. Elsberry et al. choose Z0 to be 100m, a typical value of U*/f. Gill and Trefethen (1977) introduce a model with δ=0.15 and tune the exponential decay to obtain Z0=40m. Studies of the atmospheric boundary layer during JASIN (Nicholls, 1985) suggest that Z0 should be approximately 0.2 U*/f. (Using a typical wind stress of 0.3N/m^2, Z0 would be about 30-40m.) Using this exponential decay dissipation, Thompson (1977b) applies a value of 1.25 for m. More recent versions of this type of model (e.g. Davis et al., 1981; Garwood, 1977) include dissipation as an explicit term in the energy equation. Their 'best fit' values for m (Davis et al. have m=0.39) are not necessarily applicable to models in which the dissipation is implicit.

Another type of mixed layer model calculates deepening by considering the shear across the base of the mixed layer, rather than the turbulent kinetic energy budget (discussed by Garwood, 1979). Pollard, Rhines and Thompson (1973) (to be abbreviated PRT) assume that both the mixed layer velocity, $\underline{v}$, and temperatures are uniform with depth, and that the Coriolis force will act on these velocities to produce an inertial oscillation (Pollard and Millard, 1970). The system is then closed by a stability criterion based on the bulk Richardson number:

$$Rb = \frac{g\, d\rho\, h}{\rho 0\, \underline{v}^2} \qquad (5.3)$$

Here $d\rho$ is the density jump across the mixed layer base while h is the mixed layer depth. $\rho 0$ is a typical sea water density. The current velocity is assumed to be zero below the mixed layer. PRT maintain that when the Richardson number is less than one, shear instabilities at the base of the mixed layer provide the necessary turbulence for entrainment. They find that the mean kinetic energy of the model is three times as large as the potential energy, and suggest that their shear- generated turbulence should be included in models such as the KT model.

Thompson (1976, 1977a) has produced a numerical scheme for the PRT model using a critical Richardson number of one, which he compares with a numerical KT model. The models are run to simulate the annual cycle of heating and cooling. Following comments by Garwood and Camp (1977), Thompson (1977b) adapts the KT model by altering δ as suggested by Gill and Turner (1976) and by adding the exponential energy decay of Elsberry et al. (1976) described earlier. He nevertheless prefers the PRT type model which he feels predicts mixed layer depths and temperatures more accurately. He also points out that PRT only has one adjustable parameter (the critical Richardson number) whereas the modified KT model requires an input of m, δ and Z0. While the critical bulk Richardson number may be determined by laboratory experiment, the other three parameters are less well known and usually require 'fitting' to a particular data set.

The laboratory experiment of Ellison and Turner (1959) suggests that the critical bulk Richardson number lies between 0.4 and 0.8, rather than 1.0 as PRT used. Price et al. (1978) perform a model comparison similar to Thompson's (1976). They find that the critical value is about 0.65, and point out that the laboratory experiments of Kato and Phillips (1969) and Kantha et al. (1977) also support such a value. A recent paper by Price et al. (1986) proposes a modification

to the PRT- type model of Price et al. (1978). They add a 'smearing out' process to produce smooth profiles of temperature and velocity, eliminating the sharp discontinuity at the mixed layer base. The method depends upon a local gradient Richardson number stability criterion. It will be described further in section 5.3.2.

Now that the physical processes involved in the models have been introduced, the generalised equations may be understood. Niiler and Kraus (1977) discuss in detail the equations governing upper ocean models; a brief summary will be given here. Since only a one-dimensional treatment is required, the momentum equation becomes

$$\frac{\partial \underline{v}}{\partial t} - f\,\underline{k} \times \underline{v} + \frac{\partial \overline{w''\underline{v}''}}{\partial z} = 0 \qquad (5.4)$$

$\underline{v}$ is the average horizontal current velocity; $\underline{k}$ is a unit vector in the z direction (z has been taken as positive and increasing with depth in the ocean). The double prime (") denotes turbulent deviations from the bulk velocities w and $\underline{v}$, w being the vertical velocity. The averaged product $\overline{w''\underline{v}''}$ is named the Reynolds stress, and is the vertical flux of horizontal momentum, due to turbulent motions.

Temperature changes are governed by the conservation of heat:

$$\frac{\partial T}{\partial t} + \frac{\partial \overline{w''T''}}{\partial z} = \frac{-1}{\rho 0\ Cp}\frac{\partial I}{\partial z} \qquad (5.5)$$

I is the available solar radiation at depth z. Cp is the specific heat of sea water. For simplicity, salinity changes have been ignored here.

As described earlier, the KT model depends upon evaluation of the turbulent energy budget in the mixed layer. The turbulent kinetic energy equation is (Kraus, 1972)

$$\frac{1}{2}\frac{\partial \kappa^2}{\partial t} = \underbrace{-\overline{w''\underline{v}''}\,\frac{\partial \underline{v}}{\partial z}}_{A} + \underbrace{g\,\alpha\,\overline{w''T''}}_{B} - \underbrace{\frac{\partial}{\partial z}\left(\frac{\overline{w''(w''^2 + \underline{v}''^2)}}{2} + \frac{\overline{w''p''}}{\rho 0}\right)}_{C,D} - \gamma \qquad (5.6)$$

κ is the mean turbulent kinetic energy defined by

$$\kappa^2 = \overline{w''^2} + \overline{\underline{v}''.\underline{v}''} \qquad (5.7)$$

Term A represents the work done by the stress $\overline{w''\underline{v}''}$ on the mean shear flow. When the mean shear is reduced by mixing, energy is transferred from the kinetic energy of the shear flow to eddy kinetic energy. It is sometimes referred to as the production term.

Term B describes the effect of the buoyancy force. Energy is released if cooler (and hence denser) water moves downwards while warmer water rises.

Term C represents the flux of the turbulent velocity and pressure fluctuations.

Term D is the rate of viscous dissipation of turbulent energy.

There are three methods commonly in use to solve this system of equations. The diffusion models (e.g. Munk and Anderson, 1948) assume that the turbulent fluxes are proportional to the local gradient of the transported quantity:

$$\left.\begin{aligned} \overline{-w''\underline{v}''} &= \zeta\,\frac{\partial \underline{v}}{\partial z} \\ \overline{-w''T''} &= \eta\,\frac{\partial T}{\partial z} \end{aligned}\right\} \qquad (5.8)$$

ζ and η are the eddy diffusion coefficients of momentum and heat respectively. The problem with such models is that they require a knowledge of the current shear and local stability from which the eddy diffusion coefficients must be derived empirically. Henderson- Sellers et al. (1983) discuss two turbulent diffusion models which are particularly successful in the study of stratification in lakes.

Mixed layer models (or 'bulk' models) assume the existence of a well- mixed layer, in which variations of temperature, salinity and horizontal velocity are small compared to the changes across the thermocline. The KT model and the PRT model described earlier are examples of this approach. Equations 5.4 and 5.5 may be integrated vertically from the surface to the mixed layer depth h, since $\underline{v}$ and T are assumed uniform through the mixed layer. Turbulent energy provides the potential energy to entrain denser water at the mixed layer base. The entrainment velocity, we, (the rate of deepening of the mixed layer) is calculated by integrating the turbulent energy equation (equation 5.6).

At z=0, the turbulent flux $\overline{w"T"}$ is simply the total surface heat flux Q (as calculated in chapter 3) divided by both the density and the specific heat of sea water. At the base of the mixed layer, $\overline{w"T"}$ is assumed equal to the entrainment velocity, we, multiplied by the temperature jump, ΔT, across the base. Following the terminology of chapter 3, the available irradiance I is assumed equal to SOLAR exp(-jz). Upon integrating vertically between h and the surface, the second term (B) in the turbulent kinetic energy equation becomes

$$\frac{-g\,\alpha\,h\,Q}{2\,\rho 0\,Cp} - \frac{g\alpha\,we\,h\,\Delta T}{2} + \frac{g\,\alpha\,SOLAR}{\rho 0\,Cp}\left(\frac{h}{2} + \frac{1}{j}\right)$$

It has been assumed that the solar flux at the base of the mixed layer is negligibly small, compared to that at the surface. The first term is the change in potential energy of the column due to surface heating; if Q is negative, the surface cools and potential energy is gained by the layer. The second term denotes the potential energy lost when the denser water is entrained and rises. If c is the velocity of the long internal waves on the thermocline, one may write

$$g\,\alpha\,h\,\Delta T = c^2 \qquad (5.9)$$

To find an expression for term C after integration, one must evaluate the term in ~~square~~ large brackets in equation 5.6 at the top and bottom boundaries. At the sea surface, the energy is provided by the wind, together with the surface value of term A. The way in which the wind imparts momentum to the water in the presence of waves of differing heights and lengths is not fully understood. The total flux from the wind is usually parameterised as $m1\ (U^*)^3$. m1, which differs from m above, is a specified constant, the value of which will be discussed later. At the bottom boundary, one may obtain (Niiler and Kraus, 1977):

$$\left(\frac{\overline{w''(w''^2 + \underline{v}''^2)}}{2} + \frac{\overline{w''p''}}{\rho 0} \right) = \frac{-we\ \kappa^2}{2} \qquad (5.10)$$

For the momentum flux (term A) the boundary condition at the mixed layer base is parameterised as

$$\overline{w''\underline{v}''} = \mu\ \underline{v}|\underline{v}| - we\ \underline{v} \qquad (5.11)$$

This is derived from consideration of the downward radiation of momentum by internal waves (Pollard and Millard, 1970). The radiation stress is assumed proportional to $|\underline{v}|^2$; μ is a generalised drag coefficient. Thus the contribution to term A from the momentum flux across the mixed layer base is

$$-\frac{we\ \underline{v}^2}{2} + \frac{\mu\ \underline{v}^3}{3}$$

Hence including all these expressions and assuming that κ^2 remains constant in time, the turbulent kinetic energy equation becomes

$$\frac{we(\kappa^2 + c^2 + \underline{v}^2)}{2} = m1(U^*)^3 - \frac{g\ \alpha h\ Q}{2\ \rho 0\ Cp} + \frac{SOLAR\ \alpha g}{\rho 0\ Cp}\left(\frac{h}{2} + \frac{1}{j}\right) + \frac{\mu \underline{v}^3}{3} - \int_0^h \gamma dz \qquad (5.12)$$

Niiler and Kraus (1977) discuss the relative magnitudes of these terms and also the parameterisation of the dissipation γ. κ^2 is usually much smaller than c^2 and is neglected. The most arbitrary part of the mixed layer model is the formulation of the dissipation. It is assumed

proportional to the work done by the wind ($m1(U^*)^3$), to the rate at which energy of the mean velocity field is reduced by mixing across the mixed layer base ($we\ \underline{v}^2$) and to Q if Q is negative. It is assumed also that $we >> \mu\ \underline{v}$ so that the $\mu|\underline{v}|^3$ term is neglected. Hence the turbulent energy equation may be written

$$\frac{we}{2}(c^2 - s\ \underline{v}^2) = m\ (U^*)^3 + \frac{\delta\ h\ g\ \alpha\ Q}{2\ \rho 0\ Cp} + \frac{SOLAR\ g\ \alpha}{\rho 0\ Cp}\left(\frac{h}{2} + \frac{1}{j}\right) \qquad (5.13)$$

The parameter δ was discussed earlier in connection with the KT model; it is 1.0 if Q is positive and usually 0.15 if Q is negative (Gill and Turner, 1976). The constant m has now replaced the parameter m1 introduced previously; it was m that the Kato and Phillips experiment determined. It should be noted that m includes the effect of some dissipation. The KT model uses a simplified version of this equation, setting the left- hand- side equal to zero. The PRT model is associated with the parameter s, since it describes the deepening effect of the shear stresses at the bottom of the mixed layer. They set the bulk Richardson number equal to the critical local Richardson number:

$$Rb = \left(\frac{c}{\underline{v}}\right)^2 \qquad (5.14)$$

Thus the left- hand- side of equation 5.13 becomes $0.5\ we\ (Rb - s)\ \underline{v}^2$. However the PRT model does not take into account the effects of the turbulent kinetic energy budget, only the mechanical energy budget. Price et al. (1976) find that a value for s of 0.7 is most suitable, as discussed earlier. The reader is referred to Niiler and Kraus (1977) for further discussion.

The third upper ocean model in common use is the turbulent closure model. In these models, the Reynolds stresses ($\overline{w''\underline{v}''}$, $\overline{w''T''}$ etc.) are written in terms of higher order moments of the fluctuating quantities ($\overline{w''\underline{v}''^2}$, $\overline{\underline{v}''w''^2}$ etc.) The system is closed by assuming the third order

moments to be a function of the second order moments, the bulk quantities and some empirical constants. Mellor and Yamada (1974) describe a hierarchy of such models, and show that the simplest version is the classical eddy diffusion model (e.g. Munk and Anderson, 1948). Turbulence closure models involve more arbitrary parameterisations than the mixed layer models and are more complex to use and understand. It was felt that a mixed layer model was more suitable in this attempt to study upper ocean physical processes.

The upper ocean model of Garwood (1977) combines aspects of both the mixed layer models and the turbulence closure models. Basically, it is a mixed layer model, but the buoyancy flux at the base of the mixed layer is parameterised by

$$\alpha g \, \overline{(w''T'')} = -\frac{\overline{\langle w''w'' \rangle} \; \langle \kappa \rangle}{h} \qquad (5.15)$$

$\overline{\langle w''w'' \rangle}$ and $\langle \kappa \rangle$ are the turbulent vertical velocity and turbulent kinetic energy respectively, both taken as averages over the mixed layer. The Garwood model then closes the system by expressing both of these in terms of bulk and surface quantities including U^* and the bulk Richardson number, Rb. Use of the bulk Richardson number enables the model to simulate a rapid deepening event when strong shears exist across the base of the mixed layer. For details of the equations the reader is referred to Garwood's (1977) paper.

The Garwood model was developed primarily for coupling with an ocean circulation model (e.g. Adamec et al., 1981). Garwood and Yun (1979) show that it is suitable for time scales of more than a few hours. The model has been calibrated at several weathership stations (Garwood and Adamec, 1982) in order to find the best values for the arbitrary parameters. It was felt that this model was not suitable for study in this project, since a simpler model might be better at revealing which physical processes are important. Also, it is believed

that the effect of the convergence and downwelling suggested in chapter 4 will be greater than the differences between the various upper ocean models.

Two different types of mixed layer model have been implemented here: the Kraus- Turner model (KT) (Kraus and Turner, 1967) and the Pollard- Rhines- Thompson (PRT) model (Pollard et al., 1973). Both models have been set up so that salinity and temperature may be specified on a vertical grid, as in Thompson (1976). However in practice, salinity has been taken as uniform throughout the model. In most cases, density is taken as $\rho 0=1027.1 kg/m^3$ except where density differences are required. This is known as the Boussinesq approximation. This value is chosen as representative of the temperature and salinity observed (see chapter 3 figure 3.5). As figure 3.5 shows, the variation of density over the observed temperature range is so small that errors involved in taking $1027.1 kg/m^3$ as the density are less than 0.01%. However, in taking density differences, (e.g. in calculating the Richardson number) it is obviously necessary to use the density calculated from the temperature (and salinity).

5.2 Kraus- Turner model

5.2.1 Model procedure

In running the KT model I have followed the implementation of Thompson's (1976) DKT model in which it is easy to understand the effect that each physical process is exerting. The model is initialised with a profile of imposed temperature (T) and salinity (S). In the following procedure, the time step is denoted dt and the vertical grid spacing dz. Primed quantities indicate new values.

1) Augment time $t' = t + dt$

2) Absorb heat loss or gain due to surface meteorological fluxes. If I(i) is the available solar irradiance at level i, then for all depths

i greater than 2:

$$T(i)' = T(i) + \frac{(I(i-1) - I(i))\ dt}{Cp\ dz\ \rho 0}$$

For the top layer:

$$T(1)' = T(1) + \frac{(SOLAR - H - I(1))\ dt}{Cp\ dz\ \rho 0} \qquad (5.16)$$

Cp is the specific heat capacity of sea water (3.99×10^3 J/kg/K); SOLAR and H are as defined in chapter 3.

3) Calculate the portion W (J/m^2) of the wind's energy that is available for mixing:

$$W = m\ Ewind\ dt \qquad (5.17)$$

The fraction m is taken to be 1.25. Ewind is the work done by the wind stress ($J/m^2/s$) calculated as $\rho 0\ (U^*)^3$ (see chapter 3).

4) For each level from the top downwards, calculate the potential energy needed to mix in the next level down to form a uniformly mixed layer. The mixed layer depth is taken as n dz.

$$dP = 0.5\ \rho 0\ g\ \alpha\ n\ (dz)^2\ (T(n) - T(n-1)) \qquad (5.18)$$

If this energy dP is less than the wind-given energy W, the levels are mixed and the energy used is subtracted from that available.

$$W' = W - dP$$

Thus there is less energy W' available to mix successively deeper layers. However, if potential energy is released by the mixing, $dP < 0$, (which will be the case if colder water is above warmer water), then when the mixing occurs, the released 'convective' energy is added to the energy available for mixing further down.

5) Having mixed n levels, there may be some energy remaining, which is not enough to mix in the next layer, n+1, (i.e. $W < dP$). This is then used to partially mix layer n+1, according to the formulae:-

$$r = \frac{n\,W}{(n+1)\,dP}$$

$$T'(i) = \frac{[r\,T(n+1) + (n-r)\,T(n)]}{n} \qquad \text{for } i=1 \text{ to } n$$

$$T'(n+1) = r\,T(n) + (1-r)\,T(n+1) \qquad (5.19)$$

Salinity is mixed in the same way.

6) T and S profiles are output. This model does not predict velocities nor take into account the shear produced by the wind. The wind creates a mixed layer by providing the energy for the turbulence.

5.2.2 Testing and modifications

A series of test runs have been implemented using a sinusoidal heating and cooling signal. Heating occurs from 0600 to 1800 and has a peak of 500W/m^2 at midday. The cooling signal follows the same sinusoidal function at night, so that the net heat gain of the model over 24 hours is zero. The wind forcing, Ewind, is kept constant at 5.127W/m^2, corresponding to a stress of 0.3N/m^2. Runs are carried out for 24 hours. The model extends to a depth of 300m, and initially the temperature profile is uniformly stably stratified with a gradient of 0.01°C per 100m.

The solid lines in figure 5.1 show temperature profiles output from the KT model at two hour intervals, starting with the initial profile at 0600. m has been taken as 1.25. The time step is 0.5 hours and the grid spacing 1m. As the mixed layer shallows (profiles 2 to 4) a step appears at the mixed layer base at each time step. This is the residual of the thermocline 'left behind' as the mixed layer shallows at each time step. After the 5th profile, the mixed layer begins to deepen again as the surface heating produces insufficient stratification to prevent the wind mixing and entrainment. When surface cooling begins at 1800, rapid mixed layer deepening and cooling occur as a result of both convection and wind mixing causing

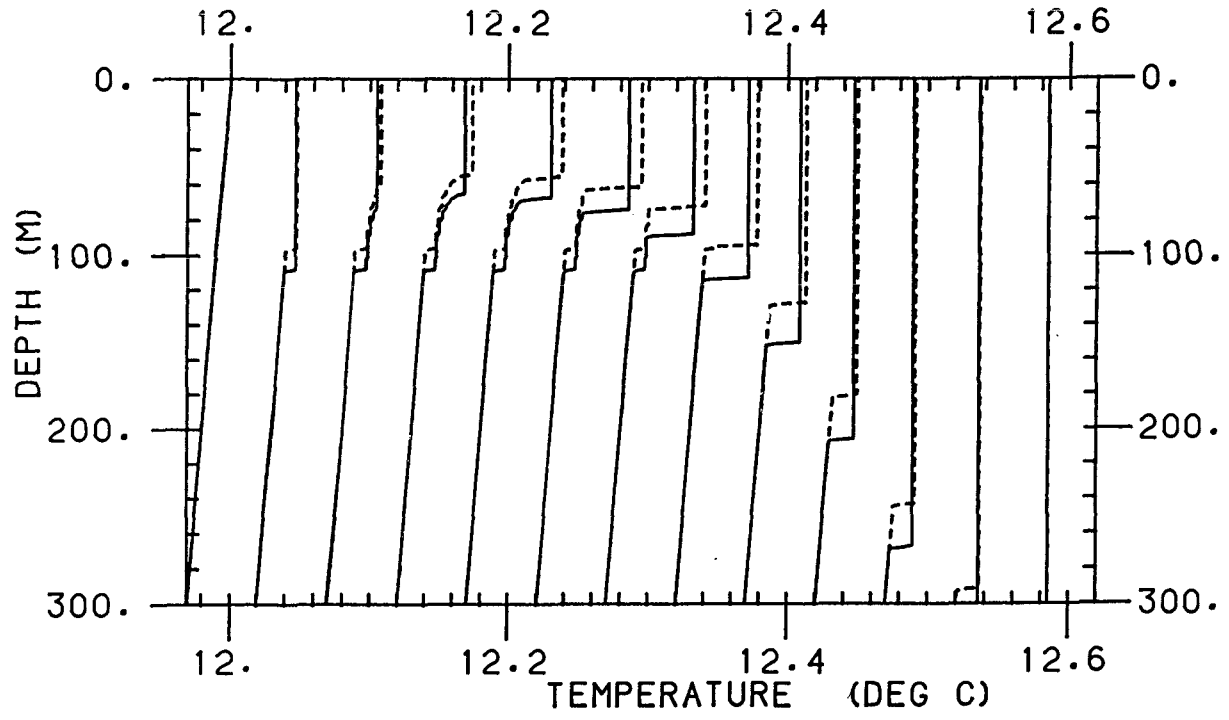

Figure 5.1 : Kraus- Turner model results using m=1.25 (solid lines) and m=1.0 (dotted lines). Time step is 0.5 hours, grid spacing 1m. Temperature profiles are plotted every 2 hours and are offset by 0.05°C. Wind forcing is constant while heating and cooling are sinusoidal (see text).

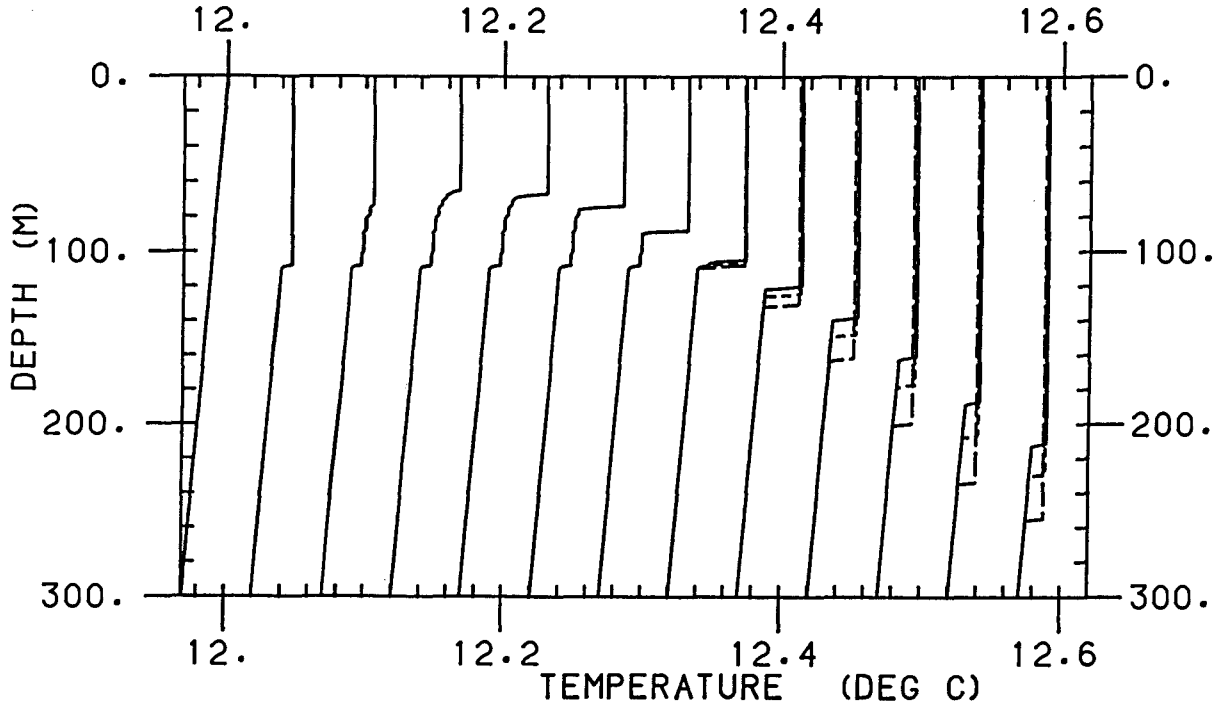

Figure 5.2 : Kraus- Turner model results with 0% (solid lines), 15% (dotted lines) and 36% (dashed lines) penetrative convection.

entrainment.

As discussed earlier, there is some debate concerning the value of m to be used. The dotted lines in figure 5.1 illustrate results from the KT model using m=1.0. There is significantly less deepening of the mixed layer with the smaller value of m. Mixed layer temperature differences are up to 0.01°C while temperature differences in the region of the mixed layer base may be as large as 0.04°C.

Gill and Turner (1976) suggest that only a small proportion δ of the potential energy released by convection is used for further mixing and deepening. Thus at stage 4 of the procedure, dP is multiplied by δ if dP is negative, before subtracting it from W. Figure 5.2 portrays results from the KT model modified in this way for values of δ of 0.0 (solid lines), 0.15 (dotted lines) and 0.36 (dashed lines) (c.f. figure 5.1 with $\delta = 1.0$). Obviously no difference is observed during the heating part of the day, but as cooling commences the smaller amounts of penetrative convection can entrain less water from below the mixed layer, which is thus shallower and less cool. Differences between each run are relatively small (the temperatures in the mixed layer change by less than 0.005°C).

Elsberry et al. (1976) propose that the turbulent energy should decrease exponentially with depth. Therefore I have modified the KT model by multiplying dP by exp(-dz/Z0) at each level as one progresses downwards in the model (as suggested by Thompson, 1977b). Figure 5.3 illustrates model results with 15% penetrative convection with the exponential decay using Z0=40m (solid lines) and Z0=100m (dotted lines). This variation obviously has a large effect on the results; for instance at about 50m the difference in temperature may be as large as 50mK.

The model was tested using time steps of both 15 minutes and one hour. It was found that altering the time step makes no significant

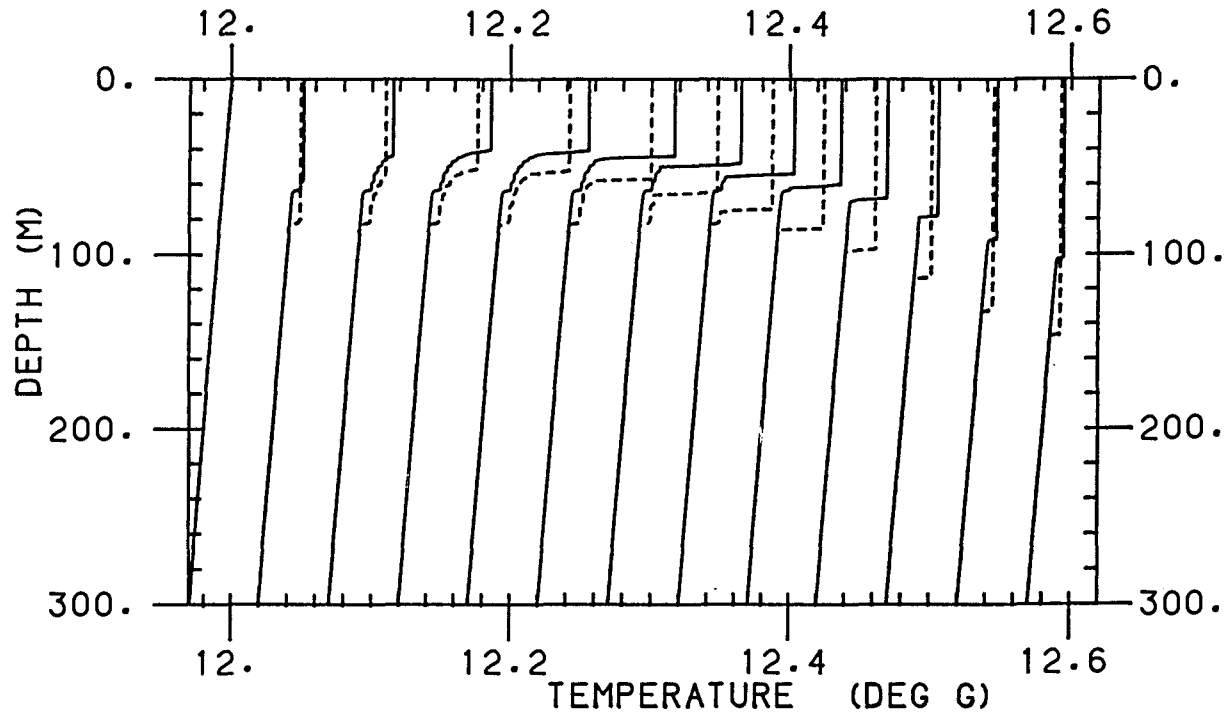

Figure 5.3 : Kraus- Turner model results with 15% penetrative convection and an exponential decay of energy with Z0=40m (solid lines) and Z0=100m (dotted lines).

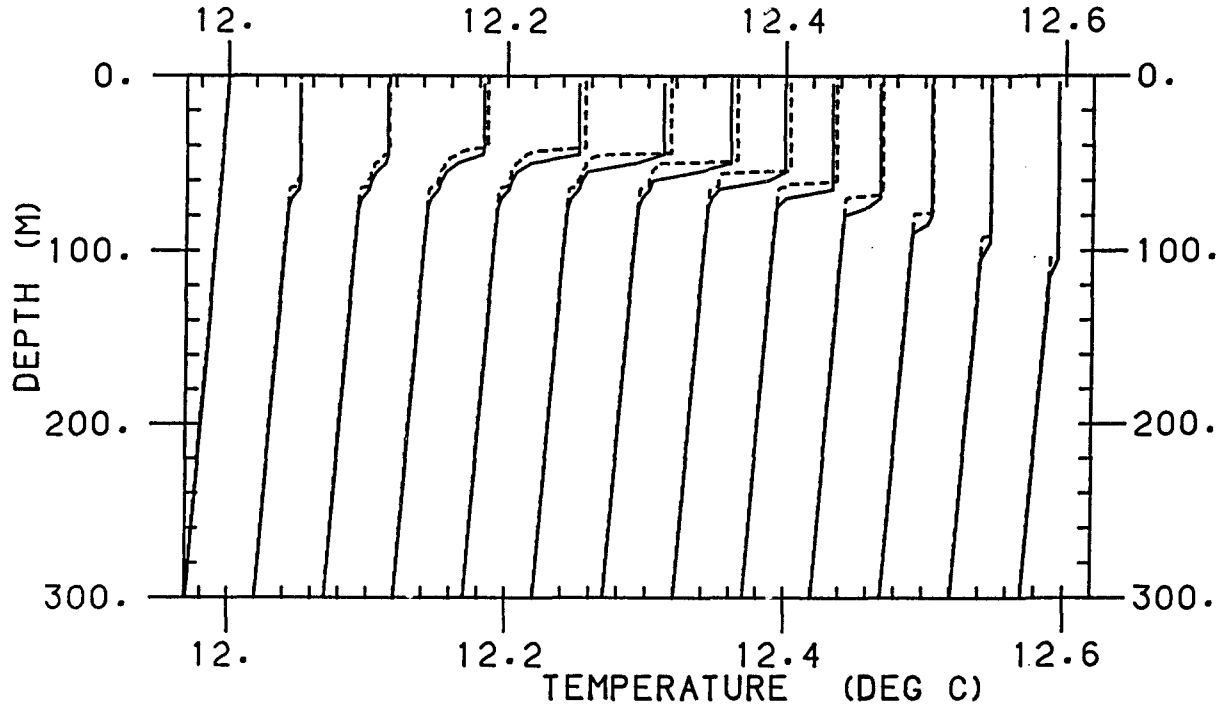

Figure 5.4 : Kraus- Turner model results with a grid spacing of 5m (solid lines) and 1m (dotted lines).

difference - the mixed layer depths are no more than 1m different while mixed layer temperature differences are less than 1mK. Figure 5.4 (solid lines) shows the results but with a grid spacing of 5m. Penetrative convection is 15%, m=1.25 and Z0=40m. The results using a grid spacing of 1m are shown here in dotted lines for comparison. Temperature differences at grid points are again of the order of 1mK, while there is some smoothing at the base of the mixed layer. The use of such a grid would of course depend upon whether the mixed layer depth was required to an accuracy of more than 5m.

It has been pointed out (Killworth, personal communication) that Thompson's method of programming the KT model loses some energy at each time step, since he does not store the value of r in stage 5. It can easily be shown that the potential energy lost by not remembering the exact mixed layer depth is

$$dP = \frac{\rho 0 \; g \, \alpha \, (dz)^2 \; n \; W \; (T(n+1) - T(n))}{2 \; dP} \qquad (5.20)$$

To conserve potential energy, I have simply added this amount of potential energy to W at the start of the next time step (stage 3). Figure 5.5 shows the KT model results with (solid lines) and without (dotted lines) this conservation of energy routine. The basic KT model has been used here, as in figure 5.1. Conservation of energy gives more entrainment during the cooling phase. The mixed layer is at most about 5m deeper, but the accompanying extra cooling is negligible (less than 1mK). Given the number of other uncertainties in the KT model, such as the values of m and δ, this effect is negligible over a short integration of a few days. Nevertheless it was implemented in subsequent runs. The effect is of course reduced with a larger time step since a similar amount of energy is lost at each time step. Indeed, it was found that with a one hour time step, the extra deepening provided was only about 2m.

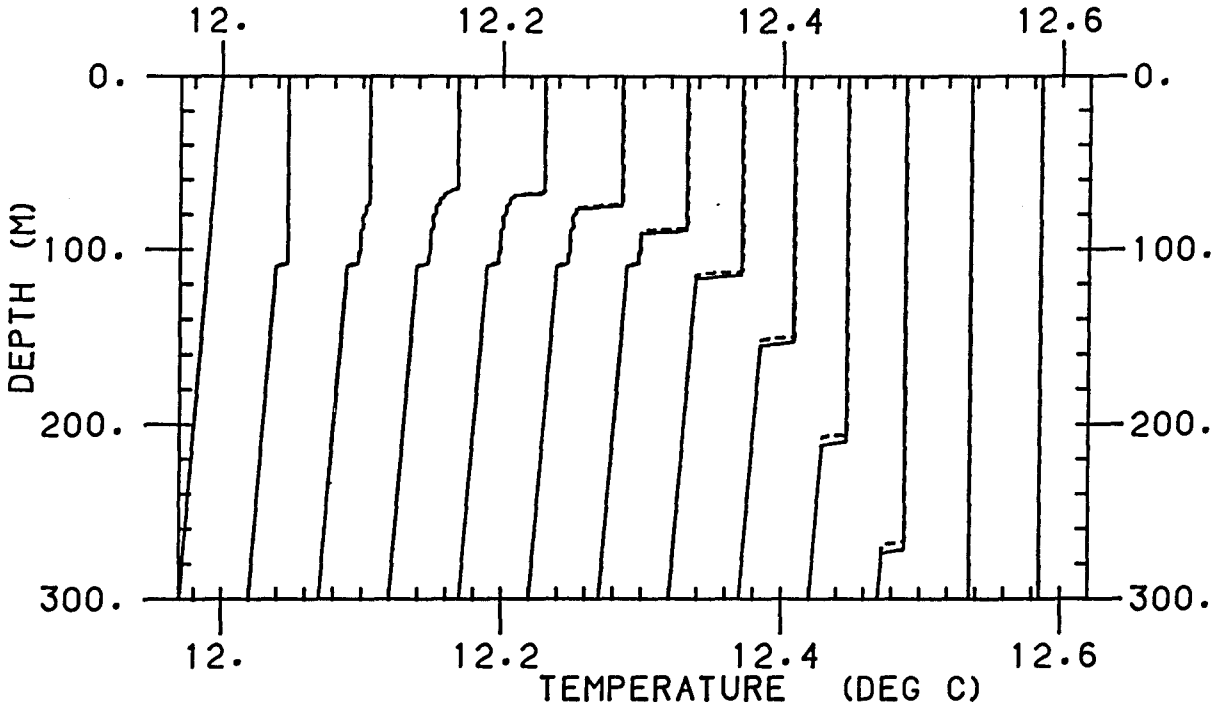

Figure 5.5 : Kraus- Turner model results adding back the potential energy lost by Thompson's (1976) partial mixing formulae (solid lines). The basic KT model is shown dotted for comparison.

It is not the intention here to discuss the various merits of each different parameterisation scheme, since this may be found elsewhere (Niiler and Kraus, 1977). Model runs using the observed meteorological forcing will be described in section 5.4. In this section a fairly standard, simple numerical model of the upper ocean has been described. This will be developed later (chapter 8) in an attempt to model Langmuir circulations.

5.3 Pollard- Rhines- Thompson model

5.3.1 Model procedure

A PRT- type model was also implemented, again following the procedures described by Thompson (1976). The model is initialised by imposed temperature (T), salinity (S) and velocity (U, V) profiles. The density is calculated from T at all depths using the equation of state discussed in chapter 3. At each time step, the following procedure is carried out:-

1) Augment time t' = t + dt

2) Absorb heat loss or gain due to surface meteorological fluxes as described for the KT model

3) Recalculate density using the equation of state discussed in chapter 3 (equation 3.14):

$$\rho(i) = \rho 0\ (1 - \alpha(T(i) - 11.972) \qquad (5.21)$$

4) Check for static instability (i.e. denser water above less dense) beginning at the surface. If unstable, mix T, S, U and V from the surface downwards until the instability no longer exists. Conserve heat, salinity and velocity (negligibly different from momentum conservation under these circumstances, since density changes are very small). In this model, the potential energy released by convection is assumed to be all dissipated, and none is available for mixing.

5) Absorb wind stress (τx, τy) in the top level and rotate velocity under the Coriolis force. f is the Coriolis parameter, $2\,\Omega \sin \phi$, and

has been taken as 10^{-4} radians/second, valid for a latitude ϕ of 45°.

$$U(1)' = U(1)\cos(f\,dt) + V(1)\sin(f\,dt) + \frac{dt\,\tau x}{dz\,\rho 0} \qquad (5.22)$$

$$V(1)' = V(1)\cos(f\,dt) - U(1)\sin(f\,dt) + \frac{dt\,\tau y}{dz\,\rho 0}$$

Similarly for all the other levels putting $\tau x = \tau y = 0$. Here I have not followed exactly the programming of Thompson (1976). He stores only the values of U and V in the mixed layer itself and ignores velocities below. I store the values of U and V at each level which means that in a retreating mixed layer, velocities may be left behind below the mixed layer where they are free to rotate under Coriolis. It is believed that Price et al. (1986) adopt the same approach.

6) From the surface downwards, test for mixed layer stability, occurring when the bulk Richardson number criterion is satisfied as was defined in equation 5.3. Specifically, it is required that:-

$$Rb = \frac{g\,d\rho\,h}{d\underline{v}^2} \geqslant 0.65 \qquad (5.23)$$

Here $d\rho$ is the difference in density between two adjacent levels, and $d\underline{v}^2$ is the velocity difference, $d\underline{v}^2 = dU^2 + dV^2$. The critical Richardson number has been taken as 0.65 following Price et al. (1978). Mix the levels from the surface downwards until the criterion is satisfied across the base of the mixed layer. This will initially mix the wind- given momentum throughout the density- defined 'mixed layer'. Then further levels are entrained if the shear- generated turbulence is energetic enough. T, S, U and V are conserved as before.

5.3.2 Testing and modifications

A series of test runs were carried out for the PRT model just as for the KT model. The same wind and heating functions were applied (see section 5.2.2). Again the model extends from the surface to 300m. The same initial profile was used for T and S, and for the test runs

the U and V velocities were taken to be initially zero at all depths.

Figure 5.6 shows the results from the PRT model with a half- hour time step and 1m grid spacing. Temperature profiles are plotted every two hours, offset by 0.02°C, as before. Profiles 2 and 3 show a shallow mixed layer forming as the heating cycle begins, the wind stress being sufficient to mix the upper ten to twenty metres. At profile 4 (midday) the mixed layer has deepened. This might seem strange since at this time the solar heating is a maximum. However, one must remember that in calculating the bulk Richardson number, the velocity term is squared while the density term is not. Therefore the heat flux needs to increase rapidly (as it does at the beginning of the sinusoidal cycle) if it is to balance the increased shear. The mixed layer depth stays approximately constant at about 70m for several hours (profiles 7 to 11). The solar heating has created a sharp temperature jump at the mixed layer base and the wind stress is unable to overcome this. There is a gradual cooling of the mixed layer (profiles 8 to 11) as the cooling cycle begins. Eventually (profile 12) the combined effect of surface cooling and wind stress is large enough to rapidly deepen the mixed layer.

Figure 5.7 shows results from the PRT model with a time step of 15 minutes. The sinusoidal heating function has been adjusted so that the total input of heat in a given time is the same regardless of the length of the time step. The only differences are in profiles 4 to 6, where the shorter time step yields a shallower mixed layer. Temperature differences in the region of the mixed layer base may be as large as 0.02°C. This is happening because the velocity input during the first 15 minute time step is rotated during the second. In one half hour, the model is adding velocity from the wind stress, then rotating, then adding velocity again during the second 15 minute step, and rotating again. With the half hour time step, the model simply

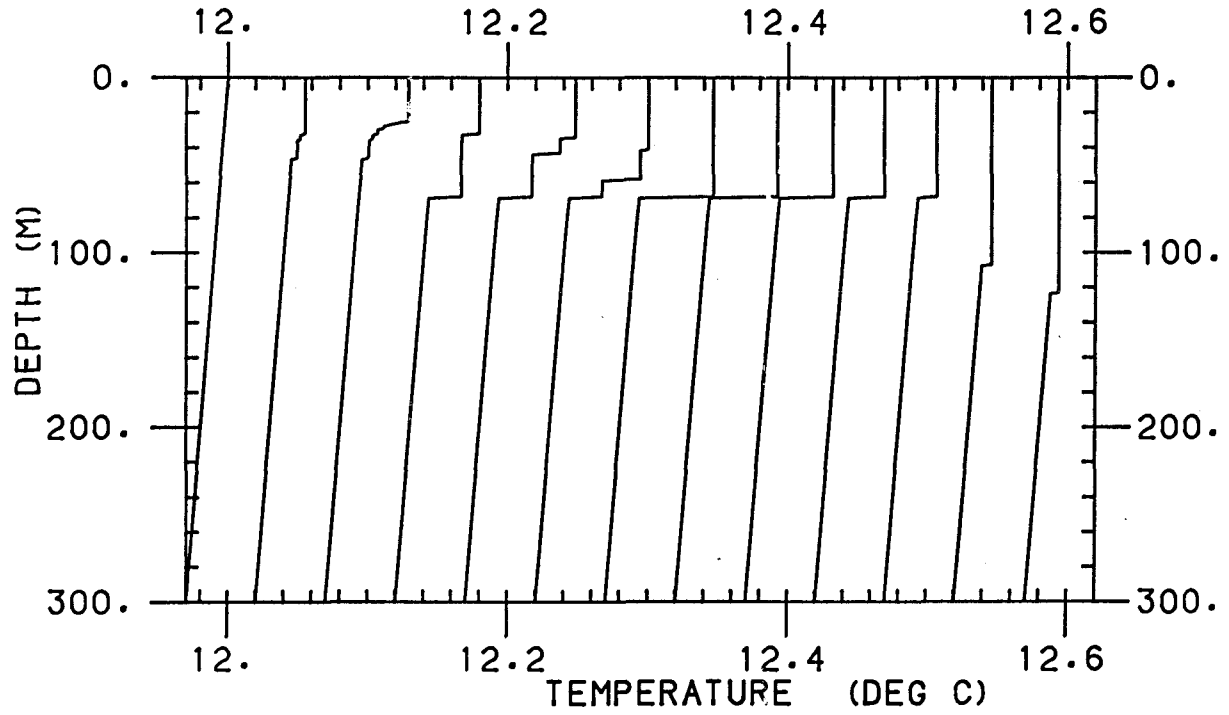

Figure 5.6 : Pollard- Rhines- Thompson model results with a time step of 0.5 hours and a grid spacing of 1m. Temperature profiles are plotted every 2 hours and are offset by 0.05°C. Wind forcing is constant while heating and cooling are sinusoidal (see text).

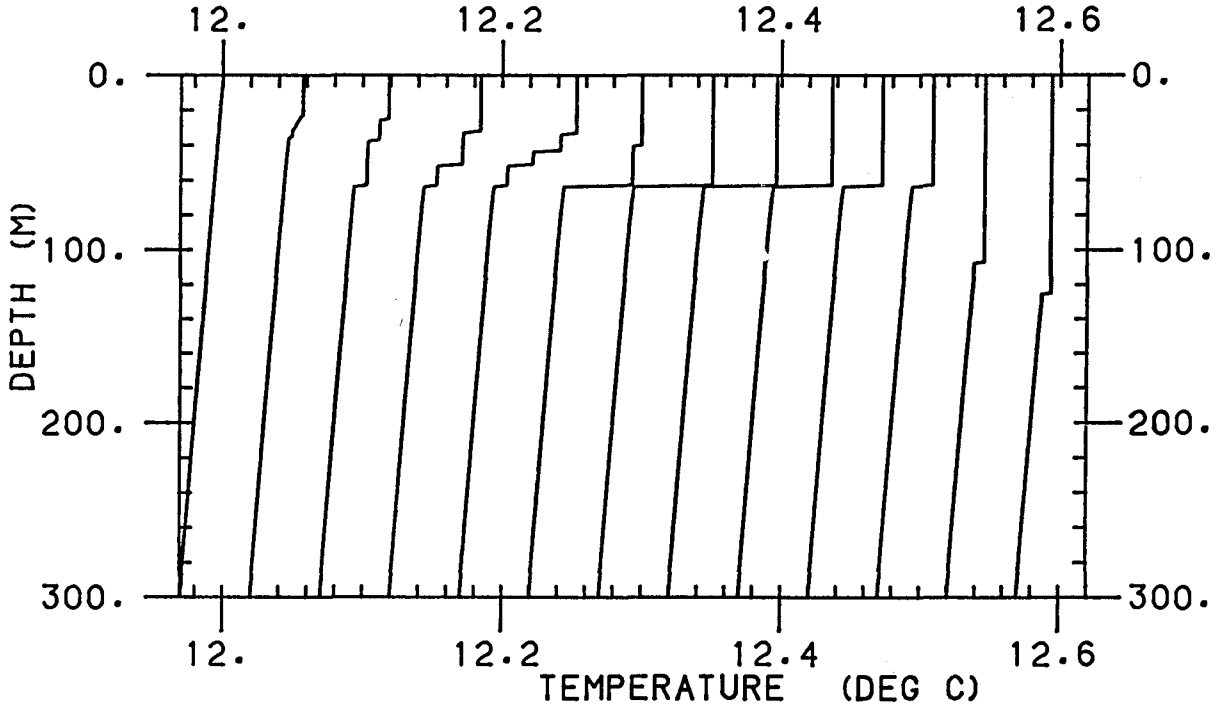

Figure 5.7 : Pollard- Rhines- Thompson model results with a time step of 0.25 hours. Otherwise as figure 5.6.

adds twice as much velocity and then rotates through twice the angle. But these processes are not linear, and the resulting vector is smaller with the shorter time step. Hence $d\underline{v}^2$ is smaller, thus the Richardson number is larger. Therefore there is less tendency to deepen and mix with a shorter time step. The magnitude of this effect will depend on the ratio of the additional wind- driven current to the pre- existing current at the beginning of that time step. It will also depend on the angle between the two; if the two vectors are nearly aligned, the effect is very small. It is not surprising then that we only see a difference for profiles 4 to 6, since at this time the additional velocity is still comparable in magnitude with the pre- existing velocity, and they are in opposite directions since rotation has occurred for about half of the inertial period.

The solid lines in figure 5.8 give PRT model results using a 1 hour time step. Here an approximation in equation 5.22 must be noted which is affecting these profiles (Alderson, personal communication). Equation 5.22 assumes that throughout the time step, the velocities are at their initial values. In reality, they are constantly rotating. The correct analytic solution to the problem is as follows (equation 5.24):

$$U(1)' = U(1)\cos(f\,dt) + V(1)\sin(f\,dt) + \frac{dt\tau x}{f\,dz}\sin(f\,dt) + \frac{dt\tau y}{f\,dz}(\cos(f\,dt)-1)$$

$$V(1)' = V(1)\cos(f\,dt) - U(1)\sin(f\,dt) + \frac{dt\tau x}{f\,dz}(\cos(f\,dt)-1) + \frac{dt\tau y}{f\,dz}\sin(f\,dt)$$

Equation 5.22, as used by Thompson (1976), simply approximates for small (f dt), thus sin (f dt) becomes (f dt) and cos (f dt) becomes 1. I have found that this approximation makes no difference at time steps of 15 minutes or half an hour, but with a time step of 1 hour, the more correct calculation of U and V produced the profiles shown dotted in figure 5.8. A significant effect occurs. For example, for the 4th

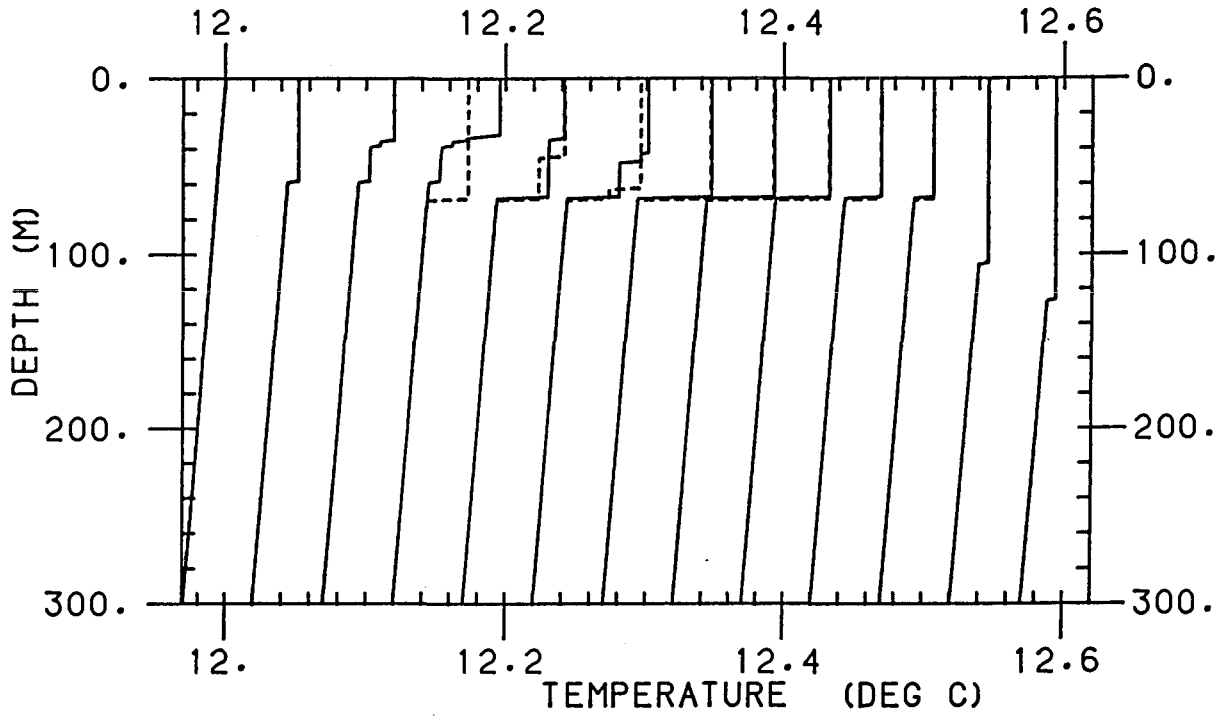

Figure 5.8 : Pollard- Rhines- Thompson model results with a time step of 1 hour (solid lines). The dotted lines are produced using the same time step but with the more exact calculation of u- and v- velocities.

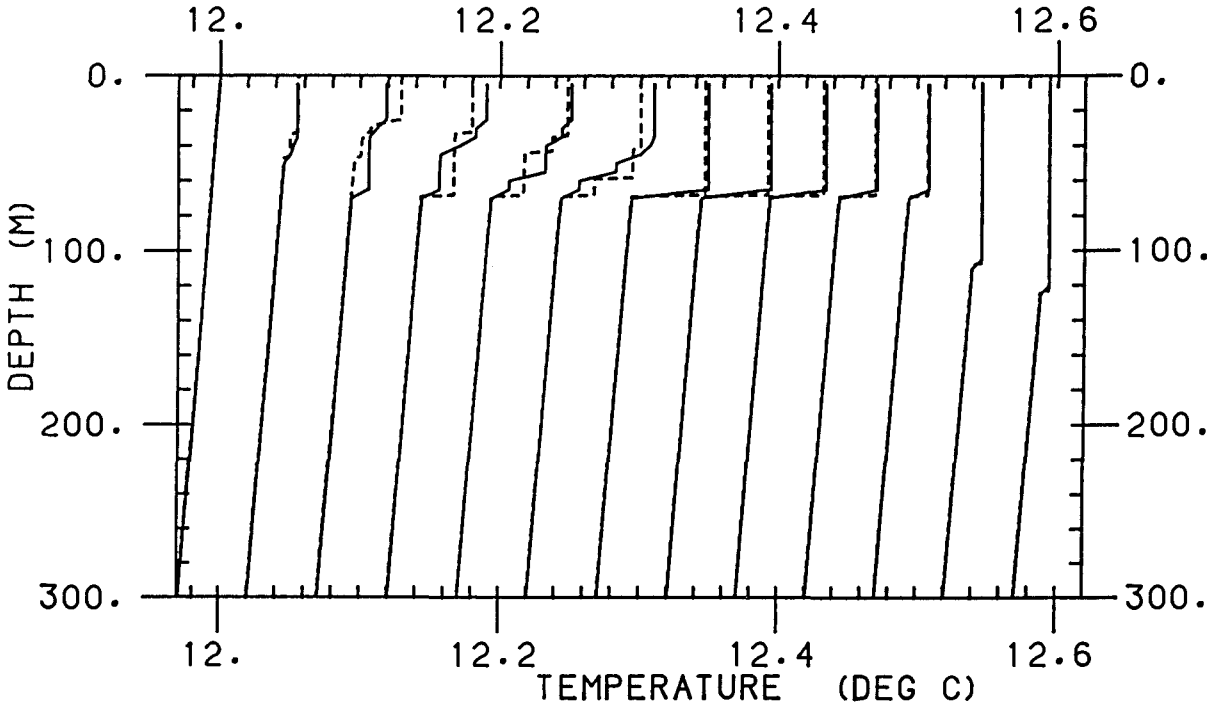

Figure 5.9 : Pollard- Rhines- Thompson model results with a grid spacing of 5m (solid lines) and 1m (dotted lines).

profile the mixed layer depth is some 40m different with temperature variations of 40mK throughout the upper 60m. Figure 5.6 may now be compared with these dotted profiles, having 0.5 hour and 1 hour time steps respectively. As just argued for the 15 minute time step, the shorter time step produces less deepening due to the rotation of the velocity vector at the intermediate time step.

Tests of various vertical grid spacings were also carried out. Figure 5.9 compares the results using a value of 5m (solid lines) and 1m (dotted lines) with a time step of 0.5 hours. The differences are larger than those for the KT model, since the mixed layer temperature is in some cases 0.01°C greater. This is due to the dependence of the mixing upon the gradients at the mixed layer base, which will vary with grid spacing.

Figures 5.10 and 5.11 give U and V velocity profiles respectively for a time step of 0.5 hours and a grid spacing of 1m. Remember that there is a constant wind forcing of $0.3N/m^2$ in the x- direction. Thus initially the U velocity increases in the mixed layer. This then rotates to the right under the Coriolis force, giving a small negative component in the northwards velocity plot. As the southwards velocity increases, the Coriolis effect produces a westwards velocity component. By midnight (10th profile) both eastwards and northwards velocities are small since the westwards velocity component due to the southwards velocity has almost counteracted the eastwards velocity component due to the wind stress.

A run was also carried out to check the agreement of the PRT numerical model with the analytical solution given by Pollard et al. (1973). For a constant wind stress τ and an initial stratification Γ, the mixed layer depth h should be the following function of time:

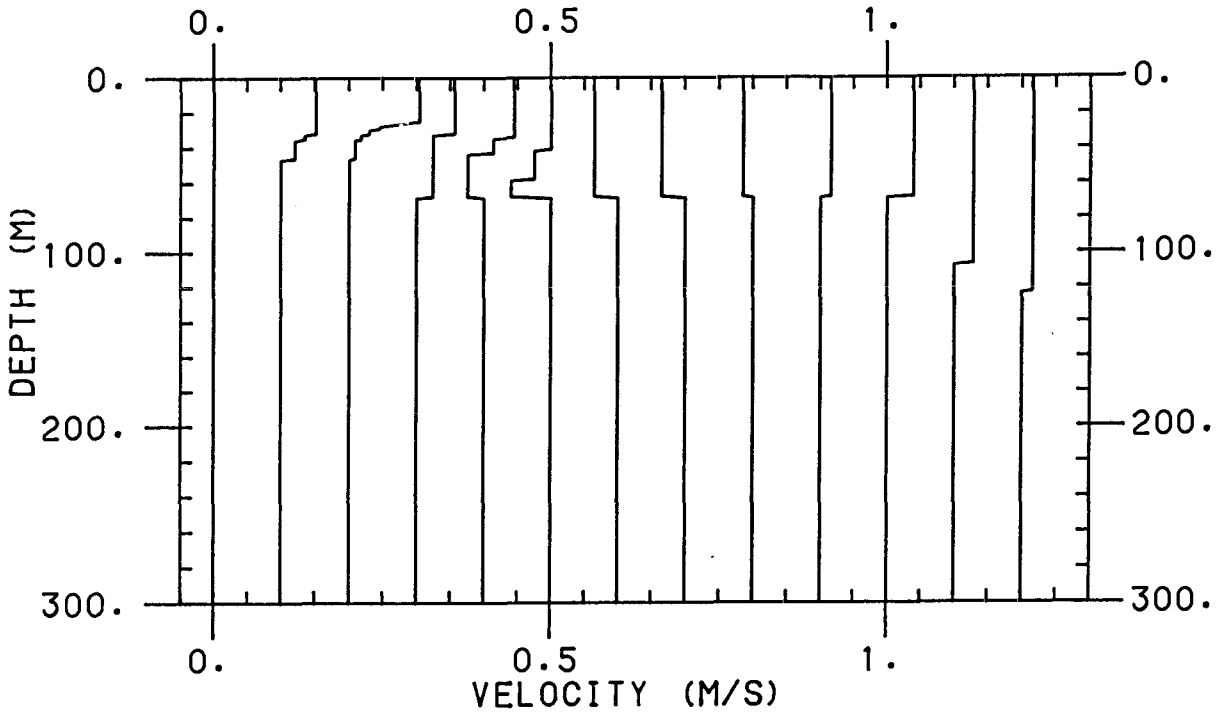

Figure 5.10 : Pollard- Rhines- Thompson model results with a time step of 0.5 hours and a grid spacing of 1m. The plot shows eastwards velocity profiles every 2 hours, offset by 0.01m/s. Forcing is as for figure 5.6.

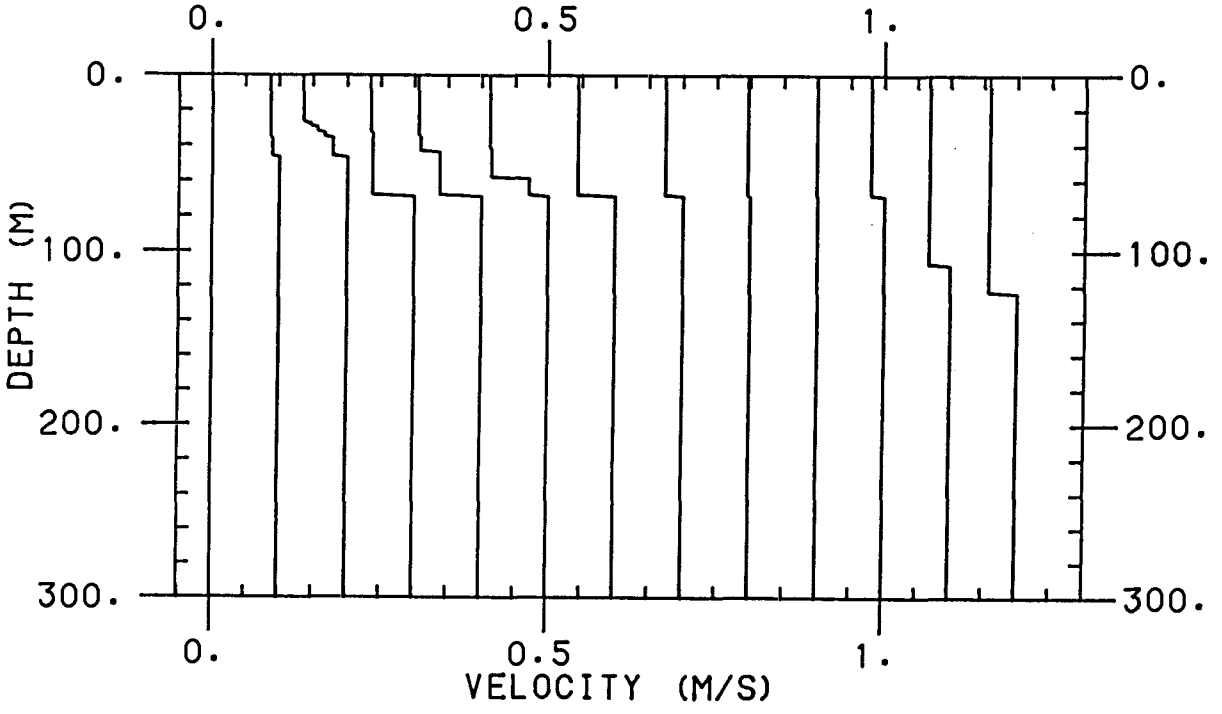

Figure 5.11 : As figure 5.10 but for northward velocity.

$$h = \left(\frac{\tau}{\rho}\right)^{\frac{1}{2}} \left[\frac{4 \quad (1 - \cos (f\ t))\ 0.65}{\Gamma\ f^2\ g\ \alpha}\right]^{\frac{1}{4}} \qquad (5.25)$$

0.65 is the critical Richardson number defined earlier. Equation 5.25 is valid until h stops increasing at $t=\pi/f$. Figure 5.12 shows the mixed layer depth of the numerical model (dotted line) (grid spacing 1m, time step 0.5 hours) and the analytic solution (solid line) for a wind stress of $0.3N/m^2$ and an initial stratification of 0.01°C in 100m. Initial velocities are zero; these are the same initial conditions as for the other test runs described, but the heating and cooling are zero. Agreement is very close, within 1m or 1 grid level. Also shown are two examples of the KT model results under the same forcing. Penetrative convection of 15% was allowed and energy was decayed exponentially using Z0=100m (dashed line) or Z0=40m (dash- dot line) as described in section 5.2.2. It is seen that the discrepancies between the two KT models and the PRT model are considerable. The KT model using Z0=40m is closer to the PRT model. One should not expect the models to agree since their deepening parameterisations are completely different.

Price, Weller and Pinkel (PWP) (1986) have proposed a modification to the PRT model, to 'smear out' the sharp discontinuity at the base of the mixed layer as mentioned in section 5.1. This was suggested by the observations of Price (1979) which showed that the transition layer between the mixed layer and the deeper water was linear and symmetric. He found that the transition layer could be described by a condition requiring the local gradient Richardson number to be greater than 0.25 for stability. The following procedure is carried out at each time step after stage 6:

7) Test the profile to find the smallest value of Rg, the gradient Richardson number:-

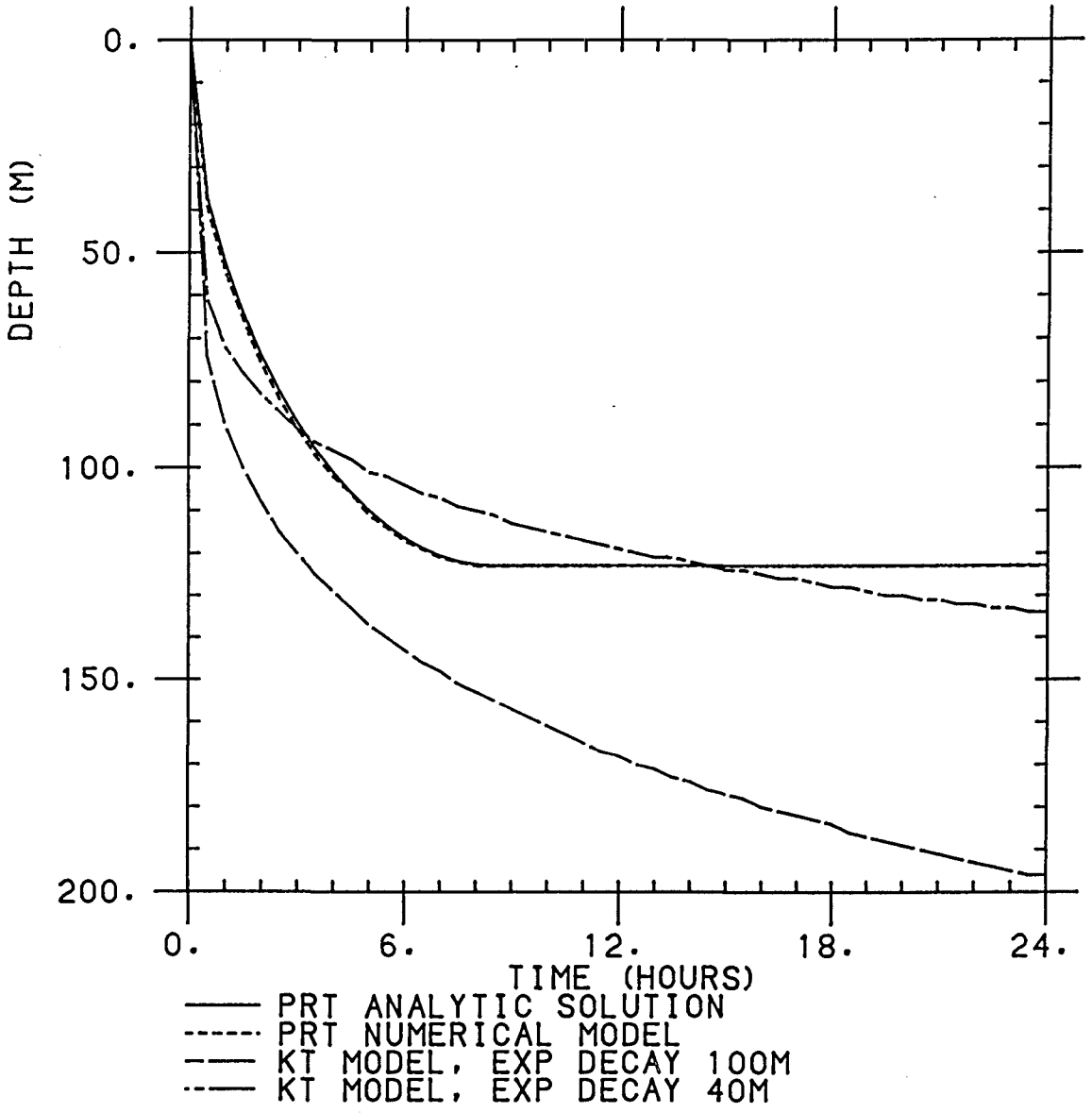

Figure 5.12 : Comparison of mixed layer depth predicted using the models described in the text. The solid line gives the PRT analytic solution for mixed layer depth as a function of time, while the dotted line shows the PRT numerical model version. The dashed line gives for comparison the KT model prediction with 15% penetrative convection and an exponential energy decay with Z0=100m, while the dash- dot line is the same model with Z0=40m.

$$Rg = \frac{g \ (d\rho / dz)}{\rho 0 \ (dV / dz)^2} \qquad (5.26)$$

Rg is calculated by first differences. It is not defined in the mixed layer itself, and is only calculated in the stratified region of the profile. If the smallest Rg is less than 0.25, then these two levels are partially mixed in U, V, T and S according to the formulae:-

$$\left.\begin{aligned} T(j)' &= T(j) - 0.5 \ (1 - Rg/Rc) \ (T(j) - T(j+1)) \\ T(j+1)' &= T(j+1) + 0.5 \ (1 - Rg/Rc) \ (T(j) - T(j+1)) \end{aligned}\right\} \qquad (5.27)$$

Rc = 0.3 is a specified constant, chosen to ensure convergence. The values of Rg are then recalculated across the base of the mixed layer, and mixed again as necessary until the profile satisfies the criterion all the way down. A smooth vertical profile is produced. T, S, U, V and ρ are all mixed similarly.

The solid lines in figure 5.13 give temperature profile results of the PRT model with the PWP modification; the basic PRT model results are shown dotted. Here a time step of 0.5 hours and a grid spacing of 1m were used. A more realistic profile is indeed produced. The mixed layer itself is slightly altered, both in sea surface temperature and in 'slab' depth. For example, the sea surface temperature at 1000 (3rd profile) is about 0.01°C lower than that of the dotted profile.

5.4 Model runs with observed meteorological forcing

Although it cannot be expected that any model will reproduce the observed temperature time series because the heat budget does not balance, it is instructive to run the models with the observed heating, cooling and wind forcing. One may determine how important is the discrepancy in the heat budget in influencing the model output. Even if the magnitude of the modelled diurnal heating signal is too small, the phase might be correct. The time lag between the signal reaching the current meters might be modelled reasonably.

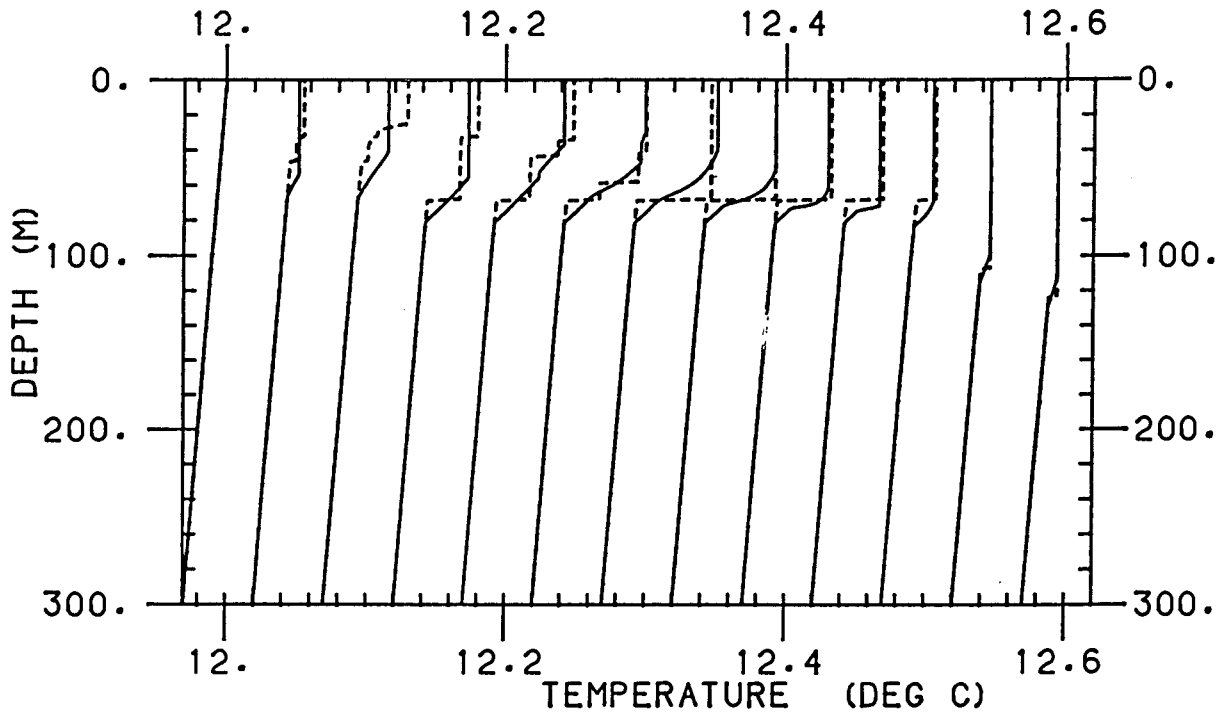

Figure 5.13 : Pollard- Rhines- Thompson model modified by Price et al. (1986) (solid lines). Basic PRT model results are shown dotted for comparison.

For these runs a time step of 0.5 hours and a grid spacing of 1m was used. The initial temperature profile is plotted in figure 5.14; the salinity profile was uniform with depth at 35.65 ppt. Figure 5.15 shows the initial U and V velocity profiles used for the PRT model. These profiles were chosen as representative of the temperatures and velocities observed at the spar at 0600 on day 67, the start of the model run.

Figure 5.16 shows a temperature time series from the KT model at the depths of the VACMs. For this run, m=1.25, δ=0.15 and Z0=100m. It may be compared with the experimental data of figure 2.8. The model results do not of course include the rapid cooling during the morning of day 69 as the spar buoy crossed the ramp (section 4.3). Figures 5.17 and 5.18 show the results from the PRT model and the PWP modified version of PRT. Obviously the heating signal at all depths is too small in all three models. There is no diurnal heating at depths below 100m, contrasting significantly with the signal observed (figure 2.8). The time lag for the heating to reach the upper current meters is several hours longer than that measured. Differences between the three models are very small compared to the disagreement between the models and the observed data. The amplitude and phase of the diurnal heating signal predicted by the KT model will be assessed further in chapter 8.

It is evident then that a one- dimensional model is unsuitable due to the heat budget problems discussed in chapter 4. A more complex model is required; section 4.5 suggests that convergence and downwelling at the VACMs should be included. This chapter has provided an understanding of the characteristics of the simple models; the Kraus- Turner model will be developed in chapter 8 to attempt to explain what is happening at the spar buoy. The next chapter, meanwhile, reviews mechanisms that might cause such downwelling.

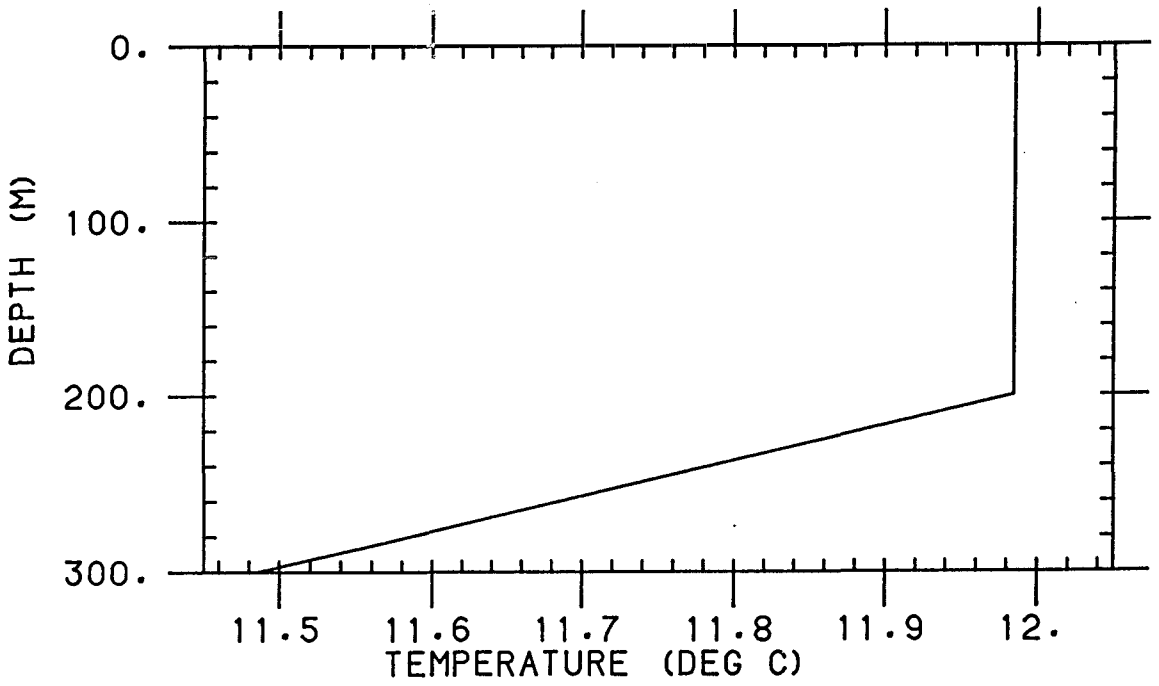

Figure 5.14 : Initial temperature profile taken from the VACMs at 67/0600, used to produce figures 5.16, 5.17 and 5.18.

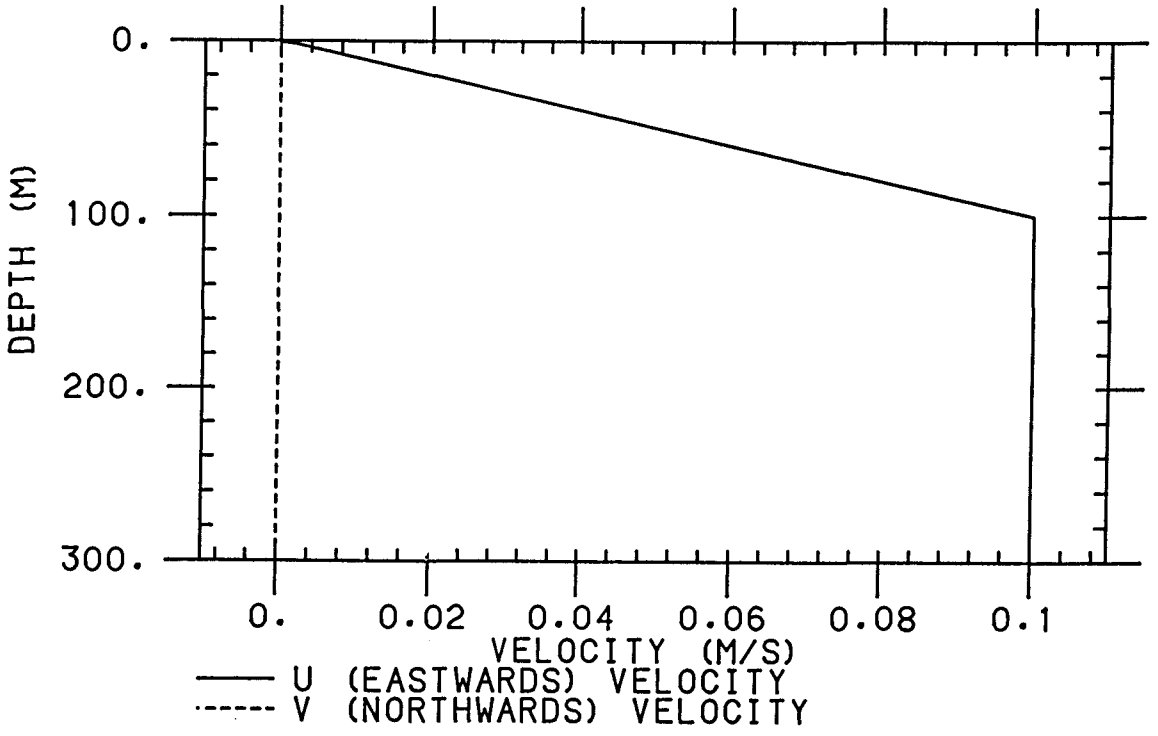

Figure 5.15 : Initial eastwards and northwards velocity profiles taken from the VACMs at 67/0600, used to produce figures 5.17 and 5.18.

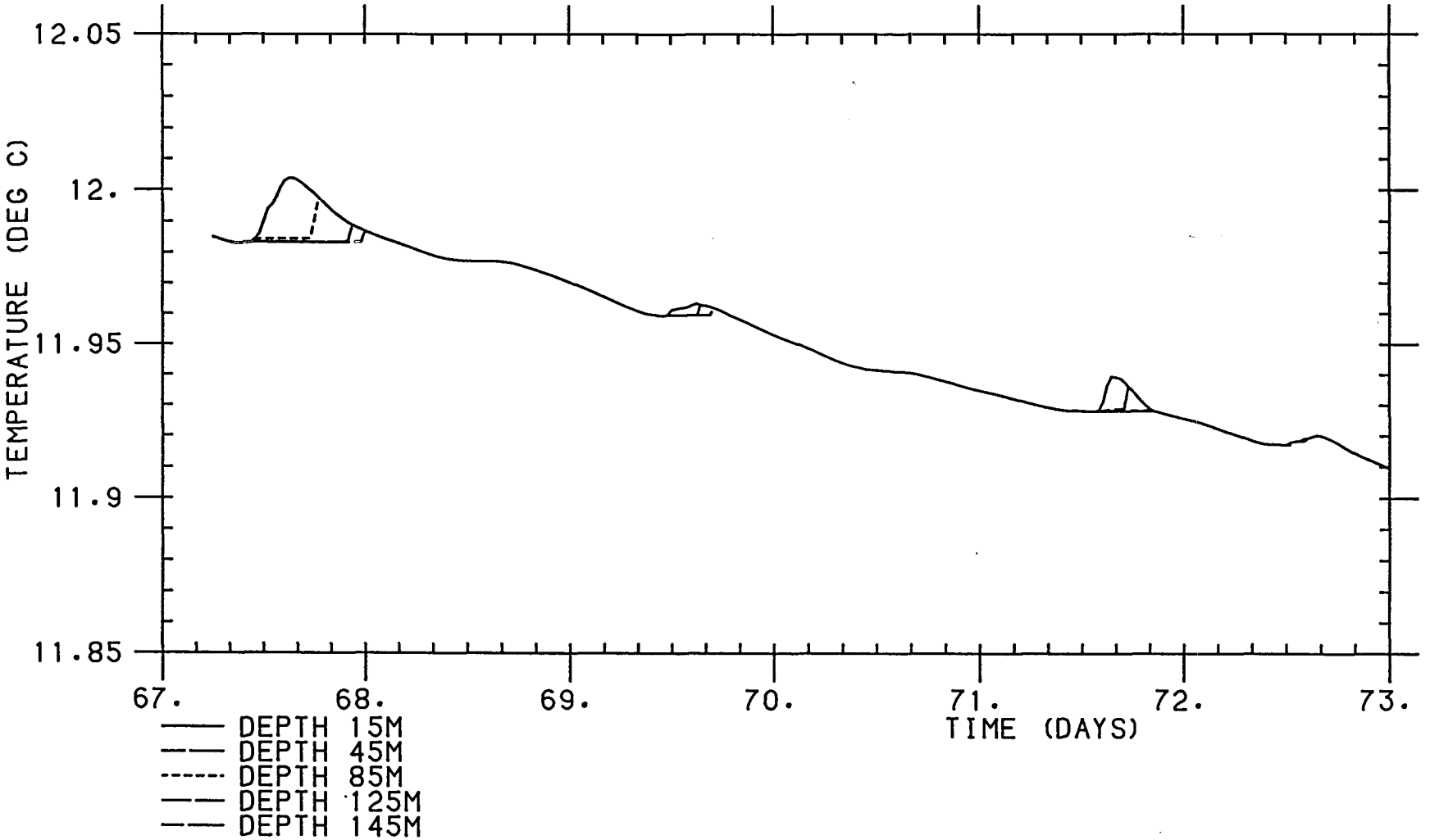

Figure 5.16 : Temperature time series at the depths of the VACMs, produced from the KT model using 15% penetrative convection and an exponential energy decay with Z0=100m.

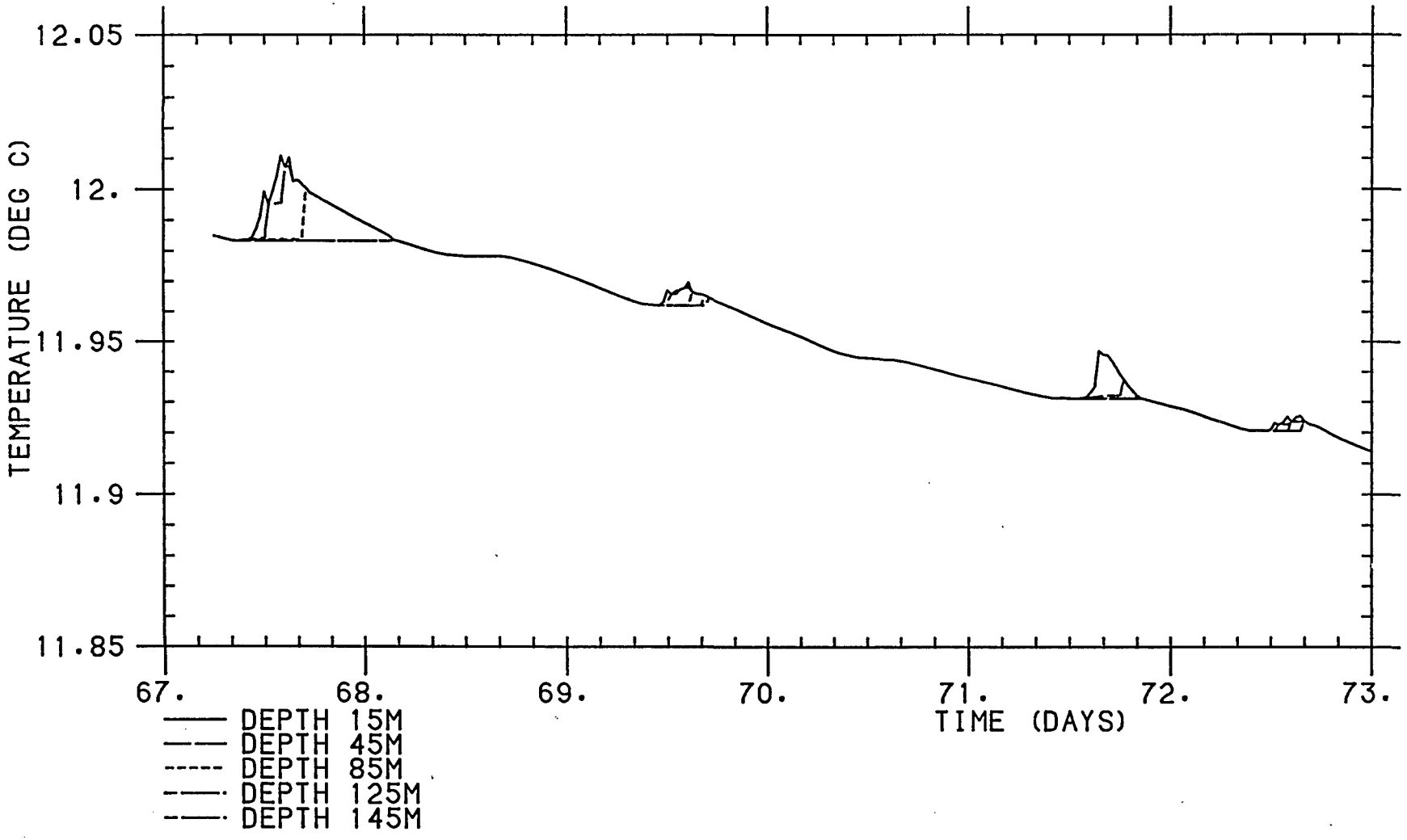

Figure 5.17 : Temperature time series at the depths of the VACMs, produced from the PRT model.

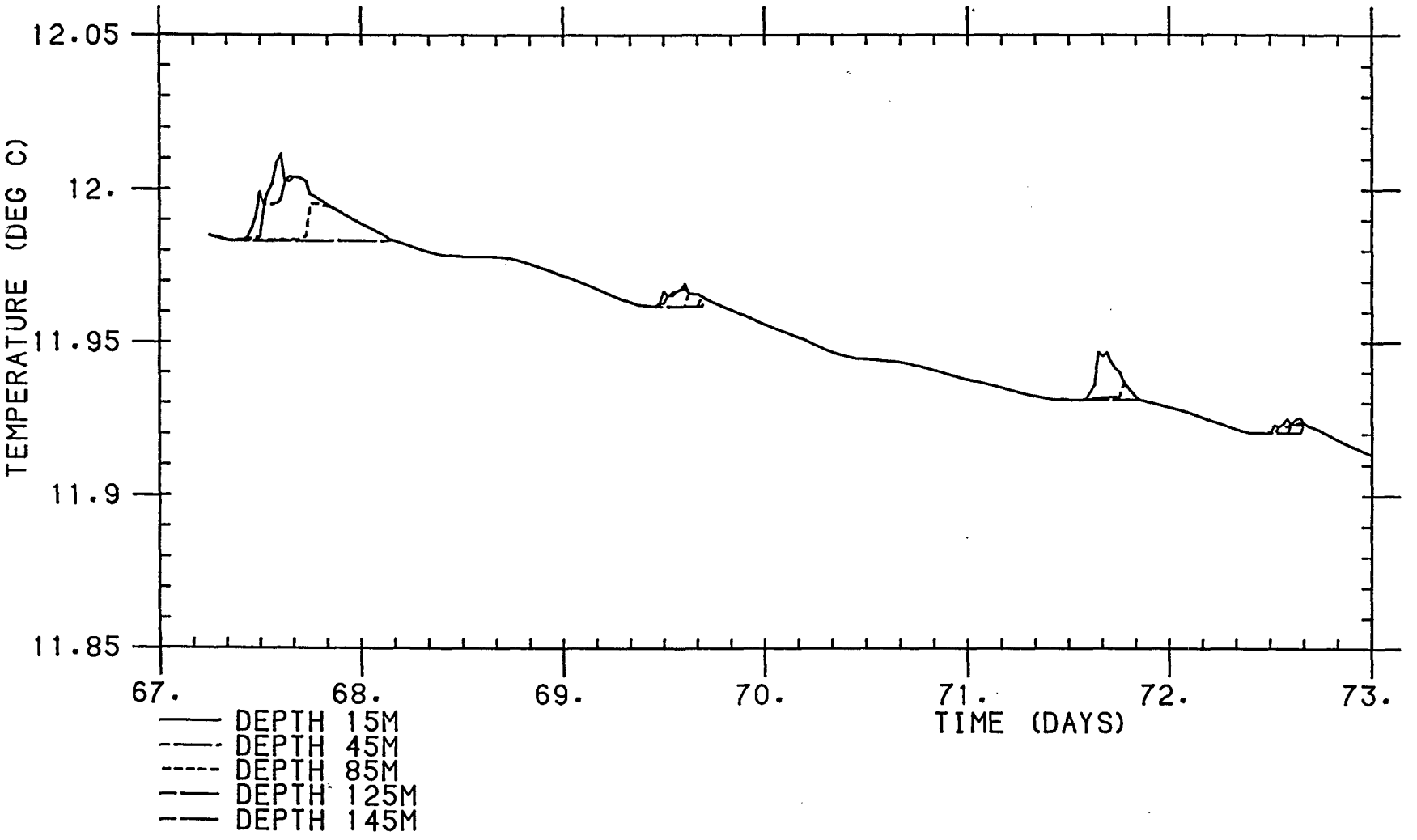

Figure 5.18 : Temperature time series at the depths of the VACMs, produced from the PRT model modified according to Price et al. (1986) as described in the text.

Chapter 6

Three- dimensional Structured Flows in the Upper Ocean

6.1 Introduction

The heat budget in chapter 4 was undertaken on the assumption that the water with which the spar buoy freely drifted would be representative of the water in the surrounding 10-20km. When deploying the spar buoy, particular care was taken to avoid regions such as fronts where horizontal gradients of temperature, density and velocity would not be small. Chapter 4 suggests that the mixed layer may have an organised velocity structure, with regions of convergence and divergence, downwelling and upwelling. This chapter will review the observations of such structures, and discuss possible mechanisms for their generation.

6.2 Langmuir circulations

6.2.1 Description

When the wind is blowing fairly strongly (at least 3m/s) and steadily over a lake, one may frequently observe regular rows of streaks, approximately parallel to the wind. These may be revealed by lines of foam, leaves or weed, or by a change in reflectivity in the streak zone. The first investigation of these "windrows" was carried out by Langmuir (1938). On a trans- Atlantic crossing, he noticed lines of floating weed (Sargassum) at a regular 100-200m spacing. When the wind changed direction by about 90°, the Sargassum rearranged into streaks parallel to the new wind direction within 20 minutes, although the direction of propagation of the waves did not.

Langmuir proposed that such convergence zones were the surface evidence of wind- driven roll vortices occurring in the upper ocean. The surface convergence and downwelling would be marked by the Sargassum. His subsequent experiments on Lake George, New York, showed that such roll vortices do exist and that the downwind velocity is

greater in the convergence regions than in between. Downwelling currents at a depth of two metres were found to be 2-3cm/s in the streaks, and upwelling currents 1-1.5cm/s in the surface divergence zones. He concluded that the cells were asymmetric, with a narrow downwelling jet accompanied by a substantial horizontal surface velocity, and a broader region of upwelling. Horizontal converging currents were found between the surface and 5m depth, but not at 10m depth. Langmuir suggested that the roll vortices would descend to the depth of the sharpest density gradient, and that, had they measured currents at lower depths, they would have observed the return flow of the circulation. He further proposed that the circulation was the "essential mechanism" in the creation and deepening of the mixed layer.

Woodcock (1944) used Langmuir's model to explain the predominant swimming characteristics of Portuguese Man-of-War jellyfish. His experiments with drift bottles confirmed Langmuir's ideas of a swift surface jet in the convergence zones. Since then, Langmuir circulations have frequently been studied, mainly in lakes and on a small scale. Biologists have found that such circulations have a noticeable effect on the distribution of living organisms in the surface layers (Sutcliffe et al., 1971).

Figure 6.1 depicts typical Langmuir circulations from a review by Pollard (1977) in which estimates are given of the observed range of magnitudes of each variable. This figure defines the axis coordinates (x,y,z) and velocity components (u,v,w) used below. A more recent review is given by Leibovich (1983).

6.2.2 Observations of Langmuir circulations

This section contains a summary of the observations of Langmuir circulations that have appeared in the literature to date.

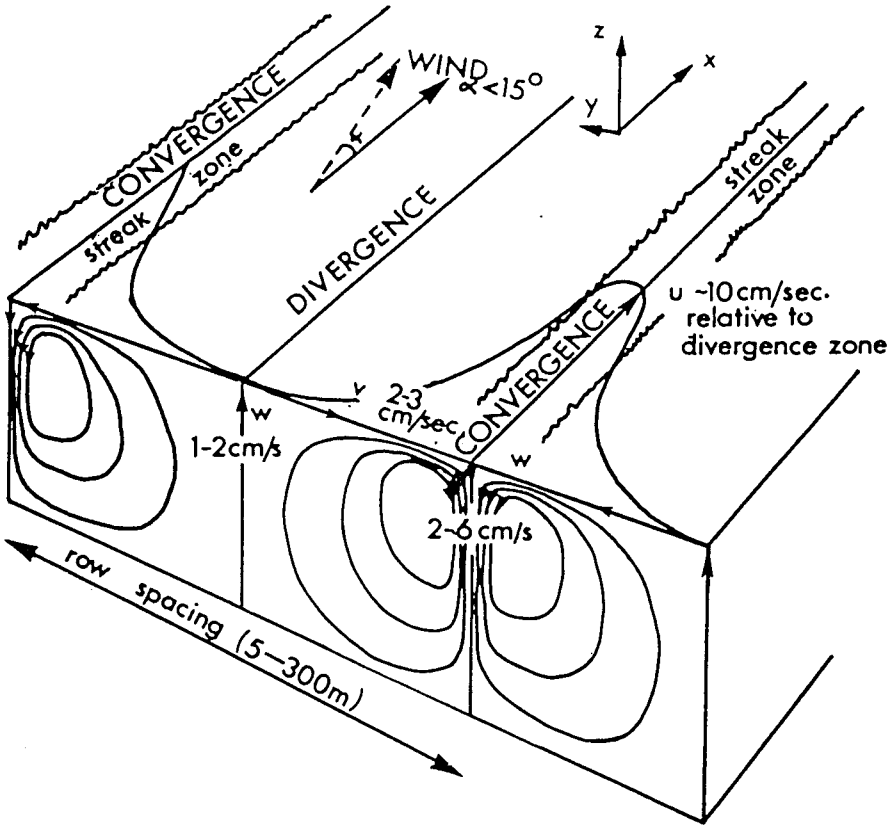

Figure 6.1 : Diagrammatic representation of the main features of Langmuir circulations (from Pollard, 1977).

Row spacing

Row spacing, the distance between adjacent downwelling zones, has been found to vary between 2m and 25m in lakes, and 2m and 300m in the ocean. Some observations suggest that row spacing is related to the depth of the thermocline. Langmuir (1938) found spacings of 15-25m in the autumn, when the mixed layer was relatively deep, but only 5-10m for a shallow, summer mixed layer. Scott et al. (1969) found that streak separation was correlated with the depth of the mixed layer, but not with wind speed or heat flux. They observed two types of streak, one occurring only for wind speeds greater than 3m/s, but being longer and better defined. When the wind died, the streaks remained "for some time". The second type of streak occurred "briefly only during gusts". Kenney (1977) shows an increase in row spacing from shallow to deep water in the well- mixed Lake of the Woods. He is doubtful whether row spacing can be reliably measured from boats, preferring to use photography from a high tower or aircraft.

Other observers find no relationship between row spacing and mixed layer depth, but a significant dependence upon wind speed. Faller and Woodcock's (1964) observations of Sargassum in the open ocean indicate a strong correlation between wind speed and row spacing. They found "some indication" of a relationship between row spacing and mixed layer depth, but it was inconclusive. Maratos (1971) detected a correlation between wind speed and row spacing. His experiments were conducted in the shallow water of Monterey Bay using aerial photographs. He found spacings of 10-20m in wind speeds of 3-7m/s. Most observers are agreed that Langmuir circulations do not occur in winds below about 3m/s, and do not depend upon surface heat flux.

Several observers have found a hierarchy of cells of various sizes in the ocean. Assaf et al. (1971) studied Langmuir circulations off Bermuda in a deep water area (3000m depth) and a shallow water area

(50m) on Plantagenet Bank. In the deeper water, they found cells of three distinct scales, the largest having 280m streak spacing, and the smaller 40m and 5m. The wind speed was about 6m/s and the mixed layer 200m deep. A large downwind surface velocity jet was detected. They note that "Langmuir cells of different sizes seemed to dominate the mixing, and no evidence of current stratification associated with the Ekman spiral was observed". However, on the same day, in the shallow water, they did find evidence of the Ekman spiral, shown by plumes of dye at different depths. This time, no medium or large scale cells were observed, only the 4-5m ones. Assaf et al. suggest that in the deep water, the rolls are caused by Ekman instability (see section 6.2.5) hence the absence of the Ekman spiral. In the shallow water, the mechanism might be wave- dominated (section 6.2.4) since the Ekman spiral coexisted with the rolls. After several other observations, they conclude that larger cells occur only in a deep mixed layer and for winds of more than 6m/s, whereas the smaller ones appear above a wind speed of 3m/s.

There is some evidence that cell scales are larger at depth than near the surface (Katz et al., 1965). Myer (1971) found scales at 1.0m twice those at 0.35m. Langmuir suggested that, just as large waves have smaller waves upon them, so "the surfaces of the larger vortices contain smaller and shallower vortices". This would imply the continual creation of smaller scale cells, which are then swept up into larger, more permanent cells. A comprehensive set of windrow observations is described by Ichiye et al. (1985). They found that rows of computer cards marking convergence zones increased in spacing with time. The average spacing within 2-4 minutes of deployment was about 6m, increasing to 20-24m after 18-20 minutes. This may be because the cards are initially influenced by the nearest small cell, but are eventually drawn into the stronger convergence zones of the

larger cells.

Row length

Langmuir (1938) reported lines of Sargassum as long as 500m in the Atlantic with a spacing of 100-200m. Most observers do not discuss length, since their rows are revealed by surface drifters marking only a short section of a row. Kenney (1977) notes that the regularity of windrows is clearer when observed from a high tower or aircraft. He defines "very regular" windrows as those whose length to spacing ratio is greater than 100. Kenney does not accept the existence of downwelling, and proposes an ever- increasing downwind motion until instability limits the length of the streak.

Downwelling velocities

Sutcliffe floats (Sutcliffe et al., 1963) have been used to measure the downwelling current via the drag on a circular disk with some buoyancy (Harris and Lott, 1973). Myer (1971) deduced vertical velocities from the dispacement of isotherms. He found the downwelling zones to be much narrower than the upwelling ones, and that the maximum velocities occurred at about half the depth of the cell. Descending currents were larger in unstable density profiles than stable ones.

Sutcliffe et al. (1963) found that for every 1m/s of wind they measured approximately 1cm/s of downwelling velocity. Harris and Lott's (1973) data agreed with this although the scatter was large. More recent measurements have been made by Filatov et al. (1981). Figure 6.2 shows downwelling speed versus wind speed for all three sets of data (from Leibovich, 1983). There are clearly other factors influencing downwelling, although the increase in sinking speed at higher wind speeds is obvious. Sutcliffe's five observations (marked x) were taken in the ocean "near Bermuda", but he gives no details of water depth, mixed layer depth or weather conditions except wind speed. Kenney (1977) points out a possible error in their disk drag

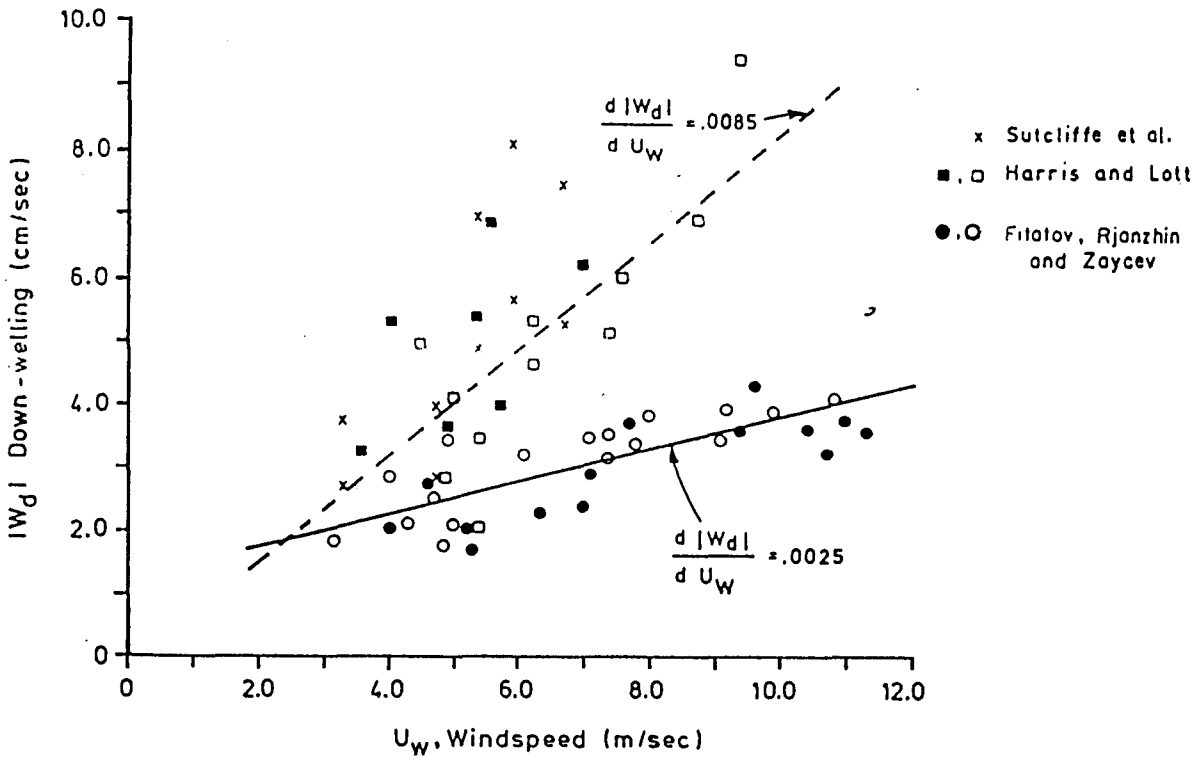

Figure 6.2 : Measured downwelling speeds below streaks as a function of wind speed. The open squares and circles correspond to surface heating, closed symbols to surface cooling. The values of windspeed denoted by the uppermost crosses have been multiplied by $\sqrt{2}$ (see text) (from Leibovich, 1983).

coefficient; therefore the values of wind speed denoted by the uppermost crosses have been multiplied by $\sqrt{2}$. Filatov measured 160 sets of downwelling currents and winds on Lake Ladoga, USSR, and gives results for both surface heating and cooling. The water depth is not clearly stated but must be at least 70m. Harris and Lott (1973) took measurements in Lake Ontario where the water depth was 12m, and their cell spacing was 3-4m. These results suggest that downwelling velocities are larger in the ocean where there is a deeper thermocline to limit the cell size. In lakes, where the bottom of the circulation may well be the lake bed, cell spacing is smaller and the downwelling velocities correspondingly decrease. Alternatively, the difference may be due to varying density stratification in the upper layers of the three cases, since a stronger stable density gradient will inhibit cell growth. Kenney (1977) disputes the existence of downwelling in windrows, preferring to consider them as a horizontal, two- dimensional variation of downwind current. His evidence is weak however, since he did regularly measure the vertical currents.

Recently, studies of large longitudinal rolls in the open ocean off California have been undertaken from the research platform FLIP (Weller et al., 1985). FLIP is a floating platform with 95m of hull underwater, but its drift velocity is caused by a combination of both upper ocean currents and windage. On several occasions, unmistakable Langmuir circulations were observed. At a depth of 23m, Weller et al. measured large downwelling velocities (20cm/s) in association with substantial downwind horizontal velocities (also O(20)cm/s). At the same time, strewn computer cards arranged themselves into "long, narrow bands approximately 20m apart". The depth of the thermocline was about 50m and wave height 1m. This downwelling velocity is about twice as large as figure 6.2 would suggest. However, Weller et al. point out that the downwelling velocities were strongly depth

dependent, being maximum between 10m and 35m in the middle of the mixed layer. Downwelling velocities above and below were smaller, typically less than 5cm/s. It may be that the discrepancy between Weller et al.'s results and those discussed above is due to the different methods of measuring vertical current. Weller et al. measure the actual velocity past a propeller sensor at a specified depth. All the other experiments used floats on which the downward force was measured. The depth at which their measurements were taken is not stated but the given values may be more representative of the mean downwelling current rather than the maximum. An alternative explanation is that, as mentioned previously, current strengths may depend on the cell size. The rolls observed here were 20m wide, larger than those of the other experiments. Since Weller et al. found a maximum downwelling at depth, rather than at the surface, their circulations may be generated differently (see section 6.2.6).

Horizontal current velocities

Observers agree that the downwind surface velocity of the convergence zones is greater than it is in between (figure 6.1). A current difference of O(10)cm/s is typical. One possible explanation for this is that it is this water which has been longest exposed to the wind stress as it approaches the convergence zones. No mention seems to be made of the variation of the downwind velocity with depth in the convergence zone.

6.2.3 Theories of Langmuir circulation

Many theories have been proposed for windrow generation; most have been discounted. One of the more obvious is thermal convection. It is known that thermal instability in the atmosphere can be aligned into rows by vertical wind shear (Kuettner, 1971) causing cloud streets. However, the oceanic observations (e.g. Faller and Woodcock, 1964; Scott et al., 1969) show conclusively that Langmuir circulations can

occur in conditions of stabilizing surface heating, so buoyancy effects cannot be the primary mechanism. Nonetheless, surface cooling will probably strengthen the rolls, if they have already been created by another mechanism.

Woodcock and Wyman (1946) suggest that roll vortices in the atmosphere cause the sea water beneath to converge and diverge. This mechanism is discounted on the grounds that the relatively rapid lateral motion of the atmospheric rolls means that the wind forcing is not sufficiently sustained for oceanic rolls to develop. Welander (1963) proposed that rolls form when surface streaks modify the wind field, thus setting up a feedback mechanism. Myer (1971) showed that this effect is two orders of magnitude too small to provide the necessary energy, although he did find cold updrafts in the wind field over streaks.

Kraus (1967) discusses the possibility of a film on the water surface damping the capillary waves in streaks, which leads to a radiation pressure and hence to the growth of a cell. Again not enough energy is made available by this mechanism (Myer, 1971), and cells can exist in laboratory experiments with no surface contaminants (Faller, 1969). Faller found during laboratory experiments that the generation of Langmuir circulations required only waves and a small shear flow in the upper ocean.

There are two remaining mechanisms for production of Langmuir circulations: wave- current interaction and instability of the Ekman spiral.

6.2.4 Wave- current interaction theories

Both Ichiye (1967) and Stewart and Schmitt (1968) observed a close connection between windrows and surface waves. Stewart and Schmitt suggested that windrows were generated by the interaction of two linear wave trains. However, Faller (1971) pointed out that it is

inconsistent to produce rotational roll vortices from an initially irrotational wave field, without some other source of vorticity. Breaking waves could provide the vorticity, but observations and laboratory experiments (Faller, 1969) show that circulations exist without breaking waves.

Craik (1970) studied the interaction between pairs of inviscid, linear wave trains intersecting at the surface, but also imposed a linear, wind- induced velocity profile in the upper layers. This theory can account for the rapid re-orientation of the Langmuir circulations when the wind changes direction. A new set of rolls will appear "as soon as the new primary shear flow is established in the upper layers of the water". There need not be a large change in the wave spectrum, since the new shear flow will interact with different waves in the spectrum already present. The short- crested gravity waves distort the vorticity field associated with the primary (linear, shear) flow, and their non- linear interaction causes a vorticity transfer from the primary flow to the secondary disturbance, the longitudinal roll vortices.

Leibovich and Ulrich (1972) criticise Craik's model. Craik assumes that the particle velocities of the wind- generated waves are small compared to the wind- driven current, and this is not usually the case. Craik predicts the maximum downwind surface current in the divergence zones, whereas the observations show that the downwind current is maximum in the convergence zones (e.g. Langmuir, 1938; Scott et al., 1969).

Craik and Leibovich (1976) (to be abbreviated CL) rectify this, mainly by including viscosity and the assumption that the motion in the surface layer is dominated by the orbital motion of the irrotational surface gravity waves. The rotational currents of the circulation studied are smaller, comparable with the Stokes drift (Phillips, 1977).

This Stokes drift is essential to the mechanism and is associated with a pair of wave trains, propagating at equal angles either side of the wind direction; it therefore varies in the crosswind direction y. As with Craik's (1970) theory, a wind- driven current u(z) is assumed, providing vorticity in the crosswind direction since it is a shear flow. The Stokes drift acts on this vorticity, and rotates it into the x- direction, thus producing longitudinal rolls.

The model predicts maximum wave heights, and hence Stokes drift, in the divergence zones, where upwelling occurs. In order to obtain a downwind velocity in the convergence zones, Craik and Leibovich claim that the surface current is dominated by a second- order current due to the Langmuir cells. This is largest in the convergence zones. They require that this velocity be greater than the upwind velocity contribution from the Stokes drift in a convergence. Hence they show that for a sufficiently strong wind, maximum downwind velocity occurs in downwelling zones. The prediction by the CL theory of maximum wave height in the divergence zones is in conflict with the observations of Myer (1971), who finds an increase in wave height in the streaks. However the observations of Thorpe and Hall (1980) show no significant difference between wave heights in and out of windrows.

Garrett (1976) proposes another model, prompted by Myer's observations. Rolls are produced by the non- linear interaction of a nearly irrotational wave field and a weaker rotational current. A WKBJ approximation method is used to show that surface waves are larger in the convergences, as Myer (1971) suggests. As waves enter a region of larger surface current (the streak), their propagation speed perpendicular to the current decreases. Their amplitude therefore increases, and vice versa on leaving the region. Momentum passes from the waves to a current as the waves slow down, so convergence towards the streak is obtained. The required vorticity is produced. Garrett

proposes that waves will preferentially break in the streak zone since they are largest there, and give more momentum to the current. Thus once a region of stronger current has occurred, the system is unstable and rolls will grow due to feedback. The theory of enhanced wave magnitude in the streak zones has been questioned (Leibovich, 1983), since Smith (1980), not using WKBJ analysis, found no wave amplification. Leibovich (1980) points out that Garrett's prediction of enlarged wave amplitude is valid only for surface waves with a small wavelength compared to cell spacing. Even if the waves are larger in the convergence zones, there is no experimental evidence of the preferential wave breaking required by Garrett's model. Thorpe and Hall (1980) found that waves break equally in and out of windrows.

Moen (1978) has taken aspects of both Garrett's and Craik and Leibovich's work to produce a model. Leibovich (1980) decides that Moen's theory is "logically inconsistent" and that the resulting equations are simply a reduced form of the CL theory.

The CL theory has been extended and improved to remove some of the initial flaws (Leibovich, 1977a; Leibovich and Radhakrishnan, 1977; Leibovich, 1977b) although the physics remains the same. Maximum wave heights are still predicted in the divergent zones. Pollard (1977) also objects to the strict restriction on the initial surface wave spectrum. For the model to produce rolls, the Stokes drift must vary in the y- direction but only change slowly with time. These variations must remain fixed in space for sufficient time to set up the circulations. This implies that the waves be phase- locked, typically for hundreds of wave periods (Leibovich, 1983). Significant wave energy must be contained in these phase- locked pairs lying at equal and opposite angles to the wind. If the energy of the wave spectrum is spread over many frequencies and directions, the Stokes drift may not vary in the y- direction as required. As Leibovich (1983) remarks,

such phase- locking "is not expected in a wind- generated sea", although it can be created in the laboratory and may occur naturally in a fetch limited situation (Craik, 1977). Figure 6.3 gives a summary of the mechanism of roll vortex generation described. It is now known as the CL1 or direct- drive mechanism.

Craik (1977) suggests an alternative theory, the CL2 or instability mechanism. This does not require the coherence in the wind- driven wave field discussed above and is therefore applicable to Langmuir rolls in a continuous spectrum of wind waves. Craik uses the same basic equations of motion as Craik and Leibovich (1976) but imposes a Stokes drift varying only with depth, and parallel to the wind direction. His stability analysis is analogous to that often used in the solution of thermal convection problems. A wind- driven shear current becomes unstable in the presence of the prescribed Stokes drift field. Craik (1977) assumes no thermal stratification but this restriction is lifted by Leibovich (1977b).

Figure 6.4 shows the CL2 mechanism. The reader is referred to Leibovich's (1983) review for further details. Faller and Caponi (1978) showed by laboratory experiment that the CL mechanisms are feasible, but could not distinguish between the two. However Faller and Perini's (1983) experiments support the CL2 theory. Leibovich and Paolucci (1980) have developed the theory to include more realistic conditions. Two- dimensional rolls are the preferred form of instability, but they do not penetrate below a characteristic depth in a stable density profile. Above this depth, disturbances of all wavelengths may occur, the smaller scale ones appearing near the surface, those of greater length growing more slowly but penetrating more deeply. In Leibovich and Paolucci's numerical model, small weak imposed perturbations cascade to larger scales until they reach the maximum allowed computationally. Cells are slightly asymmetric; the

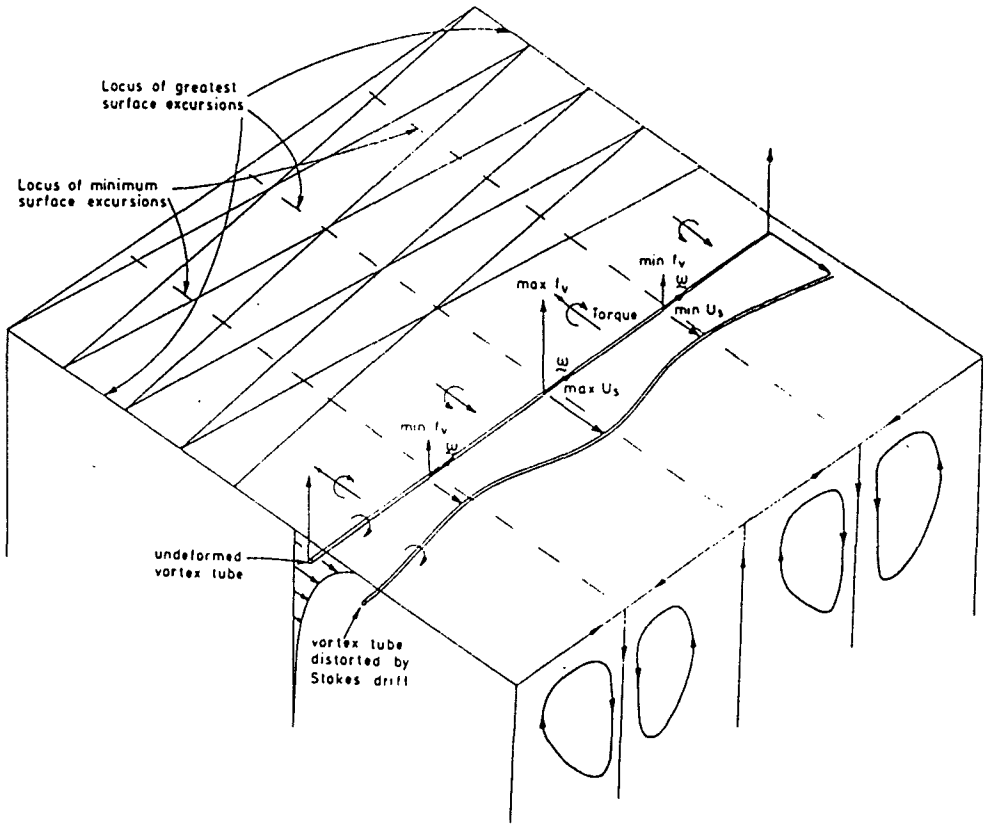

Figure 6.3 : Illustration of the direct- drive mechanism of Langmuir circulation generation. Wave crests of the assumed crossed- wave pattern are shown; the Stokes drift is higher along lines joining crest intersections. The Stokes drift variations distort the primary current and create a torque leading to overturning (from Leibovich, 1983).

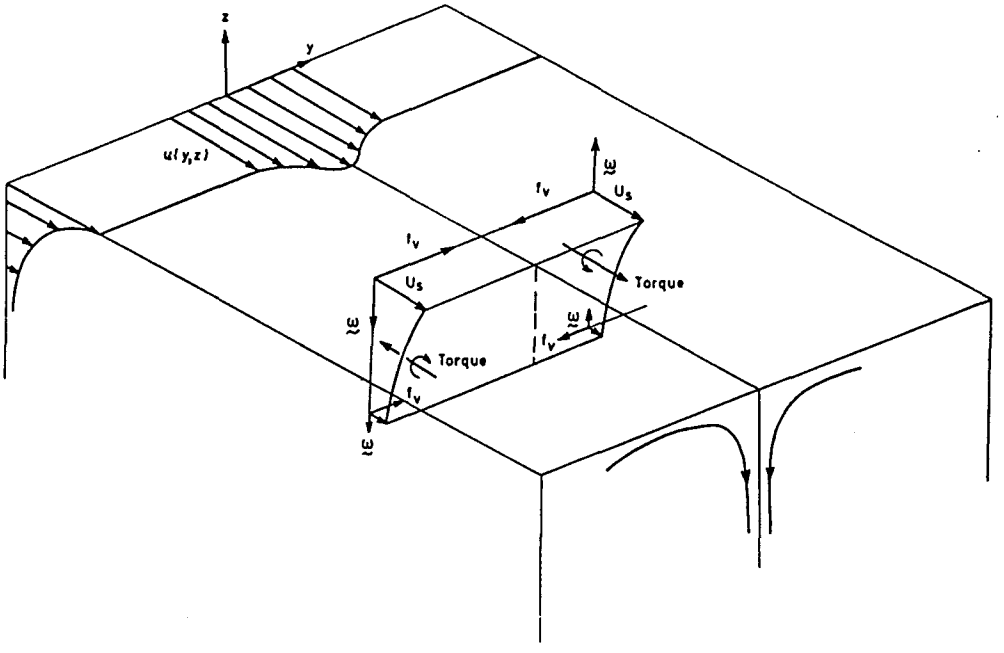

Figure 6.4 : Illustration of the CL2 or instability mechanism of Langmuir circulation generation. The Stokes drift is horizontal and decays with depth. Streamwise vorticity is induced by the Stokes drift rotation of vertical vorticity associated with spanwise variations of the current (from Leibovich, 1983).

downwind velocity is greatest at the surface and decreases with depth. Largest downwind velocities occur in the downwelling region.

Leibovich and Lele (1982) consider the generation of rolls for temperature and current profiles for which the Brunt- Vaisala (or buoyancy) frequency does not vary with depth. Interestingly, the initially linear temperature profile develops a thermocline. Figure 6.5 shows an example of the streamlines of the Langmuir circulation predicted. Leibovich and Lele also study the effects of imposing a mixed layer bounded by a thermocline, and find that the rolls cannot penetrate below the thermocline provided that "the temperature gradient is sufficiently strong and the thermocline is sufficiently thick" (Leibovich, 1983).

Recently Carnes and Ichiye (1985) have modelled Langmuir circulations using a spectral method (cf. Craik and Leibovich's finite difference scheme). Figure 6.6 shows the stream function obtained. Notice the growth of the cell with time, to a width of about 1-1.5 times the layer depth.

6.2.5 Ekman instability

Faller (1964) suggested that Langmuir circulations might be caused by instabilities of the Ekman layer. This followed earlier work (Faller, 1963) in which he describes longitudinal rolls created in the boundary layer of a large rotating tank. The laminar Ekman boundary layer produced bands in dye above a critical Reynolds number. The average angle between the bands and the surface stress on the fluid is 15°. A more- widely spaced, intermittent banded structure was also observed, which obscured the smaller bands. It was faster moving and orientated at a different angle to the surface stress; Faller considered it to be erroneous.

From Ekman instability theory, Faller (1964) predicts that:

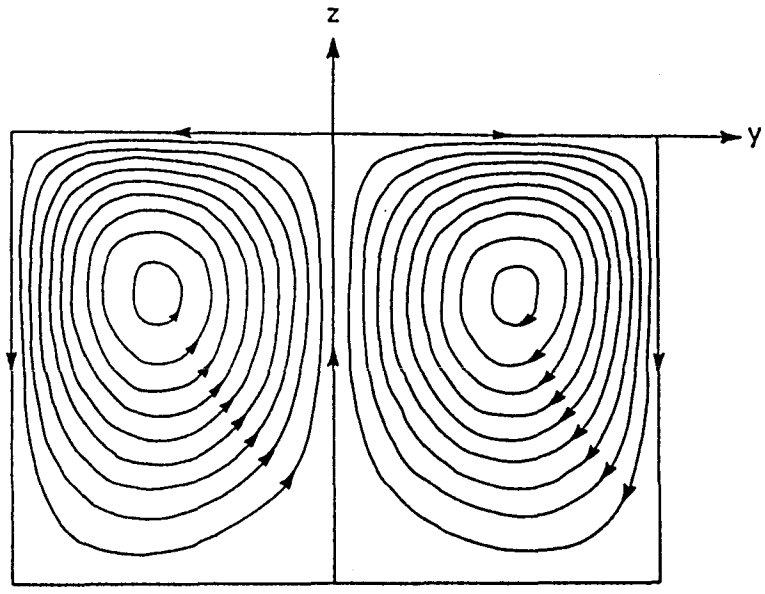

Figure 6.5 : Computed streamlines from the model of Leibovich and Lele (1982) for a Langmuir convection cell in fluid with a statically stable density stratification (from Leibovich, 1983).

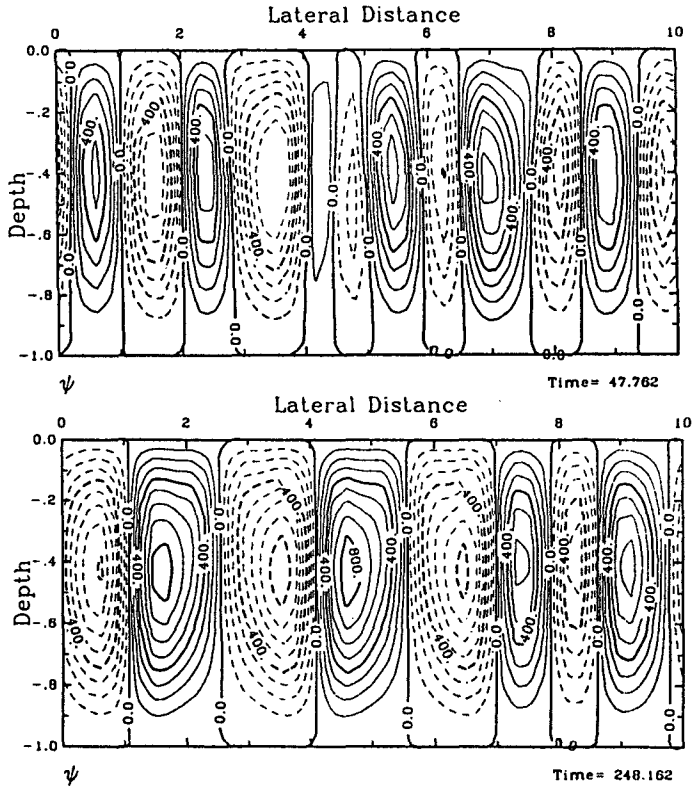

Figure 6.6 : Contours of stream function Ψ in the y- z plane. Upper plot is t=47.762, lower plot is t=248.162. The cells grow until about t=100 (approximately 1 hour). Both axes have been scaled by the mixed layer depth (from Carnes and Ichiye, 1985).

"1/ The spacing of wind rows should be dependent upon wind speed, and 2/ there should be a systematic angle between the orientation of wind rows and the direction of the wind stress on the water surface."
He uses the evidence of Faller and Woodcock (1964) to support the first requirement (see section 6.2.1). Faller also includes data collected by Sutcliffe and Baylor during their investigation of windrows (Sutcliffe et al., 1963). He finds a mean angle of 13° to the right of the wind with a standard deviation of 2°. During one experiment he notes that the wind was changing direction frequently but "the row orientation remained constant". This conflicts with the rapid reorientation observed by others (e.g. Langmuir, 1938) and points to a different generation mechanism. Faller quotes Ichiye's (1964) results of dye studies in which he also found a systematic angle of wind rows to the right of the wind. Faller concludes that the cellular motions producing the streaks must extend well into the Ekman layer, in order for the Coriolis force to sufficiently influence the flow to turn it to the right. Faller's experience is that Langmuir circulations are "nearly always present", although in the absence of surface drifters they may not always be apparent.

These ideas are placed on a sound theoretical basis by Faller and Kaylor (1966) who develop a numerical model of the flow based on instability analysis of the turbulent Ekman layer. Figure 6.7(a) shows the perturbation stream function obtained for an atmospheric boundary layer while (b) depicts the x- (downwind) component of the perturbation velocity. The rolls arise if there is an inflection point in the v-velocity profile. Lilly (1966) shows that the faster, larger- scale instability that Faller (1963) observed but thought erroneous is in fact a second type of instability, produced by a different mechanism, which he names the parallel instability. Essentially the Coriolis force releases kinetic energy from the linear shear by rotation. This

produces rolls at a lower Reynolds number (Re) but at very high Re the inflection point instability is dominant.

Faller (1971) identifies the two terms in the energy equation producing the inflection point instability and the parallel mode instability respectively. The latter includes the earth's rotation explicitly, but does not require an Ekman spiral flow, merely a shear flow $\partial u/\partial z$. If an Ekman spiral is present, both instabilities may exist together. Faller notes that other terms give thermal convection and surface wave effects (such as the Craik- Leibovich theory). He finds a non- linear transfer of energy from small to larger scales (cf. three- dimensional turbulence in which the energy cascade is from large to small turbulence). Remember that Leibovich and Paolucci (1980) also found this effect (section 6.2.4).

Welander (1963) points out several problems with Faller's Ekman instability hypothesis. His own measurements find the angle between the rows and the wind to be less than 2°. He suggests that the systematic deviation found by Faller is due to an interaction between the rolls (however produced) and the Ekman spiral flow.

Welander objects that Ekman layer instabilities cannot explain the rapid reorientation of the wind rows after a shift in wind direction (see section 6.2.1), nor the quick generation of rows by the onset of a strong wind. Faller's mechanism gives time scales for cell growth of several hours. Ekman (1905) showed that about a day is needed to fully develop the Ekman flow. Welander claims that a surface- based mechanism is therefore more likely. He suggests that this would produce an asymmetric cell, as implied by many observations (e.g. Langmuir,1938; Maratos, 1971) whereas the shear instability, acting throughout the layer, would tend to yield a more symmetric cell.

Gammelsrod (1975) has modified Lilly's (1966) parallel instability theory by including a strong shear denoted Υ, and the time scale for

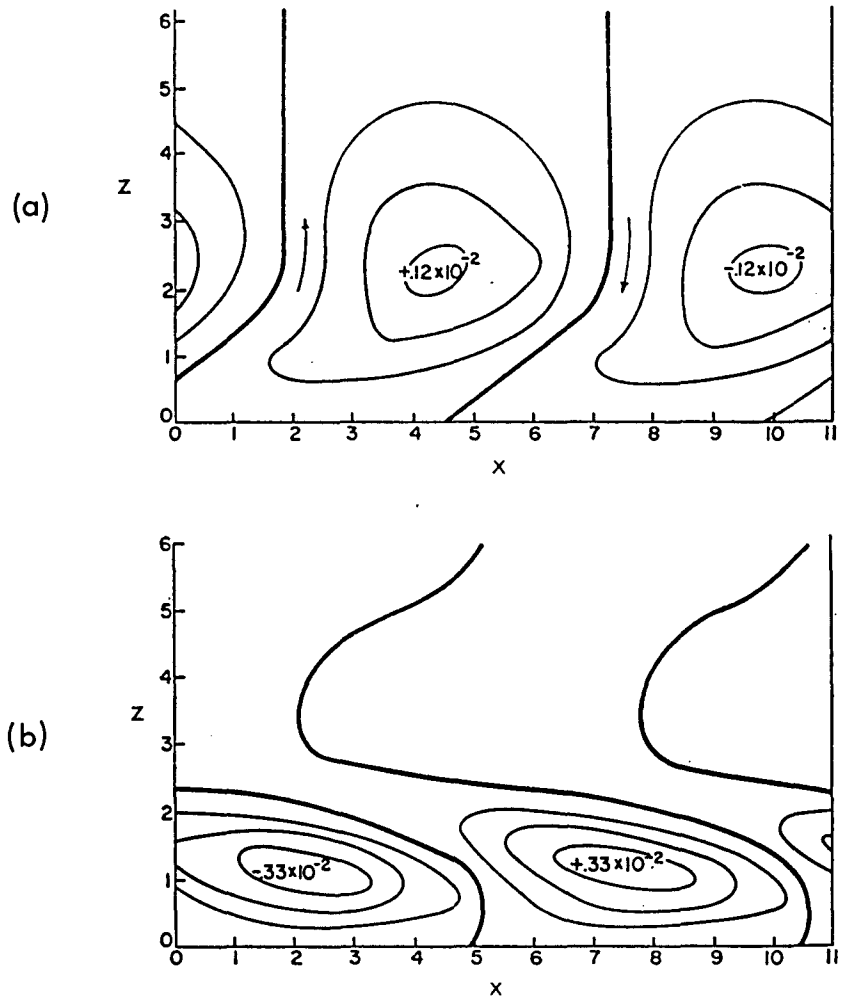

Figure 6.7 : Patterns of flow predicted for a small-amplitude unstable mode at a Reynolds number of 200, at an angle of 14° to the wind. The wind is directed out of the page. (a) The perturbation stream function. Note the large slope of the streamlines near the land surface. (b) The perturbation x- component of flow, u. Both diagrams are drawn looking upwind and are for the atmospheric case. Axes are non- dimensionalised by the Ekman depth (from Faller and Kaylor, 1966).

cell growth becomes $(\Upsilon f)^{-\frac{1}{2}}$ instead of f^{-1} (Pollard, 1977). Thus for a large enough shear, cell growth rates can easily account for the observed rapid generation, which takes place on a time scale of minutes. A mixed layer is prescribed which is shallow compared to the Ekman depth, therefore the mixed layer current is essentially uniformly sheared and parallel to the wind. The Coriolis acceleration is assumed balanced by friction. Unlike Lilly's analysis, Gammelsrod finds that the parallel instability does not vanish at high Reynolds number (i.e. in the inviscid limit). He begins with a perturbation velocity which advects the mean shear vertically. This will increase the downwind perturbation velocity, which is rotated by the Coriolis force into the y- direction. Hence downwind vorticity is produced.

There are several objections to Gammelsrod's theory. He predicts that downwind velocities are zero at the surface, being maximum at the depths at which the vertical velocities are greatest (Pollard, 1977). All the observations of dye and surface drifters (e.g. Langmuir, 1938; Assaf et al., 1971; Ichiye, 1967) show a substantial downwind surface velocity in the convergence zones (see section 6.2.1). Pollard concedes that such velocities could be added to the theory by including the non- linear interaction between a slightly non- uniform mean shear and crosswind perturbation velocities. However he also points out that Gammelsrod's cell boundaries are not vertical but slanted (as indeed they are in Faller and Kaylor, 1966). The only evidence of slanting cell boundaries is that of Thorpe and Hall (1982) (figure 6.8), showing temperature anomalies slanting with distance across the windrows. By inverting figure 6.7(a) it can be seen that the circulation slants the same way as found by Thorpe and Hall. Pollard's main criticism is that the friction force which initially balanced the Coriolis force should also be advected vertically by the perturbation velocity. The friction arises from small- scale turbulence via the Reynolds stresses which

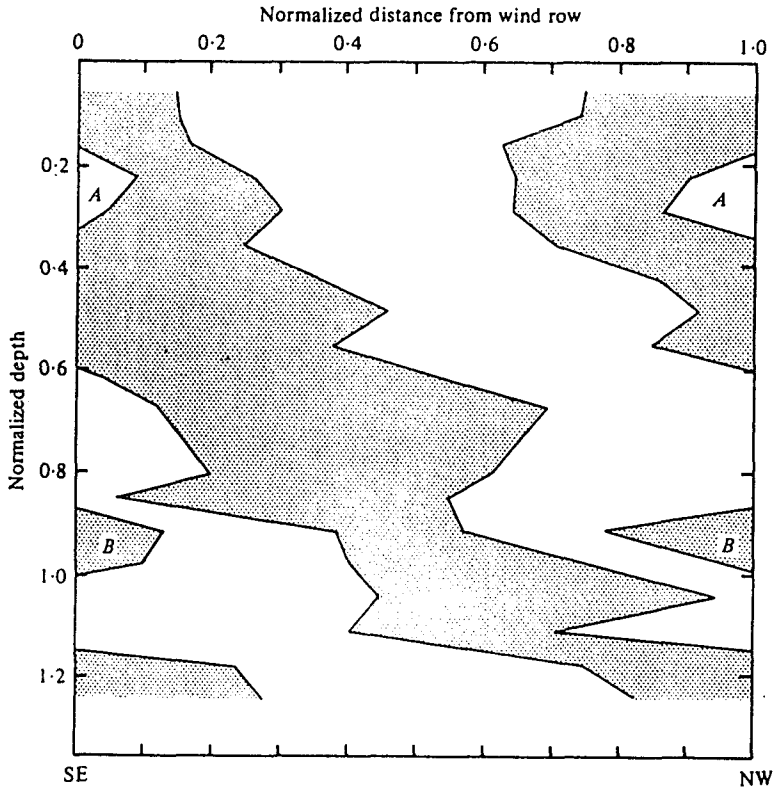

Figure 6.8 : Regions of average positive and negative temperature anomalies in a section between windrows, looking upwind. The stippled areas have positive anomalies. The mean distance between neighbouring rows has been used to normalise the depth and the distance from the row (9.45m and 8.9m for the data included here). The mixing layer has a normalised depth of at least 1.3 (from Thorpe and Hall, 1982).

should continue to balance the Coriolis force. Leibovich (1983) states other objections to Gammelsrod's theory.

Scott et al. (1969) observed two types of roll, a long- lasting, large one and a short- lived, smaller one (see section 6.2.1). Gammelsrod proposes that shear instability (producing the large rolls) is important only for steady winds, and that a surface mechanism dominates in gusty winds, producing the smaller rolls. Both may exist together. The observations of Assaf et al. (1971) also support this idea (section 6.2.1), since their largest cells do not occur in conjunction with the Ekman spiral. Small cells exist with an Ekman flow, and Assaf et al. suggest that these are wave- generated.

Faller discusses Assaf et al.'s observations in his review (Faller, 1971). He does not dispute that small Langmuir cells are generated by a wave mechanism. Energy may be fed from these into medium- sized "better organised rolls". The largest cells are formed either by a "further energy cascade to the large observed scales" or by Ekman instability. Faller's numerical model shows that a combination of the inflection point and parallel instabilities is applicable to the large cell sizes. He finds that "all but a vestige of the spiral shear flow" disappears once the cells are set up. Figure 6.9 shows the stream function at time steps 300 (a) and 500 (b) (about one hour apart), while (c) depicts the perturbation of u from the average flow along the axes of the cells, at time step 500. Notice that the cell is indeed more symmetric in shape than the Craik- Leibovich theory predicts (figure 6.5). Faller's model predicts a slow downwind surface current in upwelling zones, and a faster downwind current where downwelling occurs. Vertical velocities are largest at about half the depth of the cell. He comments that this is not consistent with the large velocities measured just below the surface by Scott et al. (1969) and concludes that the latter are probably wave- driven circulations.

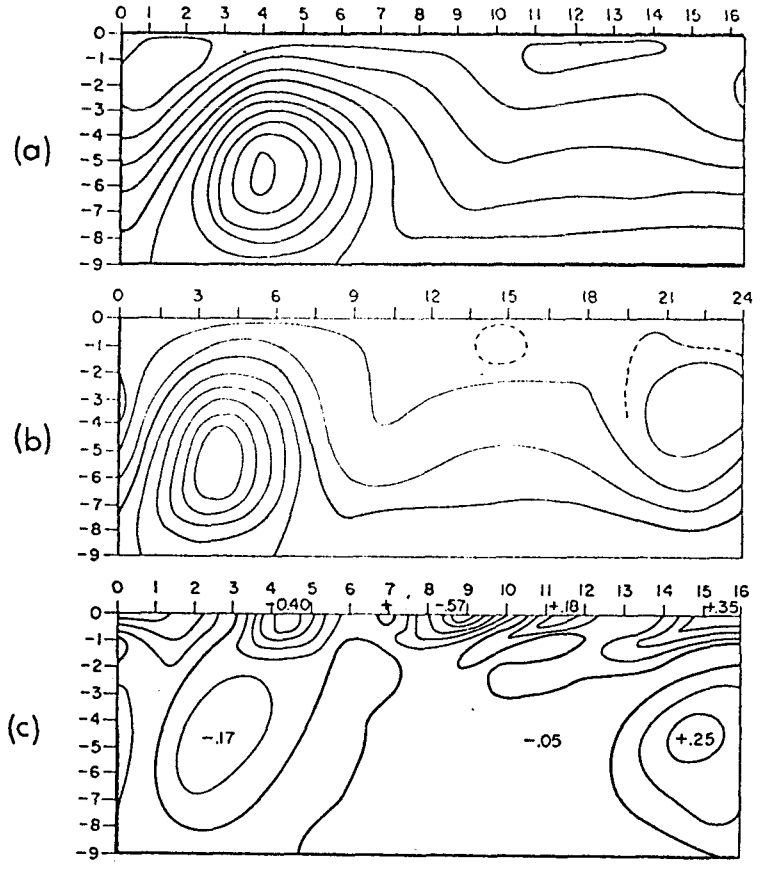

Figure 6.9 : Patterns from the numerical computation of unstable Ekman flow. (a) Stream function Ψ in a vertical cross- section at time step 300. The contour interval is 0.10. (b) Stream function at time step 500. (c) The pattern of u, perturbations from the average flow along the axes of the cells, at time step 500. Numbers indicate maxima and minima as fractions of the undisturbed surface Ekman spiral flow. The wind is directed outward from the page (from Faller, 1971).

Since Faller's 1971 paper, interest has been focussed on Ekman instabilities in the atmosphere, rather than the ocean, and also upon theoretical instability studies. These are reviewed by Brown (1980). An experimental study of atmospheric rolls was carried out by LeMone (1973, 1976). Measured angles between the rolls and the geostrophic flow (cf. the wind for the ocean) agree with the inflection point instability theory. However, predicted flow magnitudes are always too low, and LeMone proposes that buoyancy effects provide the extra energy (10-40%).

In general, inertial, thermal, Coriolis and viscous forces should be included (Brown and Lee, 1972) in the modelling of atmospheric roll vortices. Parallel mode instabilities are damped by stable stratification more than inflectional ones. Brown (1972) shows that with no stratification, the rolls are orientated approximately parallel to the mean flow, but as stratification becomes stable, they veer up to 45° to the mean flow. Brown (1980) obtains roll widths of two to four times the layer depth.

Both Faller (1971) and Brown (1980) discuss whether the assumption of an eddy viscosity coefficient is valid. The characteristic scale of turbulence in the boundary layer is usually much smaller than the scale of the rolls so an eddy viscous analogy is justified. Faller (1971) points out that his results assume a perfect Ekman spiral. If the eddy viscosity is not constant with depth (which will usually be the case since the turbulence is not uniformly distributed with depth), the Ekman spiral, and hence the roll structure, may be altered slightly. The basic flow will however remain the same.

Theoretical Ekman instabilities in the ocean have been studied by Iooss et al. (1978) and Spooner (1983). Iooss et al. run a numerical model for both the solid boundary case (atmosphere) and a free slip boundary (ocean). The oceanic results are briefly compared with the

experimental data of Faller and Kaylor (1967) and agreement is "satisfactory".

Spooner's paper deals specifically with the oceanic case. He considers two situations, a homogeneous profile and a two- layer problem. At supercritical Reynolds numbers, two maxima in growth rate occur in wavenumber space (cf. the solid boundary case with only one maximum), one for each type of instability. These maxima occur at wavenumbers different to the rigid boundary case. This means that oceanic rolls do not have the same angles to the mean flow as their atmospheric counterparts. At higher Reynolds numbers, one would expect the inflection point instability to dominate and the parallel one to vanish. Spooner finds that the two modes "fuse" at larger Re to produce one instability.

Spooner discovers that the two- layer case (two layers of different densities, no Ekman flow in the lower layer) is more stable than the homogeneous case, since the density interface damps the instabilities. When the depth of the upper layer, h, is less than twice the Ekman layer depth β ($\beta = (2\nu/f)^{\frac{1}{2}}$), both modes are stable. Spooner comments that "this would seem to make them unlikely candidates as the stirring agents which act to deepen a preexisting mixed layer". For h greater than 6β, the results for the homogeneous case are regained.

6.2.6 Discussion of Langmuir circulations

There are thus two possible ways of creating longitudinal roll vortices in the ocean. Small- scale Langmuir circulations are almost certainly caused by the interaction of a surface wave field with a sheared current. Large- scale rolls might be caused either by a wave-current interaction or the inherent instability of the Ekman sheared layer. Many oceanographers (e.g. Leibovich, 1983) use the term "Langmuir circulation" to describe only wave- generated rolls, since

they believe that all the observed streaks can be explained by a cascade of energy from small to large scale circulations. Some of the observations (e.g. Assaf et al., 1971) do however imply that the Ekman instability is a likely driving force and one cannot ignore this mechanism when considering large scale rolls, such as Langmuir's original observations.

Assuming that both mechanisms exist, it is useful to compare the different cell characteristics predicted by both theories. Both would imply that the cell size is in some way limited by the depth of the mixed layer, since the thermocline inhibits further growth. Unfortunately Iooss et al. (1978) and Spooner (1983) do not try to relate their results to the actual flow expected in an oceanic mixed layer. Kaylor and Faller (1972) describe the predicted flow but only for the rigid boundary case. It seems necessary to return to Faller (1971) to obtain a picture of the oceanic roll vortex predicted by Ekman instability (figure 6.9). The cell width is of the same order as the cell depth. Downwelling and upwelling velocities are of similar magnitude, and maxima in both are at the respective edges of the cell. The circulation is therefore largely symmetric as a body force mechanism would imply. The downwind velocity u varies in the crosswind direction, maxima of each sign occurring at the downwelling and upwelling regions. Maximum downwind velocities occur, not at the surface, but near half the cell depth. As Pollard (1977) comments when referring to Gammelsrod's (1975) theory, surface downwind velocities might be enhanced by the non- linear interaction of a slightly non-uniform mean shear and crosswind perturbation velocity. Ekman instabilities produce slightly slanting cell boundaries.

The Craik- Leibovich theories predict a different picture of cell structure. Boundaries are vertical, and the circulation is asymmetric both in the vertical z and the horizontal y directions. However the

interaction of an Ekman- like crosswind flow with a wave- generated roll vortex might also create slanted cell boundaries (Thorpe and Hall, 1982). Downwelling velocities are greater than upwelling ones. The downwind velocity in the convergence zones is greatest at the surface and decreases with depth. The streamlines produced by Leibovich and Paolucci (1980) suggest a cell width to cell depth ratio of between 0.3 and 1.0, but this seems to vary considerably and depend on the computational domain. Carnes and Ichiye (1985) (figure 6.6) show rolls growing up to 1.5 times the layer depth. Leibovich (1983) refers to work by Leibovich and Lele (1982) in which a thermocline is introduced as the lower bound. However it has not been possible to obtain a copy of this work.

The CL theories assume the rolls to be aligned with the surface wave field, although as Welander (1963) points out, the Ekman spiral will tend to rotate the cells to the right. The angle λ at which maximum Ekman roll instability growth rate occurs is variable (Leibovich and Lele, 1985). For the inviscid limit (infinite Reynolds number) λ is 23°, but at Reynolds numbers just above critical, λ is about 6°. Oceanic Reynolds numbers are likely to be large, of the order of thousands. The CL theory will allow rolls to reorientate themselves quickly in response to a change in wind direction. The Ekman instability is expected to maintain a much more stable orientation, changing only on the order of hours to days. As discussed by Leibovich and Paolucci (1980), the large- scale, stable Langmuir circulations, to which energy eventually cascades, will be affected by Coriolis even if they are wave- generated. The CL model is valid only up to about a quarter to a half of a pendulum day (one pendulum day = twice the inertial period) after which Coriolis accelerations must be taken into account. Leibovich and Paolucci discuss whether inflection points in the velocity profiles could produce an extra instability as

well as the Craik- Leibovich one. It would seem likely that in any given oceanic situation, both mechanisms will be at work, each to a greater or lesser degree.

If a given set of observed rolls are to be identified as caused by Ekman instability, one would require the following conditions:

1/ little or no observable Ekman spiral.

2/ cells aligned slightly to the right of the wind (0-30°).

3/ long lifetime (days) with changes of orientation or spacing occurring over hours or longer.

4/ approximately symmetrical cells with downwelling velocities of the same order as upwelling.

Similarly for a wave- generated Langmuir circulation, one would require:

1/ possibly some Ekman spiral (although these are very seldom observed anyway).

2/ cells aligned parallel to or slightly to the right of the dominant wave field.

3/ rapid changes of row orientation when the wind changes direction.

4/ some variation in wave height in and out of windrows.

5/ an asymmetric cell with a narrow downwelling jet.

The results of Assaf et al. (1971) provide the best- documented observations of large- scale Langmuir circulations. It would appear that the largest cells they observe are Ekman instabilities, since the Ekman spiral did not co- exist with the rolls. The mixed layer depth was 200m, and the streaks were about 280m apart, giving a cell width of 140m. Thus both observations and theories suggest that the largest cell widths are of the order of the mixed layer depth. More precise numerical simulations of a real oceanographic situation are required for both theories, as well as comprehensive oceanic observations of vertical and horizontal velocities, cell spacing, temperature profiles,

persistence and growth of Langmuir circulations.

The more recent measurements of Weller et al. (1985) are interesting. The downwelling is much more energetic than the upwelling, indicating asymmetry in the cell, and that the CL mechanism is the appropriate one. However, maximum downwind velocities are observed at half the depth of the cell in the downwelling regions, with small downwind velocities near the surface. This would suggest the Ekman instability mechanism. More information is clearly required, and it is hoped that further data from these measurements will become available.

It is a mistake to think of Langmuir circulations as a fixed, steady- state structure. The evidence suggests a constantly changing flow, with cells growing until bounded by the thermocline, and smaller cells continually being formed. The rolls will interact with, and be advected by, the mean flow, and will always be altering due to changing wind or wave fields.

6.2.7 Implications of the existence of Langmuir circulations

Such circulations will affect the mixing of heat and momentum in the mixed layer. It is both observed (Myer, 1971) and numerically predicted (Leibovich and Paolucci, 1980) that heat is advected downwards at the convergence zones. Weller et al. (1985) observed temperature anomalies of about 15mK in downwelling zones. When the near- surface temperatures were warmer than the interior of the mixed layer (midday) then positive temperature anomalies were detected in downwelling regions. Similarly at night, negative temperature anomalies were observed in downwelling zones. As pointed out by Faller (1971), the effective eddy viscosity is greatly increased by rolls. Longitudinal rolls will also affect the drifting of buoys. The crosswind currents are sufficient to draw material into the convergence zones. Weller et al. (1985) suggest that FLIP spends more time in the

convergence zones than the divergence zones.

Thorpe (1986) points out that Langmuir circulations may be the explanation behind the large downwind current in the experiments of Churchill and Csanady (1983). They found that near- surface drifters travelled downwind much faster than would have been implied by the light wind observed. They suggested that the Stokes drift of the swell waves might be the cause. Thorpe cautions that Langmuir circulations will also affect the motion of such upper ocean drifters.

McNally and White (1985) observe freely drifting buoys, drogued at various depths, having a large downwind velocity when they are in the mixed layer. The crosswind velocity component can be accounted for by considering a simple Ekman slab model (Davis et al., 1981) but the downwind velocity is larger than the windage, calculated from wind stress and drag coefficient, can predict. This 'model' ignores any downwind current caused by a two- dimensional wind stress field since all wind- driven current is assumed to be directed to the right of the wind. The buoys move in a direction about 30° to the right of the wind. By correlating the downwind velocity with the wind stress, it is found that the downwind current is wind- driven but lags the wind by 6 to 12 hours. McNally and White comment that "the large downwind residual velocity remains as yet unexplained". It is possible that neighbouring storms created downwind currents (Price, 1983). These observations might however imply that the buoys drifted into the convergence zone of a Langmuir circulation, since this would produce an anomalously large downwind velocity only while the buoy was in the mixed layer. It is known (Saunders, personal communication) that drifting buoys during JASIN exhibited a similar unexplained large downwind displacement. It might seem unlikely that a longitudinal roll structure would exist in the upper ocean for several months, but one must remember that the drifting buoys might well drift from one

convergence zone to another as the rolls evolve, grow, merge or die away.

Dyke and Barstow (1983) discuss the implications of Langmuir circulations (of all scales). They comment that whereas lake and shallow water scientists accept the importance of such rolls, offshore oceanographers are often sceptical. They give three possible reasons for this. Firstly, there is less biological activity or sediment to reveal the streaks. Secondly, windrows are harder to observe at sea due to waves and the poor fields of view from a boat. Finally, Langmuir circulations are "altogether larger" than inshore, so the streaks are further apart and may not be recognised as a coherent flow. However they note that "there have never been occasions when windrows have been looked for in the North Sea that they have not been found".

6.3 Fronts

6.3.1 Introduction

Another mechanism for local downwelling in the upper ocean is frontal activity. A comprehensive introduction to fronts is given by Roden (1976), who defines fronts as "regions of intensified motion, sharp gradients, decreased stability and increased turbulence and convection". Fronts have been observed in all oceans on scales from "local to planetary". They may move, meander, intensify or decay if the large scale oceanic or atmospheric flow alters, and they usually have intermittent regions of strong and weak gradients (see e.g. Voorhis and Hersey (1964) for observations of fronts in the Sargasso Sea, and Levine and White (1972) in the Mediterranean Sea). The generation time scale is a few days, while dissipation of a front may take months.

Fronts are associated with a surface convergence and may be revealed by slicks, foam or a streak of biological activity. The surface outcrop of a temperature front can be detected by colour and

temperature sensors from a satellite (Legeckis, 1978). Atmospheric fronts are always highly baroclinic, since temperature and density gradients occur together. In the ocean, temperature, salinity and density fronts need not appear in the same place. If temperature and salinity fronts exist together but have nearly equal and opposite effects on density, the density front will be weak or non- existent. In this case there is little baroclinicity and usually no jet stream. The front is marked by the interleaving of water masses along surfaces of constant density. The baroclinic jet will develop where there is a density gradient "of some substantial vertical extent" (Roden, 1976). Where the temperature and salinity fronts are not vertical but slanted, the jet will occur "some distance from the position of the surface front". Voorhis and Hersey (1964) define a "thermal front" as one with a gradient of at least 1°C in 10km at the surface.

Figure 6.10 shows a simplified (but often assumed) picture of a temperature front. The slope of the interface between the two water masses is of the order of 1 in 300 (Woods, 1977). Large amplitude waves with wavelengths of the order of 10km have been observed on the interface. Horizontal gradients are usually strongest in or above the pycnocline. When the pycnocline is particularly substantial, the front in the upper layer has been observed to move away up to 300km from the lower one, due to the action of strong, steady winds. Below the pycnocline, temperature, salinity and density fronts usually occur together. This is because the processes of radiative heat transfer, evaporation and precipitation are absent in the lower ocean. It is possible for a front to be entirely internal and not to be detected at the surface. These fronts are due to differential vertical motion, caused by bottom friction or a rapidly changing wind stress curl. In mid- ocean, where the baroclinic flow is weak, fronts are usually correlated to the wind stress field (Roden, 1976).

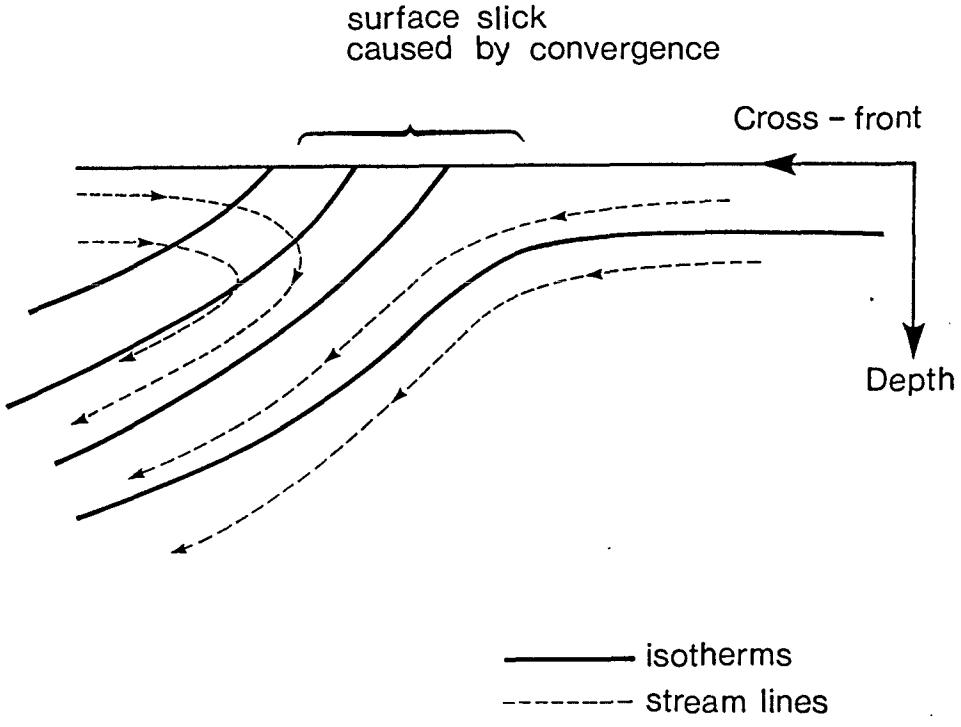

Figure 6.10 : A simplified diagram of a front and its mean flow.

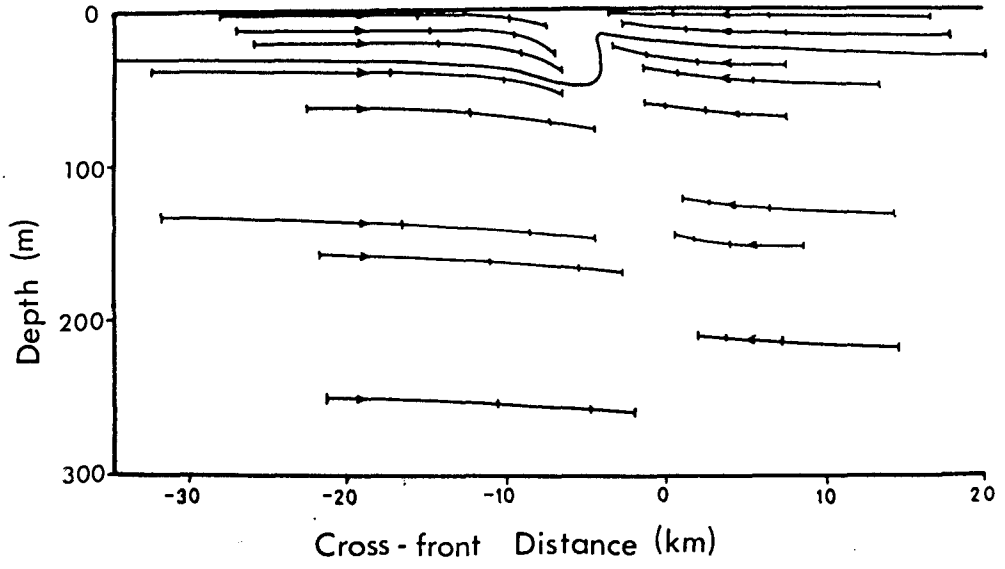

Figure 6.11 : Trajectories of selected fluid particles in the front. The positions of the particles at 19.25 hours, 38.5 hours and 77.0 hours are marked by ticks. The position of the mixed layer thermocline boundary at 77.0 hours is shown (from O'Brien et al., 1977).

There are several different types of front, discussed by Roden (1976). It may be difficult in the open ocean to separate out the forcing of fronts by several mechanisms at once. Not all types of front are relevant to our data, and these will only be briefly mentioned:

1/ fronts due to strong boundary currents, e.g. the Kuroshio and Gulf Stream fronts. These are permanent, large- scale fronts, although they may move, intensify, meander etc.

2/ fronts associated with convergence of Ekman transports, due to a strong positive wind stress shear, e.g. Roden (1975).

3/ fronts associated with the convergence of surface energy fluxes. These depend on the configuration of the surface heat and salt flux fields. They often occur at boundaries marking changes in cloud cover, wind or precipitation. They are shallow, normally less than 50m.

4/ multiple fronts attributed to baroclinic Rossby waves.

Gill (1982) lists other causes of fronts:

5/ coastal upwelling or flow over other features such as shelf breaks.

6/ a water mass boundary, such as where a river flows into the sea.

7/ convergent mean flow (MacVean and Woods, 1980).

8/ gradients in rates of stirring, for example by tides in shallow seas and estuaries (James, 1978).

The prediction of fronts is not easy. Roden (1976) states the need for meteorological data on scales of not more than a 1^{o} latitude- longitude grid, since he believes oceanic fronts to be of dimensions 50-500km. A knowledge of the subsurface flows is also necessary.

Our understanding of the dynamics and energetics of open ocean fronts is still fragmentary. Roden (1984) observes that frontal zones tend to have widths of the order of 100km, while the fronts themselves are O(10km). The fronts are "convoluted with meander wavelength of a few hundred kilometres". The predominant scales of flow are 1 to 10

baroclinic Rossby radii, and these are "mesoscale fronts". Shapiro (1981) believes that small- scale fronts are uncommon in the open ocean but very likely in shallow seas or estuaries.

6.3.2 Velocity structure of fronts

Many observers provide evidence of surface convergence in a front (e.g. Voorhis, 1969). Whales and other large mammals are found to congregate in fronts, where the plankton are more plentiful. Some suggest this as evidence of "powerful upwelling" (Rao and Murty, 1973) since nutrients would be brought to the surface and attract biological activity. It seems equally likely that the organisms are swept into fronts by the surface convergence. Roden (1975) finds that the temperature front and confluence may not be coincident. This arises when the motion is sluggish, and heating or cooling is strong and localised, so that the temperature contrast in the convergence zone is eliminated.

On all scales of front, river scale, eddy scale or large scale, downwelling is found beneath the convergence (Garvine and Monk, 1974). The Ekman convergence model of Cushman- Roisin (1981) shows however that a frontal confluence is possible with no downwelling. Unfortunately there does not seem to have been any direct measurement of vertical velocity in fronts. Garvine (1974) models velocities of a small- scale, established density front assuming a structure as in figure 6.10. He finds that the maximum downwelling velocity occurs just below the front. For the intense river plume front with strong surface convergence, observed by Garvine and Monk (1974), he obtains a maximum velocity of the order of 16-18cm/s. The model is generalised by Garvine (1979) to apply to all scales of front, by including the Coriolis effect. A strong downwelling is predicted, coincident with the surface convergence. Shapiro (1981) develops a similar model that is not stationary in time and includes the effect of the wind.

The model described by O'Brien et al. (1977) and later developed by MacVean and Woods (1980) simulates the sharpening of a front due to convergence of the mean flow. The model ocean is 500m deep and the mixed layer is initially 30m deep. An intense frontal jet forms with velocities up to 0.8m/s, and a broad, slow return flow at depth. Figure 6.11 shows the particle trajectories associated with this front. The solid line depicts the mixed layer depth as it drops about 30-40m across the front. Particles are downwelling on the left, where the less dense water is situated, and a small upwelling is predicted on the right. The magnitude of the vertical velocity increases with time, the upwelling reaching 29cm/hour and the downwelling 66cm/hour after 77 hours.

James (1978) describes a two- dimensional model of a shallow sea front caused by spatial variations in tidal mixing. His study was prompted by the observations by Savidge (1976) of the chlorophyll distribution near fronts in the Irish and Celtic seas. Savidge found convergence at the front, together with upwelling, bringing nutrients to the surface layers. The predictions of James' model are summarised in figure 6.12. Figure 6.12(a) shows the initial density structure based on observation, while (b) illustrates the v velocity with frontal jet. Figure 6.12(c) depicts the stream function, and we see that the upwelling velocity is much greater than the downwelling. The maximum vertical velocity is an upwelling of about 4cm/s. The upwelling region, on the well- mixed side of the front, is narrower than the downwelling, on the stratified side. James' circulation is illustrated in figure 6.13 from Simpson et al. (1978). The regions of convergence and divergence are marked together with the isopycnals. Simpson et al. explain that if friction is ignored, and velocities are assumed to be balanced by geostrophy, the shallow sea frontal model (Simpson, 1976) predicts a high velocity frontal jet up to 30cm/s. If friction is

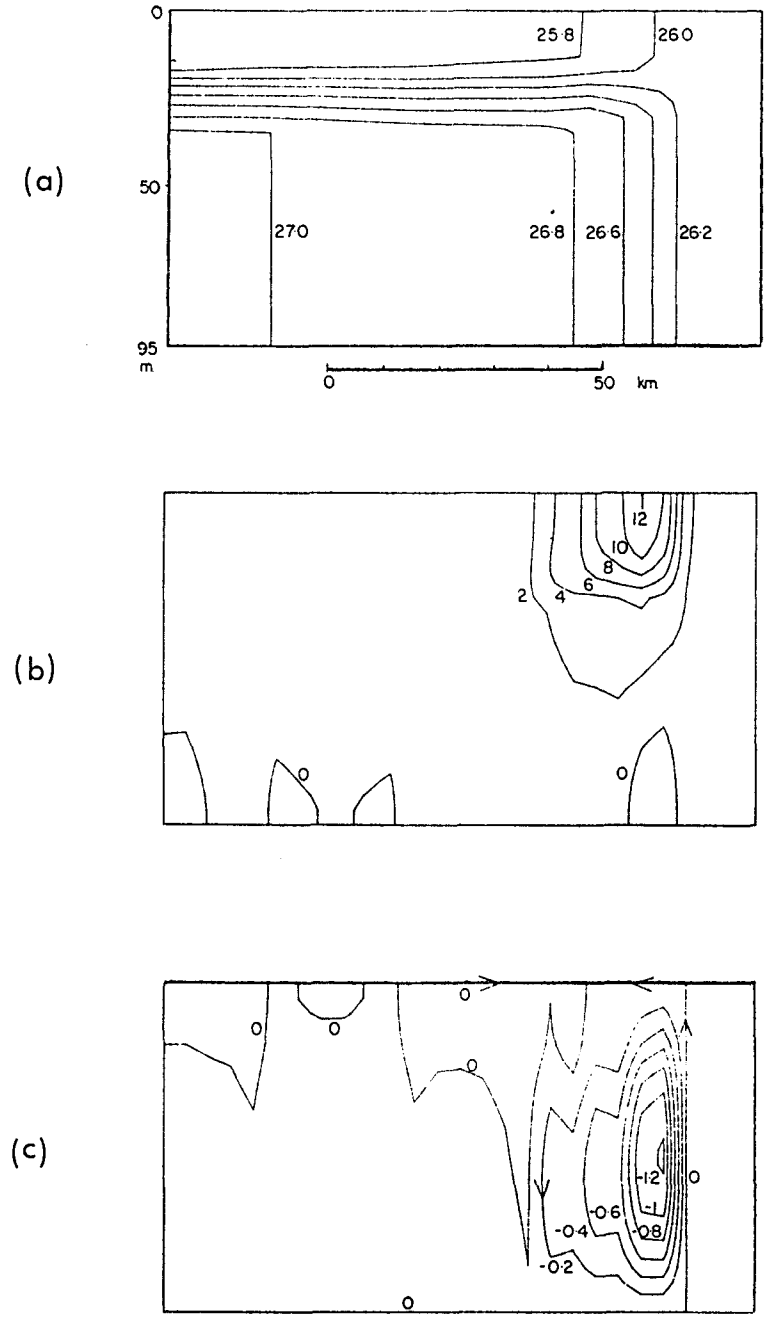

Figure 6.12 : (a) Assumed density section showing contours of potential density minus 1000kg/m^3. (b) Calculated v- velocity along the line of the front, in cm/s. (c) Calculated stream function in m^{2}s^{-1} (from James, 1978).

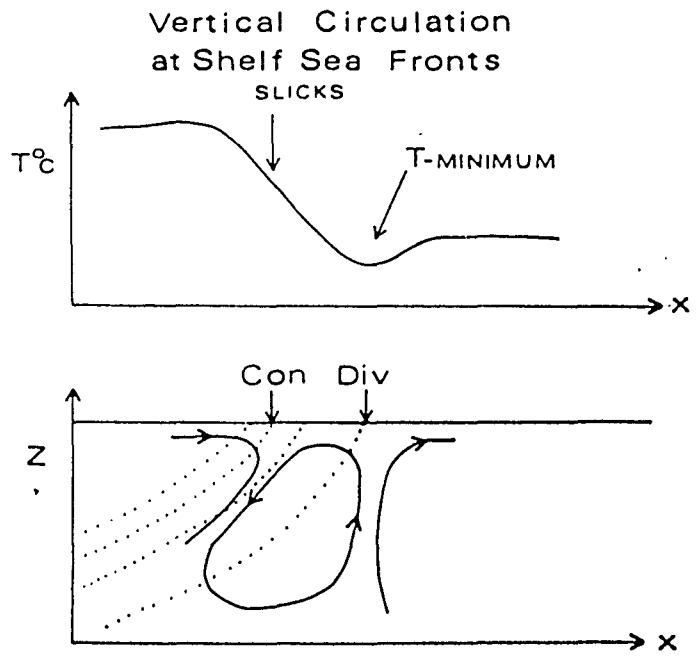

Figure 6.13 : Schematic vertical circulation suggested by observations of convergence and divergence at fronts. The dotted lines represent isopycnals (from Simpson et al., 1978).

included, as in James (1978), then a similar flow is obtained parallel to the front, but also predicted is a circulation in the vertical plane transverse to the front, due to frictional damping of the baroclinic jet (figure 6.13). Although these fronts have been observed only in shallow shelf seas, it is useful to study their characteristics. These fronts are at least of the required small scale, and it is possible that the dynamics are similar to small- scale open ocean fronts.

Simpson et al. (1978) describe experiments in the U.K. shelf seas with drogued buoys. In general, the buoys did not travel in the geostrophic flow parallel to the tidally- forced fronts. It appears that the flow is not organised in a quasi- two- dimensional pattern. They suggest that the drogue motion is due to meanders in the front. Satellite photographs do reveal changes in the front position from day to day. Since the horizontal flows are so complex, Simpson et al. do not expect to find a simple two- dimensional circulation such as that of figure 6.13. They predict that the vertical velocities would be less than 1mm/s and therefore hard to measure. Their temperature cross- sections and observations of the surface slick at the front do however give a qualitative agreement with James' (1978) model. The surface accumulation of weed and jellyfish coincides with the region of maximum temperature gradient. A minimum in observed sea surface temperature just before crossing the front implies upwelling. Woods et al. (1977) suggest that meandering flows themselves force localised regions of strong up- and downwelling along a front. Simpson et al. therefore caution that these may predominate over any steady state motions such as James predicts.

There are very few measurements of currents in fronts. Trump et al. (1985) describe their observations of a near surface front using a towed thermistor chain and a doppler shear profiler. The temperature gradient in the front is about 4°C in 30km at a depth of 40m. They

point out that "there is the suggestion of downwelling, shown by the dips in the isotherms along the top of the frontal interface". A strong vertical shear zone is observed, where the velocity gradient is 50cm/s in 40m. Trump et al. calculate that these velocities would imply a convergence at the front of approximately 16cm/s. Assuming that this convergence applies over a depth of 100m, and downwelling occurs over a scale of 8km, they show that the downwelling velocity would be about 0.2cm/s. Unfortunately they were unable to measure vertical velocities directly.

6.3.3 Discussion of fronts

It has been seen that fronts are frequently associated with convergence and downwelling zones. They can occur at all scales from river plumes to large- scale Gulf Stream meanders. They can be very persistent, since sharpness is maintained and cross- frontal mixing inhibited. Voorhis (1969) observed fronts to last for several months. However, Simpson et al. (1978) note that satellite photographs show some fronts to be stable while others are "variable and convoluted".

One might expect freely drifting buoys to converge into the frontal jet and experience downwelling. However, the situation does not appear that simple. Weller (1982) found during JASIN that all his freely drifting vertical current meters measured an upwelling velocity, some as large as 20m/day, with a mean upwelling of 5m/day. This is much larger than the calculated Ekman pumping due to the observed wind stress curl. All the buoys were below the mixed layer, so maybe buoys in the mixed layer would behave differently.

Kurasawa et al. (1983) study the heat budget at Ocean Weather Station T (29°N, 135°E), and deduce that, for this area in the Japan Sea, heat content is dominated by heat convergence on time scales of a few days to a month. Local air- sea interaction is a lesser effect. The mechanism of heat convergence is suggested to be that "small water

masses of different temperature bounded by fronts were advected through the points of sampling". These fronts have widths of about 10-20km. The Weather Station is approximately 200km from the shelf edge, and the water depth is more than 4000m, so this is not a shallow, coastal region. The spar buoy described in chapter 2 was freely drifting, so advection relative to the spar is negligible, as shown in chapter 4. However, Kurasawa et al.'s observations demonstrate that small scale fronts may exist in the open ocean.

In the open ocean, fronts usually appear to be large or medium scale structures. In the absence of shallow water processes such as differential tidal mixing (James, 1978), it seems likely that open ocean fronts are most often caused by a varying wind stress field producing Ekman convergence (Roden, 1975) or from spatial variations in the heat flux distribution. Both form fronts with widths of the order of tens of kilometres.

6.4 Conclusions

This chapter has surveyed mechanisms for downwelling regions in the ocean, such as might explain the anomalously large heating signal observed at the drifting spar buoy (chapter 4). Langmuir circulations occur on a scale from several metres to several hundred metres, and may be caused by wave- current interactions or by instabilities of the Ekman layer, or a combination of both. Fronts appear to be a larger scale process in the open ocean, with convergence occurring on scales larger than the Rossby radius of deformation (approximately 10km at mid- latitudes). Observations of Langmuir circulations have revealed downwelling velocities up to 20cm/s (Weller et al., 1985), while James (1978) predicts downwelling velocities in his tidally- forced front of no bigger than millimetres per second. Other frontal models find even smaller downwelling velocities. Large scale fronts were particularly avoided when deploying the spar buoy, so the horizontal temperature

gradients in the region are small (see chapter 4), of the order of 0.1°C in 10km. Density and salinity gradients are also small. Furthermore, there is no obvious mechanism for creating a small- scale front. It seems unlikely therefore that frontal activity caused the suspected downwelling. In chapter 7, the evidence of the SeaSoar surveys will be examined, in order to see whether any suggestion of Langmuir circulation or frontal activity is revealed.

Chapter 7

Evidence for Convergence and Downwelling

7.1 Introduction

It has been found that the calculated surface heat fluxes are insufficient to provide the entire large diurnal heating signal at the VACMs (chapter 4) and that a one- dimensional model therefore cannot simulate the time series of temperatures (chapter 5). It is postulated that the spar buoy has drifted into a convergence zone. In chapter 6 possible mechanisms for such a convergence zone were reviewed. It is possible that the spar buoy drifted into the downwelling region associated with a small- scale front, although the literature (chapter 6) suggests that vertical velocities are small (less than mm/s rather than cm/s). The more likely explanation is that the spar buoy was affected by some type of Langmuir circulation, caused either by wave-current interaction or by instability of the Ekman layer. Since the effect of the convergence is observed at the spar buoy for six days, a simple wave- current interaction theory would need to be supplemented by the influence of the Coriolis force. It may well be that both mechanisms act together to create large longitudinal rolls, like those originally observed by Langmuir (1938). In this chapter, the SeaSoar data are examined in more detail, in order to verify the existence (or otherwise) of fronts and longitudinal roll vortices.

7.2 Horizontal temperature structure changes during the survey

The horizontal temperature distribution in the area of the SeaSoar survey was discussed in chapter 4. Figures 4.4 and 4.5 showed the isotherms drawn from information along the ship track. There is a gradient of temperature across the region, with warmer water initially to the north and eventually to the east. The structure referred to as the 'ramp' possesses a gradient much larger than the rest of the region (approximately 0.03°C in 6km on day 67, and 0.03°C in 2km on day 69).

There has therefore been some confluence of the water in the region, since the ramp has become much sharper and narrower. There may therefore be an associated vertical velocity. However it was shown in chapter 4 that the Ekman pumping (curl of the wind stress) was a negligible effect, producing a vertical velocity of less than 1m/day. Such convergence may therefore be due to a front.

One may estimate the vertical velocity that might be produced by the convergence causing sharpening of the ramp. On each side of the ramp, there may be a converging horizontal velocity of 2km in two days. Assuming that continuity holds:

$$\frac{\partial v}{\partial x} = \frac{\partial w}{\partial z} \qquad (7.1)$$

If this change in velocity occurs over 4km say, then:

$$\frac{\partial w}{\partial z} = 5 \times 10^{-6} s^{-1}$$

The vertical velocity w is required to be zero at the surface. If w is assumed to vary linearly with depth, then the vertical velocity at 100m may be estimated as 0.05cm/s (50m/day). This magnitude of vertical velocity is usually associated with a substantial ocean front. In chapter 4 it was suggested that the mean vertical velocity required at the VACMs was at least an order of magnitude larger than this.

The ramp has the largest horizontal gradient (at most 0.02°C per km) of the survey area, while salinity gradients are equally small. The literature (chapter 6) suggests that such a small scale open ocean front would have inadequate vertical velocities to resolve the heat budget of chapter 4. Moreover, the spar buoy was advected across the ramp early on day 69. However the need for a convergence zone in order to satisfy the heat budget exists both before and after this advective event. The ramp is therefore not necessarily associated with the downwelling.

If the front were associated with mesoscale eddies (the only likely mechanism here), then the horizontal scale would be at least as large as the Rossby radius of deformation. This is about 10km for a mixed layer depth of 200m at a latitude of 45°N. A wide downwelling zone with vertical velocities of the order of cm/s would require an improbably large horizontal convergence. A narrow downwelling zone is therefore more likely. The most feasible explanation appears to be that small scale Langmuir- type circulations cause the downwelling in which the drifting spar is caught, but that frontal activity may cause a larger scale flow of water both horizontally and vertically, which would affect the whole region.

7.3 SeaSoar temperature profiles

In chapter 4 were shown examples of individual SeaSoar profiles (figures 4.1 to 4.3). These SeaSoar data can be examined to see if there is any suggestion of a dominant spatial scale. Of course one must be careful not to give too much weight to individual profiles which may be affected by many other processes as well as by Langmuir cells (for example, internal waves, double diffusion, biological activity). It is also important to remember that the separation between the ship and the spar buoy is usually at least one or two kilometres at closest approach.

During the SeaSoar survey, one triangular circuit was undertaken towing the instrument at a constant depth of approximately 50m. This data set would have been useful to investigate the temperature signal of what might have been a cross- section of a Langmuir circulation. However, it is unfortunate that this constant depth tow was performed on day 68 when there was very little sunshine and no diurnal warming observed at the VACMs. It is therefore impossible to detect any abnormally warm section since the large scale temperature gradients and small scale noise are of a comparable magnitude to any signal expected.

Nevertheless, there is some information to be gained from the SeaSoar data about the horizontal variability of temperature. It should be remembered that the gradient of the SeaSoar is only between 1 in 3 and 1 in 5. The SeaSoar 'profiles' are therefore more nearly horizontal than vertical. Comparing the VACM profiles with the SeaSoar 'profiles' it may be noted that the latter have more variability. It is more likely that this variability is due to horizontal structure in the water rather than vertical temperature gradients. Some examples of SeaSoar data sets will now be examined (figures 7.1 to 7.9). As well as being presented as profiles, they will be drawn as horizontal sections of temperature. In this way, it is possible to study the scales of warm or cool regions.

Figure 7.1 shows temperature profiles from the SeaSoar during the early morning of day 67, when the mixed layer was fairly uniform and deep. The VACM temperature values lie between those of the third and fourth profiles. Due to problems in handling the SeaSoar during this period, only water below 50m was sampled here. It may be difficult to visualise the horizontal temperature variability from such a diagram. Therefore these data are presented again in figure 7.2, in which the temperature data of profiles 3 and 4 are plotted against horizontal distance (solid line). The dotted line shows the depth of the SeaSoar during the two profiles. It will be noticed that there are indeed some sections in which a horizontal scale of about 100m between between adjacent warm signals is apparent. This is particularly obvious at a horizontal distance of 2812.5km, where there are two narrow regions more than 10mK warmer than the water on either side. This was the cause of the sharp gradient at about 100m depth on the fourth profile in figure 7.1. The separation of the warm spikes is about 100m, implying a cell width of 50m.

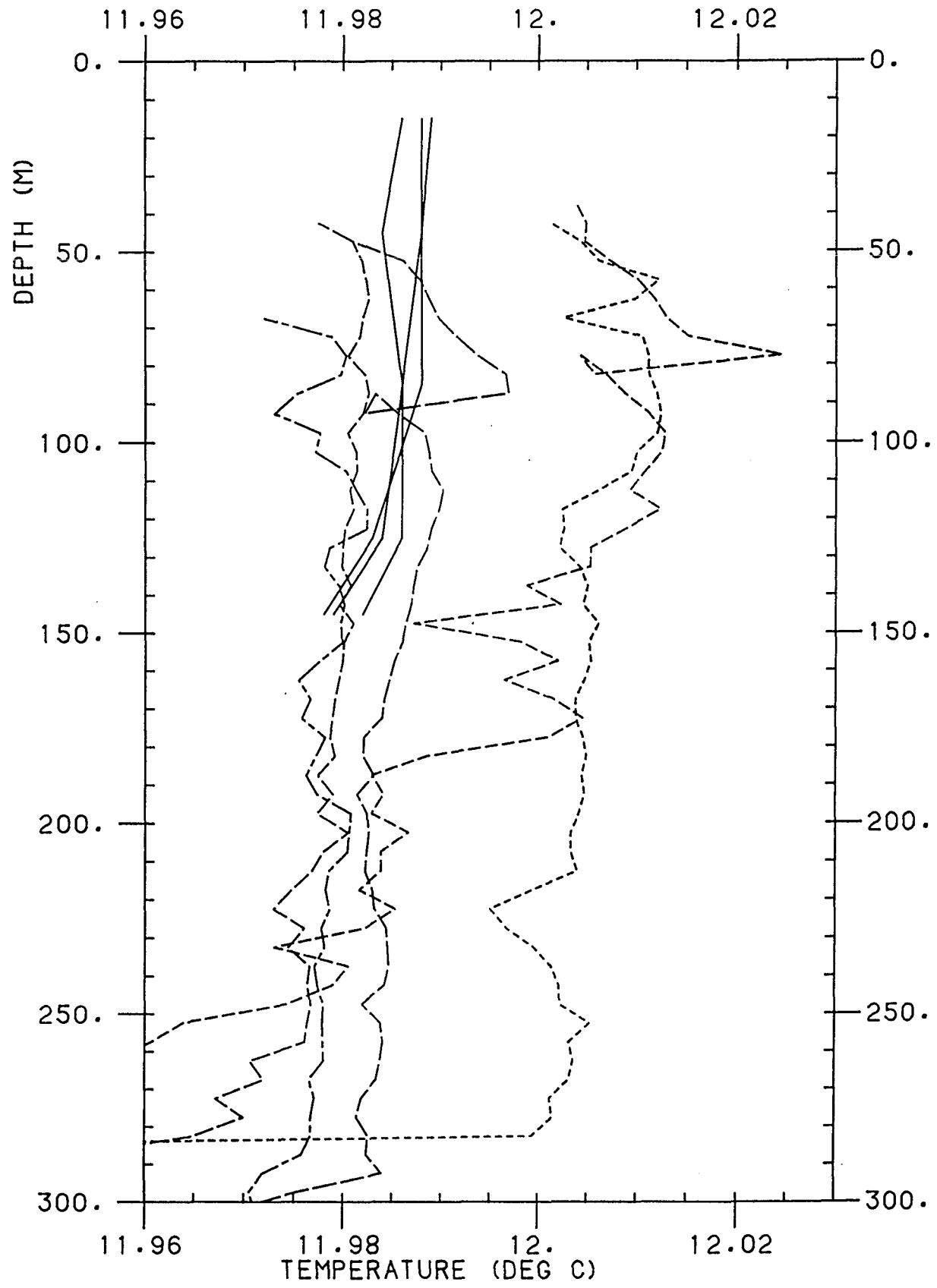

Figure 7.1 : Consecutive SeaSoar profiles between 67/0540 and 67/0610. The first profile is dotted; subsequent profiles have longer dashes; the final one is dash- dot. Several examples of profiles from the VACMs during the same period are shown as solid lines.

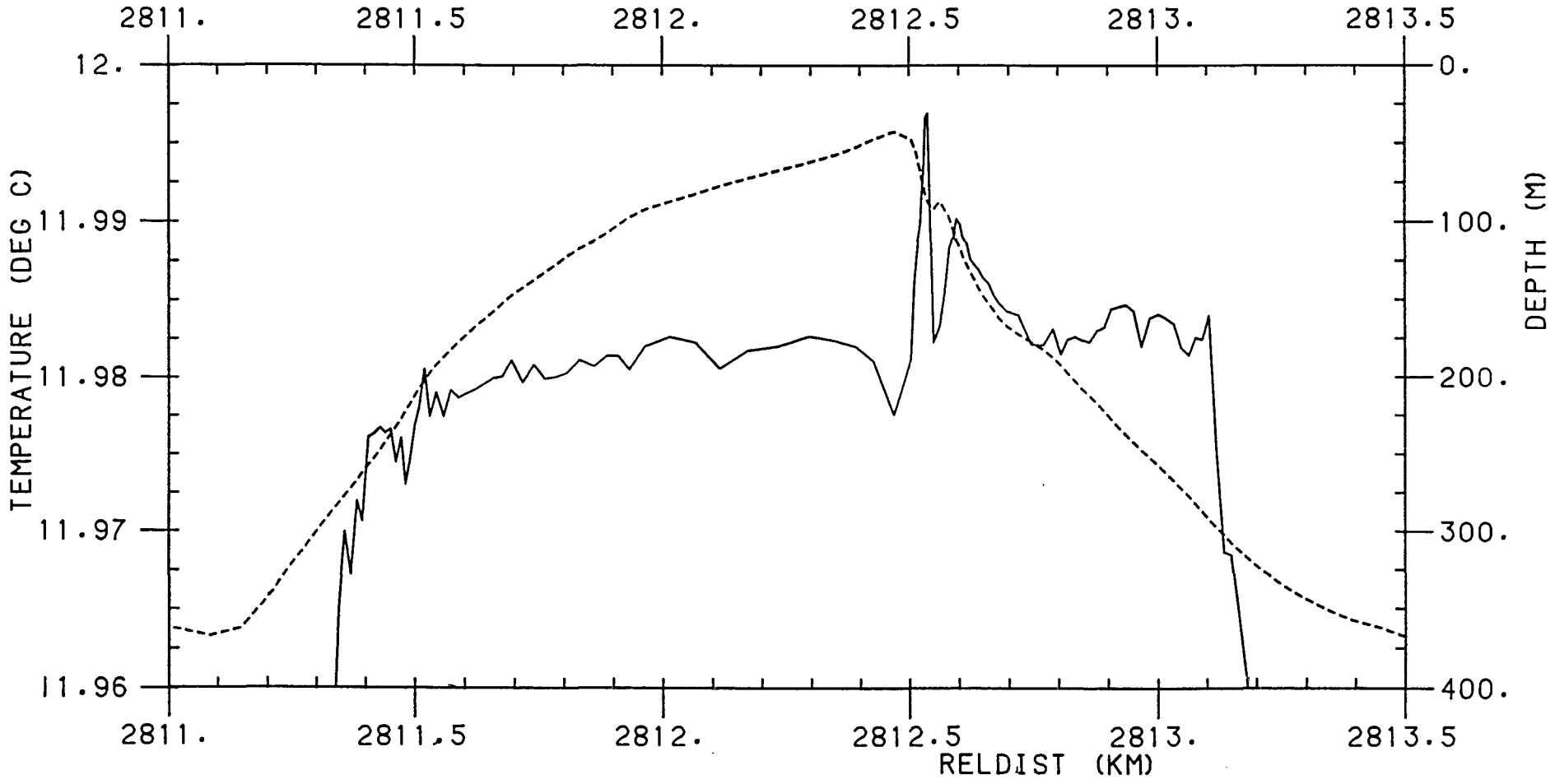

Figure 7.2 : Profiles 3 and 4 from figure 7.1, now drawn against horizontal distance travelled by the SeaSoar. The solid line shows temperature while the dotted line depicts the depth of the instrument.

Figure 7.3 portrays temperature profiles on day 68 just after midnight. The five SeaSoar profiles show a large variation in structure; the first profile is some 20mK cooler than the third, whereas the final two profiles are more similar to the first. The mixed layer depth also increases by about 70m over the five profiles. The VACM temperatures agree closely with the fourth and fifth profiles at the lower depths, but near to the surface, they lie closer to the temperatures of profile 3. There is however a large amount of variability in the temperatures recorded by the SeaSoar. The data are therefore more easily examined in figure 7.4, in which temperatures are plotted against horizontal distance (notice that figure 7.4 covers 4.5km horizontally whereas figure 7.2 spanned only 2.5km). The first kilometre on the graph reveals a system of warm and cold bands, the distance between adjacent warm regions being approximately 300m, which suggests a Langmuir cell width of about 150m. Between horizontal distances of 3063km and 3064km, there appears to be dominant structure on a scale of about 500m.

In figure 7.5 agreement is fair with the near- surface portions of the third and fourth profiles, which are both a little cooler than the water on either side. Below a depth of about 50m, however, the VACM temperatures are some 5-10mK cooler than the SeaSoar data. Looking at the same data plotted against distance (figure 7.6), it is found that for the first few kilometres, adjacent warmer patches have a separation of typically 400m, implying a cell width of 200m. At a distance of 3772km, the more rapid temperature fluctuations suggest a possible cell size of 50-100m. Given the obvious variability in the signal at all scales, it is of course difficult to pick out the dominant frequency.

The data presented in chapter 4 (figures 4.1 to 4.3) may also be examined to determine horizontal variability. Figure 7.7 shows the profiles of figure 4.1 plotted against horizontal distance. Two warm

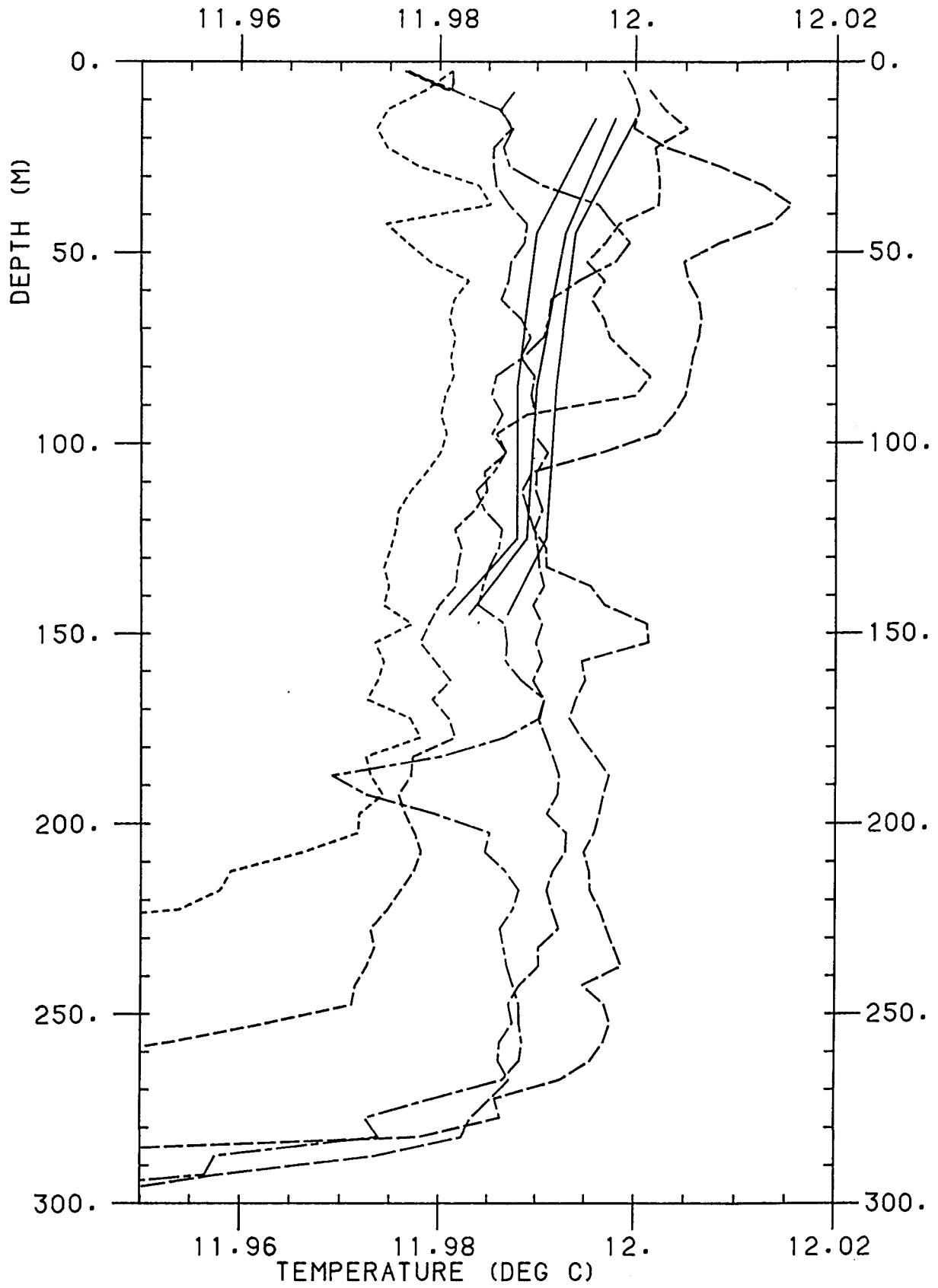

Figure 7.3 : Consecutive SeaSoar profiles between 68/0020 and 68/0050, otherwise as figure 7.1.

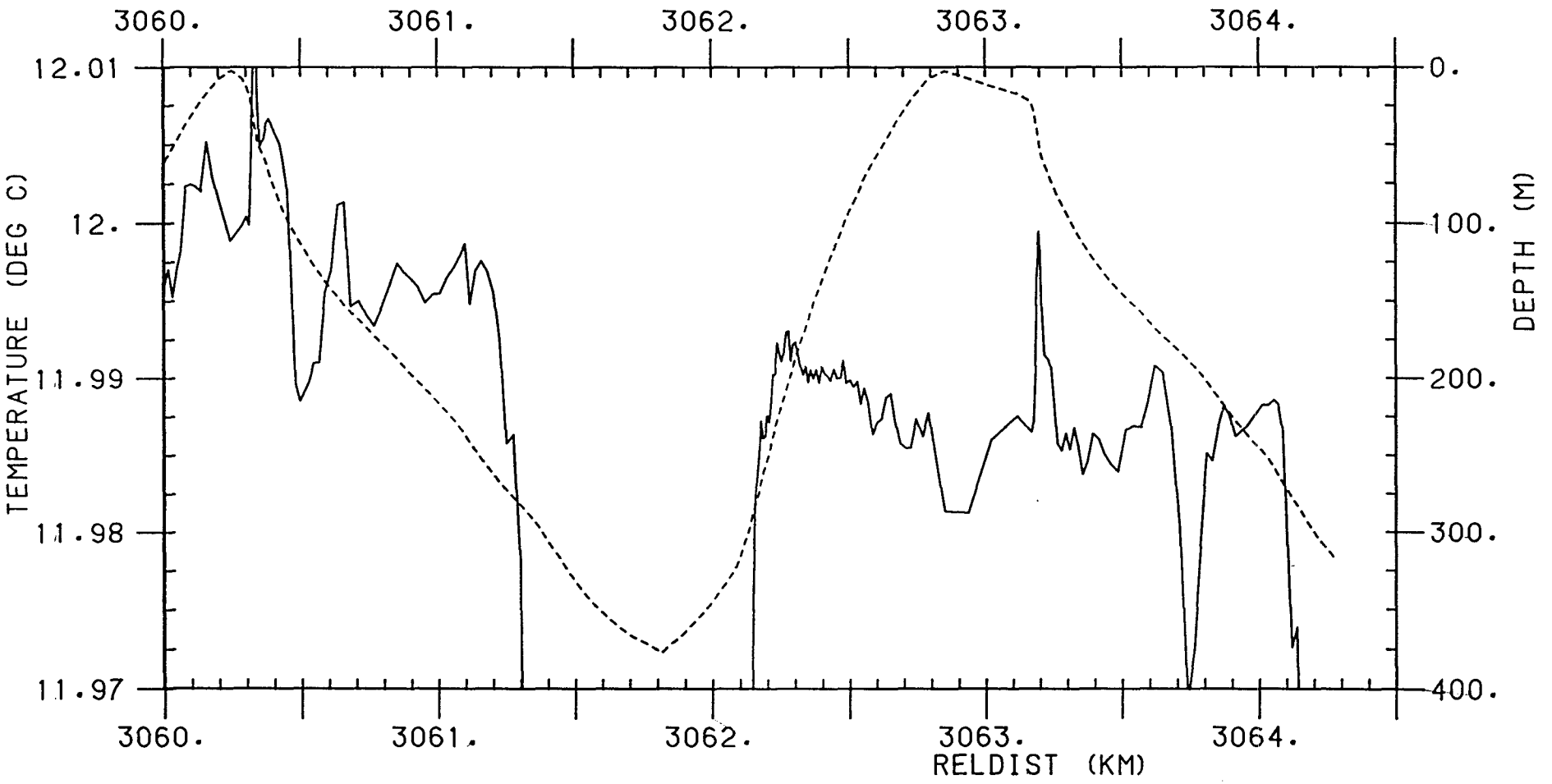

Figure 7.4 : Profiles 3 to 5 from figure 7.3, now drawn against horizontal distance travelled by the SeaSoar. Otherwise as figure 7.2.

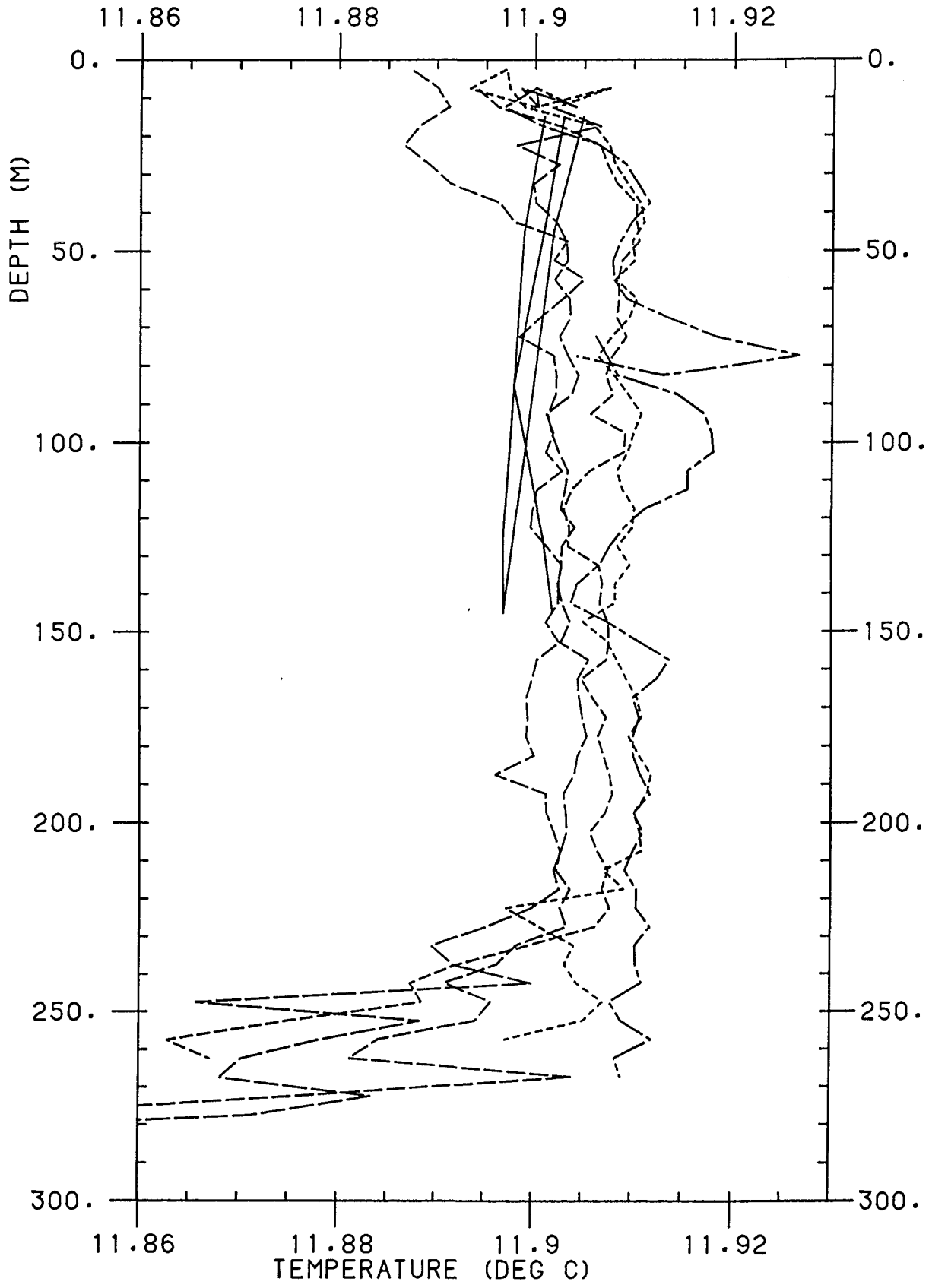

Figure 7.5 : Consecutive SeaSoar profiles between 70/0720 and 70/0750, otherwise as figure 7.1.

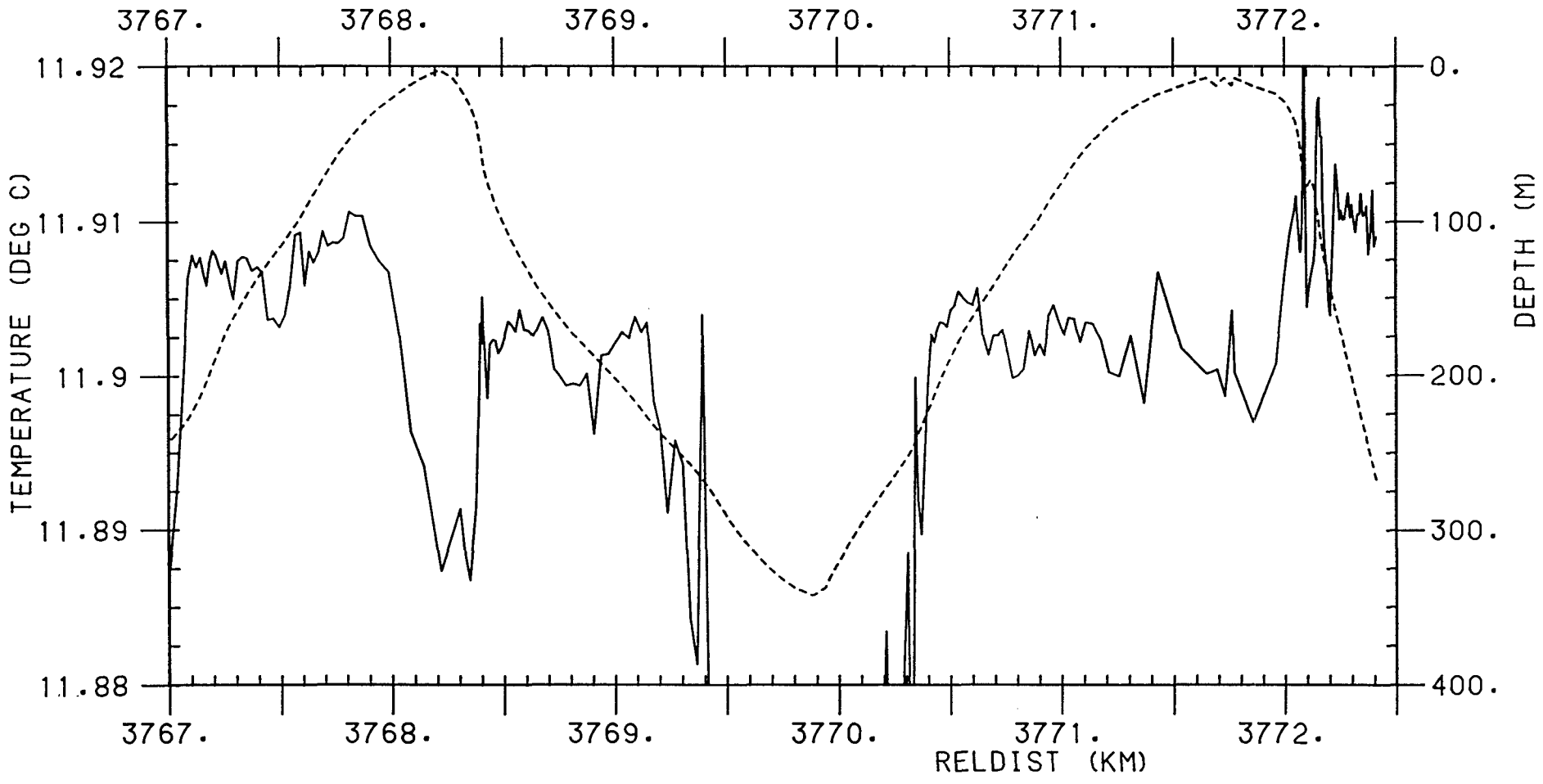

Figure 7.6 : Profiles 2 to 5 from figure 7.5, now drawn against horizontal distance travelled by the SeaSoar. Otherwise as figure 7.2.

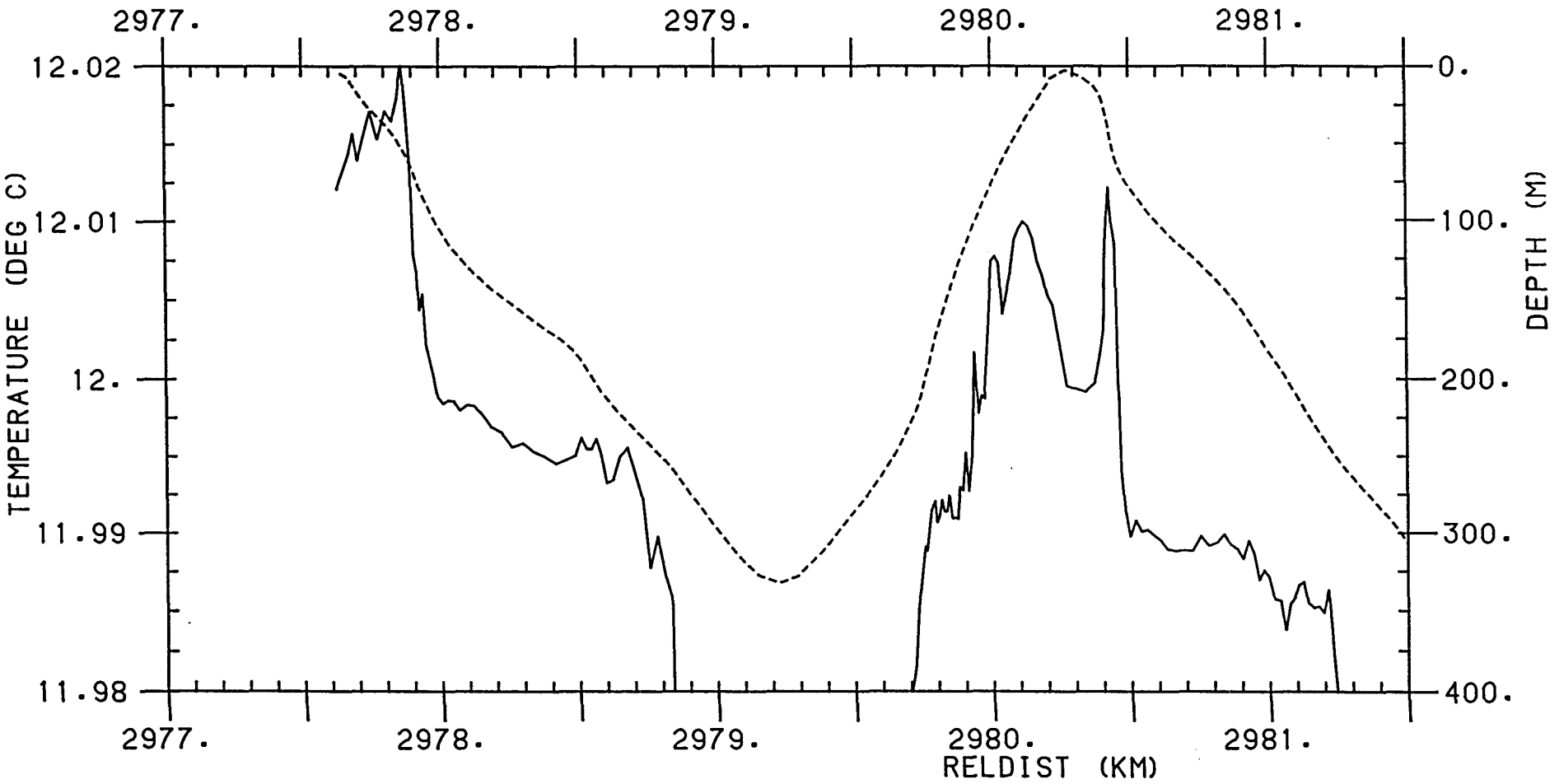

Figure 7.7 : Profiles 1 to 3 from figure 4.1, now drawn against horizontal distance travelled by the SeaSoar. Otherwise as figure 7.2. The period covered is 1830-1845 on day 67.

spikes are apparent between 2980km and 2980.5km, having a separation of about 300m. It was in these warmer patches that the VACM temperatures agreed with those of the SeaSoar (as shown in figure 4.1). These spikes suggest a Langmuir cell of width 150m, with the spar buoy drifting into the warmer water in the convergence zones; it is at the end of the daily heating period so the convergence zones would show enhanced warming.

Figure 7.8 illustrates the horizontal variability at midday on day 69 (profiles from figure 4.2). There is a regular spacing of spikes in temperature of about 300-400m, which might imply a Langmuir cell width of 150-200m. One should also notice that the point at which the VACM temperatures agreed with the SeaSoar is the narrow spike at about 3519km. The rapid variation of temperature in this region suggests that the width of the cell in which the spar buoy may be caught is only about 50m. The variation in horizontal scale between 50m and 200-300m may be an indication of the continual growth of the cells up to a width of about the mixed layer depth. The experimental evidence discussed in chapter 6 indicated that cells are continually being formed and growing, until inhibited by the density gradient of the thermocline.

Figure 7.9 shows the horizontal temperature structure from the data of figure 4.3. Between 3606km and 3607km, there is some rapid variability in temperature on a scale of about 100m, suggesting a Langmuir cell width of 50m. Again, these numbers are not to be taken as more precise than order of magnitude estimates of possible cell widths. However, it is encouraging that each of the figures examined has shown some fairly regular horizontal temperature structure of warm and cold water. A typical Langmuir cell width ranging between 50m and 200m would appear likely.

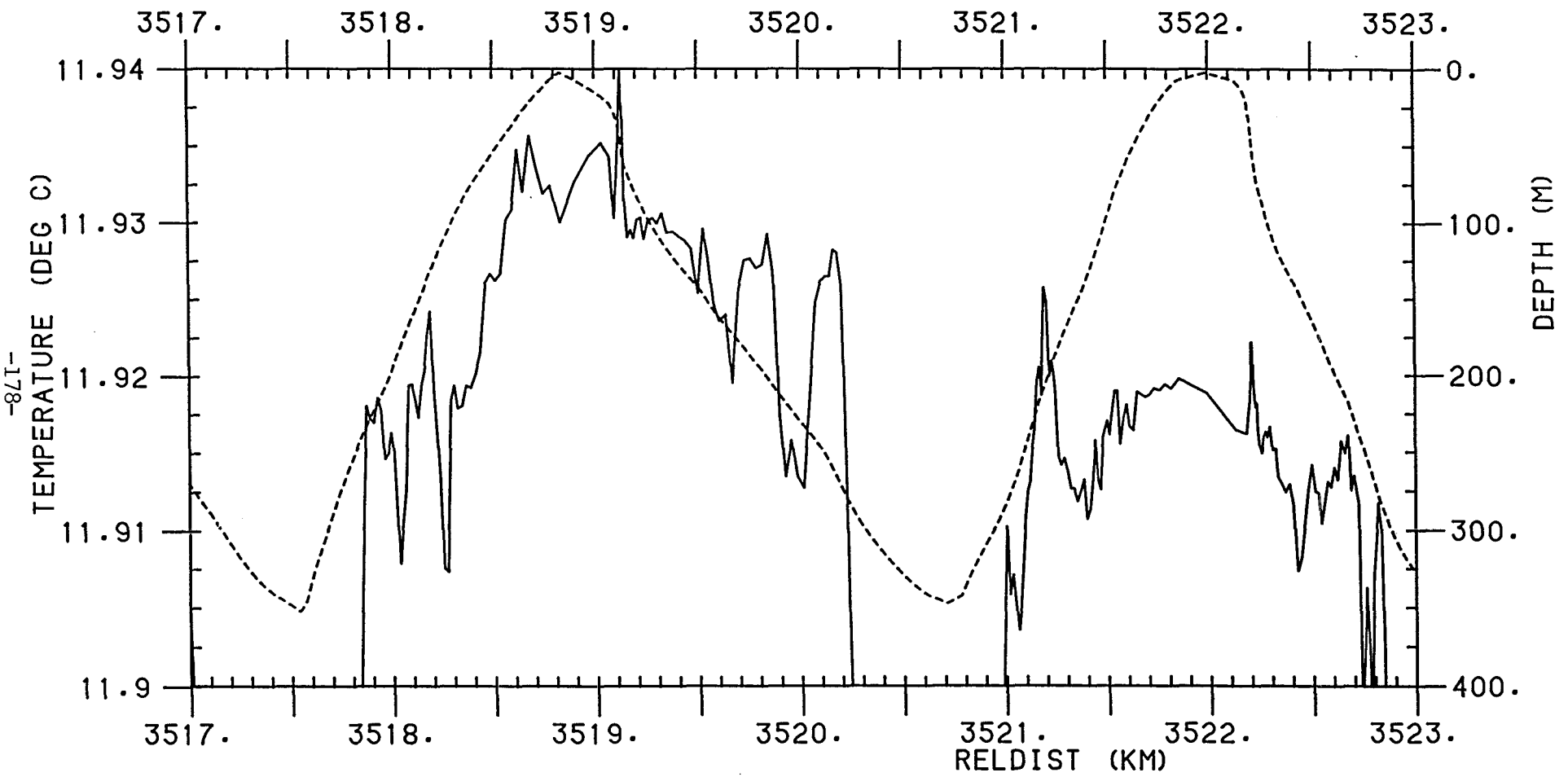

Figure 7.8 : Profiles 2 to 5 from figure 4.2, now drawn against horizontal distance travelled by the SeaSoar. Otherwise as figure 7.2. The period covered is 1230-1300 on day 69.

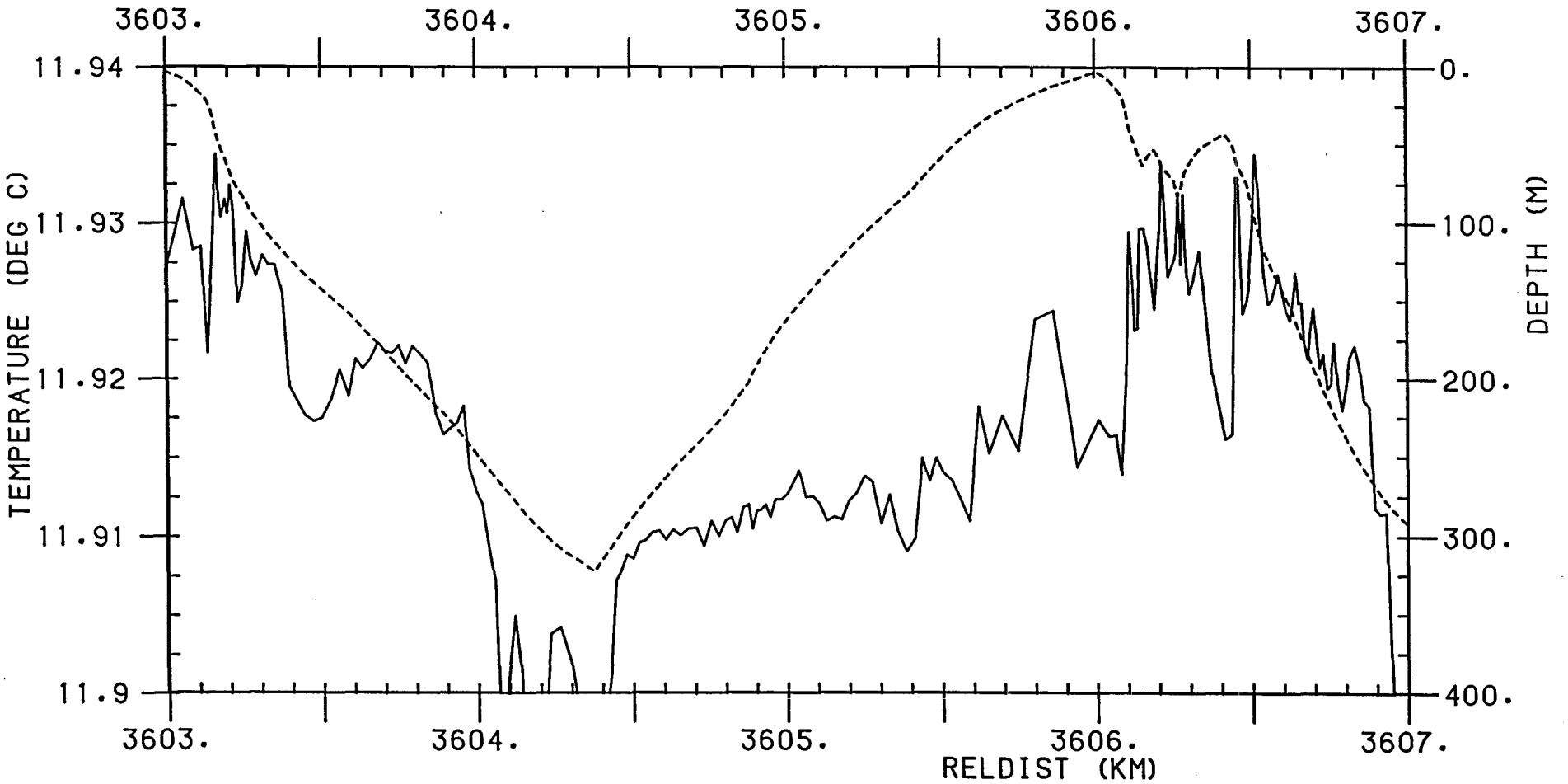

Figure 7.9 : Profiles 2 to 4 from figure 4.3, now drawn against horizontal distance travelled by the SeaSoar. Otherwise as figure 7.2. The period covered is 1950-2020 on day 69.

7.4 Other data

The previous section has surveyed the evidence of spatial scale from the upper two or three hundred metres of the SeaSoar survey. At lower depths, the SeaSoar enters the thermocline, where the temperature is dominated by the vertical gradient. Figure 2.3 showed that there is significant mesoscale structure in the thermocline, the depth of which may change by some 50m over tens of kilometres. If it were believed that fronts were the primary mechanism behind the downwelling at the spar buoy, a study of the dips in the thermocline in the region of the ramp and spar buoy would have been undertaken. However, Langmuir circulations in the mixed layer are unlikely to significantly affect the structure of the thermocline. The downwelling zone is associated with divergence at the thermocline, so should not cause the thermocline to descend. The simple model of a Langmuir circulation presented in chapter 8 will give an idea of the likely effects on the mixed layer depth. Even if Langmuir circulations do cause structure in the thermocline, the SeaSoar would be unable to detect it, since the thermocline is only sampled every two kilometres or so.

The thermosalinograph data include the near- surface temperature at the ship during the survey. This might reveal information about the surface signature of Langmuir circulations. However, the thermosalinograph data do not achieve the accuracy of a few mK required to study such small- scale features. It was felt that the more accurate SeaSoar data were more useful since the SeaSoar path was of such small gradient that the temperature structure revealed was predominantly horizontal.

7.5 Conclusions

In this chapter, a brief survey of the SeaSoar data has been undertaken. The aims were twofold: to determine whether the downwelling region, into which the spar buoy appears to have drifted,

was caused by a front or by Langmuir circulations, and secondly, to establish the likely scale of such motions. It was found that, even if the region is affected by frontal activity, this is unlikely to cause the magnitude of vertical velocity required to resolve the heat budget (chapter 4). Assuming that Langmuir circulations are a more suitable mechanism (particularly in view of the substantial volume of literature suggesting that Langmuir circulations are a frequent occurrence in the ocean), a few examples of temperature data from the SeaSoar were discussed. It was reasoned that because the gradient of the SeaSoar's path is only between 1 in 3 and 1 in 5, these data may be used to reveal the horizontal structure in the temperature field. The data suggest that Langmuir circulations may be present on scales of between 50m and 200m, with a typical value for cell width of about one or two hundred metres. This would agree with the predictions from observations and numerical models (chapter 6) that cells may grow to have a width comparable to the mixed layer depth. It is believed that the examples of horizontal structure are representative of the whole data set, since they span the six- day spar deployment, and include various times of day.

Chapter 8

A Simple Model of a Langmuir Circulation

8.1 Introduction

A simple, quasi- two- dimensional model has been developed in order to study the effect of a Langmuir circulation cell on the mixing and heating of the mixed layer. It was hoped that this would make a significant improvement to the simulation of the temperature time series at the VACMs beneath the drifting spar buoy. In this way the magnitude of the vertical velocity required at the VACMs might be estimated.

The standard model consists of a row of ten one- dimensional Kraus- Turner (KT) models as described in chapter 5. These span the circulation in the x- direction (following the terminology of chapter 6). The individual models are connected by an imposed velocity field, used to advect the temperature field both vertically and horizontally. Each model acts independently when forced by the surface cooling, heating or wind. Strictly speaking, this is not a two- dimensional model, since the equations solved are only one- dimensional; no mixing or diffusion of heat is imposed in the horizontal direction. For simplicity, however, this model will henceforth be described as the two- dimensional model, in order to differentiate between it and the one- dimensional models of chapter 5.

In applying a two- dimensional model in this way, it is assumed that the ocean is uniform in the along- roll (y) direction. Horizontal variability is expected to be much smaller in the along- roll direction than across the roll. On the other hand, it is known that the along-roll velocity is much greater in the surface convergence zone than in the divergence region (chapter 6). These along- roll velocities have been ignored.

8.2 The advection scheme

The imposed velocity field must be non- divergent; heat may only be advected in the plane perpendicular to the roll axis. It is also required that the velocity field be a smooth circulation with a narrow downwelling region and broad upwelling zone. A suitable non- divergent velocity field was found to be the solution found by Stommel (1948) for wind- driven horizontal currents in a rectangular ocean. I am indebted to Dr. Steven Alderson for suggesting this velocity field and for providing the computer programme to produce it. Stommel solved the equation:

$$\nabla^2\Psi + \xi \frac{\partial \Psi}{\partial x} = - \omega \sin\left(\frac{\pi z}{2}\right) \qquad (8.1)$$

for z between -1 and +1. ξ and ω are specified constants upon which the shape of the circulation depends. The x- varying part of the solution for stream function Ψ is a sum of two exponential functions whose values vary with ξ and ω (for further details see Stommel, 1948). The y- varying part is a sine curve. The parameter ξ gives an indication of the width of the 'boundary current' or downwelling region.

Setting both ξ and ω equal to 5 yields the asymmetrical stream function in figure 8.1. The westward intensification of the ocean boundary current here becomes the narrow and swift downwelling jet, on the left- hand- side of the domain, as shown by the closely- spaced streamlines (lines of constant stream function Ψ). The flow is symmetrical in the vertical about the 100m depth. The magnitude of the stream function itself is arbitrary here, since it is the gradient of the stream function which determines the velocity. Thorpe (1984) models the effect of Langmuir circulations on the distribution of submerged bubbles, and applies a similar two- dimensional velocity field. His stream function is however sinusoidal (and therefore

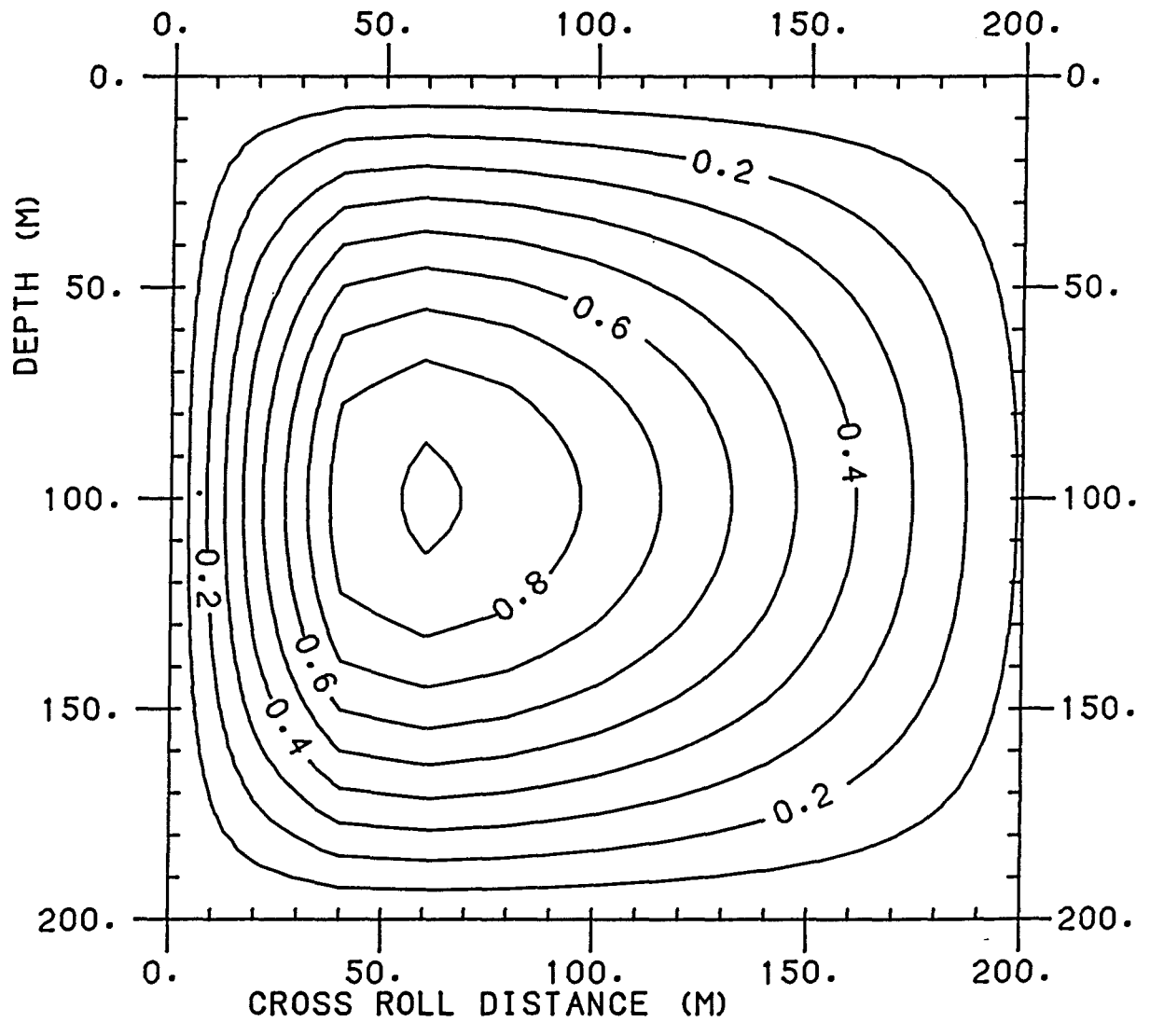

Figure 8.1 : Streamlines of the non- divergent velocity field (Stommel solution) applied to the row of one-dimensional models. Grid spacing is 5m in the vertical and 20m in the horizontal direction.

symmetrical) in both x and z directions.

The grid used in the model is illustrated in figure 8.2. Temperature T and stream function Ψ are defined at the centres of each grid box, while velocities u and w are defined at the corners. A mean velocity across each side of the grid box is calculated. The vertical grid spacing dz is 5m and the horizontal distance between models dx is 20m. The model has 10 columns and 60 rows, so the circulation is 200m by 200m. The total depth of the model is 300m but velocities are defined to be zero below 200m.

Velocities are obtained from the stream function using the equations:

$$\left.\begin{aligned} u &= -\frac{\partial \Psi}{\partial z} \\ w &= \frac{\partial \Psi}{\partial x} \end{aligned}\right\} \qquad (8.2)$$

Figure 8.3 shows the velocity field calculated from the stream function in figure 8.1. This is the velocity field which shall be used for the 'standard run'. Maximum vertical velocities are at half the depth of the cell, as Weller et al.'s (1985) observations of Langmuir circulations suggested. There is a free- slip boundary, and velocities along the boundaries are larger than in the interior. The mean vertical velocity into the grid boxes of the far left- hand column is 0.175cm/s while the maximum value is 0.275cm/s. For comparison, the mean upwelling in the far right- hand column is 0.045cm/s.

8.3 Model procedure

At each time step, the following procedure is carried out in the model:

1) Absorb surface heat fluxes in each column exactly as for the one-dimensional model (chapter 5).

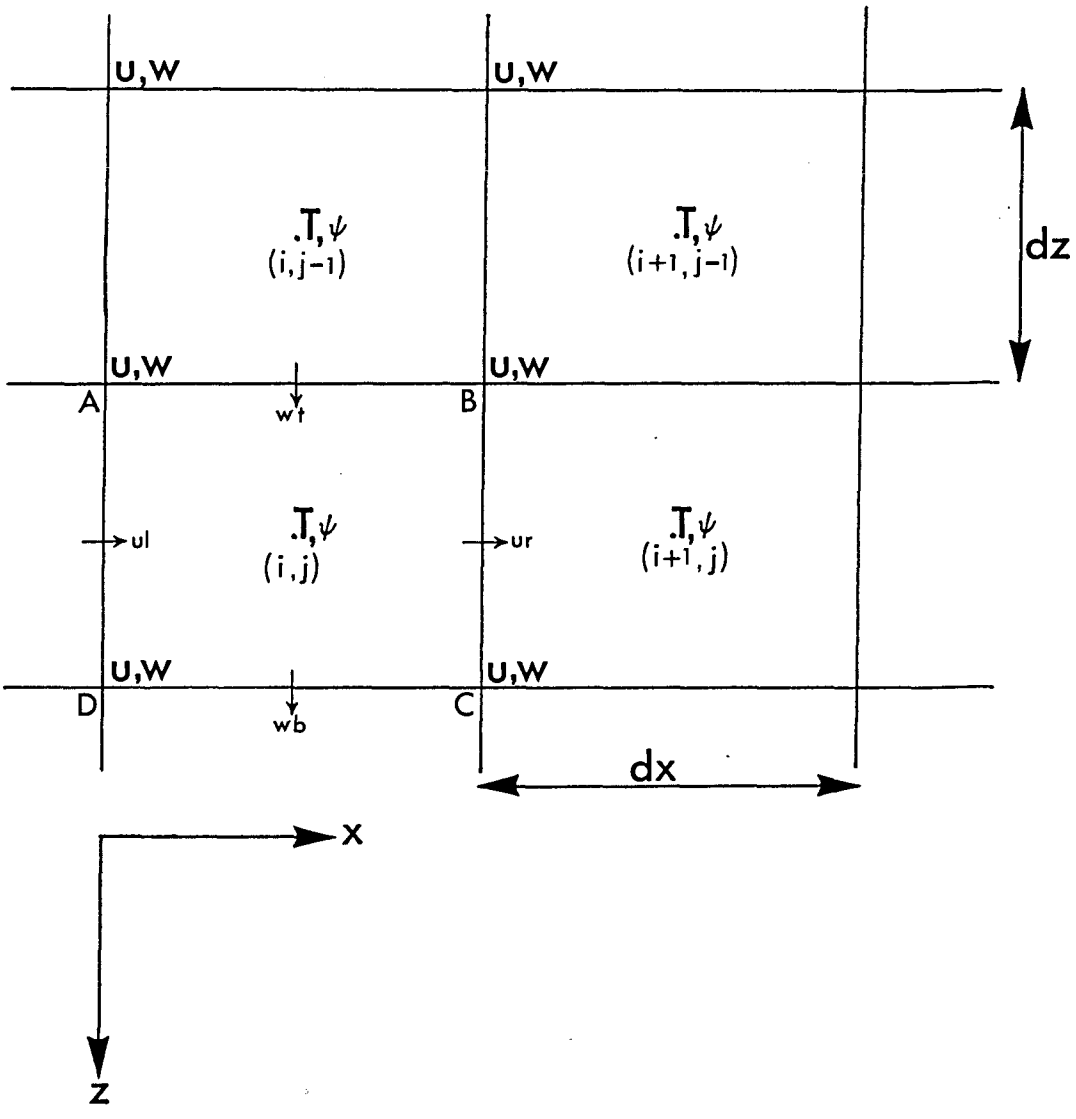

Figure 8.2 : Grid used for advection scheme. Velocities u and w are defined at the corners of grid boxes, temperature T and stream function Ψ in the middle. Fluxes into box ABCD are calculated by evaluating velocities at the arrows. dx and dz are the grid dimensions defined here; dx is 20m and dz is 5m for the standard run.

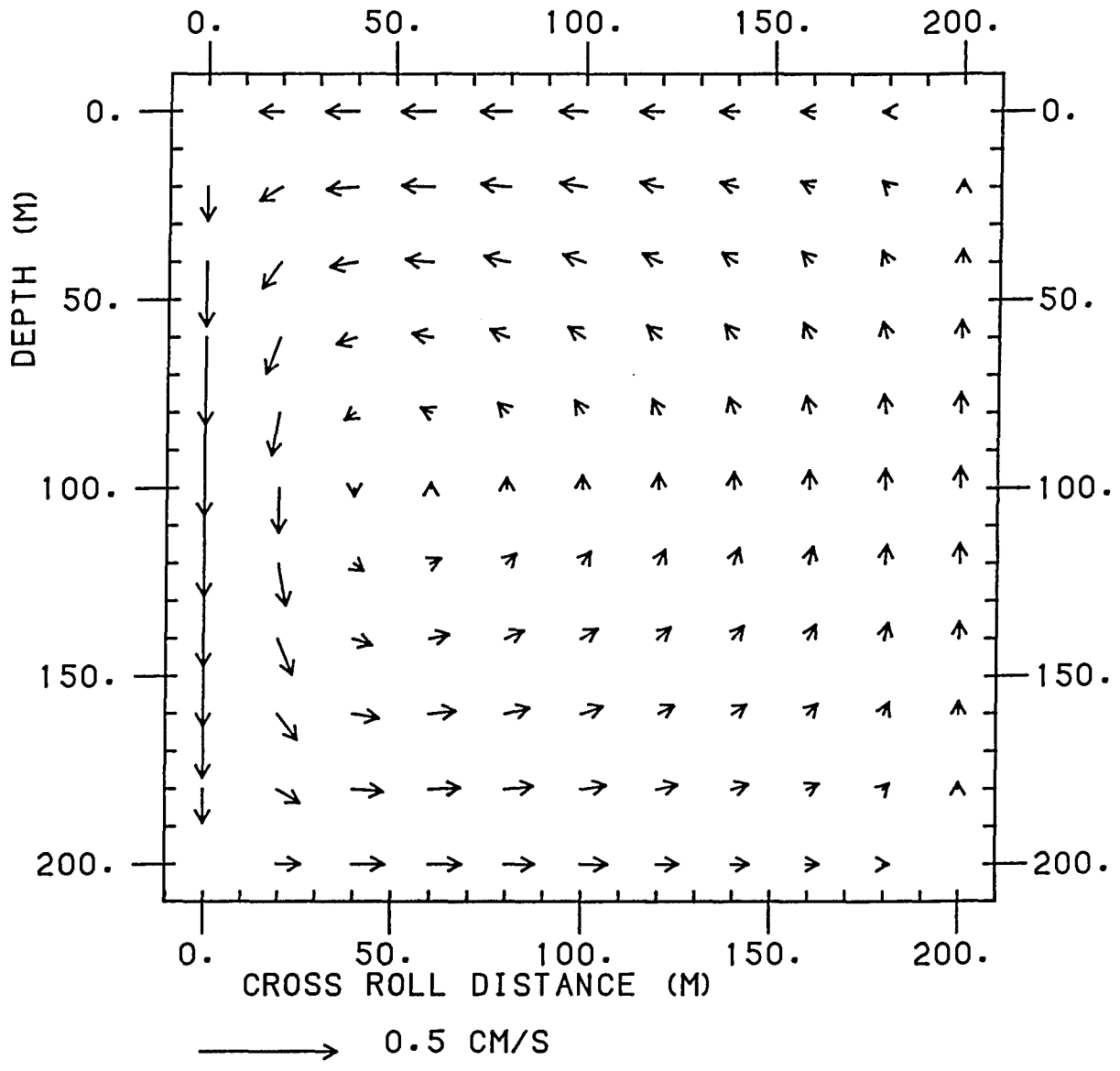

Figure 8.3 : Velocity field calculated from streamlines in figure 8.1, using the grid in figure 8.2. Velocities apply to the point at the tail of the arrow. Arrows are only drawn every 20m in the vertical for clarity.

2) Advect water both vertically and horizontally using the imposed velocity field. An upstream differencing scheme is used. Using the grid in figure 8.2 and assuming the directions of flow marked, the new temperature T'(i,j) in the box designated (i,j) is given by:

$$T'(i,j)=\frac{(T(i-1,j)ul - T(i,j)ur)\ dt}{dx} + \frac{(T(i,j-1)wt - T(i,j)wb)\ dt}{dz} \quad (8.3)$$

The velocities ul, ur, wt and wb (across the left- hand, right- hand, top and bottom edges of the grid box ABCD) are calculated as the means of the velocities at the corner points; e.g. ul is the mean of the u components at A and D.

3) Mix from the surface downwards using the procedure described for the one- dimensional Kraus- Turner model (chapter 5) for each column individually.

Obviously it is not numerically reasonable for water to cross more than one grid box in each time step. Therefore it is a condition on the size of u and w that:

$$\left.\begin{aligned} u &< \frac{dx}{dt} \\ w &< \frac{dz}{dt} \end{aligned}\right\} \quad (8.4)$$

where dt is the length of the time step, and dx and dz are the dimensions of the box as in figure 8.2. Mathematically, this is known as the Courant- Friedrichs- Lewy (CFL) condition (Roache, 1976). In this model, the critical velocity is the vertical velocity at a depth of 100m on the left- hand- side. The maximum vertical velocity into a box using the velocity field of figure 8.3 is 2.75×10^{-3} m/s. The maximum w allowed from equations 8.2 is 2.78×10^{-3}m/s (0.278cm/s) if a time step dt of half an hour is used together with a vertical grid spacing dz of 5m.

8.4 Test runs

8.4.1 Initial investigations

The advection scheme was tested to ensure that the total heat content of the whole domain was conserved. This was achieved simply by applying zero surface fluxes and allowing the heat to be advected round. The heat content was found to be unaltered within the numerical accuracy of the computer (six significant figures). Figure 8.4 shows the evolution of the temperature isotherms over 72 half- hour time steps using the velocity field plotted in figure 8.3. The initial profile is uniformly stratified to 300m; the velocity field is zero below 200m. Notice that at 24 hours and 36 hours, warmer water is penetrating below cooler water from the left- hand- side. In a real ocean this would create a static instability and overturning would occur.

The following procedure has been added after stage 3 of the model to allow convective overturning under such circumstances. I am grateful to Dr. Peter Killworth for suggesting the method used.

4) From the mixed layer base, step downwards (j increasing) in a particular column (i constant). Descend until static instability found. i.e.

$T(i,j) < T(i,j+1)$ for $j = k$

Continue stepping downwards until temperature increases again. i.e.

$T(i,j-1) > T(i,j)$ for $j = kk$

For all j from k to kk inclusive, set T(i,j) equal to the mean of T(i,j) over this range of j. Repeat stage 4 until no further static instabilities are found.

In this way the profile is adjusted iteratively to create a layer of uniform temperature beneath the stratified region, eliminating static instability. Figure 8.5 shows the temperature isotherms equivalent to figure 8.4 but allowing convective overturning. The overturning

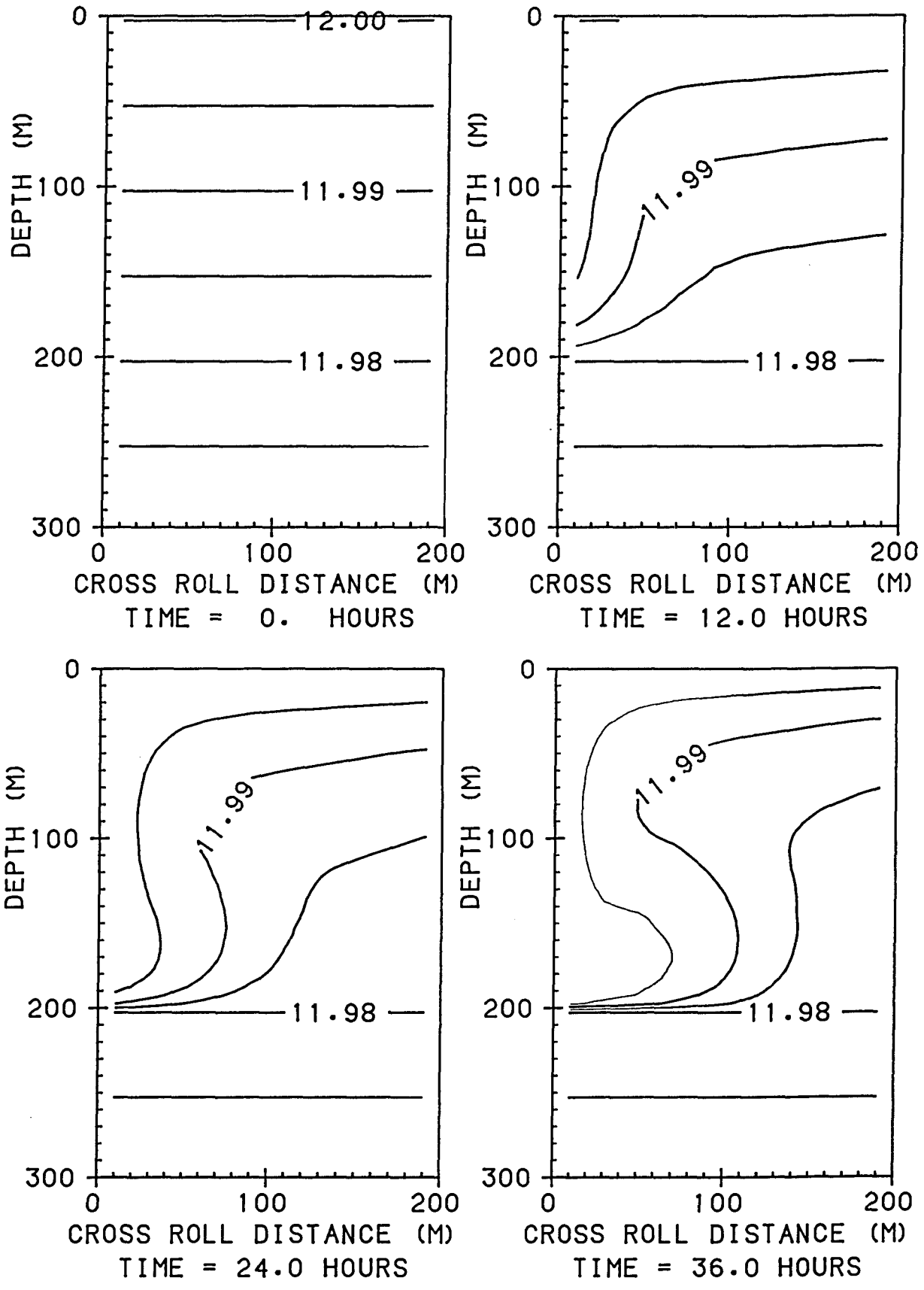

Figure 8.4 : Evolution of the temperature field across the cell at intervals of 12 hours. The first graph shows the initial state. Heat is advected according to the velocity field in figure 8.3. Temperature isotherms are plotted every 0.005°C.

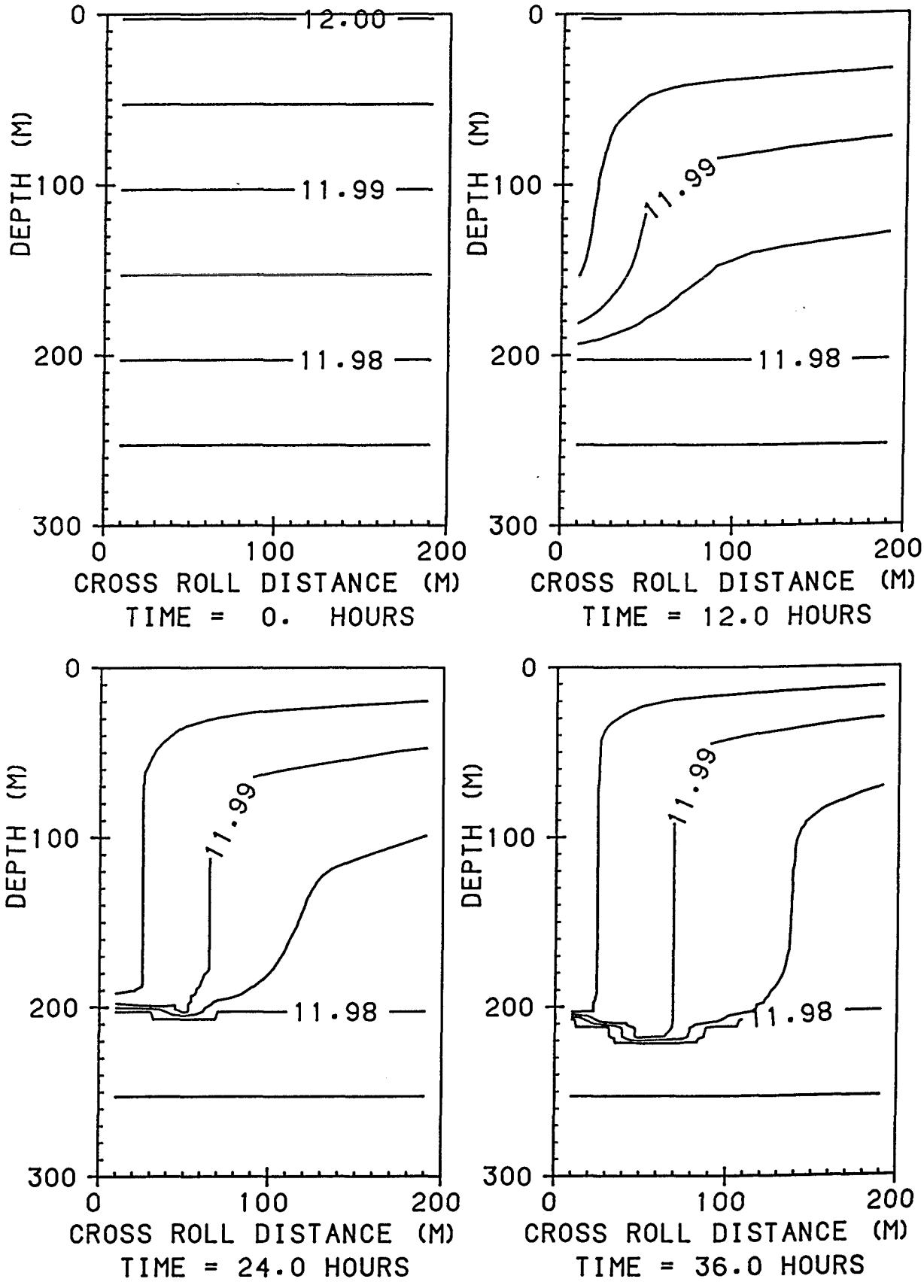

Figure 8.5 : As figure 8.4 but allowing convective overturning where advection carries warmer water beneath cooler water.

entrains some of the water below 200m into the mixed layer. Strictly, when this occurs, the velocity field should extend to the base of the mixed layer, since it was shown in chapter 6 that the Langmuir cell grows until it reaches the large density gradient of the thermocline.

Test runs were also performed using a velocity field symmetrical across the roll as well as in the vertical. The stream function Ψ was obtained by setting ξ equal to zero and ω equal to 5 in equation 8.1. The speeds were then scaled so that the strength of the circulation was approximately the same as the asymmetrical case. Figure 8.6 shows the temperature isotherms during a 24 hour run using the symmetrical advection field. Otherwise the model was the same as for figure 8.5. The downwelling zone is much less pronounced, and the heating effect takes nearly twice as long to reach the lower depths. A more significant effect is therefore obtained if the more realistic, asymmetrical cell is imposed. The stream function of figure 8.1 will be used as standard.

8.4.2 Numerical diffusion

Since an upstream differencing scheme is used for the advection, some numerical diffusion is implicit in the scheme. Some tests were performed to see whether the effect of numerical diffusion would dominate the results obtained by the model. The model was run with an initial temperature field uniform everywhere except at one grid point where a hot 'blob' was imposed. Figure 8.7 shows the advection of a hot blob of temperature 50°C initially placed at (1,1) i.e. the top left corner grid box. The velocity field is that of figure 8.3 and no convective overturning is allowed. The numerical diffusion is large; after four days the warm water has circulated round but has diffused so much that the highest contour drawn is 12.3°C. The numerical diffusion is an inevitable consequence of using an upstream advection scheme. During each time step, water is passed across all boundaries of a grid

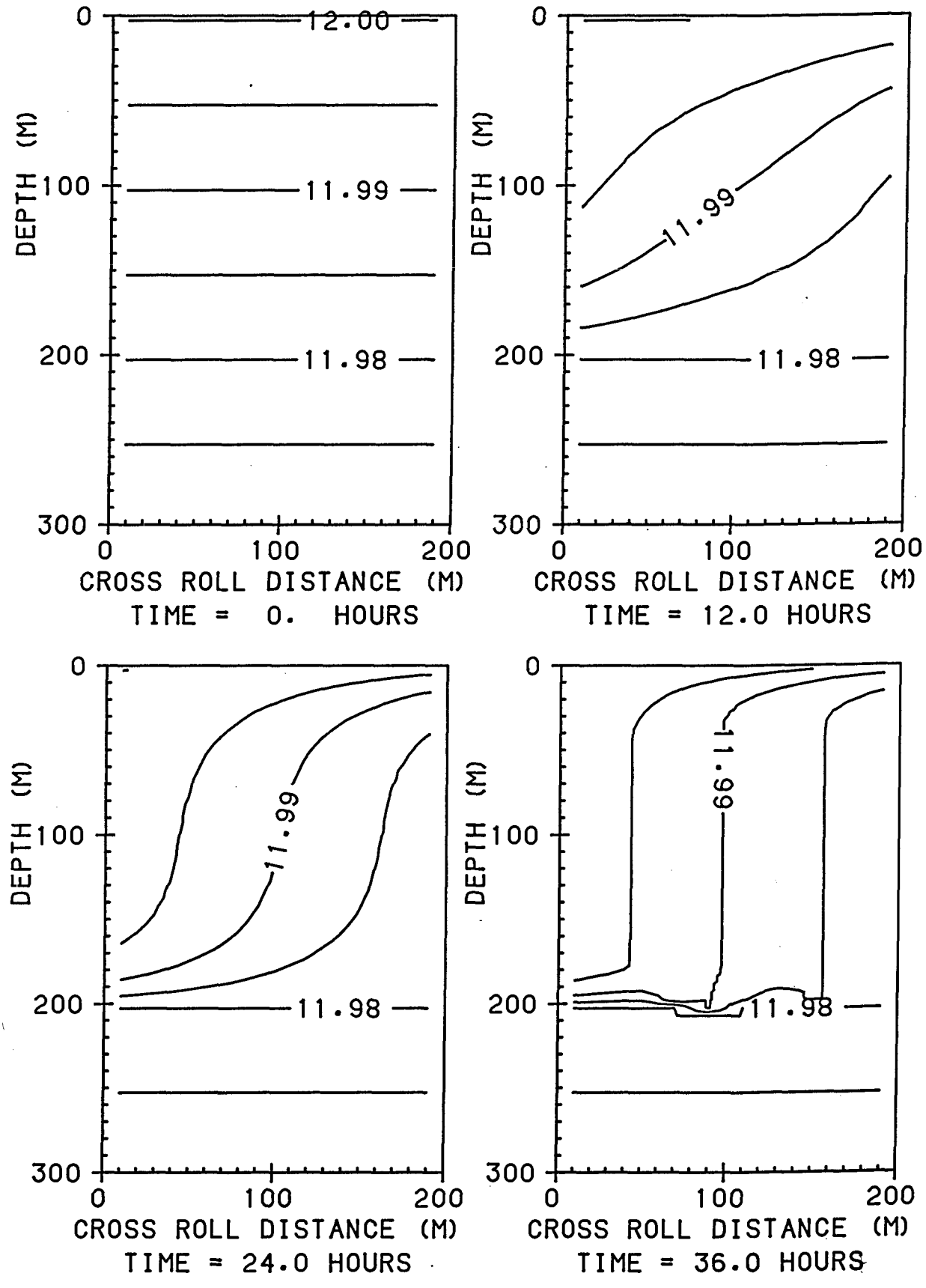

Figure 8.6 : As figure 8.5 but imposing a symmetrical velocity field.

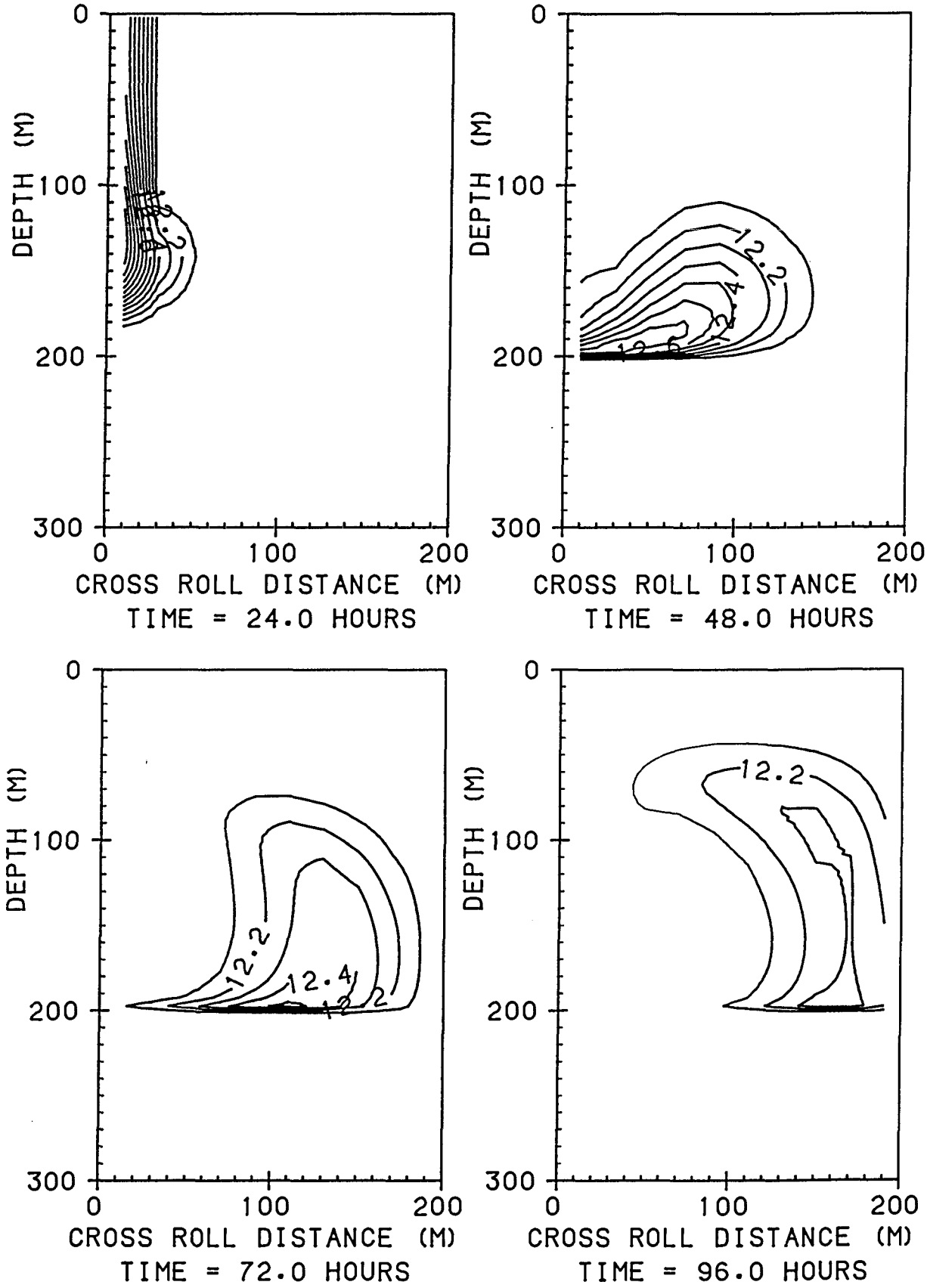

Figure 8.7 : Advection of a warm 'blob' of water at temperature 50°C, placed in the top- left- hand corner at time = 0.0 hours. The contour interval here is 0.1°C.

box. When the final grid box temperature is calculated, however, the total of all these fluxes is taken; one may visualise warm water from one side of a grid box being mixed with cool water from below, for example. The water in each grid box is assumed uniform; in reality it will not be.

The numerical diffusion is reduced if a smaller grid spacing is used. Figure 8.8 illustrates the advection of the hot 'blob' initially at 50°C as before, but using a horizontal grid spacing dx of 5m instead of 20m. The numerical diffusion coefficient for an upstream differencing scheme is 0.5 u (dx - u dt) (Roache, 1976) so a reduction in dx gives a smaller amount of diffusion. So that the initial conditions are the same, a temperature of 50°C was assigned to the four boxes between (1,1) and (4,1) inclusive. There is much less numerical diffusion; after four days the maximum temperature is 13.9°C instead 12.3°C. To test whether this reduced numerical diffusion would significantly affect the model results, runs were performed using the sinusoidal heating function and constant wind described in chapter 5. The heating is maximum (500W/m^2) at midday and minimum at midnight; the wind stress is 0.3N/m^2. Figure 8.9 shows the development of the temperature structure across the roll using the standard horizontal grid spacing of 20m, while figure 8.10, for comparison, has less numerical diffusion since a grid spacing of 5m was used. It is apparent that the reduction in numerical diffusion has had very little effect. For example, the 11.99°C isotherm has reached a depth of about 180m at 1800 in both figures; the 12.06°C isotherm is also in a very similar position. The physical processes shown in these figures will be discussed in the next section; here it is concluded that the numerical diffusion does not dominate the genuine processes in the model.

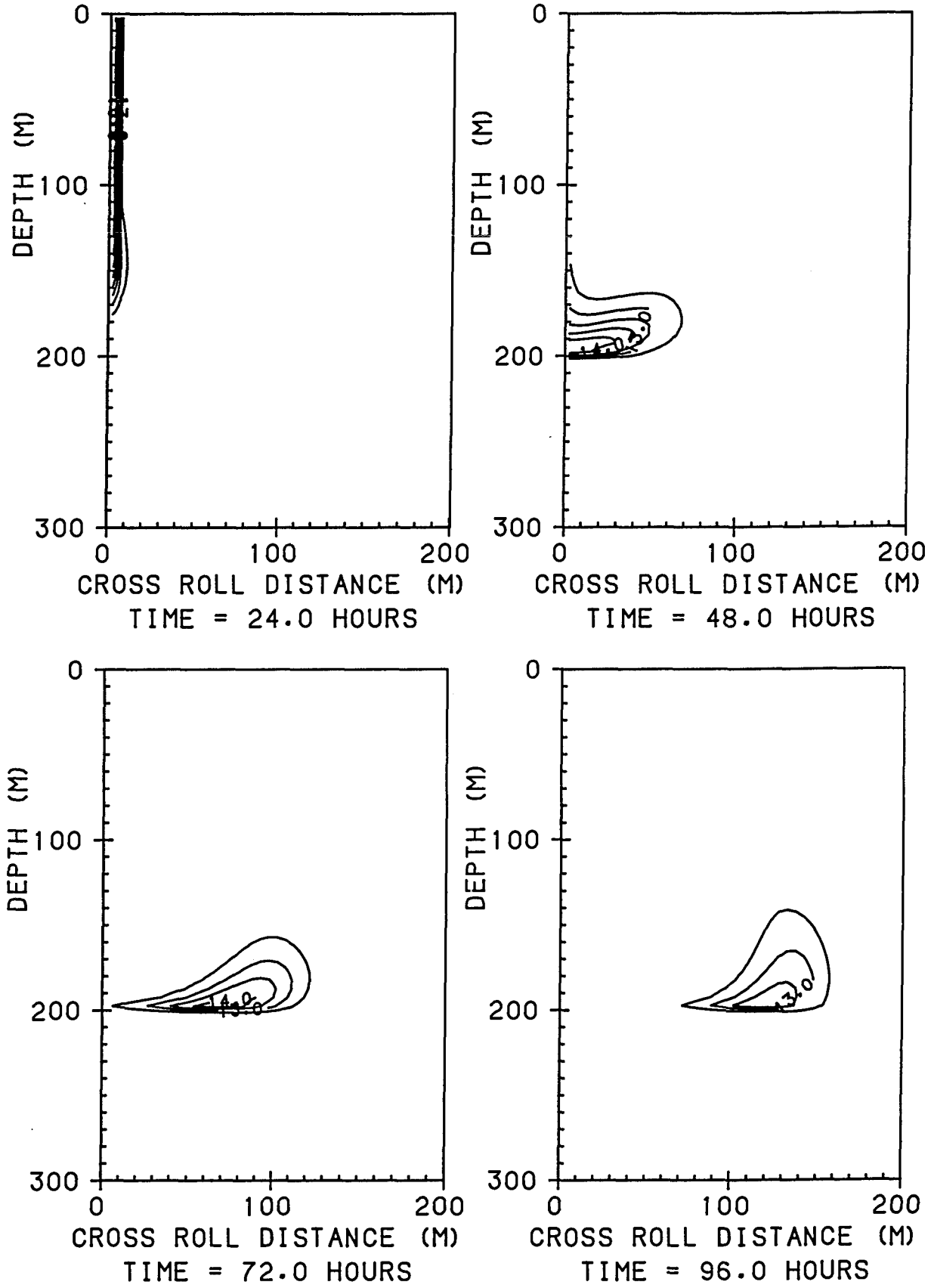

Figure 8.8 : As figure 8.7 but using a horizontal grid spacing of 5m so that the numerical diffusion is less. The first four grid boxes in the top row were assigned temperatures of 50°C. Note that the contour interval has been increased to 0.5°C.

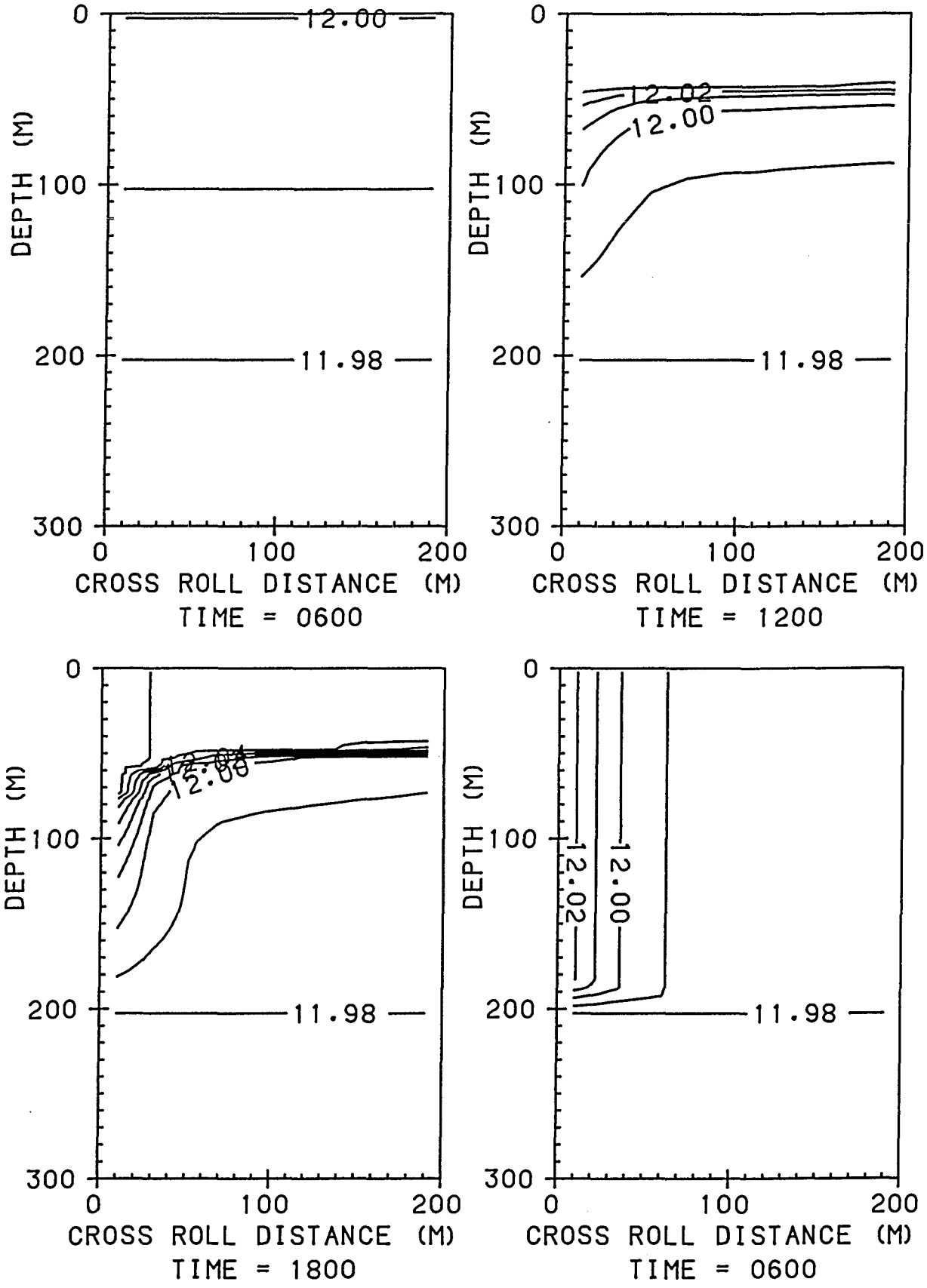

Figure 8.9 : Evolution of the temperature field at intervals of 6 hours with a sinusoidal heating function and constant wind stress. The initial state at 0600 is shown in the first graph.

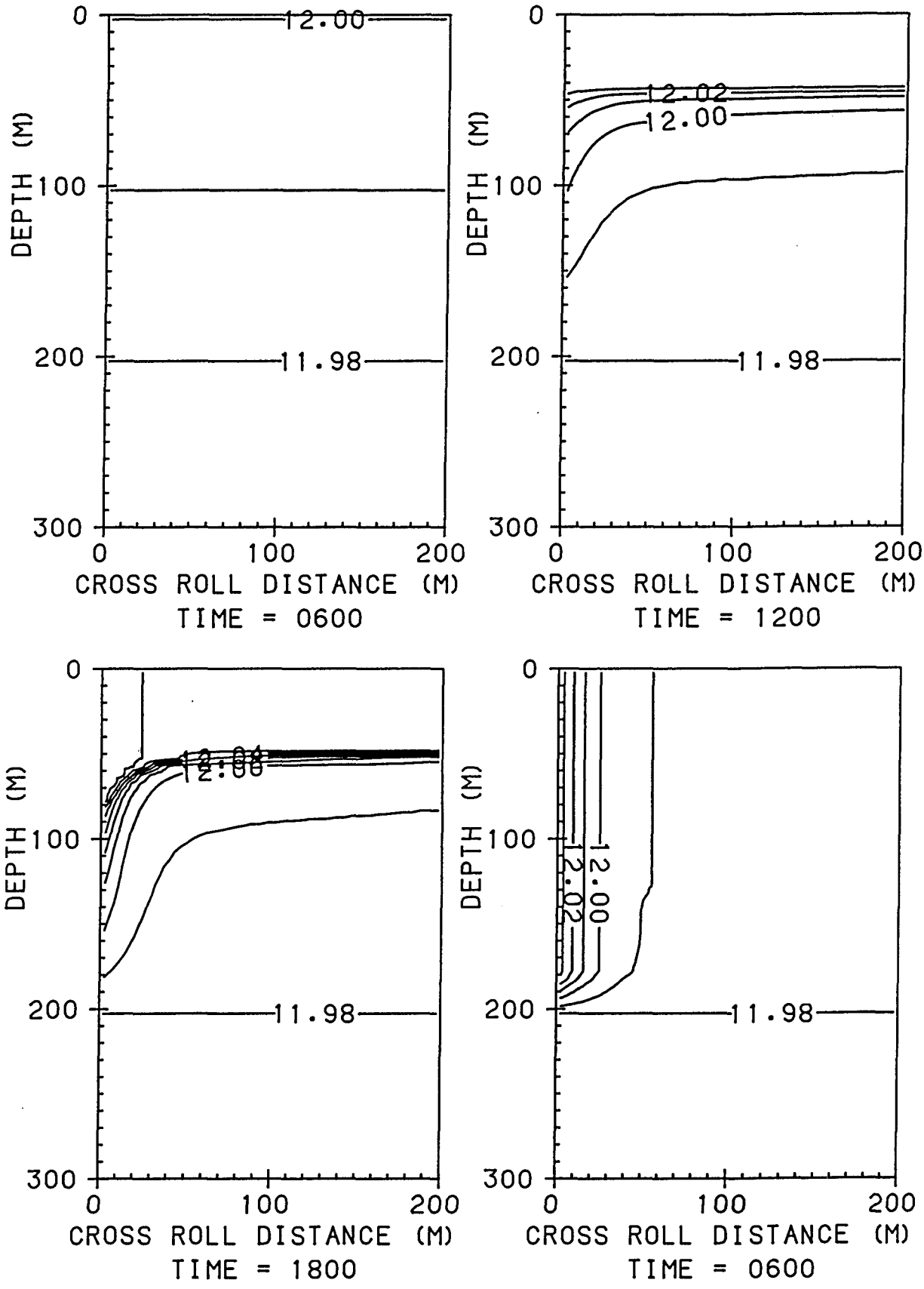

Figure 8.10 : As figure 8.9 but using a horizontal grid spacing of 5m so that less numerical diffusion is inherent in the advection scheme.

An alternative advection scheme could have been devised to reduce the numerical diffusion. A centred differencing scheme would reduce numerical diffusion but is intrinsically unstable so explicit diffusion must be added. Other schemes such as a semi- Lagrangian scheme could be attempted. However, it was felt that since this model is only a 'first guess' at modelling a Langmuir circulation, the most easily understood advection scheme would be an advantage. In any case, there are so many other uncertainties in the model, such as the size and strength of the velocity field, and the parameters of the mixed layer model itself, that the choice of advection scheme is of little relative importance.

8.4.4 Applying a sinusoidal heating function

Figure 8.9 gives the evolution of the temperature field across the roll during the 24 hour run. The first plot is at 0600, the start of the run. By 1200 a small thermocline has developed at about 50m, the limit at which wind stirring and solar heating balance. This strengthens during the afternoon until there is considerable (approximately 0.005°C/m) stratification near 50m at 1800. In the downwelling zone, however, the heat has travelled much further downwards and there is stratification to 200m. The final plot shows the temperature field at 0600 the following day, 24 hours after the start of the run. By this time a horizontal temperature gradient has become apparent, with warmer water on the left- hand- side, in the downwelling zone.

It is interesting to examine the left- hand- side of the model since this is where the spar buoy would be expected to drift. Temperature profiles at the left- hand- side are shown in solid lines in figure 8.11, while the dotted lines represent the model with no advection applied. The total heat content of the left- hand column at the end of the 24 hours is considerably larger in the advection model.

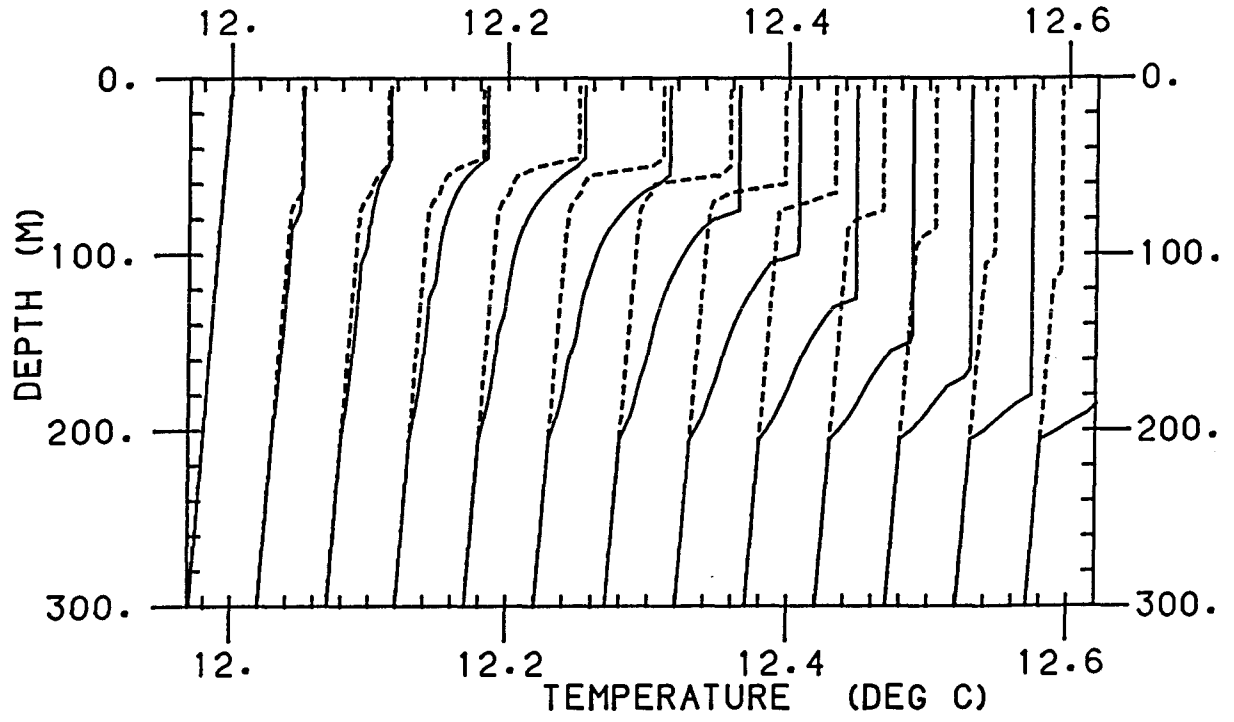

Figure 8.11 : Results from the two- dimensional model. Temperature profiles are plotted for the left- hand- side of the circulation. Dotted profiles are without advection; solid lines are with the advection field of figure 8.3.

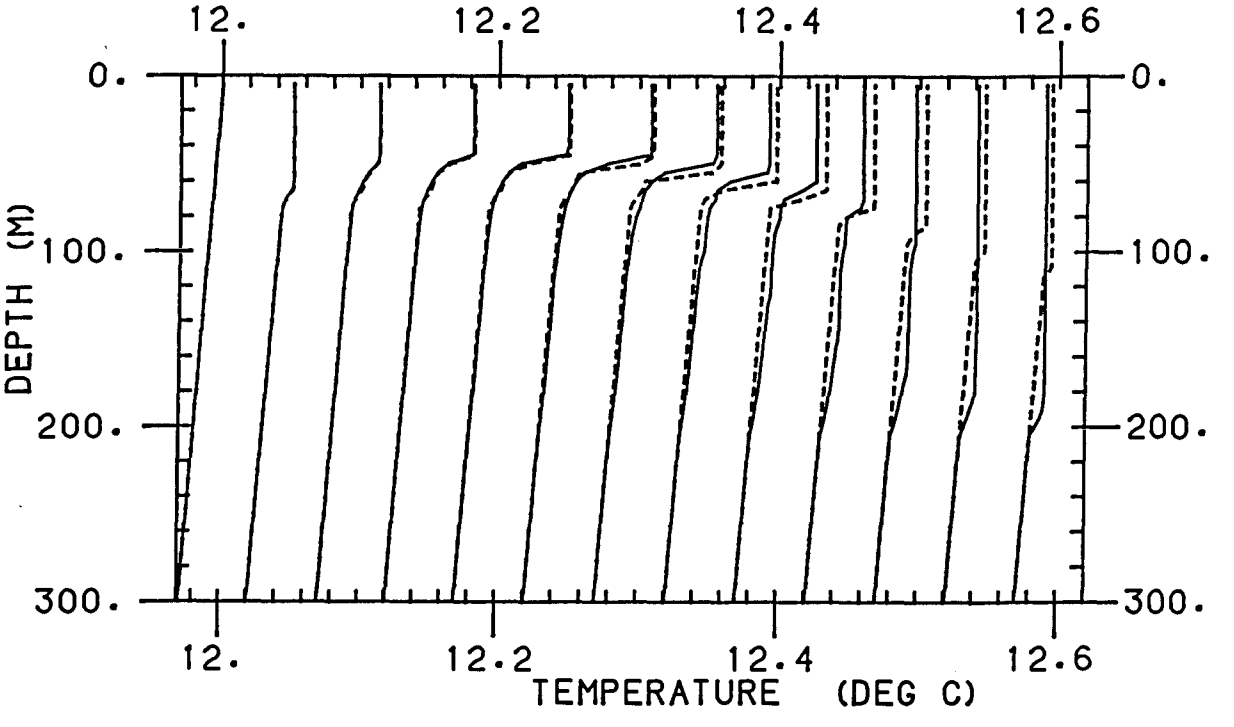

Figure 8.12 : Results from the two- dimensional model. Average temperature profiles across the circulation with (solid lines) and without (dotted lines) advection.

Between the surface and 200m, the mixed layer is on average 0.3°C warmer than in the one- dimensional model. The final mixed layer depth is nearly 100m greater than without advection. The downward transport of the absorbed solar radiation may be followed from profile to profile as the stratified section of the curve progresses downwards below the mixed portion.

Obviously the advection is affecting the amount of heat transported into the ocean on the left- hand- side. But is the circulation affecting the mean downward heat transport across the roll, or do the upwelling and downwelling balance out? Figure 8.12 shows, in dotted lines, profiles from the model with no advection, as in figure 8.11. In solid lines are depicted average profiles using all ten columns across the roll. It is seen that the circulation does indeed affect the mean downward heat transport of the whole region. The circulation has hastened the mean transport of heat into the ocean. After 24 hours, the water below about 100m is some 5-10mK warmer than it is without the circulation, whereas above 100m it is a similar amount cooler. This would imply that Langmuir circulations have a significant effect on the apparent eddy diffusion coefficient of heat. Thus it is important to know whether Langmuir circulations are present during an experimental investigation of the mixed layer. Models which predict mixed layer depth or sea surface temperature may need to use a larger eddy diffusion coefficient if Langmuir circulations are (or are likely to be) present.

If the velocity field of figure 8.3 is multiplied by four, four times as much advection is obtained. Figure 8.13 shows the temperature field corresponding to figure 8.9 but with four times the advection of the standard run. After six hours, the diurnal heating signal has already reached the bottom of the cell (200m), and has begun to travel horizontally across the cell. By 1800, warmer water penetrating below

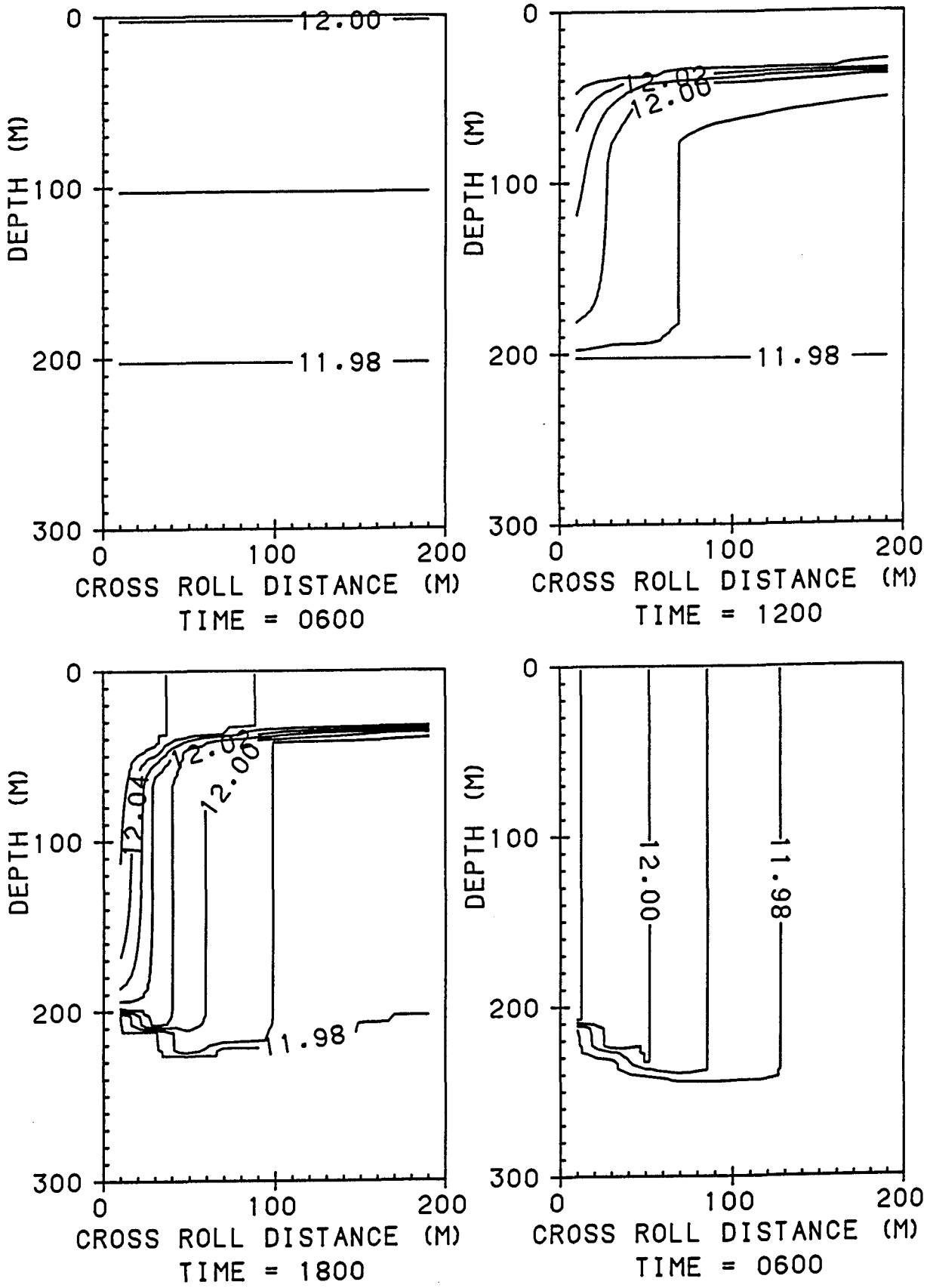

Figure 8.13 : As figure 8.9 but with four times as much advection.

cooler water has caused overturning. Water below the cell itself has been entrained.

Experiments were next performed using a different initial profile, this time imposing a mixed layer in the upper 200m, and a thermocline below (as in figure 5.14). Figure 8.14 shows the temperature field evolution over 24 hours, with the same surface forcing as figure 8.9. The standard velocity field of figure 8.3 has been used. Contours below a temperature of 11.95°C have not been plotted; the temperature gradient is simply a continuation of that between 200m and 210m. The temperature field evolves in a similar way to that in figure 8.9. If the velocity field is multiplied by four, there is this time no entrainment of water below the circulation, since the thermocline inhibits deepening.

8.4 Simulation runs

Obviously the imposed circulation does help to carry heat downwards faster and more deeply than the one- dimensional model can achieve with wind mixing alone. In order to examine the heating signal in more detail, the first day only (day 67) will be considered. Figure 8.15 illustrates the filtered, observed temperature signal at the VACMs on day 67. In figure 8.16 is shown the diurnal signal predicted by the Kraus- Turner model with no advection. Figure 8.17 shows the result of imposing the standard advection field of figure 8.3, assuming the temperature sensors to lie in the downwelling zone of the cell. It is seen that the advection has slightly improved the simulation; at 15m, the diurnal heating signal is some 10mK larger. At 125m and 145m, there is now a visible diurnal signal of about 20mK. Although this is closer to the observed signal than the one- dimensional results are, the heating is still not reaching the lower depths quickly enough. The temperature field associated with this time series is shown in figure 8.18, where isotherms are plotted every six hours. The contour

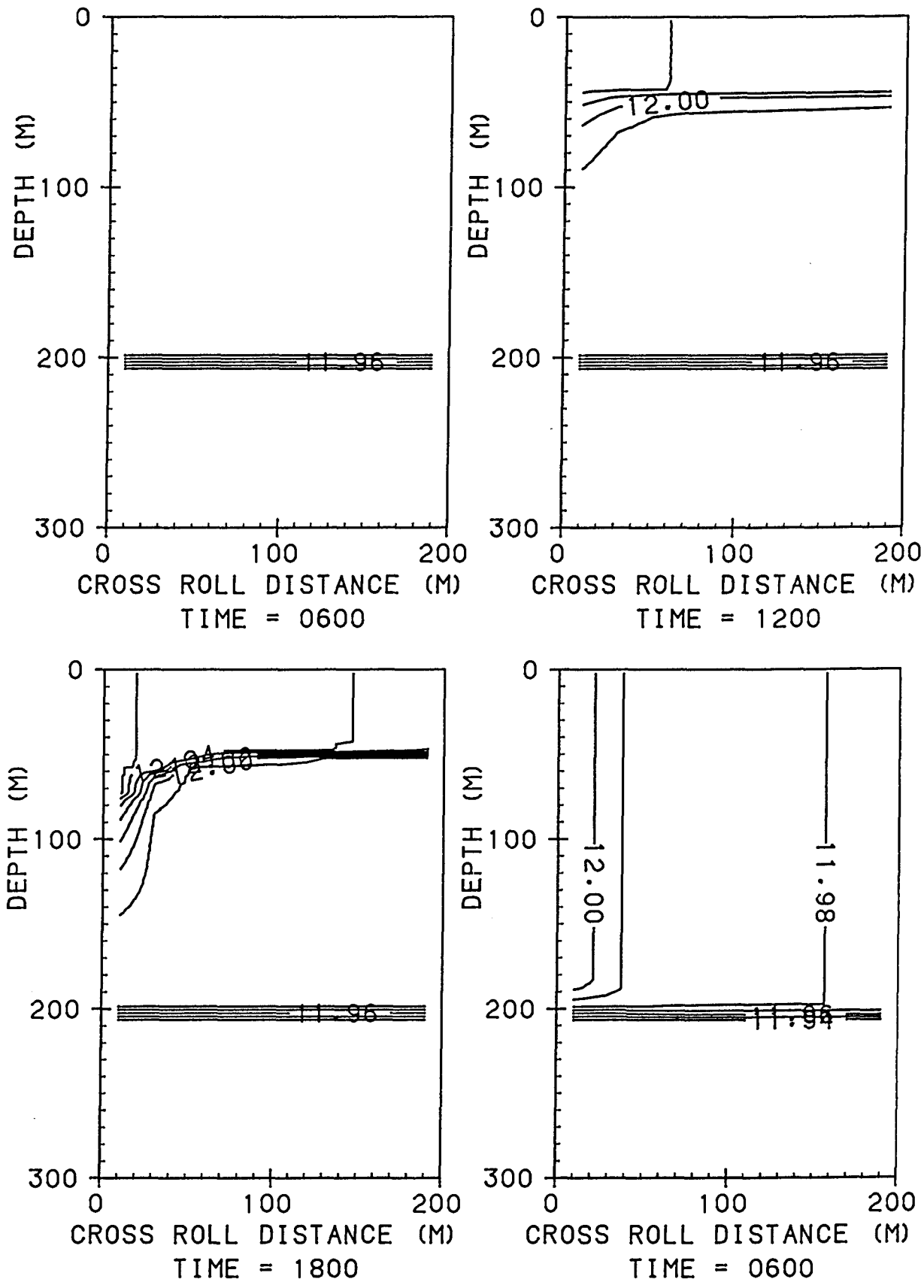

Figure 8.14 : As figure 8.9 but using the initial state shown in the first graph, including a mixed layer from the surface to 200m and a thermocline beneath. Contours of temperature below 11.94°C have been omitted for clarity. The contour interval is 0.01°C.

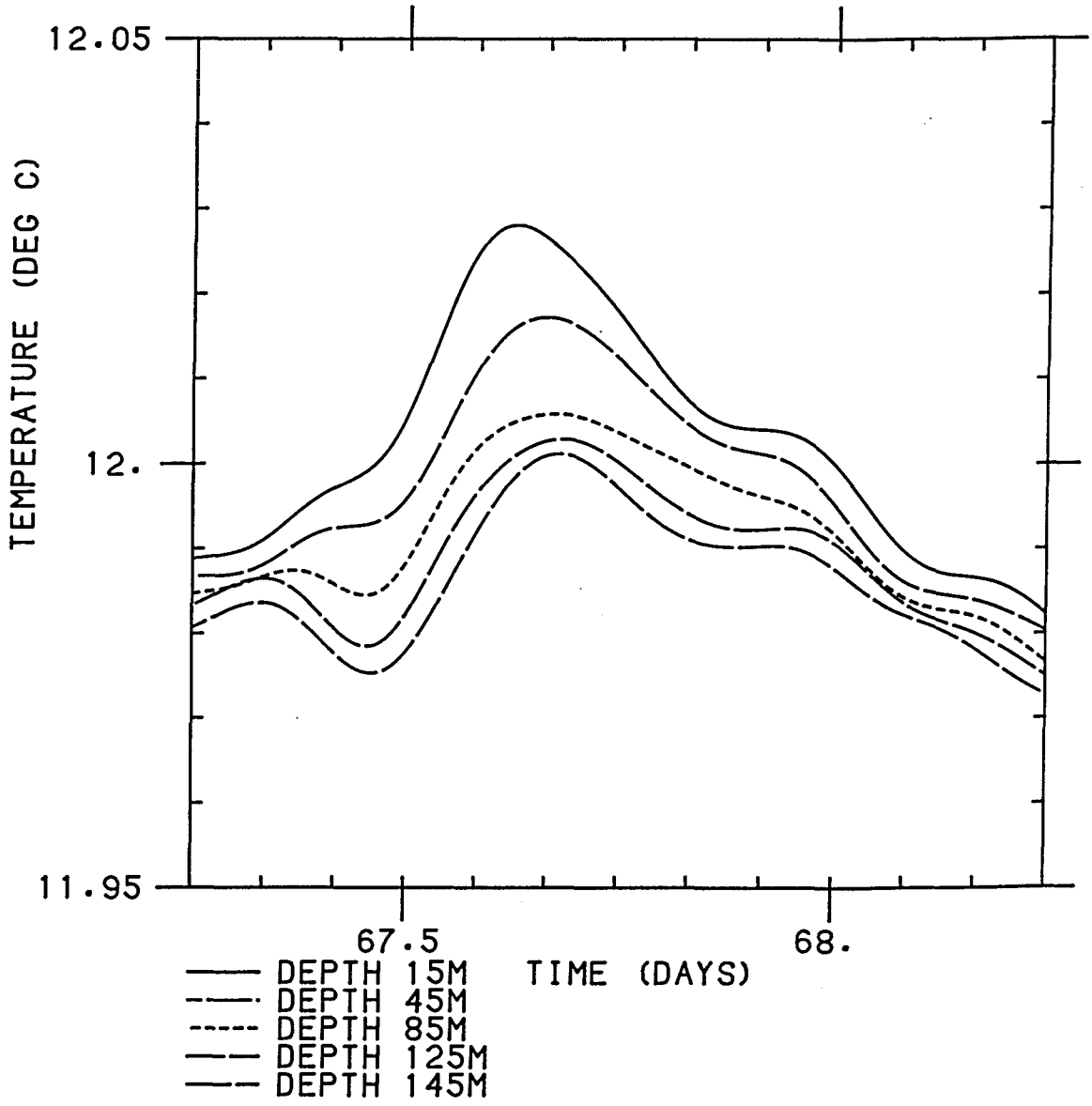

Figure 8.15 : Observed temperature signal at the VACMs on day 67. The data have been filtered to remove signals of less than a few hours period.

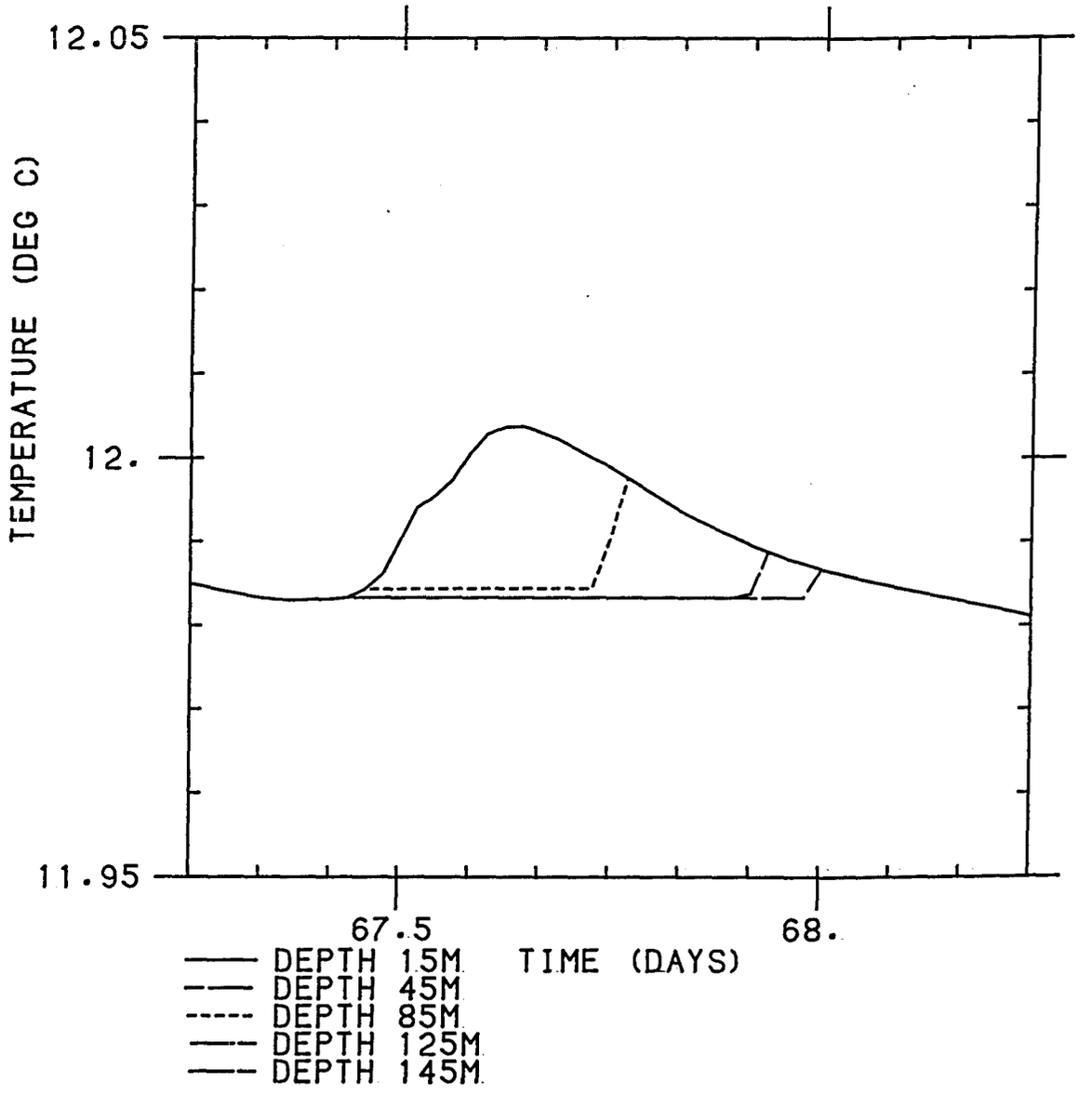

Figure 8.16 : Predicted temperature time series at the VACMs using the one- dimensional KT model.

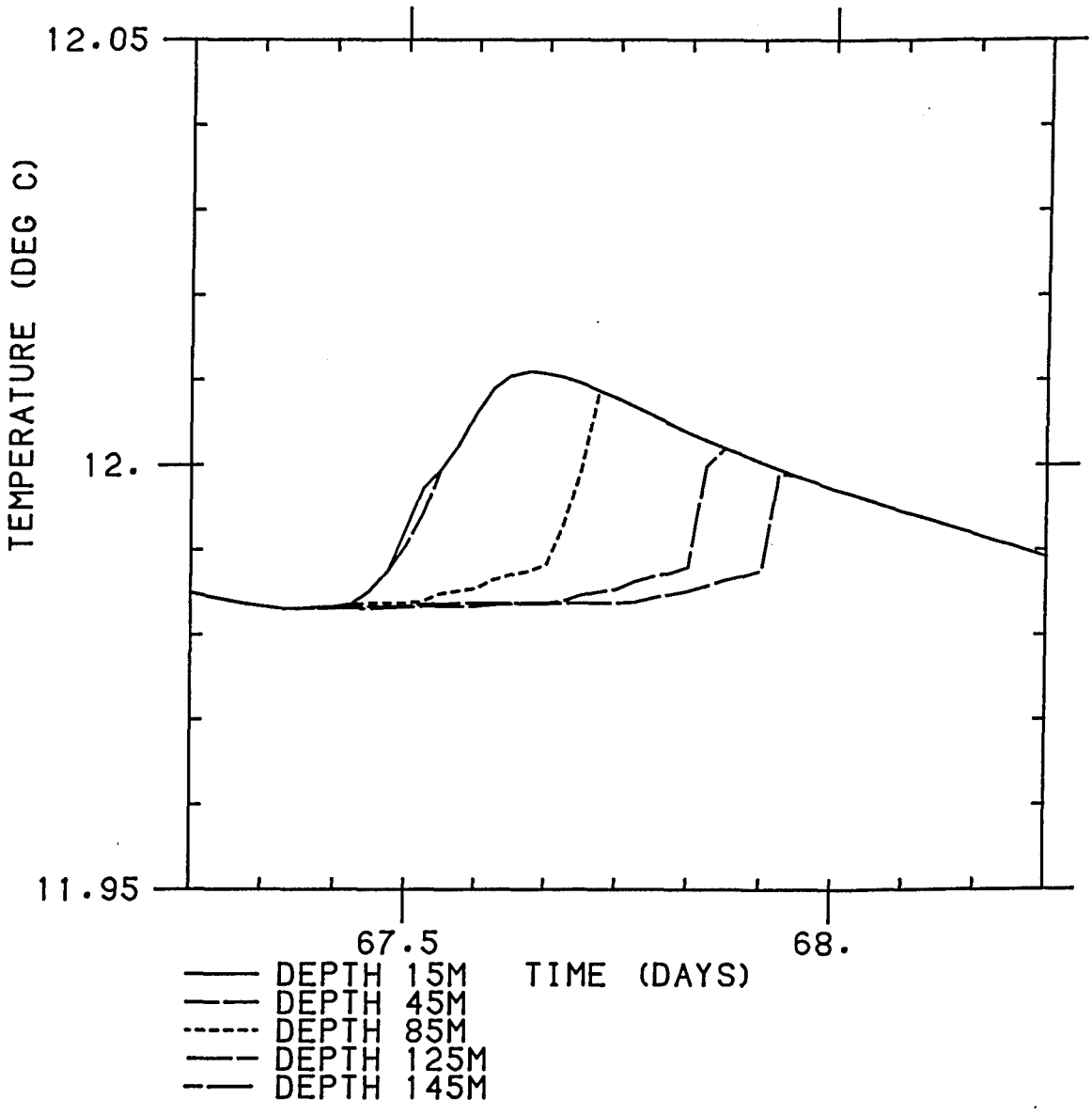

Figure 8.17 : Predicted temperature time series at the VACMs using the two- dimensional model with advection using the velocity field of figure 8.3.

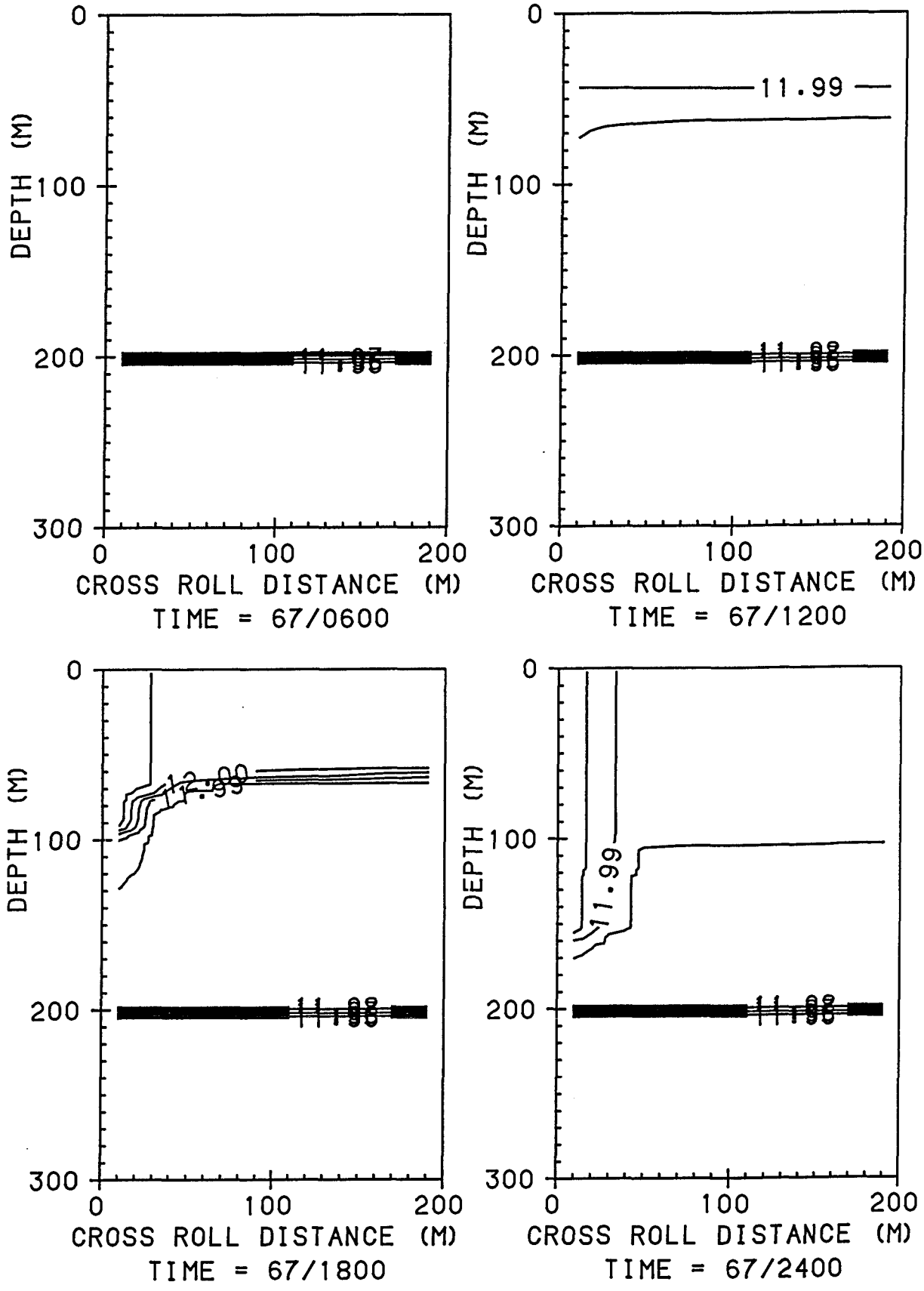

Figure 8.18 : Evolution of the temperature field across the roll during day 67. Isotherms greater than 11.95°C are plotted every 6 hours. Advection is applied using the velocity field of figure 8.3.

interval here is 0.05°C and only isotherms above 11.95°C are shown. At 1800 the 11.99°C isotherm is about 50m deeper on the left- hand- side than it is in the middle or right- hand- side.

A series of runs were undertaken to investigate the effect of increasing the circulation strength on the amplitude and phase of the observed diurnal signal. For example, multiplying the velocity field of figure 8.3 by four increases the amplitude of the signal, and decreases the time lag between the signal reaching 15m and the lower depths. For this velocity field, the mean downwelling in the left-hand grid boxes is 0.7cm/s, while the maximum into any grid box is 1.1cm/s. (In order to perform this run whilst satisfying the CFL condition, it was necessary to reduce the time step to 7.5 minutes instead of 0.5 hours; it was shown in chapter 5 that this makes negligible difference to the results.) Figure 8.19 illustrates the horizontal temperature distribution across the roll for this run. Notice particularly the strong horizontal temperature gradient that has developed by 1800. The spike in the 11.975°C isotherm at 70m across the roll occurs because the individual mixed layer models are not allowed to mix horizontally. Warmer water has entered the column from the left, and overturning has happened beneath the stratified waters of the top 50m. At 2400, cooler water can be seen upwelling on the right-hand- side.

The effect of increasing the imposed velocities is shown in figure 8.20. 'Circulation strength' gives a measure of the speed of the circulation; the velocity field of figure 8.3 is defined to have a circulation strength of 1. The one- dimensional model has a circulation strength of 0 while figure 8.19 showed results for a circulation strength of 4. Figure 8.20(a) shows the time lag of the maximum of the diurnal signal between depths of 15m and 125m. Error bars denote uncertainty in estimating the times of maximum diurnal

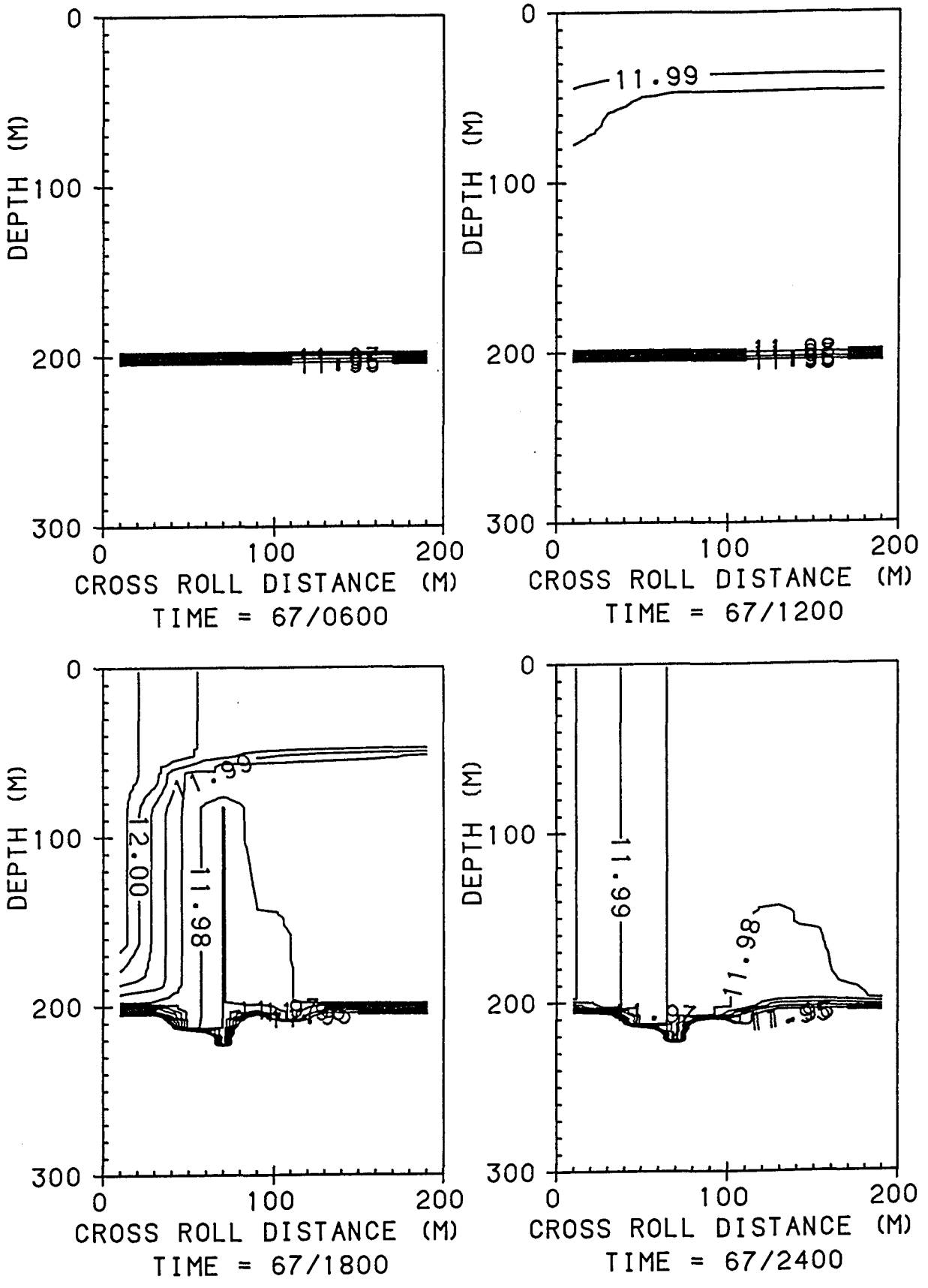

Figure 8.19 : Evolution of the temperature field across the roll. As figure 8.18 but advection is four times as large.

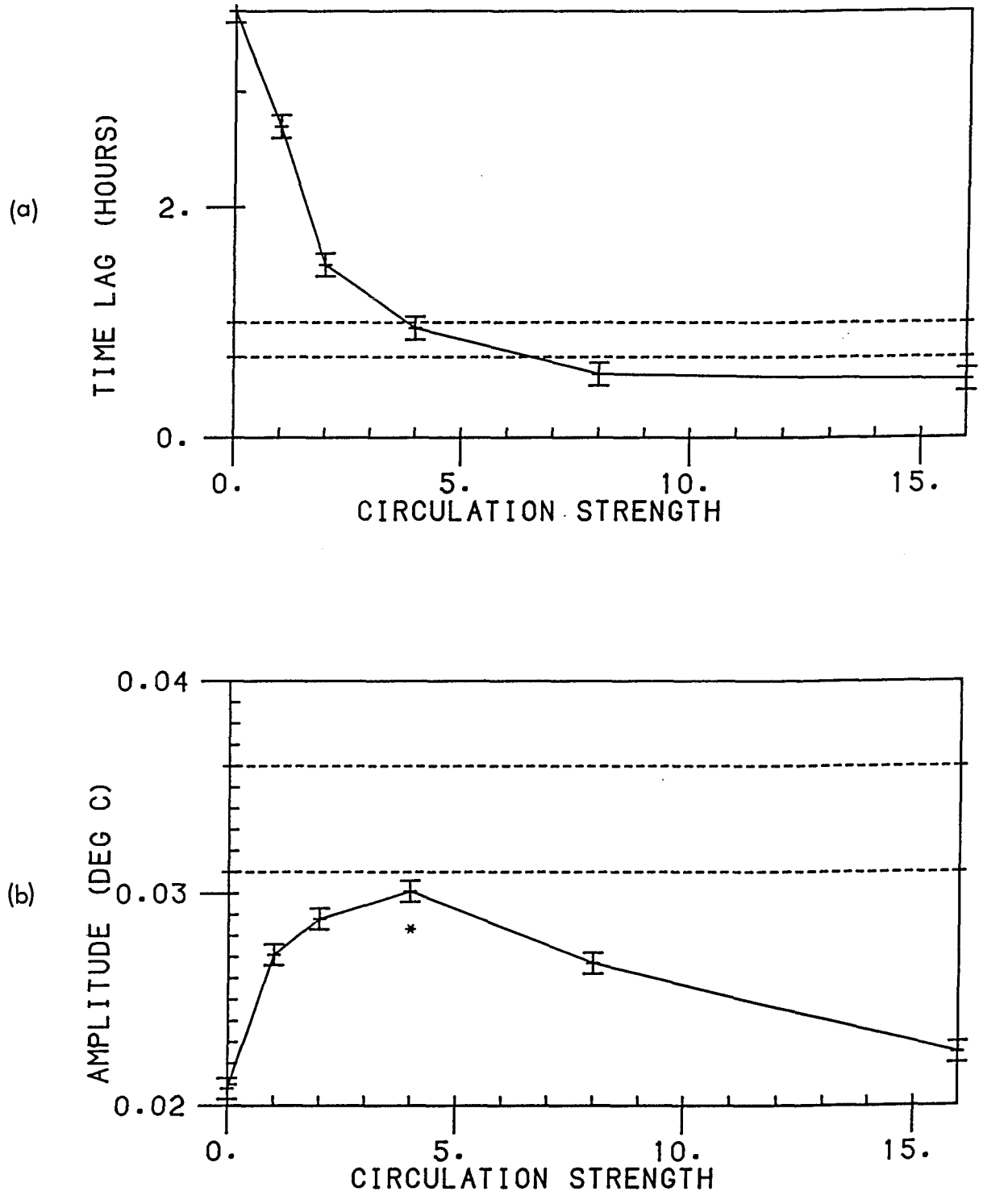

Figure 8.20 : Variation of the diurnal signal predicted by the model for various speeds of imposed circulation. (a) shows the time lag between depths of 15m and 125m. (b) shows the amplitude at a depth of 45m. The observed phase and amplitude lie between the dotted lines. The star shows the amplitude of the diurnal signal if a symmetrical circulation of strength 4 is imposed. The phase lag is the same as that obtained using an asymmetrical velocity field.

signal. The time lag observed in the data lies somewhere between the two dotted lines. The required circulation strength is therefore approximately 4 to 6. Figure 8.20(b) illustrates the variation of the maximum amplitude of the diurnal signal at a depth of 45m. The amplitude for a circulation strength of 8 is smaller than that for 4; this is because the advection is taking heat downwards more quickly; there is less stratification and the wind can mix more deeply.

The observed amplitude of diurnal signal at 45m lies somewhere between the two dotted lines. The circulation strength of 4 to 6 again seems the best fit to the data. However the modelled amplitude is still slightly smaller than that observed. The modelled signal could be increased by decreasing the width of the 'boundary current' in the imposed velocity field. By increasing ξ in equation 8.1, a narrower downwelling region would be obtained, which would enhance the diurnal signal. To test this, the symmetrical velocity field described in section 8.4.1 was applied. Even though the maximum downwelling velocity is the same, the modelled diurnal signal was smaller in magnitude, because the warm water is not swept in so quickly at the surface. The star in figure 8.20(b) gives the amplitude of the signal if a symmetrical circulation of strength 4 is imposed; it is smaller than the asymmetric case. However the phase lag is indistinguishable from that using the asymmetrical circulation of the same strength.

For completeness, the entire six day time series of temperature predicted at the VACMs using four times the advection of the standard run is shown in figure 8.21. It is interesting to note that the larger downwelling at the VACMs does not significantly affect the cooling of the column. The final temperatures at the VACMs are very similar (within 0.005°C) in both model runs. The depth of the diurnal heating cycle is however much greater with the larger advection. Comparing both with the observed data (figure 2.7) and the one- dimensional model

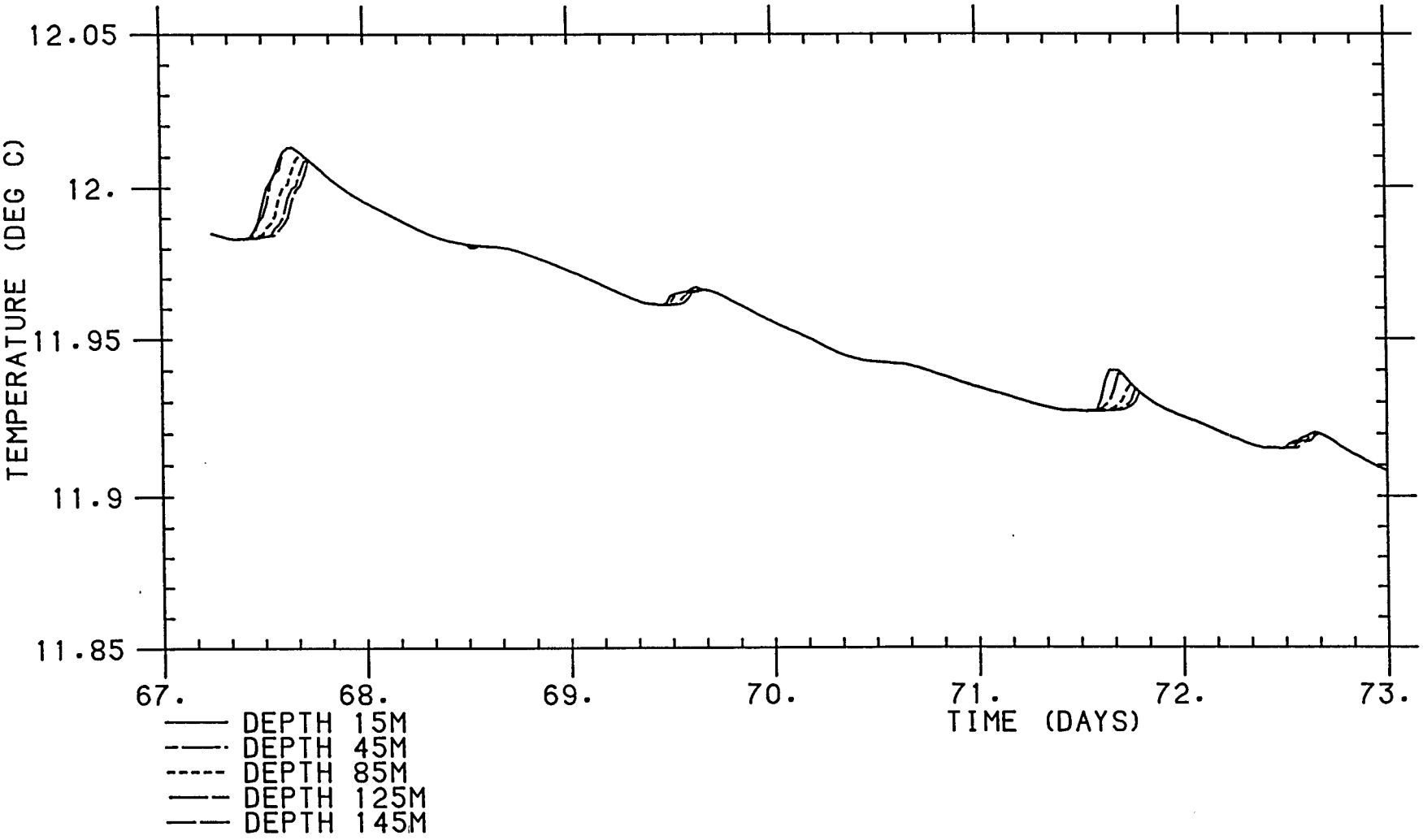

Figure 8.21 : Temperature time series at the depths of the VACMs on the left- hand column of the two- dimensional model. The advection is four times that of the standard run.

(figure 5.16), and remembering that the cooling event early on day 69 was due to horizontal advection, it is seen that the inclusion of a circulating cell has greatly improved the simulation of the data.

8.5 Discussion

This model was not developed in order to simulate exactly the temperature time series at the VACMs. It was intended as a tool to see whether the assumption of a Langmuir circulation improved our understanding of the diurnal signal, and if so, what the likely magnitude of the circulation would be. It must be remembered that there are several approximations in the model which limit its realistic nature. The assumption that the circulation may be modelled by a two-dimensional roll implies that the horizontal along- roll temperature variations are small compared to those across the roll.

The model assumes that the roll size is fixed at 200m wide and 200m deep. These dimensions were chosen after consideration of the SeaSoar data described in chapter 7, and also remembering that a Langmuir cell width is usually approximately equal to the depth of the mixed layer (chapter 6). The initial state prescribed in the model has a mixed layer of depth 200m. Experimental evidence of Langmuir circulations (chapter 6) shows that rolls tend to increase in size until limited by the depth of the thermocline. During the six- day model run, the mixed layer deepens by about 40m and so the advection field should deepen also. The justification for keeping a fixed velocity field during daytime stratification is that the density gradient built up during the day is really very small compared to that in the thermocline. Leibovich and Lele (1982) found that a thick thermocline of large gradient was required to inhibit growth of the cell.

A further assumption is that the temperature of the water in a given column may become mixed by the wind and/or convection, but the

velocity field is not allowed to be mixed. Observations (e.g. Scott et al, 1969, discussed in chapter 6) show that Langmuir circulations do exist in a well- mixed layer. It is envisaged that there are two different scales of mixed layer flow. The Langmuir cell is pictured as a large- scale (of order 200m) slow circulation, whereas the convection and wind mixing are assumed to be small scale, rapid, turbulent motions.

The model does not allow any mixing to take place in the horizontal direction, and can produce significant horizontal temperature gradients (for example, 20mK across 100m in figure 8.11). Interestingly, horizontal temperature gradients of this order of magnitude are observed in the SeaSoar data (figures 7.2, 7.4 and 7.6). This is therefore not a major failing of the model. Although numerical diffusion occurs in the model since an upstream differencing scheme is used, this has been shown not to have a significant effect on the model results.

This simple model has shown that it is possible to quantify the effect of Langmuir circulations on the development of the mixed layer. The assumption of a circulation of width and depth 200m does improve the simulation of the temperature time series at the VACMs. Tests to fit the phase and amplitude of the diurnal signal on day 67 at the depths of the VACMs showed that a 'circulation strength' of about 4 to 6 is required. The mean vertical velocity in the far left- hand column is therefore approximately 0.7cm/s, while the maximum is approximately 1.1cm/s. Although this is much larger than is usually assumed for vertical velocities in the upper ocean (metres per day, at most), it is of the same order as vertical velocities measured in Langmuir circulations (chapter 6). Therefore it is not unrealistic to infer the existence of such vertical velocities in the open ocean.

Chapter 9

Conclusions

9.1 - Summary

This thesis has discussed observations of the diurnal heating cycle during a six- day deployment of a freely- drifting, upper ocean spar buoy, beneath which were suspended instruments (VACMs) measuring temperature and horizontal velocity. Time series of temperature at various depths between 15m and 145m were obtained, which were calibrated to within an accuracy of about 2mK. At night, the upper ocean was uniform in temperature as the mixed layer deepened and cooled due to the combined effect of surface cooling and wind mixing. During the day, solar heating was sufficient to stratify the upper 150m. The diurnal heating signal observed was of the order of 30-50mK, even at 145m. Since this is well below the depth to which direct solar heating might penetrate (a few tens of metres at most), there must have been some additional process such as wind mixing, eddy diffusion or downwelling, carrying the heat downwards.

Because the measurements were taken at a spar buoy drifting with the mean current in the upper 10m, horizontal advection of water past the instrumentation should have been minimised. Using temperature data from the SeaSoar survey and the horizontal velocities measured at the spar buoy, it was possible to calculate the effect of horizontal advection past the spar buoy. Apart from a short period when the spar buoy crossed a large (30mk) ramp- like structure, the horizontal advection was shown to produce a negligible diurnal signal, which was, in any case, in antiphase with the observations. The experiment was therefore a quasi- Lagrangian one.

A high quality data set of meteorological observations was obtained at sea. This was thoroughly checked and calibrated against other instruments on the ship. The air- sea heat and momentum fluxes

were calculated using bulk formulae due to Large and Pond (1981, 1982). The heat budget of the upper 150m of the ocean was studied using the temperature time series at the VACMs and the surface heat fluxes. It was found that insufficient heat was provided by the meteorological fluxes to produce the observed temperature rises at the VACMs during the heating periods. On some days, only half of the observed temperature increase could be accounted for. The heat budget at night was more intractable, since the cooling due to entrainment of colder, denser water was not known. Therefore one could not say whether the large observed cooling, which could not all be accounted for by the surface fluxes, was caused by entrainment, or by the same mechanism as was producing the anomalously large heating signal during the morning and afternoon. During the day, entrainment is assumed small, but will cool the layer anyway, thus reducing the heating observed.

The possible explanations for this anomaly were debated. Errors in instrumentation were discounted since a patch of water could be found upstream of the spar buoy, in which temperatures recorded by the SeaSoar agreed with those at the VACMs. Estimates of the uncertainties in the meteorological fluxes were taken at their largest possible values when calculating the heat budget, so heat flux errors were rejected as an explanation. It was concluded that the only plausible interpretation of the large diurnal heating signal was that the spar buoy had drifted into a convergence zone, and experienced downwelling.

In chapter 6 the possible mechanisms for a downwelling zone were reviewed. Although frontal activity is commonplace in the upper ocean, and was initially thought a likely downwelling source, the literature suggested that downwelling velocities of at most millimetres per second would be produced, whereas velocities of order centimetres per second were required. Langmuir circulations are a frequent occurrence in the upper ocean, and have been observed to produce substantial downwelling

in their convergence zones, of up to 20cm/s (Weller et al., 1985). The theories of Langmuir cell generation were discussed. The wave- current interaction theories (Leibovich, 1983) have achieved general acceptance, but in the open ocean, cell generation by instability of the Ekman layer (Faller, 1971) cannot be ruled out. Assaf et al. (1971) observed both large rolls believed to be caused by Ekman instability, and small rolls due to wave- current interaction. It was suggested that both mechanisms may act together; wave- current interaction is a quickly acting mechanism, and over time scales of the order of a day is likely to be modified by the effects of the Ekman instability.

Data from the SeaSoar were examined at points when the ship passed the spar buoy. Since the gradient of the path of the SeaSoar was between 1 in 3 and 1 in 5, it was claimed that the variations observed in temperature were caused more by horizontal structure in the water than by vertical variability. It was concluded that the likely width of Langmuir circulations was of the order of a few hundred metres, which agreed with the observations and model predictions that cell width is of the same order as the mixed layer depth.

Finally a numerical model of a Langmuir cell was developed. It consisted of a row of one- dimensional models (introduced and tested in chapter 5), connected by a fixed, non- divergent velocity field which advected the heat both horizontally and vertically. The spar buoy and VACMs were assumed to have drifted into the downwelling zone of the cell. It was found that the downwelling did indeed increase the diurnal heating signal predicted at the depths of the VACmMs, so that it was closer to that observed. The time lag between the heating signal at the upper and lower VACMs was found to be significantly reduced to a couple of hours in the two- dimensional model. By altering the magnitude of the applied velocity field, it was shown that

the mean vertical velocity required at the spar buoy was approximately 1cm/s.

9.2 - Concluding remarks

In calculating the heat budget of the upper ocean, it is important to know that one is measuring the same patch of water throughout the experiment. For this reason, Lagrangian experiments should be conducted, using freely- drifting spar buoys or floats. However, this research has shown that freely- drifting instruments may yield biased results since they may tend to drift into convergence zones. These convergence zones may be associated with Langmuir circulations. Their effect is more likely to be observed in a deep (of order 100m) mixed layer where cell widths may be several hundred metres. Temperatures in convergence zones are likely to be anomalously warm during the day, and anomalously cool at night. The downwind current will probably also be enhanced. The downwelling and convergence will be more noticeable when a strong, steady wind has blown for several days allowing cells to develop.

Langmuir circulations have long been considered important in studies of lakes, particularly when looking at biological activity. There is evidence to suggest that horizontal roll vortices may be a frequent occurrence in the open ocean, just as cloud streets are in the atmosphere. They may not always be immediately apparent in the absence of weed or surface drifters. However the presence of Langmuir circulations will affect the mixed layer structure both vertically and horizontally, and may assist in carrying heat downwards into the ocean. It is therefore vital, during upper ocean experiments, to know whether Langmuir cells are present. This is easily done by sprinkling the ocean surface with small drifters such as pieces of floating card.

Further experimental studies of Langmuir circulations in the ocean are required using modern techniques to measure velocities and

temperatures both along and across the Langmuir cell. Recent advances in our understanding of such circulations have come mainly from the development of theories and numerical models of Langmuir cells. A comprehensive observational project to collect data at sea to test such theories should be undertaken. The methods used by Thorpe and Hall (1980, 1982) might be applied in the open ocean, using bubbles to trace the downwelling regions. The observations of Weller et al. (1985) from the drifting rig FLIP give an example of the type of experiment required. Again however it must be remembered that FLIP will spend more time in downwelling zones than upwelling zones due to the surface convergence.

As well as specifically designed experiments to study Langmuir circulations, vertical velocities should be measured more regularly whenever horizontal currents are being studied, so that data about the small- scale variability of vertical velocities are obtained. The recently- developed acoustic doppler profiler may enable the more routine estimation of vertical velocities; it may measure to an accuracy of at least 1cm/s. It is important to investigate the small-scale processes whereby heat is transferred between the atmosphere and the ocean. These will include waves and Langmuir circulations as well as wind mixing and convection. In this way better- understood parameterisations can be devised to model the air- sea interaction.

References

Adamec, D., R.L. Elsberry, R.W. Garwood and R.L. Haney, 1981, An embedded mixed- layer- ocean circulation model, Dyn. Atmos. Oceans, 6, pp 69-96

Anderson, E.R., 1952, Energy budget studies, U.S. Geol. Surv. Circ. 229, pp 71-119

Angel, M.V. et al., 1984, RRS Discovery Cruise 146: 27th March - 24th April 1984, Biological and physical investigations at 39°30'N 15°W to 46°N 14°W of the events leading up to and associated with the onset of thermal stratification. Institute of Oceanographic Sciences, Report No. 168, 69pp

Assaf, G., R. Gerard and A.L. Gordon, 1971, Some mechanisms of oceanic mixing revealed in aerial photographs, J. Geophys. Res., 76, pp 6550-6572

Bowers, C.M., J.F. Price, R.A. Weller and M.G. Briscoe, 1986, Data tabulations and analysis of diurnal sea surface temperature variability observed at LOTUS, Tech. Rep. WHOI-86-5, 51pp

Brown, R.A., 1972, The inflection point instability problem for stratified rotating boundary layers, J. Atmos. Sci., 29, pp 850-859

Brown, R.A., 1980, Longitudinal instabilities and secondary flows in the planetary boundary layer: a review, Rev. Geophys. Space Phys., 18, pp 683-697

Brown, R.A. and F. Lee, 1972, A shooting method application to the stability problem for stratified rotating boundary layers, J. Comput. Phys., 10 (2), pp 107-122

Budyko, M.I., 1974, Climate and Life, Academic Press, 508pp

Bunker, A.F., 1976, Computation of surface energy flux and annual air-sea cycle of the North Atlantic ocean, Mon. Weather Rev., 104, pp 1122-1140

Carnes, M.R. and T. Ichiye, 1985, Numerical modelling of Langmuir circulation and its application, pp 471-477, The Ocean Surface, eds. Y. Toba and H. Mitsuyasu, D. Reidel Pub. Co.

Churchill, J.H. and G.T. Csanady, 1983, Near- surface measurements of quasi- Lagrangian velocities in open water, J. Phys. Oceanogr., 13, pp 1669-1680

Craik, A.D.D., 1970, A wave- interaction model for the generation of windrows, J. Fluid Mech., 41, pp 801-821

Craik, A.D.D., 1977, The generation of Langmuir circulations by an instability mechanism, J. Fluid Mech., 81, pp 209-223

Craik, A.D.D. and S. Leibovich, 1976, A rational model for Langmuir circulations, J. Fluid Mech., 73, pp 401-426

Cushman- Roisin, B., 1981, Effects of horizontal advection on upper ocean mixing: a case of frontogenesis, J. Phys. Oceanogr., 11 (10), pp 1345-1356

Davis, R.E., R. de Szoeke and P. Niiler, 1981, Variability in the upper ocean during MILE, Deep- Sea Res., 28 (12A), pp 1427-1475

Deardorff, J.W., G.E. Willis and D.K. Lilly, 1969, Laboratory investigation of non- steady penetrative convection, J. Fluid Mech., 35, pp 7-31

Deardorff JW, GE Willis and DK Lilly, 1974, Comments on "Non precipitating cumulus convection and its parameterization", Q. J. R. Met. Soc. 100, pp 122-123

Denman, K.L., 1973, A time- dependent model of the upper ocean, J. Phys. Oceanogr., 3, pp 173-184

Denman, K.L. and M. Miyake, 1973, Upper layer modification at ocean station Papa: Observations and Simulation, J. Phys. Oceanogr., 3, pp 185-196

Dessureault, J.G., 1976, 'Batfish', A depth controllable towed body for collecting oceanographic data, Ocean Engng, 3, pp 99-111

Dyke, P.P.G. and S.F. Barstow, 1983, The importance of Langmuir circulations to the ecology of the mixed layer, in North Sea Dynamics, ed. Sundermann/ Lenz, Springer- Berlag, Berlin, Heidelberg

Ekman, V.W., 1905, On the influence of the earth's rotation on ocean currents, Ark. Mat. Astron. Fys. 2, pp 1-54

Ellison, T.H. and J.S. Turner, 1959, Turbulent entrainment in stratified flows, J. Fluid Mech., 6, pp 423-448

Elsberry, R.L., T.S. Fraim and R.N. Trapnell, 1976, A mixed layer model of the oceanic thermal response to hurricanes, J. Geophys. Res., 81, pp 1153-1162

Faller, A.J., 1963, An experimental study of the instability of the laminar Ekman boundary layer, J. Fluid Mech, 15, pp 560-576

Faller, A.J., 1964, The angle of windrows in the ocean, Tellus, XVI, pp 363-370

Faller, A.J., 1969, The generation of Langmuir circulations by the eddy pressure of surface waves, Limnol. Oceanogr., 14, pp 504-513

Faller, A.J., 1971, Oceanic turbulence and the Langmuir circulations, Ann. Rev. Ecology and Systematics, R.F. Johnston et al., editors, 2, pp 201- 236

Faller, A.J. and E.A. Caponi, 1978, Laboratory studies of wind- driven Langmuir circulations, J. Geophys. Res., 83, pp 3617-3633

Faller, A.J. and R.E. Kaylor, 1966, A numerical study of the instability of the laminar Ekman boundary layer, J. Atmos. Sci., 23, pp 466-480

Faller, A.J. and R.E. Kaylor, 1967, Instability of the Ekman spiral with applications to the planetary boundary layer, Phys. Fluids Suppl. 10, pp 212-219

Faller, A.J. and C. Perini, 1983, The role of Langmuir circulations in gas transfer across natural water surfaces, Technical Note BN-1000, Inst. for Physical Sci. and Technology, Univ. of Maryland

Faller, A.J. and A.H. Woodcock, 1964, The spacing of windrows of Sargassum in the ocean, J. Mar. Res., 22, pp 22-29

Farmer, D.M., 1975, Penetrative convection in the absence of mean shear, Q. J. Roy. Met. Soc., 101, pp 869-891

Filatov, N.N., S.V. Rjanzhin and L.V. Zaycev, 1981, Investigation of turbulence and Langmuir circulation in Lake Lagoda, J. Great Lakes Res., 7, pp 1-6

Fung, I.Y., D.E. Harrison and A.A. Lacis, 1984, On the variability of the net longwave radiation at the ocean surface, Rev. Geophys. Space Phys., 22 (2), pp 177-194

Gammelsrod, T., 1975, Instability of Couette flow in a rotating fluid and origin of Langmuir circulations, J. Geophys. Res., 80, pp 5069-5075

Garrett, C.J.R., 1976, Generation of Langmuir circulations by surface waves - a feedback mechanism, J. Mar. Res., 34, pp 117-130

Garvine, R.W., 1974, Dynamics of small- scale oceanic fronts, J. Phys. Oceanogr., 4, pp 557-569

Garvine, R.W., 1979, An integral hydrodynamic model of upper ocean frontal dynamics, Parts I and II, J. Phys. Oceanogr., 9 (1), pp 1-36

Garvine, R.W. and J.D. Monk, 1974, Frontal structure of a river plume, J. Geophys. Res., 79 (15), pp 2251-2259

Garwood, R.W., 1977, An oceanic mixed layer model capable of simulating cyclic states, J. Phys. Oceanogr., 7, pp 455-468

Garwood, R.W., 1979, Air- sea interaction and dynamics of the surface mixed layer, Rev. Geophys. Space Phys., 17, pp 1507-1524

Garwood, R.W. and D. Adamec, 1982, Seventeen years of ocean mixed layer simulations at ocean station Papa, NPS Tech. Rep. ADA 123732, 37pp

Garwood, R.W. and N.T. Camp, 1977, Comments on 'Climatological numerical models of the surface mixed layer of the ocean', J. Phys. Oceanogr., 7, pp 469-470

Garwood, R.W. and J.Y. Yun, 1979, Bulk closure model for the oceanic planetary boundary layer: a realistic and numerically efficient model, Proc. 2nd Symp. Turbulent Shear Flows, Imperial Coll., London, July 2-4

Gill, A.E., 1982, Atmosphere- Ocean Dynamics, Academic Press, New York, 662pp

Gill, A.E. and L.N. Trefethen, 1977, A mixed layer model, Ocean Modelling, 5, pp 1-4, unpublished manuscript

Gill, A.E. and J.S. Turner, 1976, A comparison of seasonal thermocline models with observations, Deep- Sea Res., 23, pp 391-401

Harris, G.P. and J.N.A. Lott, 1973, Observations of Langmuir circulations in Lake Ontario, Limnol. Oceanogr., 18, pp 584-589

Henderson- Sellers, B., 1984, A new formula for latent heat of vaporization of water as a function of temperature, Q. J. Roy. Met. Soc., 110 (466), pp 1186-1190

Henderson- Sellers, B., M.J. McCormick and D. Scavia, 1983, A comparison of the formulation for eddy diffusion in two one-dimensional stratification models, Appl. Math. Modelling, 7, pp 212-215

Hinze, J.O., 1959, Turbulence - an introduction to its mechanism and theory, McGraw- Hill, New York, 596pp

Horch, A., W. Barkmann and J.D. Woods, 1983, Die Erwarmung des Ozeans hervorgurufen durch solare Strahlungsenergie, Kiel: Institut fur Meereskunde, Bericht No. 120

Ichiye, T., 1964, On a dye diffusion experiment off Long Island, Tech. Rep. No. CU-9-64 to ONR Contract No. 266(48), Lamont Geological Observatory

Ichiye, T., 1967, Upper ocean boundary layer flows determined by dye diffusion, Phys. Fluids, 10, pp S270-S277 (Suppl.)

Ichiye, T., J.R. McGrath and M. Howard, 1985, Some dynamic features of Langmuir circulations, pp 479-486, The Ocean Surface, eds. Y. Toba and H. Mitsuyasu, D. Reidel Pub. Co.

Iooss, G., H.B. Neilsen and H. True, 1978, Bifurcation of the stationary Ekman flow into a stable periodic flow, Arch. Rat. Mech. Anal., 68, pp 227-256

Ivanoff, A., 1977, Oceanic absorption of solar energy, pp 47-71 of Modelling and Prediction of the Upper Layers of the Ocean, ed. E.B. Kraus, Pergamon, Oxford

James, I.D., 1978, A note on the circulation induced by a shallow- sea front, Estuar. Coastal Mar. Sci, 7, pp 197-202

Jerlov, N.G., 1968, Optical Oceanography, Elsevier, Amsterdam, 194pp

Kantha, L.H., 1977, Note on the role of internal waves in thermocline erosion, pp 173-177 in Modelling and Prediction of the Upper Layers of the Ocean, ed. E.B. Kraus, Pergamon Press, Oxford

Kantha, L.H., O.M. Phillips and R.S. Azad, 1977, On turbulent entrainment at a stable density interface, J. Fluid Mech., 79, pp 753-768

Kato, H. and O.M. Phillips, 1969, On the penetration of a turbulent layer into stratified fluid, J. Fluid Mech., 37, pp 643-655

Katz, B., R. Gerard and M. Costin, 1965, Responses of dye tracers to sea surface conditions, J. Geophys. Res., 70, pp 5505-5513

Kaylor, R. and A. Faller, 1972, Instability of the stratified Ekman boundary layer and the generation of internal waves, J. Atmos. Sci., 28, pp 497-509

Kenney, B.C., 1977, An experimental investigation of the fluctuating currents responsible for the generation of windrows, Ph.D. thesis, University of Waterloo, Ont., 163pp

Kraus, E.B., 1967, Organized convection in the ocean surface layer resulting from slicks and wave radiation stress, Phys. Fluids, 10, pp S294-S297 (Suppl.)

Kraus, E.B., 1972, Ocean- Atmosphere Interaction, Oxford Univ. Press, 275pp

Kraus, E.B., 1977, (editor) Modelling and Prediction of the Upper Layers of the Ocean, Pergamon Press, 325pp

Kraus, E.B. and J.S. Turner, 1967, A one- dimensional model of the seasonal thermocline. II: The general theory and its consequences, Tellus, 19, pp 98-106

Kuettner, J., 1971, Cloud bands in the earth's atmosphere: Observations and theory, Tellus, 23, pp 404-425

Kurasawa, Y., K. Hanawa and Y. Toba, 1983, Heat balance of the surface layer of the sea at OWS T, J. Oceanogr. Soc. Jap., 39 (4), pp 192-202

Laevastu, T., 1967, Cloud factor in long- wave radiation formulae, J. Geophys. Res., 72, pp 4277

Langmuir, I., 1938, Surface motion of water induced by wind, Science, 87, pp 119-123

Large, W.G. and S. Pond, 1981, Open ocean momentum flux measurements in moderate to strong winds, J. Phys. Oceanogr., 11, pp 324-336

Large, W.G. and S. Pond, 1982, Sensible and Latent heat flux measurements over the ocean, J. Phys. Oceanogr., 12, pp 464-482

Leibovich, S., 1977a, On the evolution of the system of wind drift currents and Langmuir circulations in the ocean. Part 1. Theory and the averaged current, J. Fluid Mech., 79, pp 715-743

Leibovich, S., 1977b, Convective instability of stably stratified water in the ocean, J. Fluid Mech., 82, pp 561-585

Leibovich, S., 1980, On wave- current interaction theories of Langmuir circulations, J. Fluid Mech., 99, pp 715-724

Leibovich, S., 1983, The form and dynamics of Langmuir circulations, Ann. Rev. Fluid Mech., 15, pp 391-427

Leibovich, S. and S.K. Lele, 1982, Thermocline erosion and surface temperature variability due to Langmuir circulations, FDA Rep. #82-07, Sibley School Mech. & Aerosp. Eng., Cornell Univ., Ithaca, N.Y.

Leibovich, S. and S.K. Lele, 1985, The influence of the horizontal component of Earth's angular velocity on the instability of the Ekman layer, 1985, J. Fluid Mech., 150, pp 41-87

Leibovich, S. and S. Paolucci, 1980, The Langmuir circulation instability as a mixing mechanism in the upper ocean, J. Phys. Oceanogr., 10, pp 186-207

Leibovich, S. and K. Radhakrishnan, 1977, On the evolution of the system of wind drift currents and Langmuir circulations in the ocean. Part 2. Structure of the Langmuir vortices, J. Fluid Mech., 80, pp 481-507

Leibovich, S. and D. Ulrich, 1972, A note on the growth of small- scale Langmuir circulations, J. Geophys. Res., 77, pp 1683-1688

Legeckis, R., 1978, A survey of worldwide sea surface temperature fronts detected by environmental satellites, J. Geophys. Res., 83, pp 4501-4522

LeMone, M., 1973, The structure and dynamics of horizontal roll vortices in the PBL, J. Atmos. Sci., 30 (6), pp 1077-1091

LeMone, M., 1976, Modulation of turbulence energy by longitudinal rolls in an unstable boundary layer, J. Atmos. Sci., 33 (7), pp 1308-1320

Levine, E.R. and W.B. White, 1972, Thermal frontal zones in the Eastern Mediterranean Sea, J. Geophys. Res., 77 (6), pp 1081-1086

Lilly, D.K., 1966, On the stability of Ekman boundary flow, J. Atmos. Sci., 23, pp 481-494

Lind, R.J. and K.B. Katsaros, 1982, A model of longwave irradiance for use with surface observations, J. Appl. Meteorol., 12, pp 1015-1023

Lind, R.J., K.B. Katsaros and M. Gube, 1984, Radiation budget components and their parameterization in JASIN, Q. J. Roy. Met. Soc., 110, pp 1061-1071

McNally, G.J. and W.B. White, 1985, Wind driven flow in the mixed layer observed by drifting buoys during autumn- winter in the midlatitude North Pacific, J. Phys. Oceanogr., 15, pp 684-694

MacVean, M.K. and J.D. Woods, 1980, Redistribution of scalars during upper ocean frontogenesis: a numerical model, Q. J. Roy. Met. Soc., 106, pp 293- 312

Maratos, A., 1971, Study of the near shore surface characteristics of windrows and Langmuir circulation in Monterey Bay, MS thesis, US Nav. Postgrad. Sch., Monterey, Calif.

Millero, F.J., G. Perron and J.E. Desnoyers, 1973, Heat capacity of seawater solutions from 5°C to 35°C and 0.5 to 22‰ chlorinicity, J. Geophys. Res., 78 (21), pp 4499-4507

Moen, J., 1978, A theoretical model for Langmuir circulations, Ph. D. thesis, Univ. Southampton, 235pp

Munk, W.H. and E.A. Anderson, 1948, Notes on a theory of the thermocline, J. Mar. Res., 7, pp 276-295

Myer, G.E., 1971, Structure and mechanics of Langmuir circulations on a small inland lake, Ph.D. dissertation, State University of New York, Albany

Nicholls, S., 1985, Aircraft observations of the Ekman boundary layer during the Joint Air- Sea Interaction Experiment, Q. J. Roy. Met. Soc., 111, pp 391-426

Niiler, P.P. and E.B. Kraus, 1977, One- dimensional models of the upper ocean, pp 143-172 in Modelling and Prediction of the Upper Layers of the Ocean, ed. E.B. Kraus, Oxford, Pergamon Press

O'Brien, J.J., R.M. Clancy, A.J. Clarke, M. Crepon, R. Elsberry, T. Gammelsrod, M. MacVean, L.P. Roed, and J.D. Thompson, 1977, Upwelling in the ocean: two- and three- dimensional models of upper ocean dynamics and variability, pp 178-228 in Modelling and Prediction of the Upper Layers of the Ocean, ed. E.B. Kraus, Oxford, Pergamon Press

Paulson, C.A. and J.J. Simpson, 1977, Irradiance measurements in the upper ocean, J. Phys. Oceanogr., 7 (6), pp 952-956

Payne, R.E., 1972, Albedo of the sea surface, J. Atmos. Sci., 29, pp 959-970

Phillips, O.M., 1977, Dynamics of the Upper Ocean, Cambridge Univ. Press, 336pp, 2nd ed.

Pollard, R.T., 1977, Observations and theories of Langmuir circulations and their role in near surface mixing, In A Voyage of Discovery: George Deacon 70th Anniversary Volume, ed. M. Angel, pp 235-251, Oxford: Pergamon

Pollard, R.T., 1983, Observations of the structure of the upper ocean: wind- driven momentum budget, Phil. Trans. R. Soc. Lond., A380, pp 407-425

Pollard, R.T. and R.C. Millard, 1970, Comparison between observed and simulated wind- generated inertial oscillations, Deep- Sea Res., 17, pp 813-821

Pollard, R.T., T.H. Guymer and P.K. Taylor, 1983a, Summary of the JASIN 1978 field experiment, Phil. Trans. R. Soc. Lond., A 308, pp 221-230

Pollard, R.T., P.B. Rhines and R.O.R.Y. Thompson, 1973 The deepening of the wind-mixed layer, Geophys. Fluid Dyn., 4, pp 381-404

Pollard, R.T., I. Waddington, K. Browne and K. Sherrocks, 1987, Drifting spar buoy: A compendium of measurements made during RRS Discovery cruises 145 and 146, IOS Report, in preparation

Pollard, R.T. et al., 1983b, RRS Discovery Cruise 132: 27th January - 20th February 1983, Physical oceanography of the upper ocean in winter in the eastern Atlantic ocean in the region 38-48 N, 10-21 W, Institute of Oceanographic Sciences, Cruise Report No. 147, 42pp

Pollard, R.T. et al., 1984, RRS Discovery Cruise 145: 25th February - 24th March 1984, The structure of the upper ocean at the end of winter in the region 40-47°N, 13-16°W, Institute of Oceanographic Sciences, Cruise Report No. 166, 47pp

Price, J.F., 1979, Observations of a rain-formed mixed layer, J. Phys. Oceanogr., 9, pp 643-649

Price, J.F., 1983, Internal wave wake of a moving storm. Part I: Energy budget and observations, J. Phys. Oceanogr., 13, pp 949-965

Price, J.F., C.N.K. Mooers and J.C. Van Leer, 1978, Observation and simulation of storm-induced mixed layer deepening, J. Phys. Oceanogr., 8, pp 582-599

Price, J.F., R.A. Weller and R. Pinkel, 1986, Diurnal cycling: observations and models of the upper ocean response to diurnal heating, cooling and wind mixing, J. Geophys. Res., 91 (C7), pp 8411-8427

Rao, G.V. and T.S. Murty, 1973, Some case studies of vertical circulations associated with oceanic fronts, J. Geophys. Res., 78 (3), pp 549-557

Reed, R.K., 1976, On estimation of net long- wave radiation from the oceans, J. Geophys. Res., 81 (33), pp 5793-5794

Roache, P.J., 1976, Computational Fluid Dynamics, Revised printing, Albuquerque, N.M., Hernosa Publishers, 446pp

Roden, G.I., 1975, On North Pacific temperature, salinity, sound velocity and density fronts and their relation to the wind and energy flux fields, J. Phys. Oceanogr., 5 (4), pp 557-571

Roden, G.I., 1976, On the structure and prediction of oceanic fronts, Nav. Res. Rev., 29 (3), pp 18-35

Roden, G.I., 1984, Mesoscale oceanic fronts of the North Pacific, Annal. Geophys., 2 (4), pp 399-410

Savidge, G., 1976, A preliminary study of the distribution of chlorophyll a in the vicinity of fronts in the Celtic and western Irish Seas, Estuar. Coastal Mar. Sci., 4, pp 617-625

Scorer, R.S., 1978, Environmental Aerodynamics, Ellis Horwood, Chichester, 488pp

Scott, J.T., G.E. Myer, R. Stewart and E.G. Walther, 1969, On the mechanism of Langmuir circulations and their role in epilimnion mixing, Limnol. Oceanogr., 14, pp 493-503

Shapiro, G.I., 1981, Dynamics of a small- scale oceanic front under wind action, Izvestiya, Atmos. Oceanic Phys., 17 (4), pp 302-307

Shay, T.J. and M.C. Gregg, 1984, Turbulence in an oceanic convective mixed layer, Nature, 310, pp 282-285, plus correction, Nature, 311, p84

Shay, T.J. and M.C. Gregg, 1987, Convectively- driven turbulent mixing in the upper ocean, submitted to J. Phys. Oceanogr.

Simpson, J.H., 1976, A boundary front in the summer regime of the Celtic Sea, Estuar. Coastal Mar. Sci., 4, pp 71-81

Simpson, J.H., C.M. Allen and N.C.G. Morris, 1978, Fronts on the continental shelf, J. Geophys. Res., 83, pp 4607-4614

Simpson, J.J. and C.A. Paulson, 1979, Mid- ocean observations of atmospheric radiation, Q. J. Roy. Met. Soc., 105, pp 487-502

Smith, J., 1980, Waves, currents, and Langmuir circulations, Ph.D. thesis, Dalhousie Univ., Halifax, N.S., 242pp

Smith, S.D. and F.W. Dobson, 1984, The heat budget at Ocean Weather Station Bravo, Atmosphere- Ocean, 22 (1), pp 1-22

Spooner, G.F., 1983, Stability of free surface Ekman layers, J. Phys. Oceanogr., 13, pp 663-677

Stewart, R. and R.K. Schmitt, 1968, Wave interaction and Langmuir circulations, Proc. 11th Conf. Great Lakes Res., Cent. Great Lakes Studies, Univ. Wis. pp 31-32

Stommel, H., 1948, The westward intensification of wind- driven ocean currents, Trans. Am. Geophys. Union, 99, pp 202-206

Stommel, H., K. Saunders, W. Simmons and J. Cooper, 1969, Observations of the diurnal thermocline, Deep- Sea Res., 16 (Suppl.), pp 269-284

Sutcliffe, W.H., E.R. Baylor and D.W. Menzel, 1963, Sea surface chemistry and Langmuir circulations, Deep- Sea Res., 10 pp 233-243

Sutcliffe, W.H.Jr., R.W. Sheldon, A. Prakash and D.C. Gordon Jr., 1971, Relations between wind speed, Langmuir circulation and particle concentration in the ocean, Deep- Sea Res., 18, pp 639-643

Tabata, S., 1965, Variability of oceanographic conditions at Ocean Station 'P' in the northeast Pacific ocean, Trans. Roy. Soc. Can., Ser. 4, 3, section 3, pp 367-418

Thompson, R.O.R.Y., 1976, Climatological numerical models of the surface mixed layer of the ocean, J. Phys. Oceanogr., 6, pp 496-503

Thompson, R.O.R.Y., 1977a, Erratum on 'Climatological numerical models of the surface mixed layer of the ocean', J. Phys. Oceanogr., 7, p157

Thompson, R.O.R.Y., 1977b, Reply to Garwood and Camp (1977), J. Phys. Oceanogr., 7, pp 470-471

Thompson, R.O.R.Y., 1978, Application of Kato, Kantha and Phillips experiments to the ocean, Ocean Modelling, 10, pp 4-7, Unpublished manuscript

Thorpe, S.A., 1984, The effect of Langmuir circulation on the distribution of submerged bubbles, caused by breaking wind waves, J. Fluid Mech., 142, pp 151-170

Thorpe, S.A., 1985, Small- scale processes in the upper ocean boundary layer, Nature, 318, pp 519-522

Thorpe, S.A. and A.J. Hall, 1980, The mixing layer of Loch Ness, J. Fluid Mech., 101, pp 687-703

Thorpe, S.A. and A.J. Hall, 1982, Observations of the thermal structure of Langmuir circulation, J. Fluid Mech., 114, pp 237-250

Trump, C.L., B.S. Okawa and R.H. Hill, 1985, The characterization of a midocean front with a doppler shear profiler and a thermistor chain, J. Atmos. Oceanic Tech., 2 (4), pp 508-516

Turner, J.S., 1969, A note on wind- mixing at the seasonal thermocline, Deep- Sea Res., 16 (Suppl.), pp 297-300

Voorhis, A.D., 1969, The horizontal extent and persistence of thermal fronts in the Sargasso Sea, Deep- Sea Res., 16 Suppl., pp 331-337

Voorhis, A.D. and J.B. Hersey, 1964, Oceanic thermal fronts in the Sargasso Sea, J. Geophys. Res., 69, pp 3809-3814

Welander, P., 1963, On the generation of wind streaks on the sea surface by action of surface film, Tellus, 15, pp 67-71

Weller, R.A., 1982, The relation of near- inertial motions observed in the mixed layer during the JASIN (1978) experiment to the local wind stress and to the quasi- geostrophic flow field, J. Phys. Oceanogr., 12 (10), pp 1122-1136

Weller, R.A., J.P. Dean, J. Marra, J.F. Price, E.A. Francis and D.C. Boardman, 1985, Three- dimensional flow in the upper ocean, Science, 227, pp 1552-1556

Woodcock, A.H., 1944, A theory of surface water motion deduced from the wind- induced motion of the physalia, J. Mar. Res., 5, pp 196-205

Woodcock, A.H. and J. Wyman, 1946, Convective motion in air over the sea, Ann. N.Y. Acad. Sci., 48, pp 749-776

Woods, J.D., 1977, Parameterizations of unresolved motions, pp 118-140 in Modelling and Prediction of the Upper Layers of the Ocean, ed. E.B. Kraus, Oxford, Pergamon Press

Woods, J.D., R.L. Wiley and M.G. Briscoe, 1977, Vertical circulation at fronts in the upper ocean, in A Voyage of Discovery, M. Angel (ed.), Supplement to Deep- Sea Res., 24, pp 253-275